Scanning Laser Doppler Vibrometry for Strain Measurement and Damage Detection

Stuart J. Wildy

School of Mechanical Engineering
The University of Adelaide
South Australia 5005
Australia

Supervised by

A/Prof Andrei Kotousov
A/Prof Ben Cazzolato
Dr John Codrington
Dr Sook-Ying Ho

Abstract

Numerous strain measurement and damage detection techniques have been developed over the last century. These techniques include strain gauges, digital image correlation, radiography and ultrasonic inspections. All have various advantages, as well as disadvantages, which make each suited to specific applications.

With the development of laser Doppler vibrometry, a number of techniques have been established for non-destructive evaluation, such as the measurement of bending strain, as well as damage detection using kinematic parameters, including displacement and curvature. With recent advancements in laser Doppler vibrometry technology (such as 3D scanning laser Doppler vibrometry for three-dimensional displacement measurements, improved velocity decoders and increased spatial resolution) the door has been opened to develop techniques for measuring surface strain from in-plane displacements, as well as the development of new damage detection techniques based on the fundamental principle of deformation:- the governing differential equation of displacement.

The extensive literature review contained in this thesis identified a number of gaps in the field, including the evaluation of the accuracy of quasi-static bending strain measurements using current 1D SLDV technology, the precision of full-field surface strain measurement techniques utilising 3D SLDV, and new detection techniques based on the violation of the governing differential equations of displacement. Thus, the research contained in this thesis focussed on these areas.

The first part of this thesis presents an investigation into the use of 1D and 3D scanning laser Doppler vibrometry for non-contact measurement of quasi-static bending strain in beams and surface strain in plates, respectively. The second part presents a new damage detection technique based on the governing differential equations of displacement in beam and plate structures. Two algorithms are developed to determine a violation in the governing differential equations created by either a delamination in a composite beam with out-of-plane displacements, or by a crack in a plate with in-plane displacements.

Declarations

Originality

This work contains no material which has been accepted for the award of any other degree or diploma in any university or other tertiary institution to Stuart Wildy and to the best of my knowledge and belief, contains no material previously published or written by another person, except where due reference has been made in the text.

Permissions

I give consent to this copy of my thesis when deposited in the University Library being made available for loan and photocopying, subject to the provisions of the Copyright Act 1968.

The author acknowledges that copyright of published works contained within this thesis (as listed below*) resides with the copyright holder(s) of those works.

I also give permission for the digital version of my thesis to be made available on the web, via the University's digital research repository, the Library catalogue, the Australasian Digital Theses Program (ADTP) and also through web search engines, unless permission has been granted by the University to restrict access for a period of time.

Stuart Wildy Date

---

* Wildy, S., Cazzolato, B., Kotousov, A. and Weisbecker, H. (2010) 'New experimental strain measurement technique utilising a 3D scanning laser vibrometer', *in Proceedings of the Sixth Australasian Congress on Applied Mechanics*, Perth, Australia, pp. 738-747.

Wildy, S., Kotousov, A. and Codrington, J. 2008, 'New passive defect detection technique', *Australian Journal of Mechanical Engineering*, vol. 6, no. 2, pp. 101-105.

Wildy, S., Lee, C. and Yong, S. 2008, 'Monitoring of crack propagation using a cluster of piezo-sensors', *in Proceedings of the Fifth Australasian Congress on Applied Mechanics*, Brisbane, Australia, pp. 366-371.

Acknowledgements

First and foremost, I would like thank my wife. She has been the one constant throughout my PhD candidature; helped me through the many lows, but there also to celebrate the many joys that I have experience during my postgraduate studies at Adelaide University.

More recently, I would also like to thank my good-looking six month old boy Seth. He has provided me with the drive to complete this thesis, but also the necessary distractions required during the long and hard slog of thesis writing and proofing.

Thanks to all my family who have supported me and encouraged me throughout all my studies. Without their help I would be lost.

I would also like to thank my supervisors, who have provided me with support and encouragement over the last 4 years. I would like to very much thank my primary supervisor Andrei Kotousov with his drive for progress and papers, which has lead me to publish a number of journal and conference publications throughout my candidature. Sook Ying Ho, who was there from the beginning of my candidature and provided me with valuable support and feedback. Ben Cazzolato, who introduced me to the 3D Scanning Laser Doppler Vibrometry system mid-way through my candidature, which is now the corner stone of this PhD thesis.

Lastly I would like to thank John “Dr.Cod” Codrington, who became my supervisor near the end of my candidature, but more than that he has become a good friend that has been there for me any time of day to bounce around ideas, and thoughts, but also provide me with reassurance that I was on the right track.

I would like to thank the cohort of Mechanical Engineering Postgraduate Students at Adelaide University for their friendship, as well as the weekly excursions to the Exeter for lunch.

Last but not least I would like to thank the Mechanical and Electrical workshops for their assistance in making and constructing my rigs.

Contents

List of Figures ..... **xiii**

List of Tables ..... **xxvii**

Nomenclature ..... **xxix**

Chapter 1. Introduction **1**

1.1 Strain Measurement 3

1.2 Non-Destructive Damage Detection 4

1.3 Aims and Objectives 5

1.4 Outline of Thesis 6

Chapter 2. Literature Review **9**

2.1 Strain Measurement 9

2.1.1 Strain Gauge *10*

2.1.2 Photoelasticity *12*

2.1.3 Moiré and Moiré Interferometry *14*

2.1.4 Holographic Interferometry *15*

2.1.5 Speckle Methods *17*

2.1.6 Digital Image Correlation *19*

2.1.7 Thermoelastic Stress Analysis *20*

2.1.8 Summary of Strain Measurement Techniques *21*

2.2 Damage Detection 22

2.2.1 Visual Inspection *23*

2.2.2 Acoustic Emission *24*

2.2.3 Ultrasonic *26*

2.2.4 Guided Waves *28*

2.2.5 Vibration-Based *29*

2.2.6 Radiography *31*

2.2.7 Eddy-current *32*
2.2.8 Electromechanical Impedance *34*
2.2.9 Summary of Damage Detection Techniques *35*
2.3 Scanning Laser Doppler Vibrometry 36
2.3.1 Strain Measurement Utilising SLDV *37*
2.3.2 Damage Detection Utilising SLDV *41*
2.3.3 Summary of Damage Detection Using SLDV *48*
2.4 Summary 50
2.4.1 Strain Measurement *50*
2.4.2 Damage Detection *51*
2.5 Gap in the Field of Research 51
2.5.1 Strain Measurement *52*
2.5.2 Damage Detection *53*
Chapter 3. Experimental Set Up.....55
3.1 Scanning Laser Doppler Vibrometry 55
3.1.1 Optical Configuration *56*
3.1.2 Principle of Heterodyne Interferometry *57*
3.1.3 1D SLDV System *59*
3.1.4 3D SLDV System *61*
3.1.5 Measurement Parameters *64*
3.2 Test Set Up 64
3.2.1 Out-of-Plane Displacement Experiments *65*
3.2.2 In-Plane Displacement Experiments *70*
3.3 Summary 76
Chapter 4. Development of New Strain Measurement Techniques 79
4.1 Sources of Errors in Vibrometry Measurement 80
4.2 In-Plane Strain 82

4.2.1 Previous Studies *83*
4.2.2 Kinematics of Deformation *85*
4.2.3 Investigation of In-Plane Strain *91*
4.2.4 Savitzky-Golay Differentiation Parameters *95*
4.2.5 Mesh Size *98*
4.2.6 Loading *100*
4.2.7 Summary of In-Plane Measurement *102*
4.3 Measurement of Strain at Stress Concentrations 104
4.3.1 Results *106*
4.3.1 Discussion *113*
4.3.2 Summary Strain Measurement at Stress Concentrators *116*
4.4 Bending Strain 116
4.4.1 Previous Studies *117*
4.4.2 Surface Strains for a Plate Loaded in Bending *119*
4.4.3 Investigation of Bending Strain *123*
4.4.4 Savitzky-Golay Differentiation Parameters *125*
4.4.5 Mesh Size *129*
4.4.6 Out-of-plane Loading Amplitude *134*
4.4.7 Summary of Bending Strain Measurement *134*
4.5 Summary 136
Chapter 5. Detection of Crack Damage 141
5.1 Previous Studies 143
5.2 Principles of Deformation in Thin Plates 147
5.2.1 Equations of Equilibrium *147*
5.2.2 Strain Compatibility *149*
5.2.3 Governing Differential Equation *150*
5.2.4 Application of GDE to Damage Detection *151*
5.3 GDE of Plate Displacement Algorithm 154

5.4 Displacement Error Algorithm 157
5.5 Surface Strain Algorithm 162
5.6 Summary 168

Chapter 6. Detection of Delamination in Composite Beams 171

6.1 Principles of Bending in Thin Plates 174

6.1.1 Equations of Equilibrium 174
6.1.2 Governing Differential Equations 177
6.1.3 Application of Principles for Damage Detection 178

6.2 Analytical Delaminated Beam Model 180
6.3 Governing Equation of Beam Deflection 182

6.3.1 Algorithm 183
6.3.2 Filter size 184
6.3.3 Delamination Length 187
6.3.4 Delamination Depth 189

6.4 Beam Deflection Error 192

6.4.1 Previous Studies 192
6.4.2 Algorithm 194
6.4.3 Filter Size 196
6.4.4 Delamination Length 199
6.4.5 Delamination Depth 202

6.5 Beam Curvature Error 205

6.5.1 Previous Studies 205
6.5.2 Algorithm 206
6.5.3 Filter Size 208
6.5.4 Delamination Length 211
6.5.5 Delamination Depth 213

6.6 Summary 216

Chapter 7. Conclusion 223

7.1 Strain Measurement 224

7.1.1 In-Plane Strain 225

7.1.2 Bending Strain 226

7.2 Damage Detection 227

7.2.1 Detection of Crack Damage 228

7.2.2 Detection of Delamination in a Composite Beam 229

7.3 Overview 231

7.4 Further Research Possibilities 232

References 235

Appendix A. Strain Compatibility Equations 245

Appendix B. Savitzky-Golay Differentiating Filter 247

B.1 1D Filter Structure 247

B.2 2D Filter Structure 248

Appendix C. Delaminated Beam Model 251

Appendix D. Damage Detection Results 259

D.1 Governing Differential Equation of In-Plane Displacement 261

D.2 Displacement Error 265

D.3 Surface Strain Algorithm 271

Appendix E. Related Publications 279

E.1 Referred Journal Publications 279

E.2 Refereed Conference Publications 280

E.3 Abstract Reviewed Conference Publication 282

Appendix F. Awards and Achievements 283

List of Figures

Figure 2.1. T-stacked foil strain gauge. 10

Figure 2.2. Photoelastic fringe pattern of a polycarbonate plate with a hole, loaded uniformly (Fiene 2010). 13

Figure 2.3. Moiré fringe effect. 15

Figure 2.4. Fringe pattern produced using speckle interferometry (Unknown 2008). 18

Figure 2.5. Thermoelastic stress analysis of a conrod (Stress Photonics, Inc. 2007). 20

Figure 2.6. Diagram of the acoustic emission technique. 25

Figure 2.7. Traditional ultrasonic inspection techniques, (a) pulse-echo, (b) through-transmission, and (c) pitch-catch. 26

Figure 2.8. Schematic illustration of the radiographic imaging technique. 31

Figure 2.9. Schematic illustration of the eddy-current technique. 33

Figure 3.1. Optical configuration of the scanning head. 57

Figure 3.2. Photograph of the 1D vibrometer mounted on a tripod, along with external high-resolution video camera. 60

Figure 3.3. Image of the scan grid used for detecting through-the-width delamination in a composite beam. Note that the scan points are so close together, the scan grid looks like a continuous line. 60

Figure 3.4. 3D vibrometer (PSV-400-3D) mounted on a fix support (PSV-A-T34). 62

Figure 3.5. Three-Dimensional Alignment Specimen (PSV-A-450). 62

Figure 3.6. Illustration of the principle of three-dimensional displacement measurement using a 3D vibrometer. 63

Figure 3.7. Out-of-plane displacement rig. 67

Figure 3.8. Schematic diagram of delaminated composite specimens. 69

Figure 3.9. In-plane displacement rig. 71

Figure 3.10. Experimental setup of out-of-plane measurement experiments. 73

Figure 3.11. Detailed schematics of the in-plane loading specimens. (a) plain, (b) edge crack, (c) centre crack, and (d) notch. 73

Figure 3.12. Experimental setup of in-plane measurement experiments. 75

Figure 3.13. Photograph of the scan grid utilised for (a) determining the accuracy of the in-plane strain measurement technique, and (b) evaluating the strain field near a stress concentrator. The scan grid in (b) is also utilised to investigating the in-plane damage detection techniques. 75

Figure 4.1. Positioning imprecision in the 3D vibrometer due to finite accuracy of the three-dimensional alignment. 81

Figure 4.2. Displacement field uy for a plate highlighting the positioning imprecision for different nodal spatial intervals of (a) 0.22mm and (b) 1.9mm while keeping the zoom of the digital camera constant. 82

Figure 4.3. Photograph of the 3D vibrometer focused at an aluminium dogbone specimen clamped in an Instron 1342 hydraulic test machine (Cazzolato et al. 2008). 84

Figure 4.4. Displacements measured in the x- (top row), y- (middle row) and z-directions (bottom row) on the specimen using triangular (left column) and rectangular elements (right column), excited with a 5Hz frequency (Cazzolato et al. 2008). 86

Figure 4.5. Strains measured in the x- (top row), y- (middle row) and z-directions (bottom row) on the specimen using 3-node triangular linear (left column) and 4-node rectangular bi-linear elements (right column), excited with a 5Hz frequency (Cazzolato et al. 2008). 87

Figure 4.6. The coordinate definition of the spatial position (x) and particle location (X) of a body. 89

Figure 4.7. Illustration of the rectangular plate specimen and mesh used for strain measurement. 93

Figure 4.8. Experimental measured displacements ux, uy and uz (left column) measured on the undamaged plate and their coherence $\gamma x2$, $\gamma y2$ and $\gamma z2$ (right column) to the input voltage. The plate specimen was subjected to a 1.05MPa load and the scan grid (Nx x Ny) consisted of 19x19 data points with a spatial interval (Δx and Δy) of 2mm. 94

Figure 4.9. Variation coefficient (cv, i) of the surfaces strains (εxx and εyy) versus the number of data points used ($2m + 1$) in the Savitzky-Golay differentiator with a polynomial approximation of third-order ($n = 3$). The plate specimen was subjected to approximately a 1.05MPa load and the scan grid (Nx x Ny) consisted of 19x19 data points with a spatial interval (Δx and Δy) of 2mm. 97

Figure 4.10. Variation coefficient (cRMSD) of the surfaces strains (εxx and εyy) versus the order of the polynomial order (n) used in the Savitzky-Golay differentiator spanning 9x9 data points ($m = 4$). The plate specimen was subjected to approximately a 1.05MPa load and the scan grid (Nx x Ny) consisted of 19x19 data points with a spatial interval (Δx and Δy) of 2mm. 97

Figure 4.11. Estimated strain fields (εyy) of an acrylic plate subjected a 1Hz quasi-static uniaxial load of 1.05MPa. The red dashed line indicates the limit of the m data points in from the boundary where the edge artefacts occur and the blue dashed circles indicate locations of edge artefacts. A third-order ($n = 3$) Savitzky-Golay differentiating filter was used with a filter size of 9x9 data point ($m = 4$). The scan grid (Nx x Ny) consisted of 19x19 points with spatial interval (Δx and Δy) of 2mm. 99

Figure 4.12. Variation coefficient (cv, i) of the surface strain (εxx and εyy) versus the mesh spatial interval (Δx and Δy) of a scan grid (Nx x Ny) consisted of 19x19 data points. A third-order ($n = 3$). Savitzky-Golay differentiating filter was used with a filter size of 9x9 data point ($m = 4$). The plate specimens were subjected to approximately a 1.03MPa load. 100

Figure 4.13. Variation coefficient (cv, i) of the surface strain (εxx and εyy) versus the load applied to the plate specimen. A third-order ($n = 3$) Savitzky-Golay differentiating filter was used with a filter size of 9x9 data point ($m = 4$). The scan grid (Nx x Ny) consisted of 19x19 data points with a spatial interval (Δx and Δy) of 2mm. 101

Figure 4.14. Illustration of the rectangular plate specimens and meshes used for strain measurement (a) with a notch and (b) with an edge crack. 105

Figure 4.15. The finite element meshes used to simulate the strain field of (a) notched and (b) edge crack specimens. 106

Figure 4.16. Displacements ux, uy and uz and their coherence γx2, γy2 and γz2 with the input voltage, for the rectangular plate with a notch. The plate specimen was subjected to approximately a 0.65 MPa load and the scan grid (Nx x Ny) consisted of 39x39 data points with a spatial interval (Δx and Δy) of 2mm. 107

Figure 4.17. Surface strain (εxx, εyy and γxy) for the rectangular plate with a notch:- (left) FEA and (right) experimental results. A third-order (n = 3) Savitzky-Golay differentiating filter was used with a filter size of 13x13 data point (m = 6). The plate specimen was subjected to approximately a 0.65 MPa load and the scan grid (Nx x Ny) consisted of 39x39 data points with a spatial interval (Δx and Δy) of 2mm. 108

Figure 4.18. Strains extending out from the notch. Comparison of the experimental (red line) and numerical (black dashed line) solution of εxx, (left) and εyy (right) in-line with the notch, (a, b) m = 4, (c, d) m = 5, and (e, f) m = 6. The plate specimen was subjected to approximately a 0.65 MPa load and the scan grid (Nx x Ny) consisted of 39x39 data points with a spatial interval (Δx and Δy) of 2mm. 109

Figure 4.19. Displacements ux, uy and uz and their coherence γx2, γy2 and γz2 with the input voltage, for the rectangular plate with edge crack. The plate specimen was subjected to approximately a 0.78 MPa load and the scan grid (Nx x Ny) consisted of 39x39 data points with a spatial interval (Δx and Δy) of 2mm. 110

Figure 4.20. Surface strain (εxx, εyy and γxy) for the rectangular plate with edge crack:- (left) FEA and (right) experimental results. The plate specimen was subjected to approximately a 0.78 MPa load and the scan grid (Nx x Ny) consisted of 39x39 data points with a spatial interval (Δx and Δy) of 2mm. 111

Figure 4.21. Strain extending out from crack tip. Comparison of the experimental (red line) and numerical (black dashed line) solution of εxx, (left) and εyy (right) in-line with the edge crack, (a, b) m = 4, (c, d) m = 5, and (e, f) m = 6. The plate specimen was subjected to approximately a 0.78 MPa load and the scan grid (Nx x Ny) consisted of 39x39 data points with a spatial interval (Δx and Δy) of 2mm. 112

Figure 4.22. Experimental arrangement used by Ferguson and Carpentier (1989, p. 215) for the comparison between bending strains evaluated using prototype 1D laser Doppler vibrometry and strain gauges. (a) Front view and (b) side view. 118

Figure 4.23. Previous results obtained by Goetsch and Rowlands (1991, p. 431) for the comparison between radial bending strains evaluated using 1D SLDV and strain gauges for a circular aluminium plate. The plate was vibrated at 20Hz at its centre with an unspecified load. 119

Figure 4.24. (a) A plate of constant thickness, (b) a cross-section of the plate before (lower) and after (upper) deflection. 121

Figure 4.25. Experimentally measured deflection (uz) measured on an aluminium beam (blue line) and its coherence (γz2) to the input voltage (green line). The aluminium beam specimen was subjected to a maximum free-end deflection of 50μm and the scan line consisted of 499 points (N) with a spatial interval (Deltax) of 0.97mm. 124

Figure 4.26. Variation coefficient (cRMSD) of RMSD in the bending strain of the aluminium beam specimen versus (a) the number of data points used $(2m + 1)$ in the Savitzky-Golay differentiator $(n = 3)$ and (b) the polynomial order (n) used in the Savitzky-Golay differentiator $(m = 75)$. The aluminium beam specimen was subjected to a maximum free-end deflection of 50μm and the scan grid consisted of 499 points (N) with a spatial interval (Δx) of 0.97mm. 127

Figure 4.27. (a) Estimated bending strain $(\varepsilon xx, SG)$ on the top of an aluminium cantilever beam using a third-order polynomial $(n = 3)$ Savitzky-Golay differentiating filter, utilising 101 data points $(m = 50)$. The aluminium beam specimen was subjected to a maximum free-end deflection of 50μm and the scan grid consisted of 499 points (N) with a spatial interval (Δx) of 0.97mm. The shaded area indicates m data points in from the boundary in which edge artefacts occur. (b) Schematic illustration of the deformed cantilever. 128

Figure 4.28. Close up of Figure 4.26a to clearly show the variation coefficient (cRMSD) of the RMSD in the bending strain of the aluminium beam specimen versus the number of data points $(2m + 1)$ used in the Savitzky-Golay differentiator $(n = 3)$ graph for $2m + 1$ greater than 81 data points. The aluminium beam specimen was subjected to a maximum free-end deflection of 50μm and the scan grid consisted of 499 points (N) with a spatial interval (Δx) of 0.97mm. 129

Figure 4.29. Variation coefficient (cRMSD) of the RMSD in the bending strain evaluated using a Savitzky-Golay differentiator versus the spatial interval between measurement points (Δx). The Savitzky-Golay differentiator utilised a third-order polynomial approximation $(n = 3)$ with (a) $m = 20$ and (b) $2m + 1$ spanning a fixed distance of approximately 143mm, which equal to approximately 30% of the available nodes for each spatial interval. The aluminium beam specimen was subjected to a maximum free-end deflection of 100μm..... 132

Figure 4.30. Schematic illustration of three scan grids used to evaluate bending strain, with the relative size of the filter length used to evaluate the bending strain. (a) shows the filter length of the Savitzky-Golay filter with a fixed 41 measurement nodes ($m = 20$) for each scan grid density, whereas (b) shows the filter length spanning approximately 30% of the scan grid length ($2m + 1 = 0.3N$) for each scan grid density. 133

Figure 4.31. Variation coefficient (cRMSD) of the RMSD in the bending strain versus maximum deflection experienced by the beam where $n = 3$ and $m = 75$. The scan grid consisted of 499 points (N) with a spatial interval (Δx) of 0.97mm. 135

Figure 5.1. Measurement grids used for (a) edge crack, (b) centre crack and (c) crack with a notch. 142

Figure 5.2. Laser scanned area with indicated data grid points used for Lamb wave sensing (Staszewski, Lee, B & Traynor 2007). 144

Figure 5.3. Lamb wave propagation contour plots in the time domain for 75 kHz excitation:- (a) in-plane x-direction, (b) in-plane y-direction and (c) out-of-plane z-direction (Staszewski, Lee, B & Traynor 2007). 145

Figure 5.4. RMS amplitude contour plots for 75 kHz Lamb wave propagation (a) in-plane x-direction, (b) in-plane y-direction and (c) out-of-plane z-direction (Staszewski, Lee, B & Traynor 2007). 146

Figure 5.5. Forces acting on a small element $[dx, dy]$ of a plate in which stresses vary from point to point. 148

Figure 5.6. Illustration of strain compatibility principle. 149

Figure 5.7. Flow diagram of the *GDEP* algorithm RI. 155

Figure 5.8. Acquired residual term of the GDE (RI) for a notch with various crack lengths:- (a) 0 mm, (b) 5 mm, (c) 10 mm, (d) 15 mm, (e) 20 mm and (f) 25 mm. The dark blue and dark red areas on the graph represent the location where RI has exceeded the threshold $\Phi i = 200m^{-3}$. At $x = 0$ and $x = 100$ represents the edges of the plate and the pink line defines the location of the notch and crack. A 1^{st} order polynomial ($n = 1$) 2D Savitzky-Golay smoothing filter was used with a filter size of 5x5 point ($m = 2$). 156

Figure 5.9. Flow diagram of the *displacement error* algorithm ui. 158

Figure 5.10. Acquired displacement error in the x-axis (ux) for a notch with various crack lengths:- (a) 0mm, (b) 5mm, (c) 10mm, (d) 15mm, (e) 20mm and (f) 25mm. The dark blue and dark red areas on the graph represent the location where ux has exceeded the threshold $\Theta x = 0.7\mu m$. At $x = 0$ and $x = 100$ represents the edges of the plate and the pink line defines the location of the notch and crack. A 1st order polynomial ($n = 1$) 2D Savitzky-Golay smoothing ($rx = ry = 0$) filter was used with a filter size of 3x3 point ($m = 1$). 160

Figure 5.11. Acquired displacement error in the y-axis (uy) for a notch with various crack lengths:- (a) 0mm, (b) 5mm, (c) 10mm, (d) 15mm, (e) 20mm and (f) 25mm. The dark blue and dark red areas on the graph represent the location where uy has exceeded the threshold $\Theta y = 0.7\mu m$. At $x = 0$ and $x = 100$ represents the edges of the plate and the pink line defines the location of the notch and crack. A 1st order polynomial ($n = 1$) 2D Savitzky-Golay smoothing ($rx = ry = 0$) filter was used with a filter size of 3x3 point ($m = 1$). 161

Figure 5.12. Flow diagram of the *surface strain* algorithm for (a) normal strains εii and (b) shear strain γxy. 163

Figure 5.13. Acquired mean centred surface strain in the x-axis (εxx) for a notch with various crack lengths:- (a) 0mm, (b) 5mm, (c) 10mm, (d) 15mm, (e) 20mm and (f) 25mm. The dark blue and dark red areas on the graph represent the location where εxx has exceeded the threshold $\Psi xx = 400\mu m/m$. At $x = 0$ and $x = 100$ represents the edges of the plate and the pink line defines the location of the notch and crack. A 2nd order polynomial ($n = 2$) 2D Savitzky-Golay differentiating filter was used with a filter size of 3x3 point ($m = 1$). 165

Figure 5.14. Acquired mean centred surface strain in the y-axis (εyy) for a notch with various crack lengths:- (a) 0mm, (b) 5mm, (c) 10mm, (d) 15mm, (e) 20mm and (f) 25mm. The dark blue and dark red areas on the graph represent the location where εyy has exceeded the threshold $\Psi yy = 400\mu m/m$. At $x = 0$ and $x = 100$ represents the edges of the plate and the pink line defines the location of the notch and crack. A 2nd order polynomial ($n = 2$) 2D Savitzky-Golay differentiating filter was used with a filter size of 3x3 point ($m = 1$). 166

Figure 5.15. Acquired mean centred surface shear strain (γxy) for a notch with various crack lengths:- (a) 0mm, (b) 5mm, (c) 10mm, (d) 15mm, (e) 20mm and (f) 25mm. The dark blue and dark red areas on the graph represent the location where γxy has exceeded the threshold $\Psi xy = 400\mu m/m$. At $x = 0$ and $x = 100$ represents the edges of the plate and the pink line defines the location of the notch and crack. A 2nd order polynomial ($n = 2$) 2D Savitzky-Golay differentiating filter was used with a filter size of 3x3 point ($m = 1$). 167

Figure 6.1. Experimental setup of the cantilever beam, (a) front view of the composite beam shows the scan points (red dots) used by the 1D vibrometer and (b) side view of the composite beam showing the position of the electromagnetic shaker and 1D vibrometer. 172

Figure 6.2. Shear forces and moments acting on a small element *dxdy* of a plate..... 175

Figure 6.3. Dimensioned illustration of the delaminated cantilever beam. 181

Figure 6.4. Flow diagram of the *GDEB* algorithm Rz. 183

Figure 6.5. Acquired residual term of the GDE (Rz) for a delaminated cantilever beam for four different quantities of filter points ($2m + 1$) utilised within the fourth-order polynomial ($n = 4$) Savitzky-Golay smoothing ($r = 0$) filter. The rows denote the filter widths of (i) $m = 25$, (ii) $m = 50$, (iii) $m = 75$ and (iv) $m = 100$. The columns show the (a) experimental results, (b) simulated results with equivalent noise and (c) simulated results in the absence of noise. The delamination is located between fourth and fifth layer and 50mm in length. The black line represents Rz, the grey line shows the beam curvature and the shaded section illustrates the location of the delaminated section..... 186

Figure 6.6. Acquired residual term of the GDE (Rz) for a delaminated cantilever beam for four different lengths of delamination between the mid-layers ($h2/h = 0.5$). The rows denote the lengths of the delamination and are (i) $Ld = 25mm$, (ii) $Ld = 50mm$, (iii) $Ld = 75mm$ and (iv) $Ld = 100mm$. The columns show the (a) experimental results, (b) simulated results with equivalent noise and (c) simulated results in the absence of noise. A fourth-order polynomial ($n = 4$) Savitzky-Golay smoothing ($r = 0$) filter was used with a filter width of 151 points ($m = 75$). The black line represents Rz, the grey line shows the beam curvature and the shaded section illustrates the location of the delaminated section..... 188

Figure 6.7. Acquired residual term of the GDE (Rz) for various laminate cantilever beams with a 50mm delamination at different depths. The rows denote the depths of the delamination and are (i) $h2/h = 0.125$, (ii) $h2/h = 0.25$, (iii) $h2/h = 0.375$, (iv) $h2/h = 0.5$, (v) $h2/h = 0.625$, (vi) $h2/h = 0.75$ and (vii) $h2/h = 0.875$. The columns show the (a) experimental results, (b) simulated results with equivalent noise and (c) simulated results in the absence of noise. A fourth-order polynomial ($n = 4$) Savitzky-Golay smoothing ($r = 0$) filter was used with a filter width of 151 points ($m = 75$). The shaded section illustrates the location of the delaminated section. 191

Figure 6.8. Flow diagram of the *deflection error* algorithm. 195

Figure 6.9. Acquired error in deflection (uz) for a delaminated cantilever beam for four different quantities of filter points ($2m + 1$) utilised within the third-order polynomial ($n = 3$) Savitzky-Golay smoothing ($r = 0$) filter. The rows denote the filter widths of (i) $m = 25$, (ii) $m = 50$, (iii) $m = 75$ and (iv) $m = 100$. The columns show the (a) experimental results, (b) simulated results with equivalent noise and (c) simulated results in the absence of noise. The delamination is located between fourth and fifth layer and 50mm in length. The shaded section illustrates the location of the delaminated section. 198

Figure 6.10. Acquired error in deflection (uz) for a delaminated cantilever beam for four different lengths of delamination between the mid-layers ($h2/h = 0.5$). The rows denote the lengths of the delamination and are (i) $Ld = 25$mm, (ii) $Ld = 50$mm, (iii) $Ld = 75$mm and (iv) $Ld = 100$mm. The columns show the (a) experimental results, (b) simulated results with equivalent noise and (c) simulated results in the absence of noise. A third-order polynomial ($n = 3$) Savitzky-Golay smoothing ($r = 0$) filter was used with a filter width of 151 points ($m = 75$). The shaded section illustrates the location of the delaminated section. 201

Figure 6.11. Acquired error in deflection (uz) for various laminate cantilever beams with a 50mm delamination at different depths. The rows denote the depths of the delamination and are (i) $h2/h = 0.125$, (ii) $h2/h = 0.25$, (iii) $h2/h = 0.375$, (iv) $h2/h = 0.5$, (v) $h2/h = 0.625$, (vi) $h2/h = 0.75$ and (vii) $h2/h = 0.875$. The columns show the (a) experimental results, (b) simulated results with equivalent noise and (c) simulated results in the absence of noise. A third-order polynomial ($n = 3$) Savitzky-Golay smoothing ($r = 0$) filter was used with a filter width of 151 points ($m = 75$). The shaded section illustrates the location of the delaminated section. 204

Figure 6.12. Flow diagram of the *curvature error* algorithm κ. 207

Figure 6.13. Acquired error in curvature (κ) for a delaminated cantilever beam for four different quantities of filter points ($2m + 1$) utilised within the third-order polynomial ($n = 3$) Savitzky-Golay smoothing ($r = 0$) filter. The rows denote the filter widths of (i) $m = 25$, (ii) $m = 50$, (iii) $m = 75$ and (iv) $m = 100$. The columns show the (a) experimental results, (b) simulated results with equivalent noise and (c) simulated results in the absence of noise. The delamination is located between fourth and fifth layer and 50mm in length. The shaded section illustrates the location of the delaminated section.....210

Figure 6.14. Acquired error in deflection (κ) for a delaminated cantilever beam for four different lengths of delamination between the mid-layers ($h2/h = 0.5$). The rows denote the lengths of the delamination and are (i) $Ld = 25$mm, (ii) $Ld = 50$mm, (iii) $Ld = 75$mm and (iv) $Ld = 100$mm. The columns show the (a) experimental results, (b) simulated results with equivalent noise and (c) simulated results in the absence of noise. A third-order polynomial ($n = 3$) Savitzky-Golay smoothing ($r = 0$) filter was used with a filter width of 151 points ($m = 75$). The shaded section illustrates the location of the delaminated section.....212

Figure 6.15. Acquired error in curvature (κ) for various laminate cantilever beams with a 50mm delamination at different depths. The rows denote the depths of the delamination and are (i) $h2/h = 0.125$, (ii) $h2/h = 0.25$, (iii) $h2/h = 0.375$, (iv) $h2/h = 0.5$, (v) $h2/h = 0.625$, (vi) $h2/h = 0.75$ and (vii) $h2/h = 0.875$. The columns show the (a) experimental results, (b) simulated results with equivalent noise and (c) simulated results in the absence of noise. A third-order polynomial ($n = 3$) Savitzky-Golay smoothing ($r = 0$) filter was used with a filter width of 151 points ($m = 75$). The shaded section illustrates the location of the delaminated section. 215

Figure C.1. Delaminated beam model. 251

Figure D.2. Acquired residual term of GDE (RI) for an edge crack with various crack lengths:- (a) 5mm, (b) 10mm, (c) 15mm, (d) 20mm and (e) 25mm. The dark blue and dark red areas on the graph represent the location where RI has exceeded the threshold $\Phi I = 200m^{-3}$. At $x = 0$ and $x = 100$ represents the edges of the plate and the pink line defines the location of the crack. A third-order polynomial ($n = 3$) 2D Savitzky-Golay differentiating filter was used with a filter size of 5x5 point ($m = 2$).....262

Figure D.3. Acquired residual term of GDE (RI) for a centre crack with various crack lengths:- (a) 5mm, (b) 10mm, (c) 15mm, (d) 20mm and (e) 25mm. The dark blue and dark red areas on the graph represent the location where RI has exceeded the threshold $\Phi I = 200m^{-3}$. At $x = 0$ and $x = 100$ represents the edges of the plate and the pink line defines the location of the crack. A third-order polynomial ($n = 3$) 2D Savitzky-Golay differentiating filter was used with a filter size of 5x5 point ($m = 2$)..... 263

Figure D.4. Acquired displacement error in the x-direction (ux) for an edge crack with various crack lengths:- (a) 5mm, (b) 10mm, (c) 15mm, (d) 20mm and (e) 25mm. The dark blue and dark red areas on the graph represent the location where ux has exceeded the threshold $\Theta x = 0.7\mu m$. At $x = 0$ and $x = 100$ represents the edges of the plate and the pink line defines the location of the crack. A first-order polynomial ($n = 1$) 2D Savitzky-Golay smoothing ($rx = ry = 0$) filter was used with a filter size of 3x3 point ($m = 1$)..... 266

Figure D.5. Acquired displacement error in the y-direction (uy) for an edge crack with various crack lengths:- (a) 5mm, (b) 10mm, (c) 15mm, (d) 20mm and (e) 25mm. The dark blue and dark red areas on the graph represent the location where uy has exceeded the threshold $\Theta y = 0.7\mu m$. At $x = 0$ and $x = 100$ represents the edges of the plate and the pink line defines the location of the crack. A first-order polynomial ($n = 1$) 2D Savitzky-Golay smoothing ($rx = ry = 0$) filter was used with a filter size of 3x3 point ($m = 1$)..... 267

Figure D.6. Acquired displacement error in the x-direction (ux) for a centre crack with various crack lengths:- (a) 5mm, (b) 10mm, (c) 15mm, (d) 20mm and (e) 25mm. The dark blue and dark red areas on the graph represent the location where ux has exceeded the threshold $\Theta x = 0.7\mu m$. At $x = 0$ and $x = 100$ represents the edges of the plate and the pink line defines the location of the crack. A first-order polynomial ($n = 1$) 2D Savitzky-Golay smoothing ($rx = ry = 0$) filter was used with a filter size of 3x3 point ($m = 1$)..... 268

Figure D.7. Acquired displacement error in the y-direction (uy) for a centre crack with various crack lengths:- (a) 5mm, (b) 10mm, (c) 15mm, (d) 20mm and (e) 25mm. The dark blue and dark red areas on the graph represent the location where uy has exceeded the threshold $\Theta y = 0.7\mu m$. At $x = 0$ and $x = 100$ represents the edges of the plate and the pink line defines the location of the crack. A first-order polynomial ($n = 1$) 2D Savitzky-Golay smoothing ($rx = ry = 0$) filter was used with a filter size of 3x3 point ($m = 1$)..... 269

Figure D.8. Acquired normalised surface strain in the x-direction (εxx) for an edge crack with various crack lengths:- (a) 5mm, (b) 10mm, (c) 15mm, (d) 20mm and (e) 25mm. The dark blue and dark red areas on the graph represent the location where εxx has exceeded the threshold $\Psi xx = 400$mm/m. At $x = 0$ and $x = 100$ represents the edges of the plate and the pink line defines the location of the crack. A second-order polynomial ($n = 2$) 2D Savitzky-Golay differentiating filter was used with a filter size of 3x3 point ($m = 1$). 272

Figure D.9. Acquired normalised surface strain in the y-direction (εyy) for an edge crack with various crack lengths:- (a) 5mm, (b) 10mm, (c) 15mm, (d) 20mm and (e) 25mm. The dark blue and dark red areas on the graph represent the location where εyy has exceeded the threshold $\Psi yy = 400$mm/m. At $x = 0$ and $x = 100$ represents the edges of the plate and the pink line defines the location of the crack. A second-order polynomial ($n = 2$) 2D Savitzky-Golay differentiating filter was used with a filter size of 3x3 point ($m = 1$). 273

Figure D.10. Acquired normalised surface shear (γxy) for an edge crack with various crack lengths:- (a) 5mm, (b) 10mm, (c) 15mm, (d) 20mm and (e) 25mm. The dark blue and dark red areas on the graph represent the location where γxy has exceeded the threshold $\Psi xy = 400$mm/m. At $x = 0$ and $x = 100$ represents the edges of the plate and the pink line defines the location of the crack. A second-order polynomial ($n = 2$) 2D Savitzky-Golay differentiating filter was used with a filter size of 3x3 point ($m = 1$).....274

Figure D.11. Acquired normalised surface strain in the x-direction (εxx) for a centre crack with various crack lengths:- (a) 5mm, (b) 10mm, (c) 15mm, (d) 20mm and (e) 25mm. The dark blue and dark red areas on the graph represent the location where εxx has exceeded the threshold $\Psi xx = 400$mm/m. At $x = 0$ and $x = 100$ represents the edges of the plate and the pink line defines the location of the crack. A second-order polynomial ($n = 2$) 2D Savitzky-Golay differentiating filter was used with a filter size of 3x3 point ($m = 1$). 275

Figure D.12. Acquired normalised surface strain in the y-direction (εyy) for a centre crack with various crack lengths:- (a) 5mm, (b) 10mm, (c) 15mm, (d) 20mm and (e) 25mm. The dark blue and dark red areas on the graph represent the location where εyy has exceeded the threshold $\Psi yy = 400$mm/m. At $x = 0$ and $x = 100$ represents the edges of the plate and the pink line defines the location of the crack. A second-order polynomial ($n = 2$) 2D Savitzky-Golay differentiating filter was used with a filter size of 3x3 point ($m = 1$). 276

Figure D.13. Acquired normalised surface shear strains (γxy) for a centre crack with various crack lengths:- (a) 5mm, (b) 10mm, (c) 15mm, (d) 20mm and (e) 25mm. The dark blue and dark red areas on the graph represent the location where γxy has exceeded the threshold $\Psi xy = 400$mm/m. At $x = 0$ and $x = 100$ represents the edges of the plate and the pink line defines the location of the crack. A second-order polynomial ($n = 2$) 2D Savitzky-Golay differentiating filter was used with a filter size of 3x3 point ($m = 1$). 277

List of Tables

Table 3.1. Specimen specification, parameters related to Figure 3.8. 68

Table 3.2. Specimen specifications, parameters related to Figure 3.11..... 72

Table 4.1 Comparison of Normalised strains per unit (kN) load and estimated Poisson's Ratio of the test specimen measured using an extensometer and 3D SLDV system (Cazzolato et al. 2008)..... 85

Table 4.2. Variation coefficient of the root squared mean deviation ($cRMSD, i$) between the FE and measured x- and y-strain leading up to the tip of the notch specimen ($y = 0$) that are presented in Figure 4.18. The RMSD values are provided in brackets for each case. 115

Table 4.3. Variation coefficient of the root squared mean deviation ($cRMSD, i$) between the FE and measured x- and y-strain leading up to the tip of the edge crack specimen ($y = 0$) that are presented in Figure 4.21. The RMSD values are provided in brackets for each case. 115

Table 4.4. Illustration of the number of data points ($2m + 1$) required within the Savitzky-Golay differentiating filter to encompass a nominal fixed distance of approximately 143mm for each spatial interval (Δx) investigated. 132

Table 4.5. Relationship between the variation coefficient of RMSD in the bending strain (cRMSD) in Figure 4.29a to the ratio of the number of measurement points used ($2m + 1 = 41$) within the Savitzky-Golay filter and total number of measurement points (N). 133

Table 4.6. Comparison of common strain measurement techniques. 138

Nomenclature

a	–	crack length
c_{RMSD}	–	variation coefficient of measured strain
E	–	modulus of elasticity
f	–	beat frequency measured at the photo detector of the laser beam
f_D	–	Doppler shift in laser beam
f_B	–	offset frequency of the reference laser beam
F	–	force applied to end of the cantilever beam
F_x, F_y	–	body force acting on a plate
G	–	shear modulus
h	–	plate or beam thickness
h_2	–	thickness of delaminated section on the front side of beam
h_3	–	thickness of delaminated section on the back side of beam
$h_{t,i}^{n,r}$	–	convolution weights of the Savitzky-Golay differentiation filter
I	–	intensity of the coinciding reference and object beams at the photo detector of the laser vibrometer
$I_{\max}$	–	maximum possible intensity at the photo detector of the laser vibrometer
L	–	length of beam
L_1	–	distance from clamped end of beam to the start of the delaminated zone
L_2	–	distance from clamped end of beam to the end of the delaminated zone
L_d	–	length of the delaminated section of a composite beam
ΔL	–	difference in path length between the reference and object beams
$2m+1$	–	number of measurement points utilised within a numerical differentiation technique
M_x, M_y, M_{xy}	–	bending moments applied to a small plate element
M_0	–	moment applied to end of the cantilever beam
n	–	polynomial order utilised within a numerical differentiation technique
N	–	total number of measurement points
p	–	uniformly distributed load per unit area applied to a plate

$P_n^{m,r}$ – Gram polynomial

Q_x, Q_y – shear forces applied to a small plate element

r – order of differential performed within a numerical differentiation technique

R_I – residual term of the governing differential equation for in-plane displacement

R_O – residual term of the governing differential equation for out-of-plane displacement

R^2 – coefficient of determination of a least-squares-fit

$RMSD$ – root mean standard deviation

SD – standard deviation

t – time

u_x, u_y – displacement field in the x- and y-axes, respectively (in-plane direction)

u_z – displacement field in the z-direction (out-of-plane direction)

$\hat{u}_i$ – displacement error in the i-axes

$u_{z,SG}$ – fitted displacement in the i-axes

$u_{i,m}$ – measured displacement in the i-axes

u_E – Eulerian displacement

u_L – Lagrangian displacement

v – object velocity in the direction of the laser beam

$\Delta x, \Delta y$ – spatial interval between measurement points

$x(X,t)$ – spatial position of a particle X at the time t

$X(x,t)$ – the particle located at a spatial position x at time t

$\gamma_{xy}, \gamma_{yz}, \gamma_{zx}$ – engineering shear strains in x-y, x-z and y-z planes respectively

$\hat{\gamma}_{ij}$ – mean centre of the surface shear strain

$\gamma_{ij,SG}$ – estimate of the in-plane surface shear strain using a Savitzky-Golay differentiating filter

$\bar{\gamma}_{ij}$ – undamaged estimate of the in-plane shear surface strains using a least-squares-fit

$\gamma_x^2, \gamma_y^2, \gamma_z^2$ – coherence of measured displacement in x-, y- or z-axes to the input vibration voltage

$\varepsilon_{xx}, \varepsilon_{yy}, \varepsilon_{zz}$ – normal strains in the x-, y- and z-axes, respectively

$\hat{\varepsilon}_{ij}$ – mean centre of the surface in-plane strain

$\varepsilon_{ij,SG}$ – estimate of the in-plane surface strain using a Savitzky-Golay differentiating filter

$\bar{\varepsilon}_{ij}$ – undamaged estimate of the in-plane surface strains using a least-squares-fit

Θ_i – damage detection threshold of the *displacement error* algorithm

$\hat{\kappa}$ – beam curvature error between the estimated and expected beam curvature

κ_{SG} – estimate of beam curvature using a Savitzky-Golay differentiating filter

κ_{LS} – undamaged estimate of the in-plane surface strains using a least-squares-fit

λ – wavelength of the laser beam

ν – Poisson's ratio for an isotropic material

ν_x, ν_y – Poisson's ratio for an anisotropic material in the x- and y-axes, respectively

$\sigma_{xx}, \sigma_{yy}, \sigma_{zz}$ – normal stresses in the x-, y- and z-axes, respectively

$\tau_{xy}, \tau_{yz}, \tau_{zx}$ – engineering shear stresses in x-y, x-z and y-z planes respectively

ϕ – phase difference between the reference and object beams

Φ_I – damage detection threshold of the governing differential equation algorithm

Ψ_{ij} – damage detection threshold of the surface strain error algorithm

Chapter 1. Introduction

From ships to aircraft and bridges to pipelines history has seen numerous catastrophic structural failures, such as the disintegration of the space shuttle Columbia on re-entry due to sustained wing damage (Gehman 2003), the explosive decompression of China Airlines Flight 611 from undetected metal fatigue (ASC 2005) and the Esso Longford refinery explosion caused by brittle fracture of an oil pump (Hopkins 2000). Such failures cause great inconvenience and often result in economic loss, grievous injury or even death. In many cases, the failure of a component or structure in-service is due to the presence of mechanical damage, such as fatigue cracks for metal or delamination for composite materials. Consequently, there is a need to evaluate the strength and integrity of engineering structures in order to prevent catastrophic failure due to mechanical damage.

Over the last century, a wide variety of techniques have been developed to fulfil this need for evaluation of the strength and integrity of structures which can be roughly divided into contact and non-contact methods. Contact methods include the use of strain gauges or piezoelectric materials, while non-contact methods utilise physical phenomenon such as optical effects that include diffraction and interferometry. Contact methods have obvious disadvantages as they can influence the surface strains and can require an extensive set-up and wiring. Non-contact methods avoid these issues and provide the potential for full strain field measurements, whilst not influencing the state of the stress of the structure or component under investigation (Sharpe 2008). One of the newest experimental non-contact

methods is based on Scanning Laser Doppler Vibrometry (SLDV). SLDV measures vibratory velocity, and displacement, of an object by measuring the Doppler shift of a laser beam frequency due to the velocity of the surface of the object. Mirrors attached to the servo motors within the laser heads allow multiple points to be scanned without the need for adjusting the apparatus. A number of researchers have successfully utilised the non-contact, out-of-plane displacement measurements obtained from a 1D vibrometer to estimate bending strains (Ferguson, N & Carpentier 1989), as well as developing displacement and curvature based damage detection techniques, demonstrating the potential of the method (Qiao et al. 2007b).

The emergence of 3D SLDV systems employing three laser heads (produced by Polytec GmbH, Germany) provides a fast, easy, non-contact way of measuring three-dimensional velocity and displacement components on a vibrating structure (Mitchell, West & Wicks 1998). This system has opened the door for new non-destructive evaluation techniques, such as surface strain measurement and damage detection.

The aim of the research presented in this thesis is to utilise 1D and 3D SLDV for the development and investigation of new non-destructive evaluation techniques. The body of the research is divided into two main areas. The first looks at strain measurement, which gives an indication of structural loading and can be used to evaluate whether a structure is being overloaded. This is followed by the development of damage detection techniques, which can give an assessment of structural health as even small amounts of damage can cause catastrophic failure of a structure. These two strands are complimentary to each other as evaluating the loading and health of a structure is imperative to maintain structural integrity.

1.1 Strain Measurement

Strain is the relative change in dimension of an object in response to an external loading. The use of strain measurement devices has become a standard for testing newly developed components in the automotive and aerospace industries, as well as monitoring structural integrity of energy, naval and civil structures. The most commonly utilised experimental strain analysis techniques include contact methods (such as strain gauges or piezoelectric sensors for measuring strains on brittle surfaces) and non-contact methods (such as photo-elasticity, x-ray diffraction and holographic interferometry). As previously mentioned, contact methods have obvious disadvantages and are only ideally suited for single point strain measurements. The development of optical based non-contact strain measurement techniques has paved the way for full strain field measurements without influencing the state of stress within the structure under investigation. However many of these existing optical non-contact strain measurement techniques suffer from poor signal to noise ratios, have complex setups or are limited to static/low frequency investigations (Sharpe 2008). Even though strain gauges can only provide point measurements of strain, this technique provides the best range (measurements between 3 microstrain to 10 millistrain) and accuracy (±5% of the measured strain) (Dally & Riley 2005).

In contrast to techniques using strain gauges, the scanning laser Doppler vibrometer offers great potential for accurate and high resolution displacement and strain measurement, due to its capacity for high resolution displacement measurements, and spatial resolution (Polytec 2004). However, it is important to highlight that it is only within the last few years that the technology has become available for 3D vibrometers (with sufficient spatial resolution and the associated high-resolution decoders) to be able to measure surface strain

from in-plane loading. In the current work presented, it is the first time that the 3D vibrometer has been used for measuring surface strain created by in-plane loading.

1.2 Non-Destructive Damage Detection

Non-destructive damage detection, as an industry, employs a wide variety of techniques to monitor the integrity of a structure, including penetrant, magnetic particle, eddy-current, ultrasonic, acoustic emission, radiographic and vibration testing. These techniques are normally based on known general physical principles or phenomena associated with structural damage. For example, the acoustic emission method is based on the principle that the initiation and growth of fatigue damage, failure of bonds and areas of corrosion emit ultrasonic acoustic signals which can be sensed and then evaluated. In contrast, vibration-based techniques rely on the fact that measured modal parameters (notably natural frequencies, mode shapes and modal damping) are functions of physical properties of the structure (mass, dampening and stiffness). Thus, changes of the physical properties such as the loss of a load bearing member or a loosened connection, will cause detectable changes in these modal characteristics, which again can be sensed and evaluated. However, the use of these techniques for the detection of damage in composite structures still poses significant difficulty due to the complex nature of composite materials and their various failure mechanisms (i.e. delamination, matrix cracking, etc.) (Cantwell & Morton 1992; Su, Ye & Lu, Y 2006).

Surprisingly, the quest for better non-destructive damage detection techniques for detecting structural damage has overlooked the use of fundamental principles of Solid Mechanics:- specifically strain compatibility and the equations of equilibrium. Physically, the principle

of strain compatibility defines how a body must be pieced together (no gaps, overlaps or other discontinuities within the deformed body) and the equilibrium conditions define how the displacements vary from point to point within a loaded body. The nature of these principles is closely related to typical structural damage and therefore can serve as a basis for the development of non-destructive damage detection techniques since the violation of these theoretical equations can be detected and linked to structural damage.

The main reason for this oversight is because conventional displacement and strain measurement techniques have insufficient resolution and accuracy for such purposes. Only in the last couple of years with the advancements in SLDV by Polytec GmbH, has the accurate measurement of displacement and strain fields been possible to investigate the application of these principles to damage detection. Thus in this thesis, 1D and 3D SLDV will be combined with the fundamental principles of Solid Mechanics, for the detection of mechanical damage in beam and plate structures.

1.3 Aims and Objectives

The overall aim of this research is to investigate the use of SLDV in the development of a new experimental, full-field, in-plane strain measurement technique and new damage detection techniques based on fundamental principles of Solid Mechanics.

The specific objectives of the project are:

1. to investigate the accuracy of an experimental bending strain measurement technique using current 1D SLDV technology,
2. to develop and evaluate the accuracy of a new experimental technique for the measurement of in-plane surface strain using 3D vibrometer,

3. to experimentally investigate the limitations of the developed strain measurement techniques and validate the techniques for a number of practically important cases,

4. to develop damage detection techniques based on the fundamental principles of Solid Mechanics, including the principle of strain compatibility and conditions of equilibrium, and

5. to experimentally investigate the effectiveness of the proposed damage detection techniques in detecting characteristic damage in metals and composite structures.

1.4 Outline of Thesis

This thesis presents an investigation into the use of SLDV for experimental strain measurement and non-destructive damage detection. The thesis begins with a literature review in Chapter 2 that broadly examines previous and current research into experimental strain measurement methods and non-destructive damage detection techniques and then focuses on techniques utilising SLDV technology. Chapter 3 describes the experimental setup developed for the validation of the new strain measurement methods and damage detection techniques utilising a 1D and 3D SLDV system.

Chapter 4 presents an investigation into the use of 1D and 3D vibrometers for the measurement of bending and extensional strain and evaluates the accuracy of the experimental strain measurement technique and compares the technique to previous work. Initially, the accuracy of bending strain measurements using a 1D SLDV system is established. This is followed by an investigation into the accuracy of the new in-plane strain field measurement technique (based on the 3D SLDV system) in measuring a uniform strain field arising from uni-axial loading of a plate. To validate this new in-plane strain field measurement technique, the strain fields in the vicinity of two common planar

geometries (a plate with notch and plate with edge crack) were measured and compared against numerically calculated results using finite element analysis.

Chapter 5 and Chapter 6 present an investigation into two non-destructive damage detection algorithms, based on the governing differential equations of displacement, to accurately detect crack damage in a homogeneous plate utilising in-plane displacements measured using a 3D vibrometer and through-the-width delamination in a composite beam structures from out-of-plane displacement measured using a 1D vibrometer, respectively. In order to evaluate effectiveness of the new damage detection algorithm based on the governing differential equations of displacement, two commonly used damage detection algorithms were utilised, which includes the error between the measured and ideal displacement, as well as the error between the estimated and ideal strain/curvature. In Chapter 5, several acrylic plate specimens with crack damage were manufactured with different crack lengths whereas in Chapter 5 the presented experimentation utilised a number of delaminated composite specimens manufactured with various delamination lengths and depths.

These chapters are followed by a conclusion summarising the accuracy, advantages and disadvantages, and capability of the experimental strain measurement and damage detection techniques, followed by a short discussion of the future prospects and research possibilities.

Chapter 2. Literature Review

Black and Kohser (2008, p. 246) describe non-destructive evaluation as examining a "product … in a manner that retains its usefulness for future service" and is used to "detect internal flaws, measure a product's dimensions, determine a material's structure or chemistry, or evaluated a material's physical or mechanical properties."

This chapter will broadly focus on two categories of non-destructive evaluation; experimental strain measurement and damage detection. The principles and phenomena associated with various experimental strain measurement and damage detection techniques will be discussed, as well as the advantages and limitations of each. This is followed by a review of the current literature that is related to research into the use of Scanning Laser Doppler Vibrometry (SLDV) for experimental strain measurement and damage detection. Finally, the gaps in the current available literature are identified.

2.1 Strain Measurement

Strain measurement is important for many fields of applied mechanics and engineering. The most common include contact methods using electrical resistance or piezoresistive strain gauges and non-contact methods, such as photo-elasticity, moiré, holography, speckle, digital image correlation and thermoelastic stress analysis. In the following section the most common techniques will be briefly discussed.

2.1.1 Strain Gauge

The first, and the most common sensor for the measurement of strain, is electrical resistance strain gauges. Electrical resistance strain gauges are based on the physical phenomena that the electrical resistance of an electrically conductive material will change when a strain is induced in the material. This change in electrical resistance occurs since strain causes a change in the cross-sectional area in which the current flows. To measure this resistance change, and thus the strain, typically a Wheatstone bridge circuit arrangement is typically used. There are two common types of electrical resistance strain gauge:- the foil gauge (as seen in Figure 2.1) and the semiconductor gauge (Hannah & Reed 1992; Watson 2008).

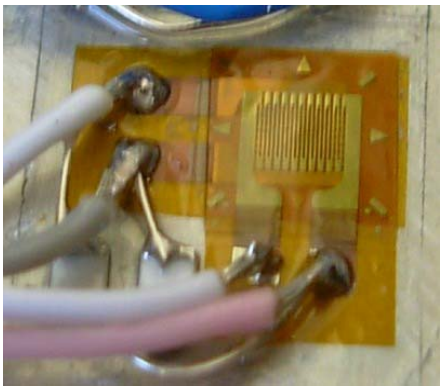

Figure 2.1. T-stacked foil strain gauge.

The sensing element used to create a foil strain gauge consists of a thin wire forming a series of parallel lines and is most commonly made from a copper-nickel alloy, which is known as Advance or Constantan. This material has linear strain sensitivity over a wide range of strains, extremely small hysteresis and excellent thermal stability at ambient

temperatures (~24ºC). Other commonly used materials include Isoelastic alloy, which has high fatigue strength properties, and Karma alloy that can provide high temperature static strain measurements. The foil strain gauge is cheap, easily implemented and can provide accurate measurements for large strains (typically 10 to 50 millistrain) and down to strains of approximately 5 microstrain, all within ±5% of the measured strain (Window 1992; Dally & Riley 2005).

Semiconducting strain gauges, like foil strain gauges, change in electrical resistance when strained, however, they utilise the piezoresistive properties of semiconducting materials. Commonly, semiconducting strain gauges are made of small, thin rectangular filaments of single crystal silicon and have strain sensitivities greater then 50 times that of a foil strain gauge. The strain limit of these gauges is typically 3 microstrain and has an accuracy of within ±2% (Window 1992; Dally & Riley 2005). The main advantages of these gauges are their high strain sensitivity, repeatability, reliability and no hysteresis (Watson 2008). However, they are disadvantaged by the nonlinearity in the strain sensitivity, large temperature effects and their high cost (Hannah & Reed 1992; Dally & Riley 2005).

The electrical resistance strain gauge is ideal for taking an accurate point measurement on a structure when the strain gradient is much less than the size of the strain gauge. The foil gauge is perfect for general purpose structural monitoring and stress analysis, where as the semiconducting gauge is more suited to measuring small strains with high accuracy under stable thermal conditions. However, the use of strain gauges for full-field strain measurement of a structure is infeasible due to the shear number of gauges, cables and data acquisition equipment required, which in effect could significantly influence the static or dynamic response of the structure (Dally & Riley 2005).

2.1.2 Photoelasticity

Photoelasticity is based on the physical behaviour of isotropic transparent noncrystalline solids that are optically isotropic when free of stress, but experience birefringence (double refraction) when stressed. When a beam of plane-polarised light passes through a stressed photoelastic material, the beam splits into two orthogonally polarised components. Each component is parallel to the direction of the principal stress at that point in the body, and the velocity of each of these components is proportional to the magnitude of the principal stress. If the emergent light is passed through a polariser that is perpendicular to the plane of vibration of the initial beam, optical interference takes place and a pattern of fringes can be observed, as seen in Figure 2.2. By studying these fringe patterns, the difference in principle stress ($\sigma_1 - \sigma_2$) can be determined at various points within the body. The optical instrument used to produce these fringe patterns is known as a polariscope and can utilise either plane or circularly polarised light (Holister 1967).

There are three applications for photoelasticity. For plane photoelastic test specimens, two-dimensional methods can be employed. If the photoelastic test specimen is not plane, then more complex and time consuming three-dimensional methods can be utilised. To investigate plane non-photoelastic materials, a photoelastic coating can be applied to the surface of the specimen and the fringe orders recorded via a reflected light polariscope (Khan & Wang, X 2001; Dally & Riley 2005).

The advantage of photoelasticity is that it is simple and inexpensive to conduct, however, the fringe patterns produced only provide information about the difference in principle stresses. A number of techniques have been suggested to separate the principal stresses, but all have characteristics that make them non-viable under certain circumstances and only a

few have achieved commercial development (Fernández et al. 2010). The characteristics that make some of these techniques non-viable include (Fernández et al. 2010):

- not being able to be applied in transmission and reflection analysis,
- not being able to use the whole field of stresses/strains,
- the deterioration of the photoelastic material due to the technique, and
- complications due to the need for the application of technologies based on other physical phenomena.

In addition, when investigating dynamic responses of a structure, the loading frequency is limited to less than half the frame rate of the camera that is used to capture the fringe patterns. The fringes can usually be extrapolated to ±0.2 fringes within accuracy of about 5%, however, only the difference in principle stress ($\sigma_1 - \sigma_2$) can be determined (Dally & Riley 2005).

Figure 2.2. Photoelastic fringe pattern of a polycarbonate plate with a hole, loaded uniformly (Fiene 2010).

2.1.3 Moiré and Moiré Interferometry

Moiré methods utilise the phenomenon that when light passes through two gratings that are overlaid, fringes are produced. The most basic method for measuring displacements using moiré interference is to have two gratings of equal line density of opaque bars and transparent interspaces, with one attached to the surface of a specimen (model grating) and the other aligned in front (master grating). The gratings must be aligned perpendicular to the displacement direction of interest. When the material is unstressed and the bars of the gratings coincide exactly, the transmitted light from the grating will appear to have a uniform field, with intensity equal to half the intensity of the incident beam. With the application of stress, the model grating deforms with the specimen, which changes the width of the grating. When an opaque bar of one grating coincides with a transparent interspace of the other, the light transmission is at a minimum and a dark band (known as moiré fringe) is formed. By measuring these moiré fringes, the displacement field in the direction of interest can be determined (Sciammarella 1982; Dulieu-Barton & Stanley 1998; Han & Post 2008b).

In addition to the above method, misaligned grating (or cross gratings) can be employed to produce parallel moiré fringes on the specimen perpendicular to the displacement direction of interest. Figure 2.3 shows the model grating and master grating aligned to produce moiré fringes in the y-direction. The displacement of the specimen in the y-direction can be determined by recording the position of the moiré fringes before and after loading (Holister 1967; Dally & Riley 2005). Lastly, the master grating can be applied via optical means, projection moiré and moiré interferometry (Han & Post 2008a, 2008b).

Moiré methods are able to measure down to the millistrain region, over a spatial resolution

of greater than 40 micrometers, within an accuracy of ±5% (Zhilkin & Popov 1976; Sciammarella 1982; Pan et al. 2006). The advantage of this method is that the full-field displacement components can be extracted, however, significant specimen preparation is required, as slight grating misalignment can significantly affect the results and dynamic loading investigation are limited to loading frequencies of half the frame rate of the employed camera (Durelli & Parks 1970; Han & Post 2008a, 2008b).

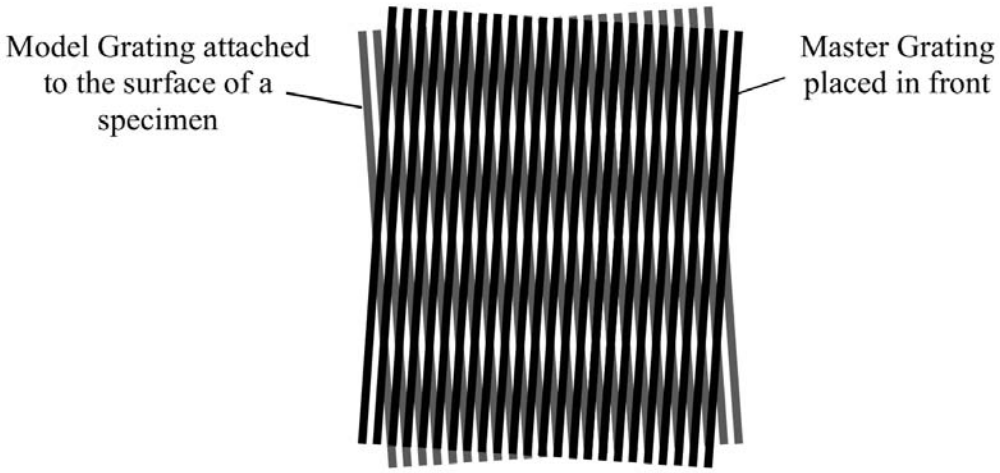

Figure 2.3. Moiré fringe effect.

2.1.4 Holographic Interferometry

Holographic interferometry for the measurement of surface displacements requires two superimposed holograms taken before and after loading of a specimen. Holograms are produced by the interference of coherent light on a photographic plate due to the difference in path length of a reflected beam from a diffuse surface of a specimen and a reference beam. When the photographic plate is double exposed with the unloaded and loaded

interference patterns, a fringe pattern is produced that represents the total displacement of the specimen. It is not possible to view the holographic image on the developed photographic plate with the naked eye. By using just the reference beam, a virtual image of the specimen can be produced from the photographic plate on the original specimen, with well defined fringe patterns (Dally & Riley 2005; Pryputniewicz 2008).

In order to extract the three components of displacement, recording of three holographic fringe patterns with unique positions for the light source and the film plane are required (Khan & Wang, X 2001). There are two techniques of measuring the displacement fringe patterns while a specimen is dynamically loaded:- real-time and time-averaged holographic interferometry. Real-time holographic interferometry is useful for measuring fringe patterns while loads are applied slowly to a specimen. The method is preformed by making a hologram of an unloaded specimen, developing the hologram and ensuring that the hologram is replaced precisely at its position in the optical arrangement. The light of the object beam and reference beam are then passed through the hologram. As the specimen deforms a virtual image is produced with fringe patterns, which can be captured via a camera (Pryputniewicz 2008).

Time-averaged holographic interferometry is able to measure the maximum modal vibratory response of structure. A single hologram is taken with an exposure time that is much greater than the period of the vibratory motion. As the period of the vibratory motion spends most of its time at the maximum and minimum displacements, the holographic image produces fringes equivalent to a double exposed hologram (Pryputniewicz 2008).

The advantage of this method is that it is possible to determine the three displacement components if required, however, determining these displacement components are

complex and requires significant experience and knowledge to effectively accomplish. Additional drawbacks involve the methods inability to investigate a structures response to multiple frequency loading and that the optical system must be highly stable in order to properly record the fringes, thus vibration isolation tables and constant temperatures are required (Ennos 1968).

2.1.5 Speckle Methods

Speckle methods utilise the phenomena that rays of coherent light, reflecting from a diffuse surface of a specimen, will cause a random interference pattern (or speckle pattern) at a plane in space. Each speckle is a spot with a unique size, shape and intensity, which is due to the local microscopic surface imperfections. There are three speckle methods:- speckle photography and speckle interferometry and Shearography (Dally & Riley 2005; Gan & Steinchen 2008).

Speckle photography employs a single beam of coherent light and a double exposure of the speckle image when a specimen is loaded and unloaded. The double exposure of the speckle image, known as a specklegram, can then be used as diffraction grating. When the specklegram is illuminated with coherent light and projected on to a screen, fringes patterns are produced containing information about the in-plane displacement field. However, if the specimen moves too far, the two speckle patterns will not be comparable (decorrelated) and fringes will not be produced (Inechen, Eglin & Dändliker 1980; Sjödahl 1995, 1997).

Speckle interferometry is similar to speckle photography, however, the separate components of displacement can be determined. To measure a component of in-plane

displacement, two beams of coherent light are used to illuminate the specimen, which are orientated in the displacement direction of interest at opposite angles of inclination, and a camera positioned parallel to the specimen to record the speckle images. In order to measure out-of-plane displacements, again two beams of coherent light are utilised, however, one is used to illuminate the specimen and the second is utilised as are reference focused on the camera. A double exposure of the speckle image, when the specimen is loaded and unloaded, provides a fringe pattern with information regarding the displacement component, as seen in Figure 2.4. Like holographic interferometry, vibratory motion can be investigate utilising real-time and time-average techniques (Dally & Riley 2005; Gan & Steinchen 2008).

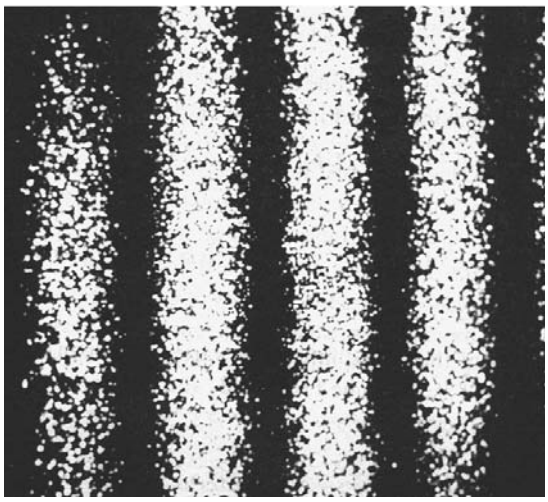

Figure 2.4. Fringe pattern produced using speckle interferometry (Unknown 2008).

The advantage of speckle methods is that a grating is not required to be placed on the specimen to produce moiré-like fringe patterns. However, the produced fringe patterns are poorly defined when compared to moiré and holography techniques and require high

quality vibration isolation systems and like any technique that employs a camera to capture images, the loading frequencies that can be investigate are limited to less than half the frame rate of the camera (Dally & Riley 2005).

2.1.6 Digital Image Correlation

Digital image correlation essentially compares a surface pattern of a plane specimen from two digital images in order to establish the displacement field. To create a good surface pattern the surface of the specimen is usually sprayed with paint and ordinary white light utilised to illuminate the surface of the specimen. Two- and three-dimensional displacement fields can be measured using one camera or two cameras, respectively (Dally & Riley 2005; Sutton 2008).

The advantage is this technique is that it utilises inexpensive equipment, non-specialised materials, can measure large displacements and the size of the specimen that can be investigated is only limited to the magnification of the camera (Dally & Riley 2005; Sutton 2008).

The drawback of two-dimensional digital image correlation is that any rigid body out-of-plane displacement introduces errors in measurement of the pixel location. With the three-dimensional image correlation, the out-of-plane displacement can be measured, however, there is a more complex calibration process involved. Lastly, the loading frequencies that can be investigated are limited by half the frame rate of the employed cameras. The accuracy of the two- and three-dimensional digital image correlation methods in locating unique points and to establish their locations in x-y plane is with in about 0.02 and 0.08 pixels, respectively (Dally & Riley 2005).

2.1.7 Thermoelastic Stress Analysis

Thermoelastic stress analysis utilises an infrared camera to measure the full-field temperature changes on the surface of a material when loaded dynamically within its elastic region. Under adiabatic conditions, the temperature change at a point is proportional to the change in the sum of the principal stresses at that point. As the infrared camera can take full-field measurements over the entire surface of the specimen (as seen in Figure 2.5), information on the principal stress sum field can be obtained (Thomson 1994; Dulieu-Barton & Stanley 1998; Greene, Patterson & Rowlands 2008; Robinson et al. 2009).

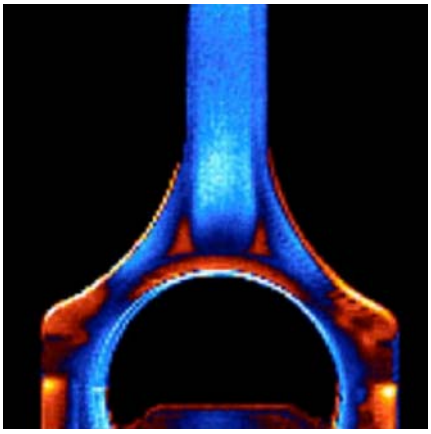

Figure 2.5. Thermoelastic stress analysis of a conrod (Stress Photonics, Inc. 2007).

This method is simple, requires no surface preparation to the specimen and can provide a stress resolution similar to a strain gauge with a high spatial resolution. However, the method can only resolve the sum of the principal stresses and, thus post processing is required to separate the individual stress components. In addition, the test structure must be loaded at a high enough frequency in order to be adiabatic. Unfortunately, at high

frequencies, any surface coatings on the test structure severely reduces the thermal signal, leading to poor stress resolution (Dulieu-Barton & Stanley 1998; Greene, Patterson & Rowlands 2008).

2.1.8 Summary of Strain Measurement Techniques

There are many advantages to each of these techniques and each are very well suited to their specific applications, however, they all have a number of significant disadvantages, which can affect their effectiveness in strain measurement.

The strain gauge technique is specifically suited for acquiring a simple point strain measurement on the surface of a structure. However, they can only be used on structures where the strain gradient is much smaller than the length of the strain gauge. If strain gauges were utilised to evaluate the strain field on a structure, the number of strain gauges required, would influence the state of the stress of the structure and would require extensive wiring. The difficult set up of this technique is a common problem with many of the strain measurement techniques. In addition, a significant factor that can affect the accuracy and resolution of the strain gauge is the improper bonding to or miss-alignment of the strain gauge to the surface of a test specimen. This is indicative of many techniques that require surface preparation or the bonding of material to a surface of a test specimen. This disadvantage also affects many of the reviewed strain measurement techniques, including photoelasticity, moiré and thermoelastic stress analysis.

All the techniques reviewed (with exception of strain gauges), employ the use of cameras to capture real-time surface displacement or stress measurements. This use of cameras limits loading frequency of the test specimen under investigation to less than half the frame

rate of the camera. In addition, techniques that produce optical fringed patterns (such as photoelasticity, moiré, holography and speckle methods) suffer from high signal to noise ratios due to external vibration and, therefore, these techniques require significant vibration isolation. Lastly, a disadvantage common to holographic interferometry and digital image correlation, is a complicated experimental setup and complex data processing is required to separate individual components of displacement. However, these two techniques are the only two of the reviewed techniques that can simultaneously evaluate three-dimensional displacement components on the surface of a structure.

While the reviewed strain measurement techniques have their individual strengths when used in specific applications, a need for further research into new strain measurement techniques is required that avoids these identified disadvantages.

2.2 Damage Detection

Damage is a daily occurrence in mechanical and civil engineering structures. Defects within a structure, such as accidental or accumulated structural damage and deterioration due to mechanical or environmental influences, may significantly reduce a structure's bearing capacities and lead to a catastrophic accident. For existing structures, the negative impact of mechanical damage can be reduced through early detection, assessment and monitoring. Over the last century, a profusion of damage detection techniques have been developed based on various principles and phenomena, including visual inspection, acoustic emission (Nair & Cai 2010), ultrasound (Maev 2009), vibration (Fan & Qiao 2010), radiography, eddy-current (Auld & Moulder 1999) and electromagnetic impedance (Annamdas & C. Soh 2010).

2.2.1 Visual Inspection

Visual inspection is one of the oldest and most widely used non-destructive evaluation techniques. Roberts (1992) in *Non-destructive Testing Techniques* estimated that it accounted for almost 80% of all inspections for damage within structures and components. Primarily, this technique relies on the human eye to visually identify damage on the surface of a component or structure. However, the techniques also incorporate the use of other human sensory systems such as hearing and touch. Spencer (1996, p. 2) defined visual inspection as,

> "…the process of examination and evaluation of systems and components by use of human sensory systems … using such behaviours as looking, listening, feeling, smelling, shaking, and twisting … wherein observations are correlated with knowledge of structure and with descriptions and diagrams from service literature."

Basic visual inspection involves illuminating the test surface with light and using the eye to examine the surface. Surface damage can then be detected from changes in the reflected light. The inspection can reveal the general condition of a component, the presence of oxide film or corrosive products and the presence, as well as orientation, of cracks (Raj, Jayakumar & Thavasimuthu 2002). A number of visual aids have been developed to magnify human vision, as well as provide visual access to inaccessible places. Examples of visual aids include the microscope, borescope and endoscope. In addition, various methods have been developed to further aid the eye in identifying cracks, such as liquid penetrant and magnetic particle techniques.

As established in various engineering texts such as Grandt (2004), Raj (2002) and Roberts (1992), the basic visual inspection is quick and simple to conduct, portable and provides

immediate results, as well as being economical and all most always available, as basic visual inspection only requires the human eye. However, there are a number of disadvantages associated with this technique. The test surface requires cleaning before inspection and must be visually accessible. Surface defects can only be detected and there is a high probability of misinterpretation, i.e. mistaking of scratches for cracks. In addition, the detection of surface damage is sensitive to the direction and colour of illuminating light. Lastly, the probability of successful damage detection is strongly affected by human factors such as experience, mood, attitude and fatigue (Roberts 1992; Raj, Jayakumar & Thavasimuthu 2002; Grandt 2004).

2.2.2 Acoustic Emission

The American Society for Testing and Materials (2010, p. 674) defines acoustic emissions as the "phenomena whereby transient elastic waves are generated by the rapid release of energy from localised sources within a material, or the transient waves so generated." According to Hellier (2003), the acoustic emission monitoring technique for damage detection was first investigated by Joseph Kaiser in 1950 and presented in his PhD dissertation *Investigation of Acoustic Emission in Tensile Testing*. Kaiser (1950) showed that acoustic emission can indicate the potential failure of a material or structure and that the frequency spectra may be used to characterise the damage failure mechanism, i.e. twinning, dislocation motion or cracking (Palmer & Green 1977).

Using acoustic emission sensors, such as a piezoelectric patch, ultrasonic bursts caused by damage stimulated by an applied load can be recorded and used to locate the damage, as well as evaluate their rate of growth as a function of the applied stress (Chang & Liu 2003;

Hellier 2003; Nair & Cai 2010). Figure 2.6 shows the process of acoustic emission monitoring for crack detection.

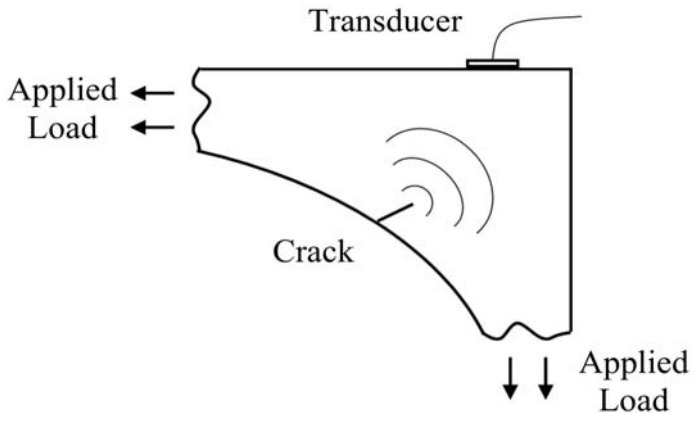

Figure 2.6. Diagram of the acoustic emission technique.

Identified in various engineering texts, such as Hellier (2003), Bray and McBride (1992), and Grandt (2004), the main advantage of using acoustic emission is that the technique is highly sensitive to crack growth, thus using only a few sensors, a large structure can be monitored and the location of growing cracks can be determined. In addition, it is a passive technique, which means that a component or structure can be monitored while in-service for long term testing, which also makes this technique a low cost non-destructive evaluation option. However, acoustic emission methods do not provide the capability to determine the size of flaws. It is well known that it is difficult to interpret the data produced from acoustic emissions, as a structure can produce acoustic signals from mechanisms other than flaws in its components, such as slight movement of bolts. These unwanted signals can complicate acoustic emission monitoring for complex structures.

2.2.3 Ultrasonic

Ultrasonic inspection techniques are based on the principle that ultrasonic sound waves will reflect from internal defects (i.e. cracks) within a material. Ultrasonic waves are vibrational waves with a frequency higher than the 20kHz hearing range. However, Bray and McBride (1992) state most ultrasonic damage detection is accomplished between frequencies of 200kHz to 20MHz. There are three types of ultrasonic inspection techniques, including pulse-echo, through-transmission and pitch-catch, as illustrated in Figure 2.7.

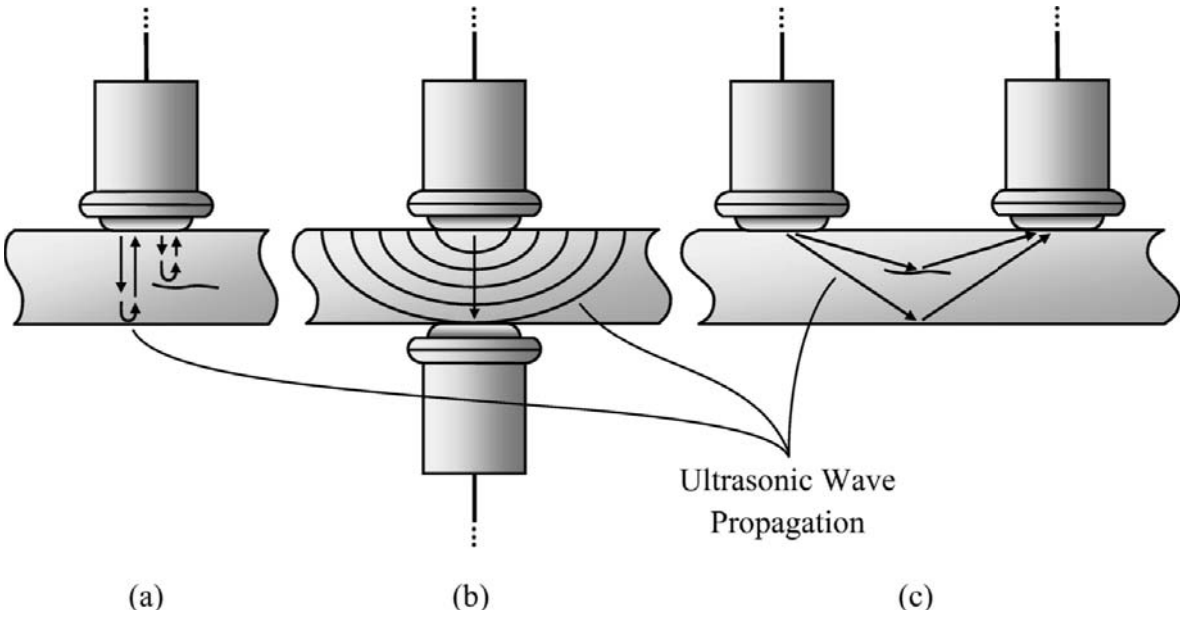

Figure 2.7. Traditional ultrasonic inspection techniques, (a) pulse-echo, (b) through-transmission, and (c) pitch-catch.

According to Cartz (1995), the ultrasonic through-transmission technique for the detection of crack damage in metals was first developed by Sokolov in 1929. This technique

involves generating a continuous sound wave with a transmitting transducer on one side of the test specimen, while measuring the sound energy on the other side with a receiving transducer. Any flaws that occur between the transmitter and receiver cause losses in sound energy, which allow the flaws to be detected.

In 1945, Firestone (1946) developed the ultrasonic pulse-echo technique for damage detection. This technique involved generating 5MHz vibrational waves into the surface of a test specimen via a quartz crystal transducer for 1 microsecond. Using the same quartz crystal transducer, the echoed or reflected vibrational waves are measured. In an undamaged specimen the pulsed waves are reflected from the opposite boundary of the test specimen and the time that the pulsed waves take from being transmitted to received (known as the time of flight) is proportional the thickness of the test specimen. If a flaw is situated in the path of the pulsed waves, the quartz crystal transducer will measure reflected waves before the expected time of flight for the pulsed waves to reflect off the opposite boundary, thus, indicating the presence, but also the location, of the flaw.

According to Hellier (2003), Sproule independently developed the pitch-catch technique for damage detection about the same time as Firestone. Similar to the pulse-echo techniques, a transducer is utilised to generate a sound pulse into the test specimen, however, a second transducer on the same side as the transmitter is utilised to receive the reflected signal. Hellier (2003) reported, that a few year later Sproule developed a transducer that could generate pure shear waves along the surface of a test specimen, and utilised this transducer for his pitch-catch technique, which is now widely use in detecting damage in welded joints.

As expressed by various engineering texts, such as Bray and McBride (1992), Hellier

(2003) and (Blitz & Simpson 1996), the advantages in using ultrasonics for damage detection are that the equipment required to conduct an inspection is relatively inexpensive and portable, but also provides high speed testing capabilities. In addition, an ultrasonic inspection only requires one side of the test specimen to conduct a test, and can detect and locate both internal and surface flaws in thick, as well as thin, materials. Lastly, ultrasonic inspection can be performed on both metallic and non-metallic materials. However, limitations of ultrasonic inspection are that the coupling of ultrasonic transducers to rough surfaces is difficult, evaluating damage in complex structure is impractical due to an increase in the number of wave reflections, flaw imaging is complex and extensive training of operators is required.

2.2.4 Guided Waves

A variation of ultrasonic inspection is the guided wave technique, which utilises the phenomena of Lamb waves. These Lamb waves can propagate in thin plate and shell-like structures and travel large distances with very little amplitude loss (Rose 1999). Guided wave techniques work by, firstly, exciting a piezoelectric element with an applied oscillatory voltage, which excites the structure locally and produces a Lamb wave. This oscillatory voltage is normally pulsed causing a pulsed Lamb wave, which then travels radially away from the piezoelectric element. The wave then becomes incident on structural discontinuities (such as cracks, delamination, corrosion and structural features) and is scattered. These scattered Lamb waves are then measured by the same or another piezoelectric element. However, a need arises to distinguish between damage and structural features from the measured scattered Lamb waves. This is typically undertaken by measuring a baseline signal for the health state of a structure, to provide a reference to

compare with and remove the unwanted signals from future tests. Once the filtered signal is obtained, damage sensitive features are then extracted using a signal-processing algorithm. A pattern recognition technique is then required to locate, classify and estimate the severity of the damage. Finally, these techniques always involve some threshold value to decide whether damage is actually present in the structure (Raghavan & Cesnik 2007).

It should be noted that though the use of piezoelectric elements make the guide wave technique cost-effective, the Lamb waves generated by the piezoelectric elements can produce undesired Lamb wave modes and create difficulty in signal interpretation. This means that appropriate Lamb modes have to be selected and sophisticated signal processing with interpretation software is required to identify individual types of damage (Su, Ye & Lu, Y 2006).

2.2.5 Vibration-Based

Vibration-based damage detection techniques are based on the principle that modal parameters (frequency, mode shapes and modal dampening) are functions of the physical properties of the structure (mass, damping and stiffness).

Doebling et al. (1996), Carden and Fanning (2004), and Fan and Qiao (2010) have cited and reviewed numerous vibration-based techniques for damage assessment of structures, while categorising each technique by the vibration feature extracted for the use in identifying damage, such as natural frequencies, mode-shapes, curvature/strain, to name a few. Fan and Qiao (2010) also identify that each damage identification method can be based on vibration measurement that can be classified as either a ‘model-based method’ or ‘response-based method’. Fan and Qiao (2010, p. 2) states that:

> "The model-based method assumes that a detailed numerical model of the structure is available for damage identification; while the response-based method depends only on experimental response data from structures."

As discussed by Doebling et al. (1996), Carden and Fanning (2004), and Fan and Qiao (2010), the use of natural frequency for the identification of damage within a structure is one the most basic vibration-based damage detection techniques, as natural frequencies of a structure are coupled with its stiffness and mass. The attraction of this technique is that only a few sensors are required to measure the natural frequencies of a structure with little experimental noise. However, the use of natural frequencies has a number of drawbacks. The natural frequencies of a structure is a global parameter of that structure, therefore localised small damage (such as cracks) may not significantly change the natural frequencies, or the changes may be obscured by changes caused by environmental or operating conditions. In addition, modelling a structure and determining potential damage locations due to a change in natural frequency can be quite complicated and may produce non-unique solutions for the damage locations and/or severity.

Another group of vibration-based techniques that overcame the drawbacks of natural frequency based methods are the mode shape based methods. The advantage of using mode shapes over natural frequencies for damage detection is that they are more sensitive to localised damage, able to potentially identify multiple damage locations, and is less affected by environmental conditions. However, to measure the mode shapes of a structure a large number of sensors are required and these measurements are more prone to noise.

Fan and Qiao (2010) state that "many researchers [have identified] that the displacement mode shape itself is not very sensitive to small damage, even with high density mode

shape measurement" and have identified mode shape curvature/strain as a more promising vibration feature for the identification of damage.

2.2.6 Radiography

Roentgen (1896) first developed Radiography in 1895 with his discovery of X-rays. Radiography is based on the phenomena that radiation passing through a material is attenuated depending on the density and composition of the object. Due to the attenuation in radiation, a radiograph can be produced, which is a two-dimensional image that shows the intensity distribution of X-rays or gamma rays that have passed through an object. For the detection of damage in a component or structure, a flaw will lead to reduction in attenuation of radiation and enable the flaw to be detected, as illustrated in Figure 2.8.

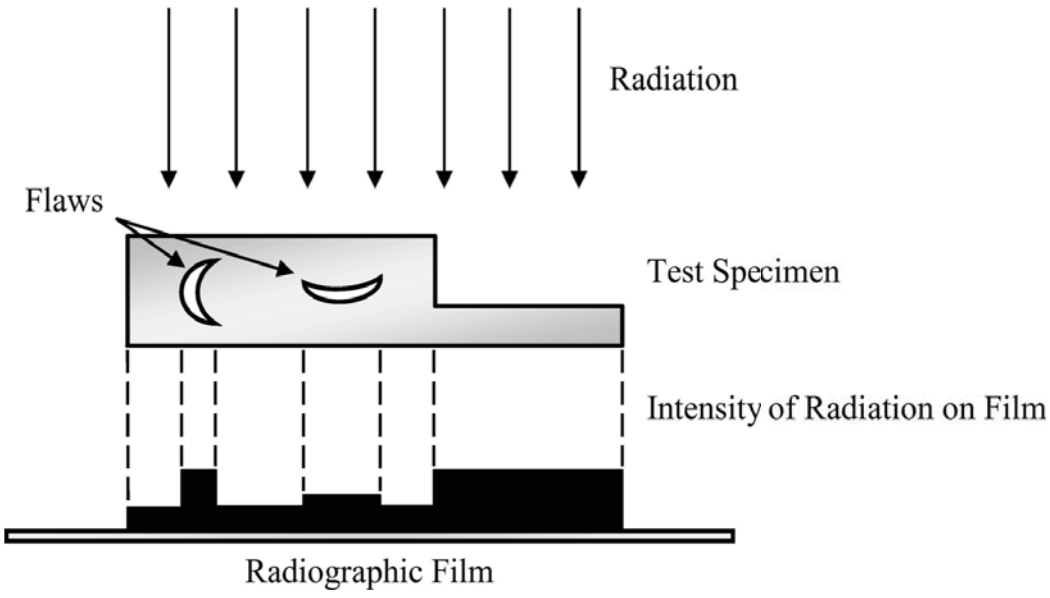

Figure 2.8. Schematic illustration of the radiographic imaging technique.

Bray and McBride (1992) and Hellier (2003) identify the strengths of radiography, which are that internal and external damage can be detected in a wide range of solid materials, complex shapes and thicknesses. The test specimens under inspection do not require any surface preparation. In addition, a radiographic inspection can provide a permanent record or real-time viewing of the inspection, as well as a three-dimensional image with the use of computerised tomography technology. However, the downsides of radiography are that access to both sides of the test specimen are required, energy required to penetrate the test specimen will increase with thickness, and obviously the health hazard radiation poses to the operator.

2.2.7 Eddy-current

The eddy-current damage detection technique is based on the principle of electromagnetic induction. As discussed by Bray and McBride (1992), when an electric current flows through a coil of wire a concentrated electromagnetic field is created. An energised coil with alternating current placed near the surface of a metallic material will produce currents in the material, which flow in the opposite direction to the current in the coil, as illustrated in Figure 2.9. These induced currents, known as eddy-currents, produce an electromagnetic field that opposes the field created by the coil. The eddy-current electromagnetic field, in essence, provides a resistive component into the coil circuit and, thus, modifies the magnitude and phase of the coil current. Therefore, any cracks, voids or other discontinuities within the material that disrupts the eddy-current flow will have a significant affect on the eddy-current electromagnetic field and, thus, the magnitude and phase of the coil current, which can be measured.

American Society for Metals (1972) and Bray and McBride (1992) state that the advantages of the eddy-current technique for damage detection are that it is a non-contact technique with high sensitivity to small surface and near surface cracks and that the testing equipment is light, portable and relatively inexpensive, as well as being perfectly suited for automated high speed testing. The eddy-current technique is, however, limited to inspecting materials that are electrically conductive and has a limited inspection depth. In addition, the evaluation of damage is largely qualitative and often affected by variability the material, geometric and electrical parameters of a test specimen.

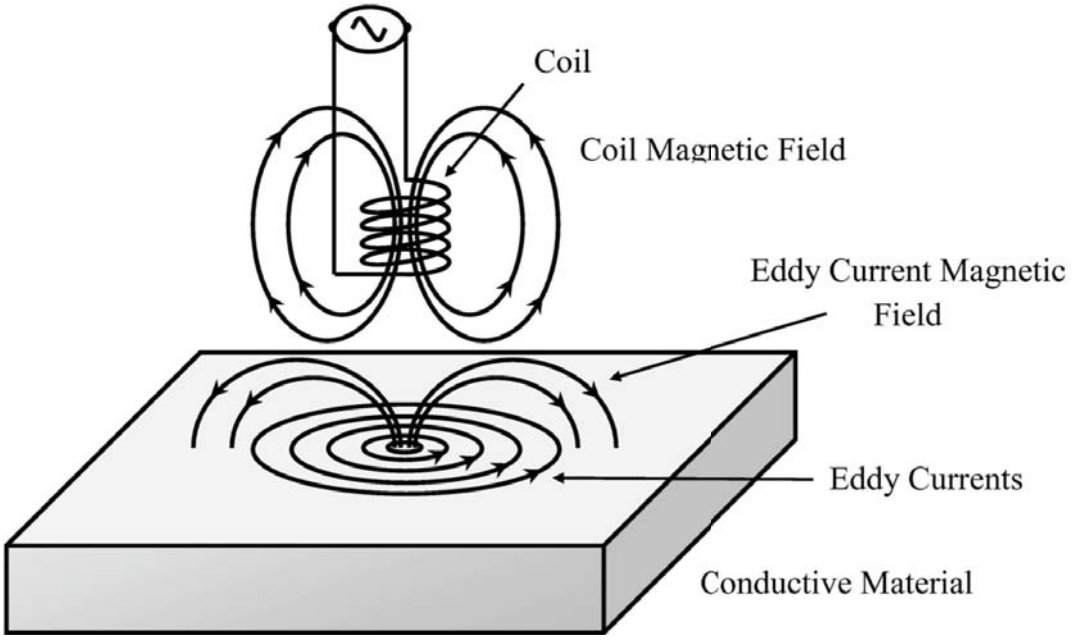

Figure 2.9. Schematic illustration of the eddy-current technique.

2.2.8 Electromechanical Impedance

The Electromechanical Impedance technique is based on two principles. Firstly, damage causes a change in the local mechanical impedance of a structure. Secondly, the electrical impedance of piezoelectric materials is directly related to the mechanical impedance of its host structure. Therefore, structural damage can be qualitatively determined by monitoring the electrical impedance of an attached piezoelectric material and comparing it to a baseline measurement (Giurgiutiu & Cuc 2005; Park & Inman 2005).

Liang et al. (1994) clearly showed that the electrical impedance of piezoelectric patches attached to a structure was directly related to the mechanical impedance of that structure. This allowed the monitoring of the localised mechanical properties of a structure by measuring the electrical impedance of an attached piezoelectric patch. Therefore, any changes in the electrical impedance signature could indicate localised damage in that area.

Zagrai and Giurgiutiu (2001) investigated the capability of this technique to detect crack damage. They found that a crack presence near the sensor significantly modified the real part of the electromechanical impedance spectrum and the modification decreased as the distance between the sensor and the crack increased.

The main advantage of the electromechanical impedance technique is that modelling of a structure and possible damage conditions are not required, allowing the technique to be easily applied to complex structures. In addition, the technique is sensitive to local minor changes and provides easy to interpret results (Park & Inman 2005). However, the technique requires relatively high electrical power compared to passive damage detection techniques (Mascarenas et al. 2007). In addition, as the mechanical impedance of a

structure is related to its local mechanical properties, changes in loading and ambient temperature can affect the damage detection technique and make it difficult to detect and locate structural damage (Park & Inman 2005).

2.2.9 Summary of Damage Detection Techniques

This section has provided a brief overview of common non-destructive evaluation techniques for the detection of damage in a component or structure, detailing the positive and negative aspects of each.

Techniques that require trained personnel to be able to evaluate damage within a structure (including visual, ultrasonic, radiographic and eddy-current inspection), leads to the possibility for human factors (such as mood, attitude, experience etc.) to affect the detection of damage. In addition, these techniques require that appropriate access to the structure under investigation is available in order to carry out an inspection.

Surface preparation is another significant issue for these techniques, including ultrasonic, guided wave and electro-mechanical impedance inspection, as these techniques require an adequate coupling between the sensor and surface of the test object. If improper surface preparation is carried out before utilising these techniques, false positives or false negatives of detected damage may result.

A significant disadvantage related to radiographic and electromechanical inspection is that they consume a considerable amount of energy to perform inspection of a test object for damage.

A number of techniques are able to identify the presence or location of damage, however,

they are unable to quantitatively identify the size or intensity of the damage. These techniques included acoustic emission, frequency based and electromechanical impedance inspection.

This review of damage detection techniques illustrates that there is a need to develop new techniques based on physical parameters or phenomena accompanying the damage evolution that have thus far not been explored. This literature survey of damage detection techniques has identified that each technique is based on a physical or mechanical principle or utilise phenomena accompanying the damage evolution. Thus, while there are multiple techniques that utilise physical principles, the use of the fundamental principles of Solid Mechanics has not be utilised, specifically the principle of strain compatibility and the conditions of equilibrium, which when combined produces the governing differential equations of displacement.

2.3 Scanning Laser Doppler Vibrometry

The Scanning Laser Doppler Vibrometry (SLDV) is non-contact vibration measurement system that can evaluate vibration velocity and displacement at fixed points on a structure, over a wide bandwidth. The technology is based on the Doppler effect where the vibratory velocity and displacement are evaluated from measured shifts in the frequency of backscattered (partially reflected) laser beam light off a moving object. The Polytec PSV-400 Vibrometer system (utilised in the investigations carried out in this thesis) can scan the entire surface of a structure by automatically probing a set of pre-defined measurement grid points. The are currently two varieties of vibrometers for vibration measurement, which include a 1D system that can measure the out-of-plane vibration vector and a 3D

system that can provide the 3D vibration vector (Polytec 2011). Further information on the operation and configuration of SLDV is in Section 3.1.

SLDV has significant advantages in measuring three-dimensional displacement components on the surface of a structure over other currently available technologies, for instance holographic interferometry and digital image correlation. This is because the vibrometer can measure displacements in the frequency domain, which is in turn able to remove extraneous noise such as ground borne vibrations. In addition, the vibrometer measures the displacement over a mesh of points attached to an image of the structure. This allows the vibrometer to investigate high loading frequencies applied to a test specimen. Conversely, holographic interferometry and digital image correlation, require the use of a camera to record displacements of a test specimen, which limits the loading frequency that can be applied to the test specimen to half the frame of the camera. Therefore, this section surveys the literature relating to non-destructive evaluation techniques that utilise SLDV for strain measurement, as well as damage detection techniques.

2.3.1 Strain Measurement Utilising SLDV

One of the first investigations into the use of a laser Doppler vibrometer to measure strain on the surface of a structure was conducted by Ferguson and Carpentier (1989). In this study, the authors investigated the use of a prototype 1D laser Doppler vibrometer for the measurement of surface bending strain of a beam. Their investigation looked at measuring dynamic bending strains on the surface of a beam excited by discrete frequencies ranging from 30Hz to 700Hz, as well as a 0Hz to 200Hz broadband frequency. To evaluate the

bending strains, Ferguson and Carperntier used a central finite-difference approximation. The estimated bending strain for discrete frequencies showed fair agreement to strain gauge measurements, however, the estimated power spectral density of the bending strain for the broadband frequencies did not correlate with measurements from the gauges, which was mainly due to the assumptions made when deriving the bending strain transfer function.

Goetsh and Rowlands (1991), investigated use the use of the 1D SLDV to estimate the strains on an aluminium and composite circular plate driven sinusoidally. The laser vibrometer was then used to measure the displacement at numerous of locations. To evaluate the bending strain Goetsh and Rowlands fitted a polynomial or cubic spline to the measured displacement data and then differentiated the fitted function analytically. The estimated strain results, evaluated using the measured displacements, were in reasonable agreement to strains measured using strain gauges.

In 1992, Miles et al. (1994) developed a method for estimating the power spectral density of bending strain of a randomly excited beam based on the simultaneous measurement of vibration from a stationary and roving sensor. Miles et al. suggested that a 1D vibrometer could be used as this roving sensor to perform discrete vibration measurements. Three years later, Xu and Miles (1996b) successfully validated the method using a base excited cantilever beam and a 1D vibrometer. The experiment consisted of a cantilever beam vibrated at the fixed end with a broadband force and an accelerometer mounted at the free end, which was utilised as the fixed sensor. Xu and Miles showed that the strain spectral density obtained using the 1D vibrometer and accelerometer measurements were in good agreement with direct measurements using a strain gauge. The method was then applied to

full-field bending strain measurements of a randomly exited plate structure (Xu & Miles 1996a).

Moccio and Miles (1996) developed a method for estimating the transfer function between the bending strain of a beam structure and the input force by performing the second spatial derivative of the transfer function of the displacement, measured using a 1D vibrometer. To evaluate the bending strain transfer function, the measured transfer function of displacement, relative to the applied force, is curve fitted over the spatial domain using orthogonal polynomials as basis functions and then differentiated twice with respect to the spatial co-ordinate. Moccio and Miles performed an experiment to evaluate the potential of the method to estimate the bending strain transfer function using the 1D vibrometer and then compared the bending strain transfer function measured using strain gauges. This experiment showed excellent agreement between the 1D vibrometer and strain gauge techniques for the estimation of the bending strain transfer function.

With the advent of the 3D laser Doppler vibrometry system, Mitchell at al. (1998) suggested that "with the full-surface response descriptions one can consider the development of strain distributions over the surface." A decade later, Mitchell's suggestion became a reality when Schüssler (2007) demonstrated the use of 3D laser Doppler vibrometry for full-field in-plane strain estimate at a Vibrometry Technology Workshop at Loughborough University. Cazzolato et al. (2008) then successfully developed a method for evaluating in-plane strains using two-dimensional 3-node linear and 4-node bi-linear finite elements. However, the use of finite elements was found to be very sensitive to systemic errors within the vibrometer measurement system.

In 2011, Schüssler et al. (2011) published a conference paper presenting Polytec's new

StrainProcessor software for the 3D SLDV system to evaluate dynamic surface stress and strain distributions. The software is based around the 3-node linear finite elements developed by Cazzolato et al. (2008), with an additional smoothing filter. The paper looked at validating the StrainProcessor Software by investigating the dynamic strain distributions produced on a cantilever test structure, vibrated with sine excitation at the first 6 natural frequencies. Though, Schüssler et al (2011) were very vague on the finer details of the StrainProcessor software, their results measured from strain gauges and simulations from finite element analysis were in good agreement with strains evaluated using Polytec's StrainProcessor.

Vuye et al (2011) investigated the use of 3D SLDV in conjunction with the Polytec StrainProcessor for the measurement of the dynamic strain distribution on a fan blade. The resonant frequencies of the fan blade were first measured and a finite element model was updated to closely match the actual fan blades vibrational response. Dynamic strains for the first 5 natural frequencies were then estimated along a line on the fan blade using the 3D vibrometer with the aid of the Polytec StrainProcessor. Vuye et al. (2011) investigated the effectiveness of the StrainProcesser in evaluating the dynamic strains from 3D SLDV measurements, by comparing the results with that measured from strain gauges and simulated by a finite element model. They found that there was general agreement between the dynamic strains simulated by the finite element model, measured by the strain gauges and estimated using Polytec StrainProcessor. However, there was still significant deviation in the strain estimate using the Polytec StrainProcessor, to that observed from the strain gauges and finite element model.

Cazzolato et al. (2008) first identified from their research that further development was

needed in order to be able to successfully evaluate the full-field in-plane surface strains on an object from in-plane displacements measured using a 3D vibrometer. This includes an investigation of various filtering and differential algorithms in order to produce a robust and an accurate full-field surface strain measurement system, and the development of the technique to evaluate strains in shell-like structures.

2.3.2 Damage Detection Utilising SLDV

With the advent of SLDV, a range of new techniques for damage detection were able to be investigated due to the ability of the system to perform rapid non-contact vibration measurements at large number of points with a high spatial resolution. The current research involving the use of SLDV for damage detection includes the use of deflection, curvature, and frequency response of a structure, as well as the measurement of induced ultrasonic wave propagation on the surface of a structure. A literature survey of each of these research areas will be discussed.

2.3.2.1 Out-of-Plane Deflection

In 2000, Ghoshal et al. (2000) investigated the use of operational deflection shapes of a structure measured by a 1D vibrometer to identify an added mass to a wind turbine blade. The laser was used to measure the vibration response at various points on the wind turbine blade to a periodic chirp excitation. The laser vibrometer computer then automatically computes a Fourier transformation of the vibratory response and the operational deflection shapes correspond to the real deflection amplitudes at each point at a specific vibration frequency. The operational deflection shape will approximately coincide with a mode shape of the structure if the excitation frequency is at a natural frequency and damping is

small. From their experimental investigation, Ghoshal et al. showed that at the third natural frequency of the blade, the operational deflection shape was observed to be symmetric, however, the operational deflection shape became non-symmetric when the same excitation frequency was interrogated with the attached mass. Ghoshal et al. (2000) proposed a simple method to identify structure damage by interrogating a symmetric operation deflection shape of a healthy structure and periodically monitor that operation deflection shape for changes.

Two years later, Waldron et al. (2002) performed a numerical investigated for the localisation of damage by investigating the difference in the velocity of damaged and undamaged operational deflection shapes, at resonant frequencies. Damage was identified by the presence of a discontinuity in the difference of these shapes. Waldron et al. found from this study that when constraining the beam under investigation, using fixed-fixed or pinned-pinned constraint, detection of damage was easer than when the beam is fixed-free. In addition, higher natural frequencies were found to be more sensitive to damage. Further investigations were undertaken by Ghoshal et al. (2003) to use this technique for the detection of delamination damage in composite beam and plate structures. Delamination was then identified in the structure by anomalies in or loss of symmetry of the operational deflection shapes. Sundaresan et al. (2003) then applied the techniques to a wing panel to detect a crack in a fastener hole in the interior of the panel. However, the use of this technique was unsuccessful in locating the damage.

In 2000, Pia and Jin (2000) developed a technique, known as Boundary Effect Evaluation, for evaluating damage in plate and beams structures. This technique was based on the phenomenon that damage in a structure introduces new boundaries, which create spatially

localised effects to the steady state high frequency dynamic response of the structure. By interrogating the boundary effects of operational deflection shapes, measured by a 1D vibrometer, damage can be localised. The technique essentially comprised of sliding-window least-square fitting of the generalised solution of a uniform, free, harmonically vibrating beam to the measured operational deflection shape of a beam that is being excited at a single natural frequency by a piezoelectric actuator. Pia and Jin (2000) related the coefficients of the fitted generalised solution to different physical parameters, such as boundary conditions, elastic energy, kinetic energy, curvature and the spatial derivative of curvature. They investigate the use of these parameters, as well as the standard deviation of the fitted to the measured deflection over the sliding window, for the use in detecting singular and multiple saw cuts damage. The various parameters were able to effectively detected single and multiple saw cut locations, and did not require a baseline measurement of the undamaged structure. The technique was also successfully applied to two-dimensional operational deflection shapes to detect damage in rectangular (Jin & Pai 2000) and circular (Pai, Oh & Lee, S 2002) plate structures.

A thorough numerical investigation was conducted by Pai and Young (2001) into use of the Boundary Effect Evaluation method for the detection of damage in beam structure for various types of damage (surface slots, through-the-width internal holes, side slots), damage location, added mass, added stiffeners, noise, sliding windows length and mode frequency selection. These simulations were then followed by experimental investigation of defect detection in beams with multiple damage sites. Finally, an experimental investigation was conducted on a thick cantilever beam with a through-the-thickness fatigue edge crack.

Pai et al. (2003) developed a method to locate and estimate the depth of a surface slot in a beam. Experimentally the technique was able to successfully locate and estimate the depth of the slot down to 10% of the beam thickness. Further developments were carried out by Pai et al. (2004) in order to be able to detect damage at a boundary constraint location by identifying a deviation from the known boundary conditions. Finally, Pai et al. (2004; 2006) successful applied the use of the one-dimensional Boundary Effect Evaluation method to detect damage in an aircraft wing panel, such as small added masses and slots cut into the panel stiffeners.

A number of drawbacks of the technique were identified by Pai et al. (2004). Firstly, damage is difficult to detect if located at a node, and thus a number of operational deflection shapes need to be interrogated in order to provide a reliable inspection. In addition, although high frequency operation deflection shapes are more sensitive to damage, they may not be able to be excited with current actuating methods in thick, stiff and/or heavy structures. Lastly, the test specimen must have uniform thickness, as uniformity introduces boundary effects into the operational deflection shapes.

2.3.2.2 Curvature Measurements Utilising SLDV

The use of curvature, as a damage identification technique, was first proposed by Pandey et al. (1991), where they used changes in curvature to identify and locate damage in beam structures. Pandey et al. conducted numerical experiments on a cantilever beam and a simply supported beam, where finite element analysis was used to obtain the displacement. A central-difference approximation was then utilised to calculate the curvature from the displacement. The results showed that the absolute changes in the curvature were localised

to the region of the damage and the magnitude of the changes increased with an increase in size of the damage (Pandey, Biswas & Samman 1991).

In 2007, Qiao et al. (Qiao et al. 2007a, 2007b) investigated the use of a 1D vibrometer to evaluate various curvature mode-shape algorithms, which included the *gapped smoothing method* (Ratcliffe & Bagaria 1998), *generalized fractal dimension* (Hadjileontiadis, Douka & Trochidis 2005), *strain energy method* (Cornwell, Doebling & Farrar, C 1999), for the detection of delamination damage in beam and plate structures. From these results Qiao et al. observed that these damage detection algorithms, were successful in identifying the presence, location, and relative size of comparatively large delaminated zones in composite beam and plate structures.

Cao and Qiao (2009) then developed an algorithm for the detection of delamination, which evaluates the curvature from measured beam deflection using an *à trous* Laplace operator that has been smoothed using a Gaussian filter. Using a smoothing Teger energy operator (Kaiser 1993) to intensify the damage features, the algorithm was successful in locating the damage, which was identified by large peaks at the boundaries of the delaminated zone.

Benefits of the curvature approach, identified Pandey et al.(1991), is that curvature can be obtained directly, by measuring strains, instead of the typical use of displacement or acceleration measurements. However, a drawback for this method is that to obtaining curvature of a structure, measurements are required from across the whole structure.

2.3.2.3 Guided Waves Measurements

A variation of the traditional Pitch-Catch guided wave inspection techniques is the use of a 3D vibrometer to measure the out-of-plane or in-plane surface vibration created by a Lamb

wave in a plate or shell-like structure. This technique was initial explored by Professor Wieslaw Staszewski at the University of Sheffield, United Kindom, but is now currently continued at the AGH University of Science and Technology in Krakow, Poland.

In 2004, Staszewski (2004) investigated the use of a 1D vibrometer for the measurement of Lamb waves in thin plate structures. Staszewski's aim was to utilise this application of Lamb wave sensing for a damage detection technique. When measuring the Lamb waves in an aluminium plate generated by piezoceramic actuator via a 1D vibrometer, Staszewski reported a significant level of noise in the measured Lamb wave signal and investigated three signal processing algorithms, which included the Savitzky-Golay filter, the Kaiser-Bessel filter and orthogonal wavelet denoising. Staszewski found that vibrometry measurements utilising any of the filtering techniques provided results that were in good agreement with numerical simulations, as well as measurements taken from piezoceramic sensors.

In the same year, Mallet et al. (2004) conducted a series of experiments using 1D vibrometer on two aluminium plates; one with a 10mm x 5mm rectangular slot and the other with a 0.5mm hole with 1mm notches induced each side. The 1D vibrometer produced a full-field measurement of the maximum out-of-plane velocity component of a pulsed Lamb wave generated by a piezoceramic actuator. Mallet et al. found that a change in velocity amplitude of the Lamb waves in the vicinity of the damage location was a good indicator that damage was present within the structure. However, further work still needs to be conducted to determining the severity of the damage.

Leong et al. (2005) continued this work and investigated the detection of fatigue crack damage. Two techniques were investigated:- velocity amplitude analysis and time of flight

analysis. This study found that a 1D vibrometer can be used to provide full-field measurements of local velocity amplitude and time-of-flight variations of excited Lamb waves in order detect fatigue crack damage longer than 6mm.

Lee and Staszewski (2007) investigated the use of Lamb wave interaction modelling to improve damage detection monitoring strategies. In this work, Lee and Staszewski validated simulated results with 1D SLDV. They found that the relative change in time-of-arrival, due to slot damage within a plate, was smaller than the equivalent change in velocity amplitude.

In 2007, Staszewski et al. (2007) first employed the use of a 3D vibrometer to measure the out-of-plane and in-plane Lamb wave components generated within metallic plate structures in order to detect fatigue crack damage. The technique involved scanning a grid of points to measure the full-field RMS velocity amplitude of pulsed Lamb waves generated by a piezoceramic actuator and it was successful in locating and estimating the severity of the fatigue crack. A few years later, Staszewski et al. (2009) applied the use of 3D SLDV Lamb wave sensing to detect delamination damage within a composite structure. The technique involved scanning a grid of points to measure the maximum peak-to-peak velocity amplitudes of pulsed Lamb waves generated by a piezoceramic actuator. The technique was successful in detecting an increase in velocity amplitude at the location the delaminated zone in the out-of-plane Lamb wave component and, thus, is able to estimate the size of the delaminated zone, which was in good agreement with results obtained from ultrasonic testing.

The advantage of the vibrometry Lamb sensing over the classical piezoceramic sensing is that complex Lamb wave propagation modelling or baseline measurements of the

undamaged structure are not required to locate the damage, no signal processing is performed to extract damage related features, and the technique is not affected by temperature variations. These advantages make the technique very straightforward in analysing and interpreting the location and severity of damage (Staszewski, Lee, B & Traynor 2007).

2.3.3 Summary of Damage Detection Using SLDV

This section has surveyed the current literature related to the application of SLDV for use in two different categories of non-destructive evaluation, specifically strain measurement and damage detection.

The survey of strain measurement systems utilising SLDV has revealed that many bending strain investigations have been conducted since the development of commercially available vibrometers. However, there has not be been an investigation into the accuracy that can be achieved with more recent developments in SLDV systems. In addition, a thorough investigation into the use of a 3D vibrometer to measure full-field in-plane strains has not yet been conducted, nor has there been an investigation of the different types of differentiation and filtering techniques that could be utilised to evaluate strains, while limiting the level of noise in the estimation.

At the same time, there have been various techniques that have been developed to detect damage with the advent of SLDV. These techniques are based on basic mechanical principles, such as deflection and curvature shapes, as well, the physical phenomena of the large propagation distances experienced by Lamb waves in plate structures.

The techniques based on measured operational deflection shapes essentially applies a

sliding-window least-square fit, of the general solution of the deflection of an undamaged beam or plate specimen, to the operational deflection shape of a beam or plate specimen under investigation measured using a 1D vibrometer. These fitted results are usually compared to the measure operational deflection shape and damage was identified by sharp discontinuities in the difference of fitted to measured displacement. The techniques were found to be sensitive to damage for the high frequency deflection shapes, however, damage was hard to detect if positioned at a node (zero displacement in the deflection shape). In addition, the specimen under investigation must have uniform thickness across the specimen.

The techniques based on curvature, similar to the techniques based on operational deflection shapes, usually apply a sliding-window least-square-fit, of the general solution of the deflection of an undamaged beam specimen, to the deflection shape of the beam specimen measured using a 1D vibrometer. The least-squares-fit is then utilised to evaluate the second derivate of the deflection with respect to its length, i.e. curvature. The evaluated curvature is then compared to previously recorded undamaged curvature of the beam specimen under investigation and damage location was identified a differences in the curvature at the damage region.

Guided ultrasonic techniques utilise the phenomena of Lamb waves, which when excited in a plate can propagate large distances. A number of techniques have been developed based on the reflection of these waves caused by damage. Current techniques using SLDV technology include the use of three-dimensional velocity amplitudes of pulsed Lamb waves propagating through a plate structure measured using a 3D vibrometer. Damage is detected by observing an increase in the velocity amplitude at the damage region. The

advantages of this SLDV technique is that no undamaged baseline measurement is required to locate the damage, no signal processing needs to be preformed and the technique is not affected by temperature variations.

2.4 Summary

A literature review related to this study, broadly identified existing strain measurement and damage detection techniques. This was then followed by a review of current techniques that utilise SLDV technology. From the literature review several key deficiencies in the current damage detection and strain measurement techniques have been established.

2.4.1 Strain Measurement

The reviewed strain measurement techniques have a number of advantages that make them suited for specific applications, however, they also have numerous disadvantages. The main disadvantage of the reviewed strain measurement techniques is that majority utilise cameras to capture the displacement field, which strain is then evaluated from. The use of cameras limits the strain measurement technique to investigate loading frequencies to less than half the frame rate of the camera. Secondly, the use of moiré-like fridge patterns to determine displacement requires significant vibration isolation to avoid poor signal to noise ratios. Therefore, a need was identified for the development of new strain measurement techniques based on SLDV, which can provide broad spatial strain maps, like the imaging methods, while at the same time measure high frequency displacement so that unwanted noise can be filtered out using Fourier analysis, similar to what can be done with strain gauges. To date, a number of researchers have investigate the use of 1D SLDV to measure bending strain, however, there is no current study using the most current 1D

SLDV system. In addition, with the recent development of 3D SLDV, initial research as been conducted into a full-field surface strain measurement technique, thus, further development is needed using advanced filtering methods in order to reduce noise, as well as, an investigation in to the accuracy of the new technique.

2.4.2 Damage Detection

Conversely, each damage detection technique has various disadvantages, which include the need for trained personnel to perform the inspection, require surface preparation to conduct the inspection, high energy consumption, and only being able to detect the presence of damage and not pin-point its location. However, the key disadvantage is that all these techniques have difficulty in identifying the presence of damage, if not the location, in composite materials.

Research into developing techniques using SLDV systems has shown promise for detecting and locating various types of damage, including delamination within composite materials. These techniques include the use of displacement, curvature and guided ultrasonic waves. However, there are other kinematic principles that still have not yet been investigated, specifically, the governing differential equations of displacement.

2.5 Gap in the Field of Research

This chapter has broadly discussed specific non-destructive evaluation techniques for strain measurement and damage detection, and has presented a literature survey on techniques that utilise SLDV.

Therefore the findings from the literature review established the following gaps in the field

of research:

- The accuracy of quasi-static bending strain measurements using current 1D SLDV technology had not been thoroughly investigated,
- the precision of a newly developed full-field surface strain measurement techniques utilising 3D SLDV had not been established, and
- that a damage detection technique based on the violation of the governing differential equations of displacement had not been previously researched.

It is stressed again that the development of in-plane strain measurement and damage detection techniques based on the governing differential equations of displacement have only been possible in the last few years with the advent of 3D SLDV, as well as the advancements into high resolution velocity decoders and spatial measurement resolution.

Hence, the global aim of this research is to investigate and develop new non-destructive evaluation techniques for strain measurement and damage detection utilising 1D and 3D SLDV.

2.5.1 Strain Measurement

An number of researchers have investigate use of 1D SLDV for the evaluation of bending strain measurements, however, there has not been a recent investigation into the accuracy of evaluated quasi-static bending strains of a beam using the most current vibrometry technology. Although, there has been some preliminary research conducted into the development of full-field in-plane strain using a 3D vibrometer, today date, no extensive research has been conducted into the accuracy of the technique using 3D SLDV

measurements. With regards to strain measurement, the specific objectives of this research are to:

- determine the accuracy of a bending strain measurement technique for various filter parameters,
- develop a new strain measurement technique utilising 3D SLDV and Savitzky-Golay differentiating filter,
- determine the accuracy of in-plane strain measurement technique for various filter parameters, and
- determine optimum parameters for each technique and determine future work.

2.5.2 Damage Detection

All non-destructive evaluation techniques for damage detection reviewed in this chapter are based on a physical or mechanical principle or utilize phenomena accompanying the damage evolution. However, the literature has shown a lack of research into the utilisation the general mechanical principles:- strain compatibility and conditions of equilibrium. By combining these two principles, the governing differential equations of displacement for beam and plate structures can be derived. With regards to damage detection techniques, the specific aims are to:-

- develop, investigate and validate new damage detection techniques based on the governing differential equations of displacement locate delaminate damage beams and crack damage in plates.

Chapter 3. Experimental Set Up

For any new research to be developed, existing technologies need to be adapted or new ones to be manufactured. This chapter details the experimental setup developed for, and used in, this research into strain measurement and damage detection utilising a 1D or 3D Scanning laser Doppler vibrometry (SLDV) system. The principles of operation of the SLDV system will be first discussed, including the optical configuration of the scanning head, the interferometry principle the system is based on, the arrangement of the 1D and 3D SLDV systems and measurement parameters used for each test. Following this, a description of the experimental setup used to conduct the in-plane and out-of-plane experiments will be outlined, as well as the design of the test specimens.

3.1 Scanning Laser Doppler Vibrometry

Polytec scanning laser Doppler vibrometers utilise a helium-neon laser to measure the vibratory displacement and velocity at a point on the surface of an object in the direction of the laser beam through laser heterodyne interferometry. The interferometer signal is decoded within the laser head control box by a velocity decoder from which an analogue voltage signal proportional to the velocity is produced (Polytec 2004, p. A–3). An individual laser head can only measure vibrations in one direction (of the laser beam). Therefore when utilising a 1D SLDV system (PSV-300), only the displacements of an object that are in-line with the laser beam can be determined from the velocity signal. By

employing three laser heads, the 3D SLDV system (PSV-400-3D) can focus the three laser beams at a point on an object, from which displacement components in three orthogonal directions can be obtained via an orthogonal decomposition of the three velocity signals (Polytec 2004, p. A–2). The optical configuration of the vibrometer and the heterodyne interferometry principle it is based on will be discussed in the proceeding sections.

3.1.1 Optical Configuration

The laser scanning head consists of a laser, beam splitters, quarter wave-plate, lens, scanning mirrors, Bragg cell and optical detector. The optical configuration of the head is shown in Figure 3.1. A helium-neon laser is utilised to provide a linear polarised beam, which is initially split at the first beam splitter into a beam that will be focused at the object of interest and a reference beam to compare to the reflected beam from the object. The object beam then passes through a second beam splitter and a quarter wave plate. A lens and scanning mirrors are used to focus the object beam and position it to a point on the object surface, from where it is reflected back along the same path. The reflected object beam passes through the quarter wave plate a second time and is then deflected by the second beam splitter to a photo detector. At the same time, the reference beam is passed through a Bragg cell and deflected by the third polarised beam splitter to coincide with the object beam onto the photo detector. The Bragg cell provides a frequency offset which allows the sign of the velocity to be determined (Polytec 2004, p. A–3).

When the object beam and reference beam coincide at the detector an interference signal is produced, from which the detector creates a proportional electrical signal. This signal is converted to object velocity through the use of a digital velocity decoder in the controller.

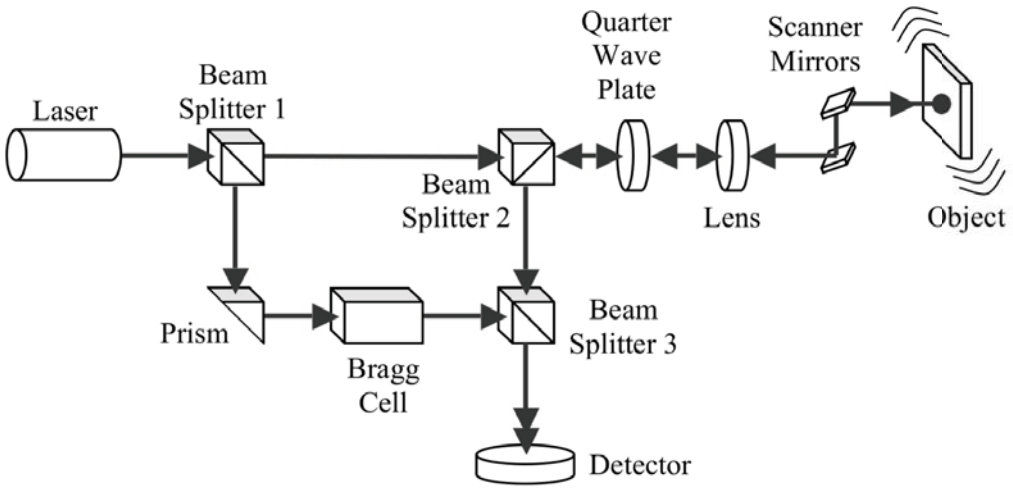

Figure 3.1. Optical configuration of the scanning head.

3.1.2 Principle of Heterodyne Interferometry

Interferometry is based on the principle that two coherent light beams will interfere when made to coincide. At the photo detector, the intensity (I) of the coinciding reference and object beams vary with the phase difference (ϕ) between the beams and can be expressed as (Karasik, Rinkevichius & Zubov 1995),

$$I(\phi) = I_{\max} \cos^2\left(\frac{\phi}{2}\right) \tag{3.1}$$

where I_{max} is the maximum possible intensity of the combined beam. The phase difference between the two beams (ϕ) is dependent on the difference in path lengths (ΔL) and has the relationship,

$$\phi = 2\pi \frac{\Delta L}{\lambda} \tag{3.2}$$

where λ is the wavelength of the laser beam.

As the object beam is scattered back from a moving object, the path difference (ΔL) changes with time and, thus, so does the phase difference (ϕ). This causes a moving interference pattern on the optical detector, which can be used to determine the displacement. To determine the direction of the displacement, directionally sensitive counting of the passing fringe pattern is performed (Polytec 2004, p. A–1).

The object beam scattered back from the moving object also experiences a small frequency shift (f_D), known as a Doppler shift. This Doppler shift is proportional to the velocity (v) of the object and is expressed as (Albrecht et al. 2003):

$$|v| = \frac{\lambda}{2} f_D \quad \left(= \frac{1}{2}\left|\frac{\partial \phi}{dt}\right| = \frac{\lambda}{4\pi}\left|\frac{\partial \phi}{dt}\right|\right) \tag{3.3}$$

If the object beam coincided with the un-modified reference beam at the detector, a beat frequency equal to the Doppler shift would be observed. However, the measured object velocity using this Doppler shift would be independent of its direction. In order to determine the directional velocity of the object from the Doppler shift, the reference beam is passed through a Bragg cell, which shifts the light frequency by 40MHz (Polytec 2004, p. A–1). The directional velocity of the object can then be determined. The modulation frequency reduces below 40MHz when the object moves towards the vibrometer and increases above 40MHz when the object moves away. A velocity decoder can then transform the Doppler frequency shift measured at the detector into a voltage signal proportional to the object velocity. Once Fourier analysis is performed on the vibratory velocity signal, the discrete vibratory displacement frequency components can then be evaluated by,

$$s = \frac{v}{2\pi f} \tag{3.4}$$

where f is the discrete frequency component of interest.

3.1.3 1D SLDV System

The 1D SLDV system (PSV-400) consists of the laser scanning head (PSV-400-MR), high resolution digital camera (A-CAZ-1000), controller (OFV-5000), junction box (PSV-E-401-3D) and workstation computer (PSV-W-400-3D). The laser head is mounted on a tripod (seen in Figure 3.2) and positioned such that the front face of the laser head is parallel and in-line with the specimen. In addition, a high resolution camera is also mounted on a tripod and positioned next to the laser head, which provides a high resolution video feed of the object under investigation. The laser position, focus and measurement are then controlled using the workstation computer. In order to perform a measurement, a two-dimensional alignment of the laser to the specimen surface is performed using the scanning head video feed. This allows the laser to be positioned exactly to a designated scan point on the specimen in the workstation video feed. A scanning grid is then placed on the specimen over the workstation video feed, which can be seen in Figure 3.3. The laser will precisely move to each scan point within the grid when performing scan measurements.

Figure 3.2. Photograph of the 1D vibrometer mounted on a tripod, along with external high-resolution video camera.

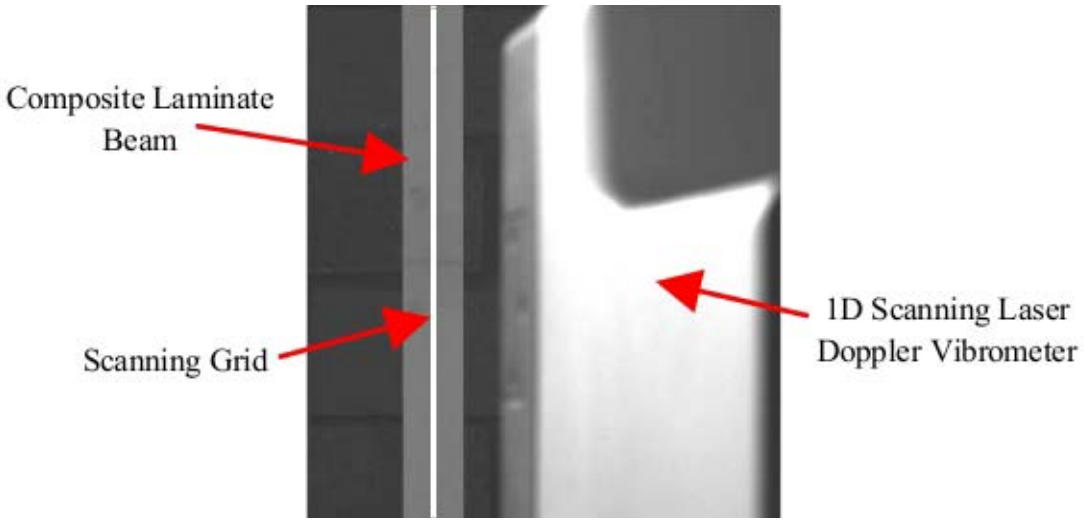

Figure 3.3. Image of the scan grid used for detecting through-the-width delamination in a composite beam. Note that the scan points are so close together, the scan grid looks like a continuous line.

3.1.4 3D SLDV System

The 3D SLDV system consists of three independent scanning heads (PSV-400-MR), a high resolution digital camera (A-CAZ-1000), one junction box (PSV-E-401-3D), three controllers (OFV-5000) and workstation computer (PSV-W-400- 3D). The laser scanning heads are arranged on a fixed support (PSV-A-T34), seen in Figure 3.4, where the top, left and right scanning heads are positioned at 0, 270 and 90 degrees, respectively. The high resolution digital camera, which provides a high resolution video feed of the object under investigation, is mounted at the centre of this support. The fixed support allows the 3D SLDV system to be moved without having to redo the alignment of the three laser heads.

To perform a measurement at a specific point on a specimen, each laser needs to be able to be positioned exactly at that point and the location of that point in space needs to be known. In order to align the lasers to a three-dimensional coordinate system, an alignment specimen (PSV-A-450) is used, seen in Figure 3.5. The alignment specimen consists of a square flat plate with 16 crosshairs etched into its surface and a protrusion at the centre of the plate with an additional four crosshairs at the tip. Each crosshair represents a known coordinate in space with respect to the centre of the square flat plate surface. Each laser is positioned to the centre of a crosshair on the flat surface of the alignment specimen. Once the lasers have been centred at the crosshair location, the workstation records the laser head mirror angles, as well the position of the crosshair on the workstation video feed. This is repeated for three more crosshairs on the flat surface and one crosshair on the protruding surface of the alignment specimen. Using the known crosshair coordinates and the respective laser head mirror angles, a non-linear optimisation calculates the position and orientation of the scanning heads in space, as well as the accuracy of the alignment.

Figure 3.4. 3D vibrometer (PSV-400-3D) mounted on a fix support (PSV-A-T34).

Figure 3.5. Three-Dimensional Alignment Specimen (PSV-A-450).

The fixed support is then positioned in front of the specimen, where a two-dimensional alignment of each laser to the specimen surface is performed using the workstation video feed. Measurement scan points can then be placed on the specimen over the workstation video feed. When performing scan measurements, all three laser beams are accurately positioned on the measurement point of interest using triangulation software (PSV-S-TRIA) and measure the vibration data in the direction of the beam. From the three-dimensional alignment, the vector of each beam is known and the vibration data can be converted into the orthogonal coordinate system related to the specimen under investigation, as seen in Figure 3.6.

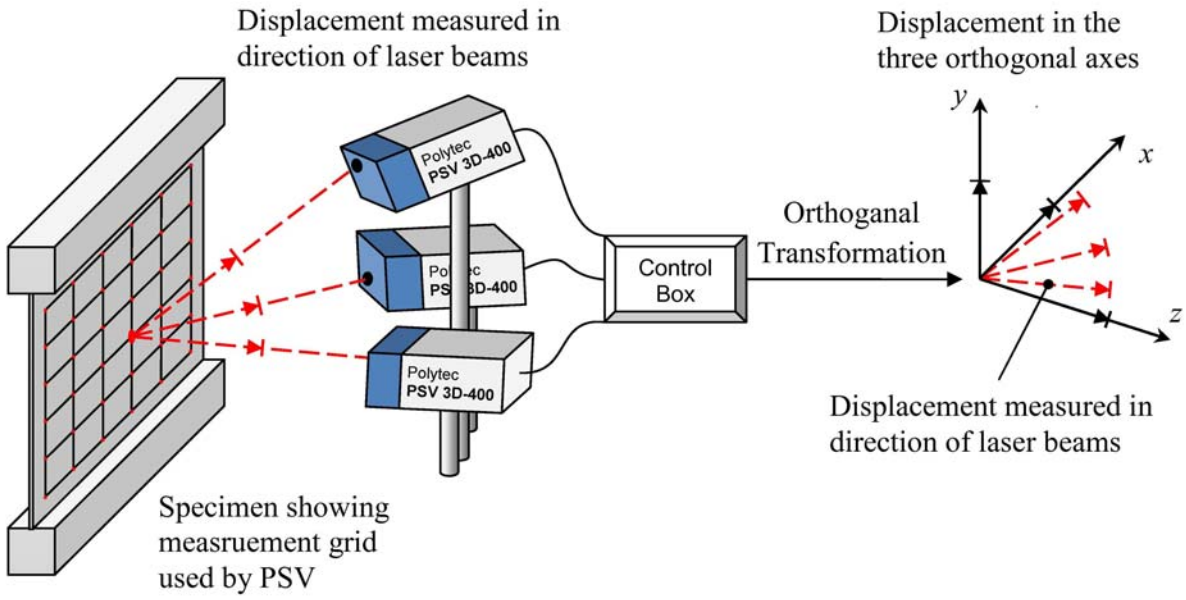

Figure 3.6. Illustration of the principle of three-dimensional displacement measurement using a 3D vibrometer.

3.1.5 Measurement Parameters

Using either the 1D or 3D SLDV system, measurements of oscillatory displacement were undertaken in the frequency domain, as the phase information between measurement points is essential to determine kinematic variables (such as strain). A transfer function between a reference input (input vibration voltage) and the oscillatory displacement measured by a laser head provide the necessary phase information.

For all tests conducted, the vibration signals were sampled at a frequency of 512Hz. A Fourier analysis was conducted with frequency resolution of 500mHz. In addition, every test specimen was oscillated at a 1Hz frequency. As this frequency is a multiple of the frequency resolution, a rectangular window was utilised. To screen out non-correlated motion such as airborne noise, ground-borne noise and most importantly motion associated with surface roughness, 64 averages were taken with an overlap of 75%.

3.2 Test Set Up

In this study, two sets of experiments were conducted that utilise the 1D or 3D SLDV systems.

The out-of-plane displacement experiments were conducted to investigate the use of a 1D vibrometer for evaluating bending strain and several damage detection algorithms in beam structures. A rig was designed to allow a beam specimen to be suspended from a clamped end and vibrated at a free end via an electromagnetic shaker. Aluminium beam specimens were used for the bending strain experiments, while composite beam specimens with fabricated through-the-width delamination, varying in size and depth, were utilised to investigate different damage detection algorithms.

The purpose of the in-plane displacement experiments was to determine the accuracy of measuring surface strains and a number of damage detection algorithms when utilising a 3D vibrometer. The rig was designed to impart uni-axial loading of a plate specimen while keeping the out-of-plane displacement minimal. Plate specimens were made of 2mm PMMA and fabricated with stress concentrators (e.g. notch, crack) in-order to investigate and validated the strain measurement techniques, as well as testing the effectiveness of damage detection algorithms.

The following sections will discuss in detail the experimental setups for each type of experiment.

3.2.1 Out-of-Plane Displacement Experiments

From the literature, several different types of out-of-plane displacement rigs have been previously utilised in the measurement of bending strain and the detection of damage in beam structures using a 1D vibrometer (Ferguson, N & Carpentier 1989; Ghoshal et al. 2003; Pai & Huang 2006; Qiao et al. 2007a). A cantilever arrangement was most commonly employed, however, the bending strain measurement studies utilised an electromagnetic shaker to provide the out-of-plane displacement (Ferguson, N & Carpentier 1989; Moccio & Miles 1996; Xu & Miles 1996a), whereas the damage detection studies utilised a piezoelectric element (Pai & Young 2001; Ghoshal et al. 2003; Pai, Young & Lee, S 2003; Pai et al. 2004; Pai & Huang 2006; Qiao et al. 2007a).

Within the bending strain measurement studies two styles of experiments were conducted, free end and base excitation. Ferguson and Carpentier (1989) developed a rig that had a vertically mounted cantilever beam, excited by an electromagnetic shaker at the free end.

Ferguson and Carpentier developed this rig in order to evaluate bending strains excited at low discrete frequencies (between 30Hz and 700Hz) and at the natural frequencies due to a 0-200Hz broad band signal. Conversely, Xu and Miles (1996a) utilised a horizontally mounted cantilever beam that was excited at its base by an electromagnetic shaker. The aim of Xu and Miles' experiment was to determine the bending strain power spectra from a band-limited random white noise signal over a frequency range of 5-1000Hz.

Damage detection techniques that utilise 1D vibrometer displacement measurements to detect damage on beam structure all have a similar experimental arrangement (Pai & Jin 2000; Pai & Young 2001; Ghoshal et al. 2003; Pai, Young & Lee, S 2003; Pai et al. 2004; Pai & Huang 2006; Qiao et al. 2007a):- a cantilever is mounted vertically, with the lower end clamped, and a piezoelectric element is glued to the beam just above the clamped end. These experiments were designed to detect damage in a beam structure using high frequency harmonic vibration, using either a deflection shape or curvature algorithms.

The research presented in this thesis involved designing a rig, which closely matched that used by Ferguson and Carpentier (1989) in their investigation into the evaluating low frequency bending strains. This is because this current study is a quasi-static investigation of strain measurement and damage detection, and the use of electromagnetic shakers would therefore provide controllable displacements at low frequencies, where as piezoelectric elements utilised in other damage detection techniques would not be able to provide adequate out-of-plane displacements at quasi-static frequencies. Hence, an out-of-plane displacement experiment rig was designed to be able to provide controlled displacements to a beam specimen, using an electromagnetic shaker. It should be noted that the focus on quasi-static measurements is not due to limitations in the vibrometer (which can work in

the ultrasonic range), but rather the assumptions used to derive the damage detection algorithms.

As seen in Figure 3.7, the rig frame is made of steel rectangular hollow section. At the top of the rig an aluminium clamp was designed to vertically hang a specimen of approximately 3mm thickness. Attached to the other end of the specimen is an additional aluminium clamp where an electromagnetic shaker can impart a vibrational input. The electromagnetic shaker is mounted on a steel rectangular hollow section behind the specimen in order to vibrate the beam.

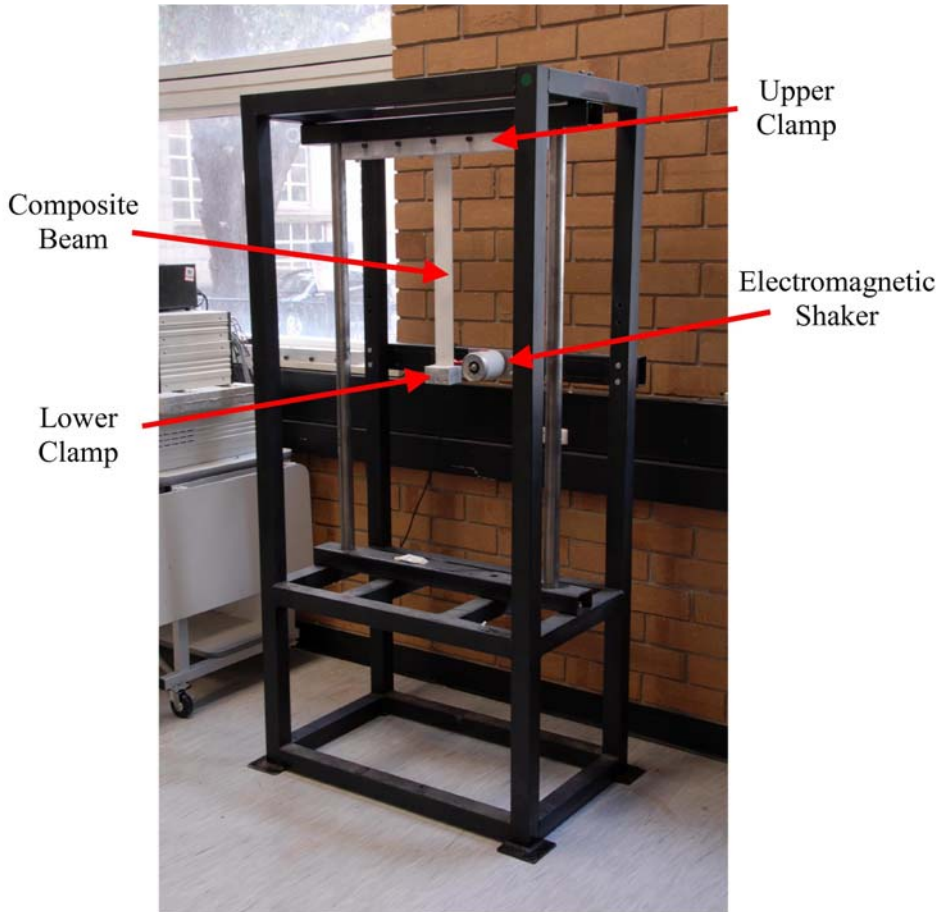

Figure 3.7. Out-of-plane displacement rig.

Table 3.1. Specimen specification, parameters related to Figure 3.8.

Specimen #	Delamination Length, (mm)	Delamination Depth (between layer)
1	NA	NA
2	25	4/5
3	50	4/5
4	75	4/5
5	100	4/5
6	50	½
7	50	2/3
8	50	¾
9	50	5/6
10	50	6/7
11	50	7/8

The bending strain measurements were performed on a nominal 3mm Aluminium specimen with in-plane dimensions of 540 x 50mm. For the damage detection tests, a composite laminate material was utilised with fabricated through-the-width delamination of varying lengths and depths, which can be seen in Table 3.1. These composite specimens were created to investigate the effectiveness of the proposed damage detection algorithm in detecting delamination of various lengths and depths. The composite specimens were made of E-glass bidirectional, 8 harness satin, 300 gsm fabric and vinyl ester resin matrix. The specimens were manufactured using a wet lay-up technique and left to cure at room temperature. The composite beam specimens were prepared with in-plane dimensions 540mm x 30mm and were laid-up with 8 layers of fabric producing a 2.85mm thickness. To create a delaminated section, two pieces of 20 micron Teflon film were placed between specific layers. The specimens were created with a centrally located delaminated zone

across the width of the beam. A schematic drawing of the delaminated specimen can be seen in Figure 3.8.

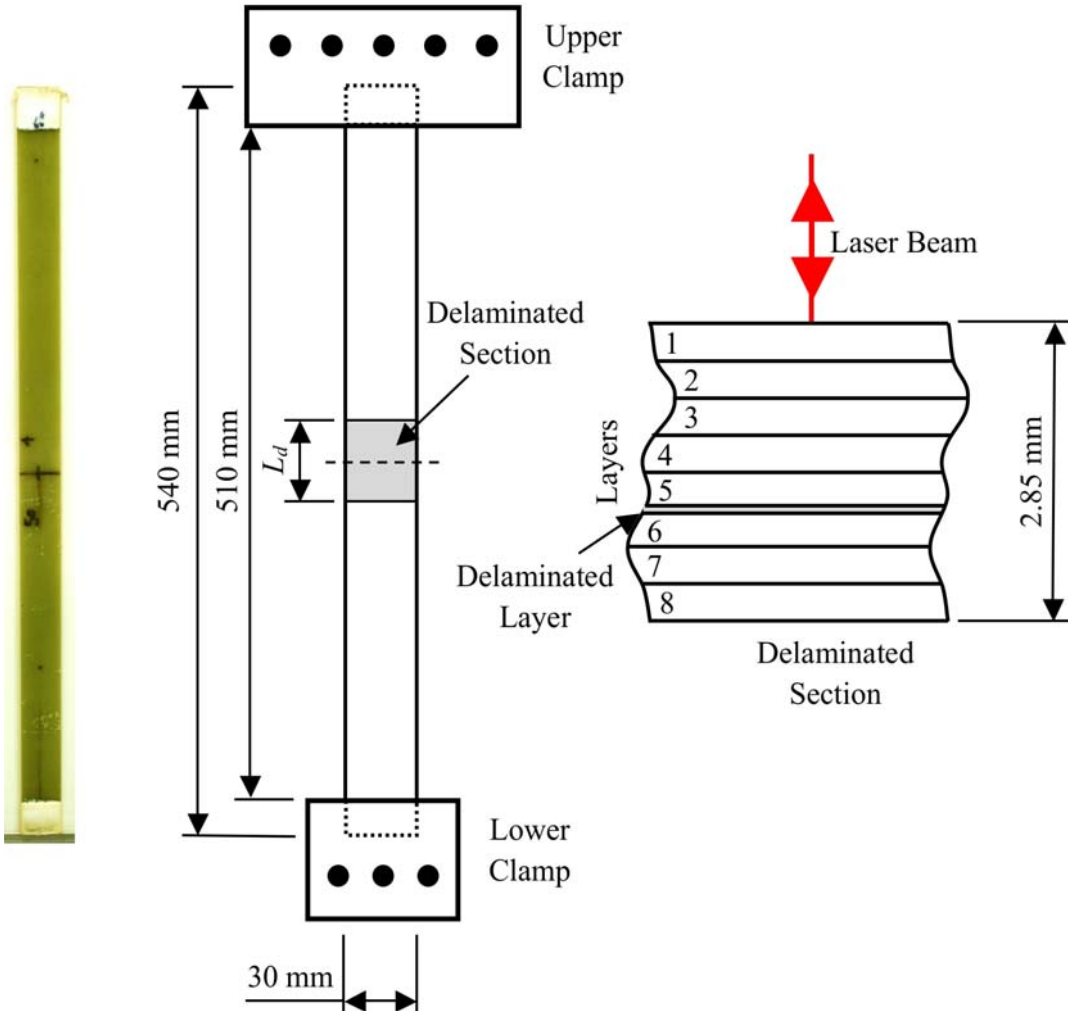

Figure 3.8. Schematic diagram of delaminated composite specimens.

Once a specimen is secured in the test rig and the shaker is attached, the 1D vibrometer is mounted on a tripod and placed at a stand-off-distance of approximately 1.109m, such that the laser beam is in a signal maxima and the whole specimen can be scanned with scanning mirrors at angles that do not exceed 10 degrees. The experimental setup can be seen in

Figure 3.10. Using the workstation computer, the laser is aligned to the specimen (as described in Section 4.3) and a single line of 501 scan point are placed along the centreline of the beam. The in-built voltage generator of the SLDV system is used to generate a 1Hz sinusoidal vibrational input of approximately 0.1mm amplitude into the free end of the beam. A 1Hz sinusoidal vibrational input was utilised for these experiment, as a quasi-static investigation of the strain measurement and damage detection techniques was desired. Therefore, the vibrational frequency selected needed to be below the first natural frequency of the beam specimens, which was 12Hz for the aluminium beam and approximately 14Hz for the composite beams. The voltage signal is fed into a voltage amplifier, which then drives the electromagnetic shaker and thus the beam. The generated vibration signal is then used to determine the phase information from the measured out-of-plane displacements. Using the parameter specified in Section 4.5, a scan typically takes 4.5 hours. The reason for the length of the scan is due to the frequency resolution selected (0.5mHz), the number of average (64), the signal overlap chosen (75%) and the number of measurement point used (501).

3.2.2 In-Plane Displacement Experiments

To investigate the use of in-plane displacements measured by a 3D vibrometer for the determination of surface strain and the detection of damage in plate structures, a new experimental rig needed to be developed. This was due to the fact that surface strain measurement and damage detection using in-plane displacements measured from a 3D vibrometer were new areas of research that had not yet been explored.

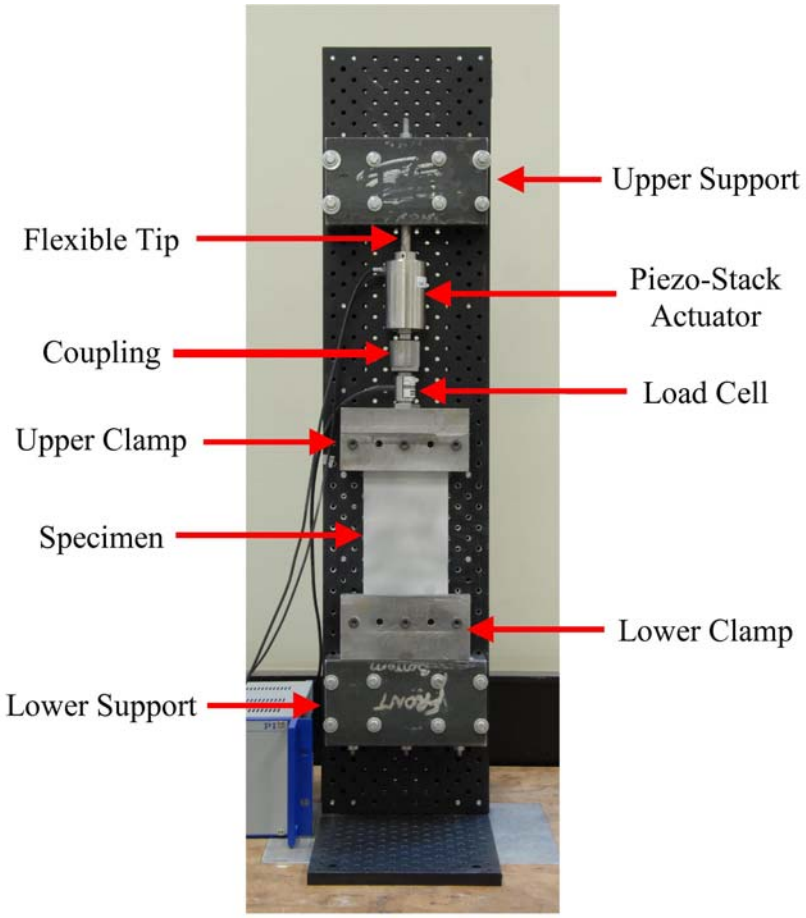

Figure 3.9. In-plane displacement rig.

The test rig was designed for cyclic uni-axial loading of a plate specimen, and is shown in Figure 3.9. The specimens were positioned between two clamps. The lower clamp was fixed to the lower support block, while the upper clamp was connected in series to a 15kN load-cell (Novatech F204), a piezo-stack actuator (Physik Instrumente P-235.40 PICA) and fixed to the upper support block. Between the load-cell and upper support a flexible tip (Physik Instrumente P-176.60) was used in an attempt to isolate the piezo-stack from bending and torsional loads. The lower and upper support blocks were attached to an optical breadboard (Thorlabs MB2090/M), which allowed the distance between the clamps

to be varied. The piezo-stack actuator can achieve a push force of 30kN and a pull force of 3.5kN over a stroke of 60μm.

Specimens for the in-plane experiments were laser cut from 2 mm thick transparent acyclic (PMMA). The specimens were 215mm long by 100mm wide, with a slot at either end to allow for the clamp tightening bolts. A number of specimens were created for the in-plane experiments, as shown in Figure 3.11. These included an undamaged plate, a plate with a notch, varying crack lengths propagating from a notch, varying length edge cracks and varying length centre cracks. The cracks were not grown, but laser cut into the specimens, which provided a 0.3mm slot with a rounded crack tip. The notch utilised was of ninety degrees and 20mm long, and cracks investigated were of 5, 10, 15, 20 and 25mm in length. A detailed list of test specimens is shown in Table 3.2. For the in-plane surface strain measurement experiments, the undamaged plate specimen was used to evaluate the accuracy of the measured strain fields, while the notch without a crack and the 20mm edge crack were utilised to investigate the accuracy of the measured strain fields in the vicinity of a stress concentrator.

Table 3.2. Specimen specifications, parameters related to Figure 3.11.

Specimen Type	Crack Length, a (mm)
Plain	NA
Edge Crack	0, 5, 10, 15, 20, 25
Centre Crack	0, 5, 10, 15, 20, 25
Notch with Crack	0, 5, 10, 15, 20, 25

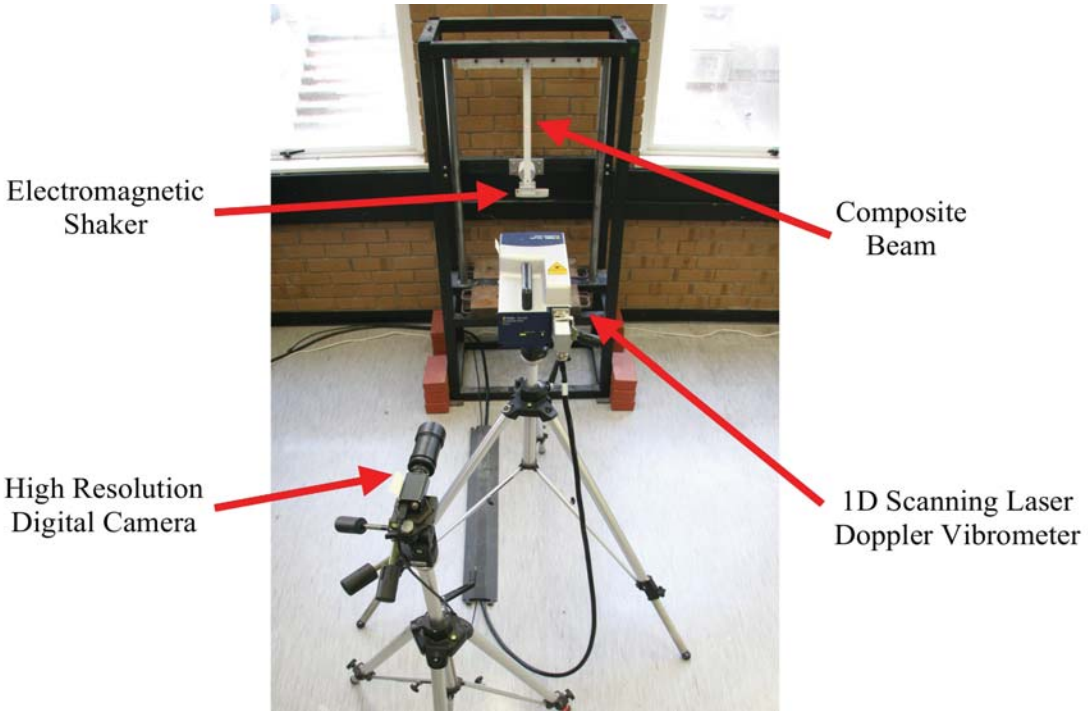

Figure 3.10. Experimental setup of out-of-plane measurement experiments.

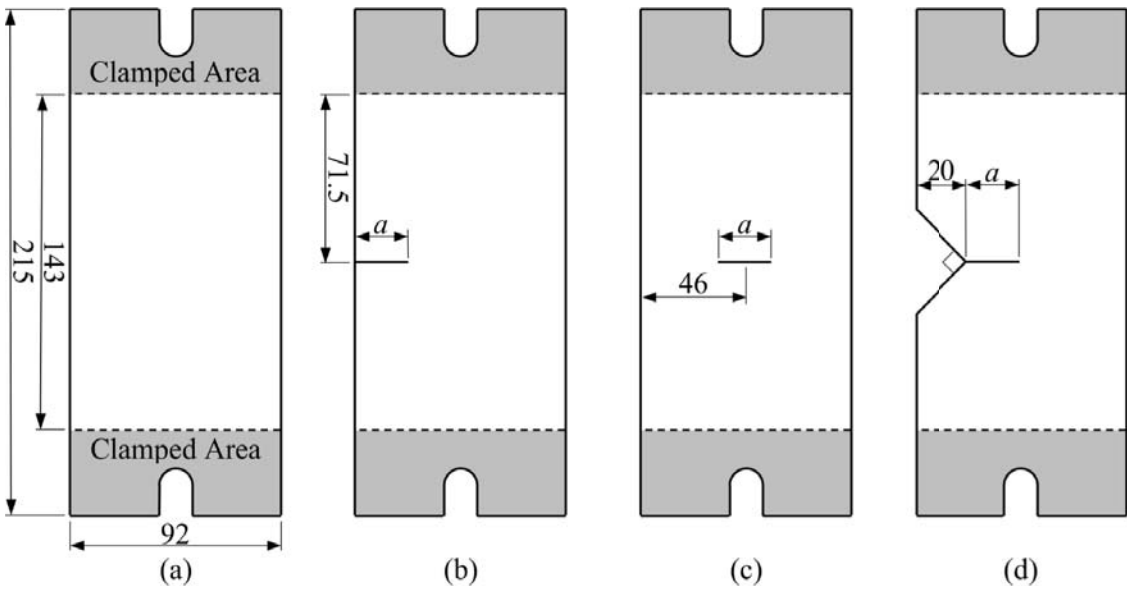

Figure 3.11. Detailed schematics of the in-plane loading specimens. (a) plain, (b) edge crack, (c) centre crack, and (d) notch.

After the specimen was aligned within the clamps of the test rig, the 3D SLDV system mounted on its fixed support was then positioned in front of the test rig (as shown in Figure 3.12) at a stand-off distance of approximately 931mm. Using the workstation computer, a two-dimensional alignment of the lasers to the specimen was then performed. This two-dimensional alignment allowed all three lasers to be positioned at any point on the specimen using the workstation computer. Using this two-dimensional alignment, a square grid of scan points was then placed on the specimen. Examples of the square scan grids used in this study are show in Figure 3.13. The piezo-stack actuator was position controlled using a dSPACE system and provided a 1Hz cyclic displacement to the specimen. The control signal was feed into the 3D SLDV system in order to determine the phase information of measured displacement signal. Before starting a test, the cyclic load applied to the specimen is recorded using the load cell. Using the measurement parameters specified in Section 4.5, a single in-plane displacement experiment typically takes 15 hours to measure the displacement at 1521 points (i.e. 39x39 points). The reason for the length of the scan duration is due to the frequency resolution selected (0.5mHz), the number of average (64), the signal overlap chosen (75%) and the number of measurement point used (1521).

Figure 3.12. Experimental setup of in-plane measurement experiments.

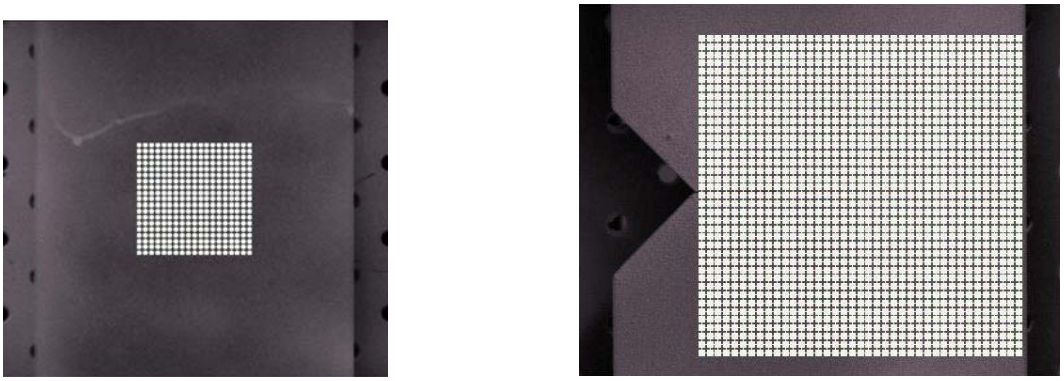

(a) (b)

Figure 3.13. Photograph of the scan grid utilised for (a) determining the accuracy of the in-plane strain measurement technique, and (b) evaluating the strain field near a stress concentrator. The scan grid in (b) is also utilised to investigating the in-plane damage detection techniques.

3.3 Summary

This chapter presents the experimental setup utilised to investigate the strain measurement and damage detection techniques. Firstly, the optical configuration and operational principle of SLDV was discussed, followed by a detailed description of the 1D and 3D SLDV systems and how each system is aligned to and displacement measured from a test specimen.

The description of two experimental test rigs was presented. One experimental test rig was designed to provide out-of-plane deflection to a beam structure and a second test rig was developed to produce in-plane displacement in a plate specimen. Using these experimental test rigs, four experimental investigations were conducted:- the evaluation of strain and the detection of damage using both the 1D and 3D SLDV systems.

Two forms of strain measurement were investigated, bending strain evaluated from measured out-of-plane beam deflections using 1D SLDV and surface strain evaluated from measured extensional displacements using 3D SLDV. The bending strain measurements were conducted on an aluminium beam specimen of uniform thickness. An aluminium beam specimen was utilised as the aluminium is isotropic and would provide a uniform bending strain across its length. In addition, the surface strain measurements were evaluated using acrylic plate specimens. Acrylic was utilised as it provides a larger strain across the length of the specimen than metal, for a given applied force. The aim of these strain measurement experiments was to determine their accuracy, and, in addition, to evaluate the effectiveness of the surface strain measurement technique in measuring surface strains in the vicinity of stress concentrators.

With regards to the damage detection techniques, there are two categories that were examined:- the detection of through-the-width delamination in a composite laminate beam using out-of-plane deflection measured by a 1D vibrometer and the detection of crack damage in a plate using extensional deformations measured by a 3D vibrometer. The delamination detection experiments utilised e-glass fibre composite specimens with prefabricated through-the-width delamination of various lengths and depths. In addition, the crack detection experiments utilised acrylic specimens with prefabricated crack damage, created by laser cutting. The aim of these damage detection experiments was to investigate the effectiveness of the newly proposed damage detection algorithms in detecting the prefabricated damage and to determine the minimum detectable size of the various damage scenarios.

Chapter 4. Development of New Strain Measurement Techniques

This chapter presents the development of two experimental techniques for quasi-static strain measurement that utilise scanning laser Doppler vibrometry (SLDV). The first technique uses a 3D vibrometer to measure extensional strain produced by in-plane loading and the second technique uses a 1D laser to obtain the bending strain induced by out-of-plane loading. Bending strain measurement using 1D SLDV was first investigated by Ferguson and Carpentier (1989) using a finite-difference differentiation approach. The measurement of extensional strain using 3D SLDV, however, is a new technique that has only been possible in the last few years with the development of high quality 3D systems. Both techniques presented in this chapter employ a Savitzky-Golay differentiating filter to evaluate the strains from measured surface displacements, and the formulation and approach of evaluating the accuracy of each strain measurement technique is discussed in detail. The optimal parameters for accurately measuring quasi-static bending and surface strains were established, including the polynomial order and filter length used within the Savitzky-Golay filter and the spatial interval between measurement points. In addition, the effect of the stress amplitude applied to the specimen was also examined. For validation of the developed extensional strain technique, the strain field near several stress concentrators was measured and compared with finite element simulations. This was used to evaluate the accuracy of the technique.

4.1 Sources of Errors in Vibrometry Measurement

There are two main factors that contribute to measurement errors when using SLDV systems. The first is due to perturbations in the movement of the object from external sources (e.g. ground-borne vibrations) and second is the finite accuracy of the laser beam position on the object being measured. In the work presented in this chapter, in order to reduce uncorrelated measurement noise due to perturbations in the vibratory movement of the object, the velocity was measured in the time domain and then filtered via a Fourier transformation and averaged 64 times. This was done within the PSV-Software for the SLDV system used in this study.

Systemic errors in velocity measurements can occur due to the finite accuracy of the laser beam position on the measurement object. These errors are a result of the quality of the alignment of the laser beams to the specimen. The 1D and 3D SLDV systems are aligned to a specimen differently and thus have alternate reasons for systemic errors in the finite accuracy of the laser beam position. For the 1D SLDV system (discussed in Section 3.1.3), the laser is first positioned in front and parallel to the specimen and a two-dimensional alignment is performed that aligns the laser beam to specimen using the video image on the computer. Systematic errors occur due to the finite accuracy of the system in recording the exact location of the laser beam to the video image, causing a misalignment. With regards to the 3D SLDV system (discussed in Section 0), a three-dimensional alignment is performed where the three laser beams are aligned to a point on the three-dimensional alignment specimen (Figure 3.5). After the alignment is performed, the software indicates the alignment uncertainty (positional accuracy) of each laser beam to a selected scan point

in space, which is typically in the order of 0.2-0.5mm. Therefore, each laser beam will be slightly misaligned when positioned at each scan point by an amount less than the magnitude of the alignment uncertainty. An illustration of the alignment uncertainty of the laser beams to selected scan point is shown in Figure 4.1. To ensure that the laser beams are position exactly in the same spot during a measurement scan, a software routine called 'video triangulation' is utilised that moves each laser beam to the closest pixel in the video image that defines the scan point. After video triangulation of the laser beams is performed, the position of the scan point will differ slightly from the original position specified by the video by an amount less than the magnitude of the alignment uncertainty.

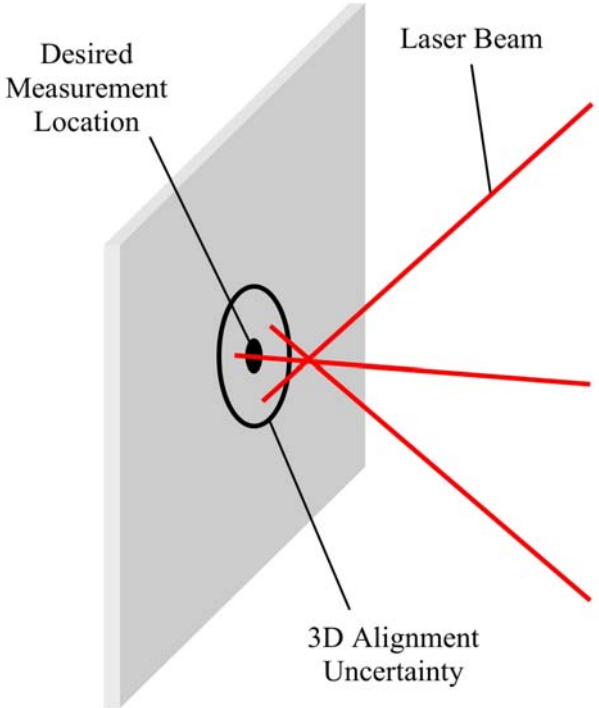

Figure 4.1. Positioning imprecision in the 3D vibrometer due to finite accuracy of the three-dimensional alignment.

The effect of this alignment uncertainty is shown in Figure 4.2 for measurement grid intervals of approximately 0.2mm and 2mm, while keeping the zoom of the digital camera constant. The fine mesh (Figure 4.2a) exhibits a non-uniform displacement field on non-uniform measurement grid, while the coarse mesh (Figure 4.2b) shows a smoother displacement field on a more uniform mesh. This demonstrates that as the mesh size approaches the size of the alignment uncertainty, the mesh becomes distorted.

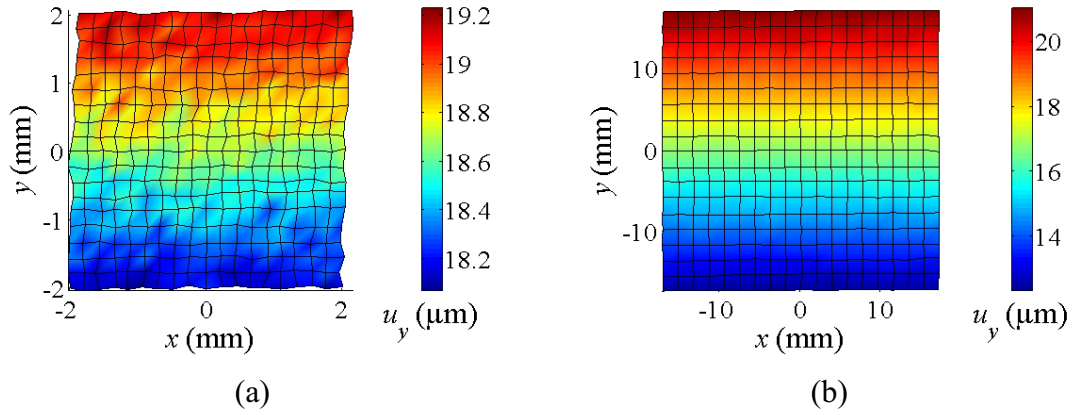

Figure 4.2. Displacement field u_y for a plate highlighting the positioning imprecision for different nodal spatial intervals of (a) 0.22mm and (b) 1.9mm while keeping the zoom of the digital camera constant.

4.2 In-Plane Strain

In many engineering applications the surface strains resulting from extensional displacement are required to be evaluated. This section presents a new technique for evaluating surface strains using 3D SLDV. The 3D vibrometer is capable of measuring three-dimensional displacements on the surface of an object, allowing for the evaluation of

surface strains. Only a few studies in the use of 3D SLDV for the measurement surface strains resulting from extensional displacements have been published in the last few years. In this current study, an in-depth investigation was conducted into how the accuracy of the technique is affected by numerical differentiation method parameters, spatial interval between measurement points and amplitude of loading.

4.2.1 Previous Studies

Cazzolato et al. (2008) demonstrated that surface strain distribution from the displacement field measured using a 3D vibrometer was possible by utilising strain finite element shape functions. Two types of strain finite element shape functions were employed:- 3-node triangular linear elements and 4-node rectangular bi-linear elements.

To validate the strain measurement procedure, Cazzolato et al. performed cyclic tests on an aluminium (Young's modulus, $E = 77$GPa) dogbone specimen (cross-section of 38mm by 12mm and a reduced lengthwise section of 125 mm). They carried out the cyclic tests on the specimen using an Instron 1342 hydraulic test machine operating under load control. The lasers were positioned on separate tripods and placed approximately 711mm from the specimen to ensure a visibility maximum for the lasers (as seen in Figure 4.3).

Using this laser setup, the displacement of the specimen were measured (as seen in Figure 4.4), which showed that there was rigid body motion along all three axes, despite the specimen being mounted in the Instron which was supposed to induce motion only along the y-axis.

The dynamic strain fields in the x-y plane (presented in Figure 4.5) were then calculated by applying the 3-node triangular and 4-node rectangular strain interpolation functions to

the measured displacements, shown in Figure 4.4. The mean and standard deviation of the elemental strains for the specimen (in Figure 4.5) were found to be,

$$[\varepsilon_{xx} \quad \varepsilon_{yy} \quad \gamma_{xy}] = [-184 \pm 23\mu\varepsilon \quad 552 \pm 36\mu\varepsilon \quad 6 \pm 50\mu\varepsilon]$$

$$[\varepsilon_{xx} \quad \varepsilon_{yy} \quad \gamma_{xy}] = [-154 \pm 23\mu\varepsilon \quad 552 \pm 36\mu\varepsilon \quad 4 \pm 69\mu\varepsilon]$$

for the triangular and rectangular grids respectively. Additionally, they found that the ratio of the x-strain to y-strain gives Poisson's ratios of 0.33 and 0.28 respectively.

Figure 4.3. Photograph of the 3D vibrometer focused at an aluminium dogbone specimen clamped in an Instron 1342 hydraulic test machine (Cazzolato et al. 2008).

To provide a comparison to the laser measurements, contact strain measurements were made using a mechanical extensometer. The normalised results from the extensometer and laser are shown in Table 4.1. From a regression on this data, a Young's modulus of 77.3 GPa and a Poisson's ratio of 0.36 were obtained. From the dynamic x- and y-strains derived by these two independent methods they were able to show that the two methods

show similar mean values (see Table 4.1). However, the use of the 3-node triangular and 4-node rectangular interpolation functions exhibits significant standard deviations in evaluated x- and y-strains. Both the 3-node triangular and 4-node rectangular strain interpolation function produced a standard deviation 6.5% (36 microstrain) in ε_{yy} from the measured mean values ($\bar{\varepsilon}_{yy} = 552$ microstrain). However, there was a significant increase in the standard deviation of the ε_{xx} for both the 3- and 4-node strain interpolation functions; 12.5% (23 microstrain) and 26% (40 microstrain) from the measured mean values ($\bar{\varepsilon}_{xx} = -184$ microstrain and $\bar{\varepsilon}_{xx} = 154$ microstrain), respectively.

Table 4.1 Comparison of Normalised strains per unit (kN) load and estimated Poisson's Ratio of the test specimen measured using an extensometer and 3D SLDV system (Cazzolato et al. 2008).

	$\mu\varepsilon_x$	$\mu\varepsilon_y$	ν
Extensometer	-10.4	28.3	0.36
Triangular Mesh	-9.4	28.3	0.33
Rectangular Mesh	-7.9	28.3	0.28

4.2.2 Kinematics of Deformation

To use 3D SLDV for the measurement of strain on the surface of a plate, subjected to in-plane loading, an understanding of the kinematics of plate deformation is required. This subsection discusses the two types of deformation (Lagrangian and Eulerian displacement descriptions) and how the Eulerian displacement description applies to measurement of strain using 3D SLDV.

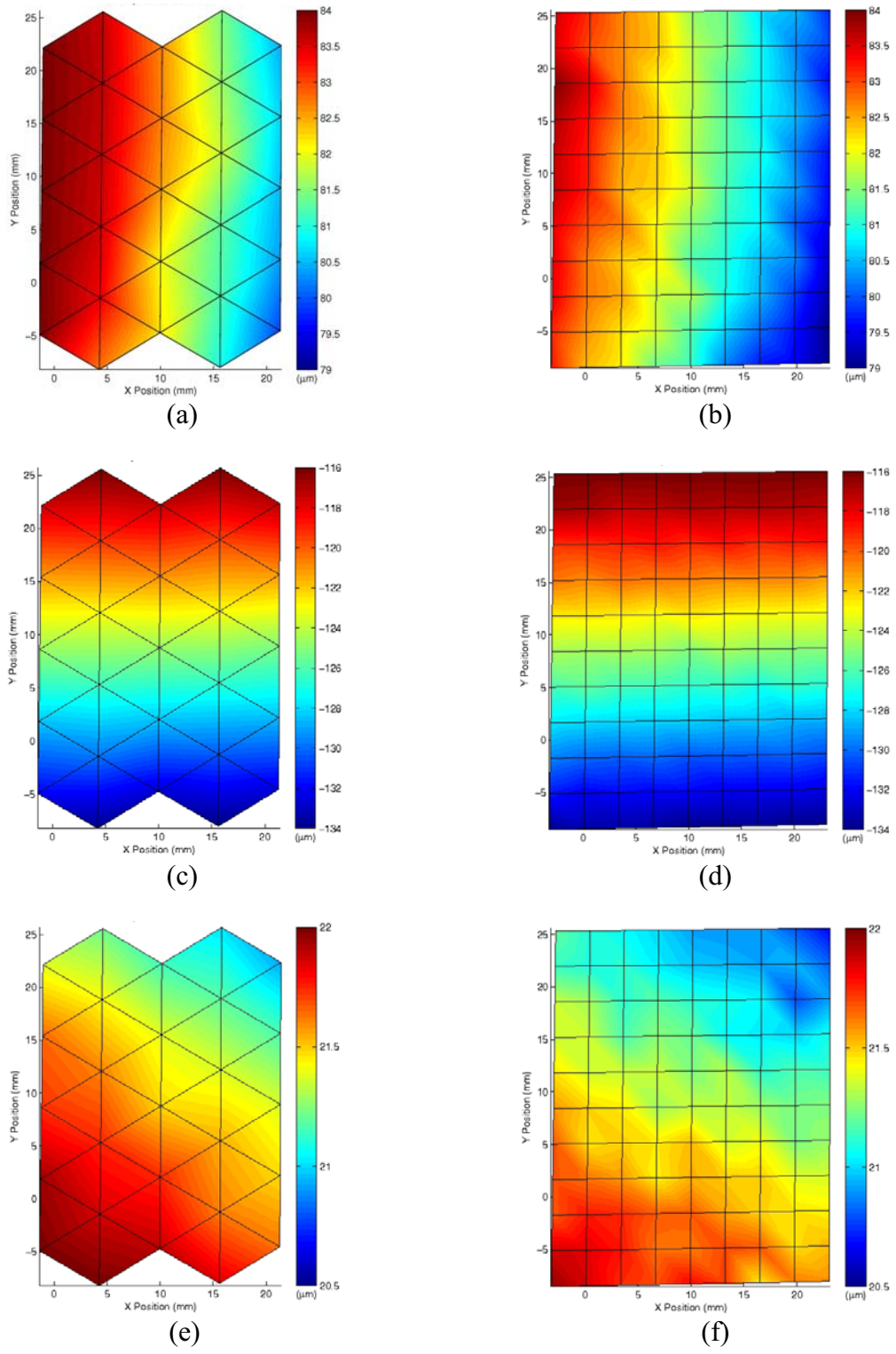

Figure 4.4. Displacements measured in the x- (top row), y- (middle row) and z-directions (bottom row) on the specimen using triangular (left column) and rectangular elements (right column), excited with a 5Hz frequency (Cazzolato et al. 2008).

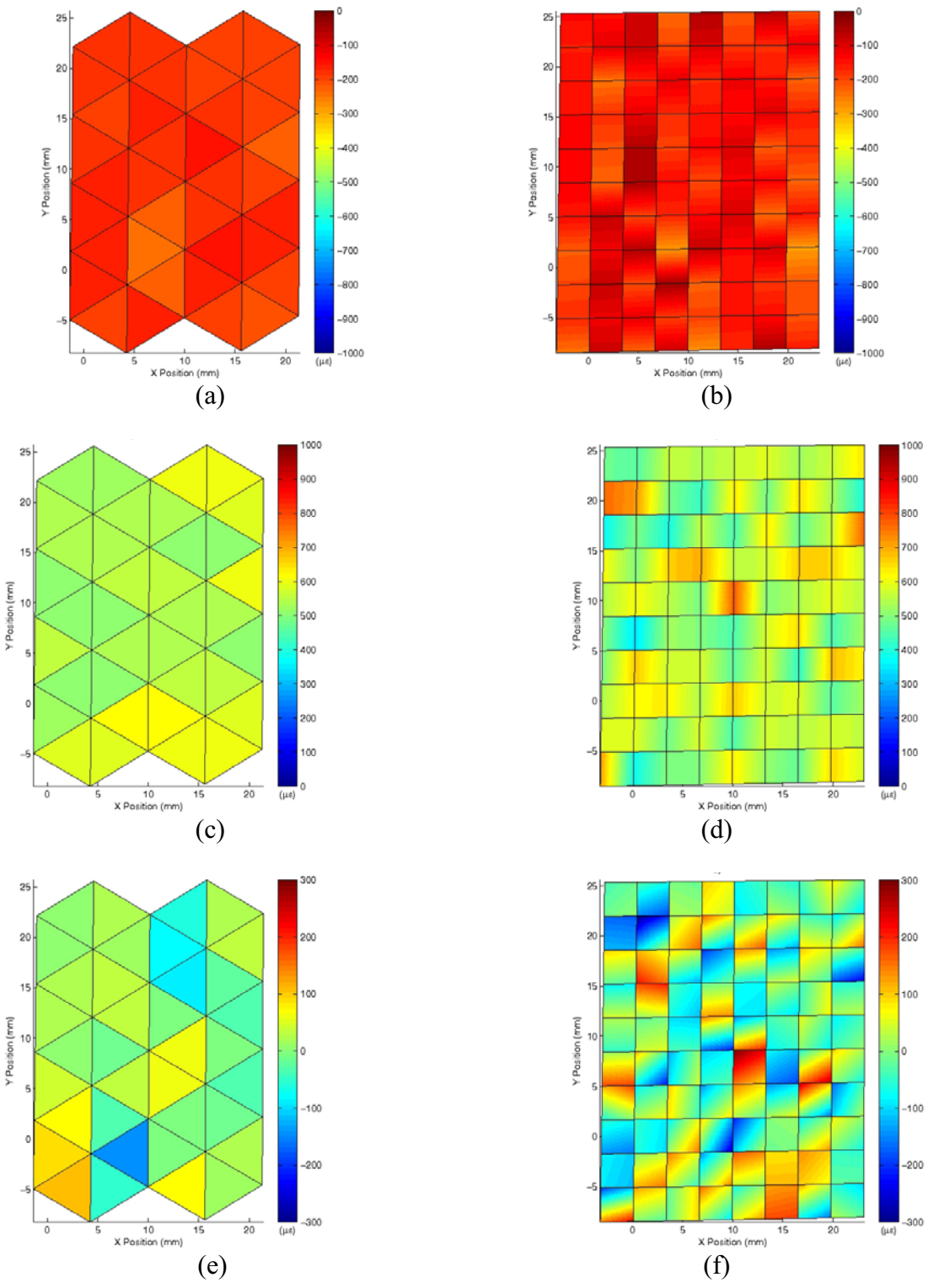

Figure 4.5. Strains measured in the x- (top row), y- (middle row) and z-directions (bottom row) on the specimen using 3-node triangular linear (left column) and 4-node rectangular bi-linear elements (right column), excited with a 5Hz frequency (Cazzolato et al. 2008).

The displacement components of an object are able to be defined using either a Lagrangian or Eulerian description. Consider a one-dimensional body and denote X as the element or particle of the body and x as the spatial position or coordinate, as seen in Figure 4.6. Displacement defined by a Lagrangian description (u_L) measures the spatial position $x(X,t)$ of a particle X at the time t and can be mathematically given as

$$u_L(X,t) = x(X,t) - x(X,t_0) \tag{4.1}$$

whereas displacement defined by an Eulerian description (u_E) measures the particle $X(x,t)$ at a spatial position x at time t and can be given as

$$u_E(x,t) = X(x,t_0) - X(x,t) \tag{4.2}$$

where t_0 is the initial time step.

Consider the Eulerian description of displacement, where the particle $X(x,t)$ is measured at the spatial position x_5. At two separate time steps t_0 and t_1, as shown in Figure 4.6, the measured particles are

$$X(x_5,t_0) = X_5 \tag{4.3}$$

$$X(x_5,t_1) = X_3 \tag{4.4}$$

Therefore, the Eulerian displacement becomes

$$u_E(x_5,t_1) = X(x_5,t_0) - X(x_5,t_1) = X_5 - X_3 \tag{4.5}$$

providing a displacement of two particle intervals.

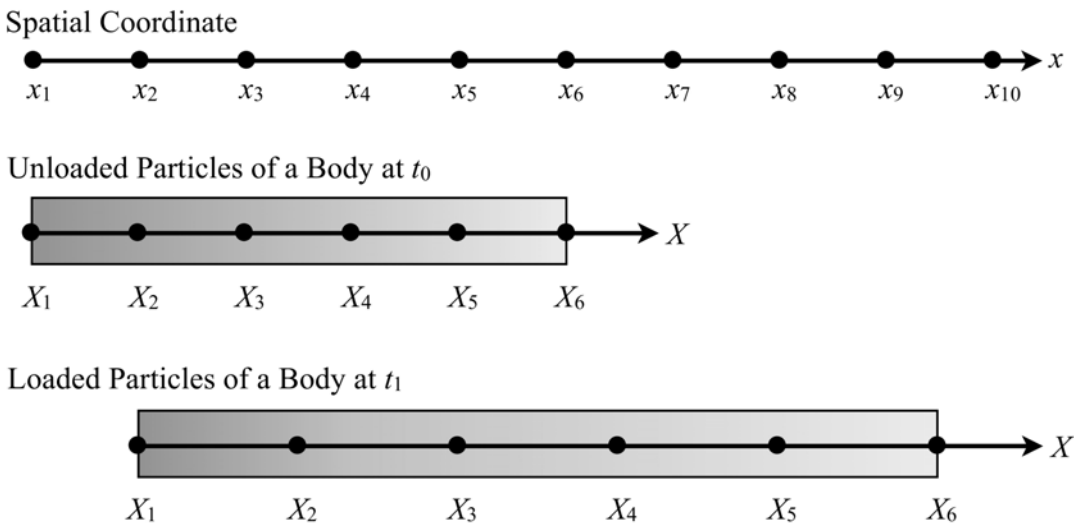

Figure 4.6. The coordinate definition of the spatial position (x) and particle location (X) of a body.

Now consider the Lagrangian description of displacement, where the spatial position $x(X,t)$ is measured at the particle location X_5. At the separate time steps t_0 and t_1 the measured spatial positions are

$$x(X_5, t_0) = x_5 \tag{4.6}$$

$$x(X_5, t_1) = x_8 \tag{4.7}$$

giving an Lagrangian displacement of

$$u_L(X_5, t_1) = x(X_5, t_1) - x(X_5, t_0) = x_8 - x_5 \tag{4.8}$$

which provides a displacement of three spatial intervals.

When measuring at the same initial point the two displacement descriptions provide different results. From the two displacement descriptions, the Eulerian (E_{ij}) and

Lagrangian (L_{ij}) finite strain tensor can be derived and is expressed by, respectively,

$$E_{ij} = \frac{1}{2}\left(\frac{\partial u_i}{\partial X_j} + \frac{\partial u_j}{\partial X_i} - \frac{\partial u_k}{\partial X_i}\frac{\partial u_k}{\partial X_j}\right) \tag{4.9}$$

$$L_{ij} = \frac{1}{2}\left(\frac{\partial u_i}{\partial x_j} + \frac{\partial u_j}{\partial x_i} + \frac{\partial u_k}{\partial x_i}\frac{\partial u_k}{\partial x_j}\right) \tag{4.10}$$

However, when the displacement and displacement gradient of an object is sufficiently small (i.e. a displacement gradient less than 10%), the product terms $\left(\frac{\partial u_k}{\partial x_i}\frac{\partial u_k}{\partial x_j}\right.$ and $\left.\frac{\partial u_k}{\partial X_i}\frac{\partial u_k}{\partial X_j}\right)$ in the Eulerian and Lagrangian strain tensor become negligible and the two strain tensors become approximately equal. This is known as small deformation theory (Mase 1969). In this study the displacement and displacement gradients applied the plate specimens are sufficiently small and allows small strain theory to be applied. Using small strain theory, the strains components can be expressed as,

$$\varepsilon_{xx} = \frac{\partial u_x}{\partial x} \tag{4.11}$$

$$\varepsilon_{yy} = \frac{\partial u_y}{\partial y} \tag{4.12}$$

$$\varepsilon_{zz} = \frac{\partial u_z}{\partial z} \tag{4.13}$$

$$\gamma_{xy} = \frac{\partial u_y}{\partial x} + \frac{\partial u_x}{\partial y} \tag{4.14}$$

$$\gamma_{zx} = \frac{\partial u_x}{\partial z} + \frac{\partial u_z}{\partial x} \tag{4.15}$$

$$\gamma_{yz} = \frac{\partial u_z}{\partial y} + \frac{\partial u_y}{\partial z} \tag{4.16}$$

where ε_{xx}, ε_{yy} and ε_{zz} are normal strains in the x-, y- and z-axes and γ_{xy}, γ_{zx} and γ_{yz} are the engineering shear strains in the x-y, x-z and y-z planes, respectively.

This sub-section has shown that there are two ways of describing deformation:- as either Eulerian or Lagrangian. In relation to measurements taken using a vibrometer, the displacements are measured under an Eulerian description. The reason is that the laser beam of the vibrometer measures the displacement of an object at a spatial position, rather than a specific location on the object (Lagrangian description) like a strain gauge. When considering small displacements, the two descriptions are approximately equal and small strain theory can be applied. In this investigation of extensional strain on small displacements will be investigated. This theory provides a basis of the surface strain measurement technique utilising the 3D vibrometer.

4.2.3 Investigation of In-Plane Strain

To investigate the accuracy of the 3D vibrometer in measuring surface strains, a 2mm thick acrylic plate of in-plane dimensions 92mm x 143mm was utilised (as seen in Figure 3.11a) and oscillated sinusoidally at 1Hz in the y-direction to provide uniaxial quasi-static loading conditions. The measurements for the plate were conducted with a mesh (N_x x N_y) of 19 x 19 points in the x- and y-directions (seen in Figure 4.7). The vibrometer measured the vibration signals at a sampled frequency of 512Hz. To obtain the displacement data at the

1Hz loading frequency, Fourier analysis was conducted at frequency resolution of 500mHz, using a rectangular window and 64 averages with 75% overlap.

An example of the measured displacements in the x-, y- and z-axes due to the 1Hz uniaxial loading of 1.05MPa in the y-direction are shown in the left column of Figure 4.8. The displacements u_x and u_y (see Figures 4.8a and 4.8c, respectively) are reasonably uniform and parallel to the measurement grid. In addition, the region of zero displacement in the x-direction is centrally located in the measurement area. This indicates that the 3D SLDV system is aligned adequately in the x-y plane of the specimen. However, the out-of-plane displacement reveals that the specimen is subjected to some bending, likely due to misalignment within the mechanical test rig.

The coherence (γ_x^2, γ_y^2 and γ_z^2) of the measured displacements to the input voltage applied to the piezo-stack used to drive the specimen is shown in the right column of Figure 4.8. The displacement in the y-direction (u_y) has very high coherence to the input voltage, whereas the displacement in the x-direction (u_x) has significantly low coherence. The lowest coherence is observed where the displacement in the x-direction (u_x) is close to zero. The low coherence indicates that the displacement in the x-direction has reached the noise floor for the specific experimental arrangement and data acquisition parameters used. In order to get coherent displacement measurements for this setup, the displacement in each axis needs to be greater than approximately 2μm, which is 1.3% of full scale. For the given displacement field in Figure 4.8, the bending strain arising from the out-of-plane displacement (Equations (4.33) and (4.34) discussed in Section 4.4.2) can be estimated to be a maximum of $(\varepsilon_{xx})_{bending} = 1.2$μm⁄m and $\left(\varepsilon_{yy}\right)_{bending} = 5.3$μm⁄m, whereas the

strain caused by the extensional displacement (Equations (4.11) and (4.12)) yield $\varepsilon_{xx} = 95\mu m/m$ and $\varepsilon_{yy} = 255\mu m/m$. The components of bending strain caused by the out-of-plane displacement are much less than the extensional strains and are therefore considered negligible.

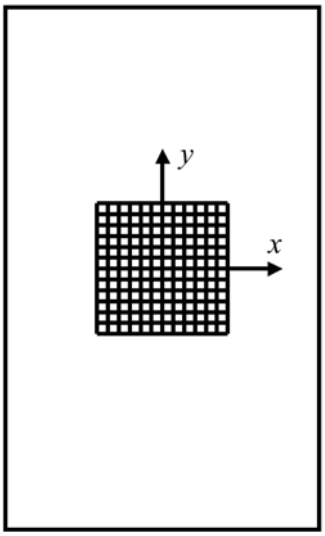

Figure 4.7. Illustration of the rectangular plate specimen and mesh used for strain measurement.

The measured strain field of a rectangular plate under tensile loading yields a uniform results. To compare the accuracy of the derived strain fields for different loading and mesh refinement a variation coefficient is utilised, which is defined as the ratio of the standard derivation (SD_i) of the strain to the mean value ($\bar{\varepsilon}_{ii}$) and is expressed as,

$$c_{v,i} = \frac{SD_i}{|\bar{\varepsilon}_{ii}|} \tag{4.17}$$

where i represents either the x- or y-direction

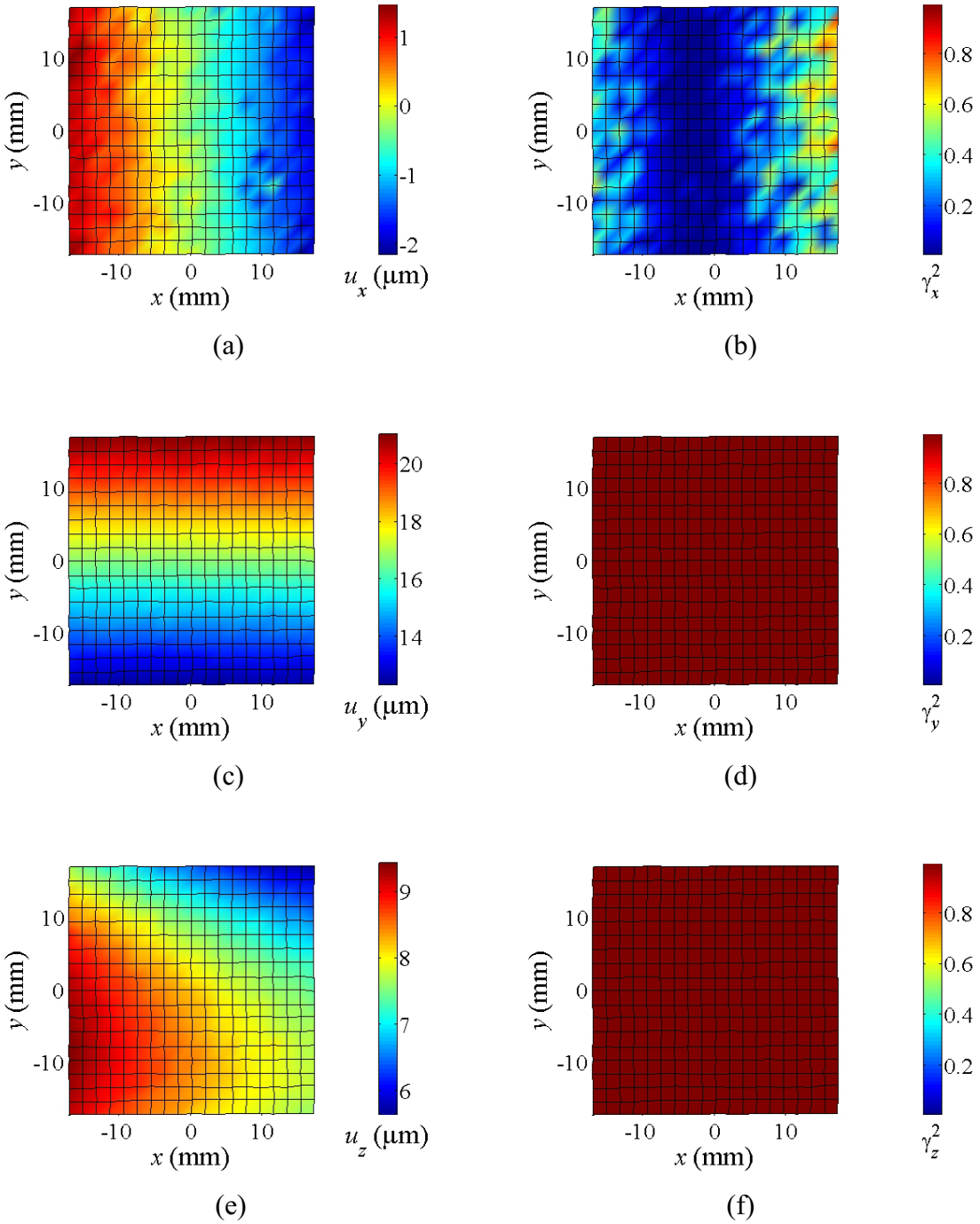

Figure 4.8. Experimental measured displacements u_x, u_y and u_z (left column) measured on the undamaged plate and their coherence γ_x^2, γ_y^2 and γ_z^2 (right column) to the input voltage. The plate specimen was subjected to a 1.05MPa load and the scan grid (N_x x N_y) consisted of 19x19 data points with a spatial interval (Δx and Δy) of 2mm.

Using this equation, it is possible to investigate the affect different parameters have on the accuracy of the measured surface strains, for instance, the selection of numerical method parameters, mesh size and applied load.

4.2.4 Savitzky-Golay Differentiation Parameters

To evaluate surface strain components from measured extensional displacements on the surface of a flat object, a two-dimensional numerical differentiation method is required. The Savitzky-Golay differentiating filter can be expressed in a two-dimensional form and still keep its advantages (i.e. preserves features of the distribution such as relative maxima, minima and width). The 2D Savitzky-Golay differentiating filter essentially performs a local two-dimensional polynomial regression (of degree n) on a distribution of $2m+1$ by $2m+1$ points to determine the smoothed value of the r_x and r_y derivatives of the displacement (g_{i_x,i_y}) with respect to the x- and y-direction, respectively, for each point. The 2D Savitzky-Golay differentiator has the form (Gorry 1990; Kuo, Wang, H & Pickup 1991),

$$f_{n_x,n_y}^{r_x,r_y}(t_x,t_y) = \frac{1}{\Delta x^{r_x}\Delta y^{r_y}} \sum_{i_x}^{m_x} \sum_{i_y}^{m_y} h_{t_x,i_x}^{n_x,r_x}\ h_{t_y,i_y}^{n_y,r_y}\ g_{i_x,i_y} \tag{4.18}$$

where Δx and Δy are the distances between each data point and $h_{t_x,i_x}^{n_x,r_x}$ and $h_{t_y,i_y}^{n_y,r_y}$ are the convolution weights for data point (i_x, i_y), with polynomial order n_x and n_y, and derivative order r_x and r_y with respect the x- and y-direction, evaluated at point (t_x, t_y). When applying the Savitzky-Golay differentiating filter to the x-direction then $g = x$ and $f = X$, and when applied to the y-direction $g = y$ and $f = Y$. A detailed explanation of

the 2D Savitzky-Golay differentiating filter can be found in Appendix B.2. To evaluate x-, y-normal and shear-strains using the Savitzky-Golay differentiator, respectively, then,

$$\varepsilon_{xx}(t_x, t_y) = X^{1,0}_{n_x,n_y}(t_x, t_y) \tag{4.19}$$

$$\varepsilon_{yy}(t_x, t_y) = Y^{0,1}_{n_x,n_y}(t_x, t_y) \tag{4.20}$$

$$\gamma_{xy}(t_x, t_y) = X^{0,1}_{n_x,n_y}(t_x, t_y) + Y^{1,0}_{n_x,n_y}(t_x, t_y) \tag{4.21}$$

Figure 4.9 shows the variation coefficient ($c_{v,i}$) of the surface strain for the acrylic plate specimen (ε_{xx} and ε_{yy}) subjected to a 1Hz sinusoidal load with 1.05MPa amplitude, versus the number of data points used ($2m + 1$) in a third-order polynomial ($n = 3$) Savitzky-Golay differentiating filter. In this test, the scan grid (N_x x N_y) consisting of 19x19 data points with spatial interval (Δx and Δy) of 2mm was placed in the middle of the acrylic plate specimen.

Figure 4.10 plots the change in the variation coefficient against the polynomial order used in the Savitzky-Golay differentiation. From this figure, the variation coefficient of the strain estimate reduces with increasing data points used in the filter. The variation coefficient of ε_{yy} is less than ε_{xx} because the better signal-to-noise ratio of the displacement in y-direction (of load). In addition, the variation coefficient is observed to increase with an increase in polynomial order. As expected, a first-order polynomial ($n = 1$) used within the Savitzky-Golay differentiating filter best approximates the constant strain fields produced by the uniform uniaxial applied displacement in the y-direction.

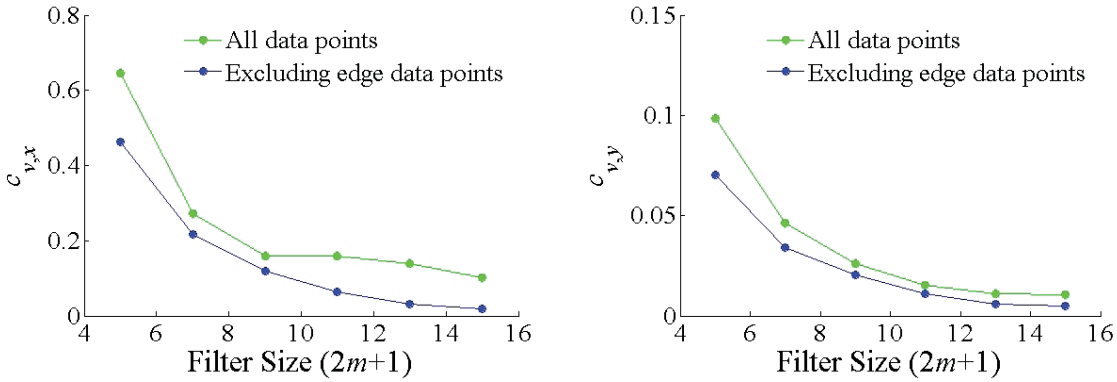

Figure 4.9. Variation coefficient ($c_{v,i}$) of the surfaces strains (ε_{xx} and ε_{yy}) versus the number of data points used ($2m+1$) in the Savitzky-Golay differentiator with a polynomial approximation of third-order ($n=3$). The plate specimen was subjected to approximately a 1.05MPa load and the scan grid (N_x x N_y) consisted of 19x19 data points with a spatial interval (Δx and Δy) of 2mm.

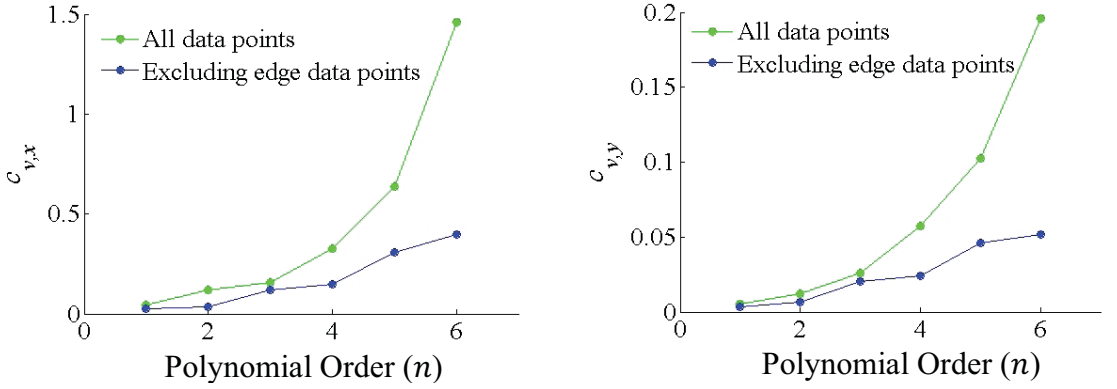

Figure 4.10. Variation coefficient (c_{RMSD}) of the surfaces strains (ε_{xx} and ε_{yy}) versus the order of the polynomial order (n) used in the Savitzky-Golay differentiator spanning 9x9 data points ($m=4$). The plate specimen was subjected to approximately a 1.05MPa load and the scan grid (N_x x N_y) consisted of 19x19 data points with a spatial interval (Δx and Δy) of 2mm.

Figures 4.9 and 4.10 also illustrate the affect of artefacts produced at the edge points of the Savitzky-Golay filter up to m points in from the boundary nodes, by separately considering all of the data points when evaluating the variation coefficient (green line) and the data points excluding the edge data points (blue line). These artefacts are characterised by areas of deviations from the trend of the evaluated strain field at these m points in from the boundary nodes, as seen in Figure 4.11. Figure 4.10 shows that edge artefacts significantly increase the variation coefficient of the evaluated strain fields when the polynomial approximation utilised within the Savitzky-Golay differentiating filter is greater than third-order.

For the experimental configuration investigated, a Savitzky-Golay differentiating filter using a polynomial approximation of equal or less than third-order ($n \leq 3$) and a filter width greater than or equal to 9 x 9 data points ($m \geq 4$) resulted in a standard deviation less than 15.9% (14.7 microstrain) and 2.6% (6.4 microstrain) from the mean values ($\bar{\varepsilon}_{xx} = -92.5$ microstrain and $\bar{\varepsilon}_{yy} = 247$ microstrain) in ε_{xx} and ε_{yy}, respectively,

4.2.5 Mesh Size

When considering the mesh density of the scan points, there needs to be a compromise between the spatial interval between the points and the errors that arise from the finite accuracy of the laser beam alignment. Ideally, a small mesh density would provide high strain resolution. Realistically however, at small mesh densities the finite accuracy of the laser beam alignment will begin to significantly distort the evaluated strain fields. Therefore, it is necessary to determine the smallest mesh density that is not significantly affected by the finite accuracy of the laser beam alignment.

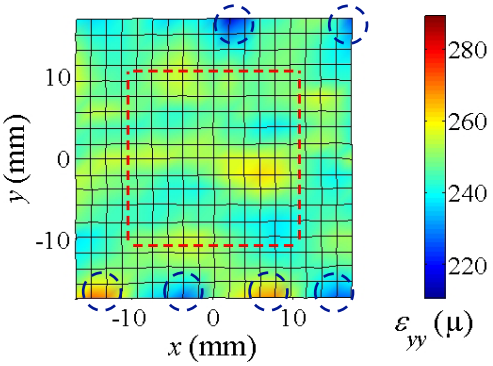

Figure 4.11. Estimated strain fields (ε_{yy}) of an acrylic plate subjected a 1Hz quasi-static uniaxial load of 1.05MPa. The red dashed line indicates the limit of the m data points in from the boundary where the edge artefacts occur and the blue dashed circles indicate locations of edge artefacts. A third-order ($n = 3$) Savitzky-Golay differentiating filter was used with a filter size of 9x9 data point ($m = 4$). The scan grid (N_x x N_y) consisted of 19x19 points with spatial interval (Δx and Δy) of 2mm.

In Figure 4.12, the variation coefficients ($c_{v,i}$) of the surface strains (ε_{xx} and ε_{yy}) are shown for varying mesh spatial intervals of a scan grid of 19x19 data points. The error in the x-direction is much higher than in the y-direction, which is due to the significantly lower amplitudes of displacement in this direction (and thus lower signal-to-noise ratio). The variation coefficient is observed to sharply increase for mesh intervals less than 1.5mm, which can be attributed to the finite accuracy of the laser beam alignment. In addition, there is a slight increase in the variation coefficient when the spatial interval was set to 5.2mm. At this spatial interval, the scan grid covers an area of 94mm x 94mm, which brings the grid very close to boundaries of plate specimen. Thus, this slight deviation can be attributed to the measurement points in vicinity of the boundary of the plate specimen.

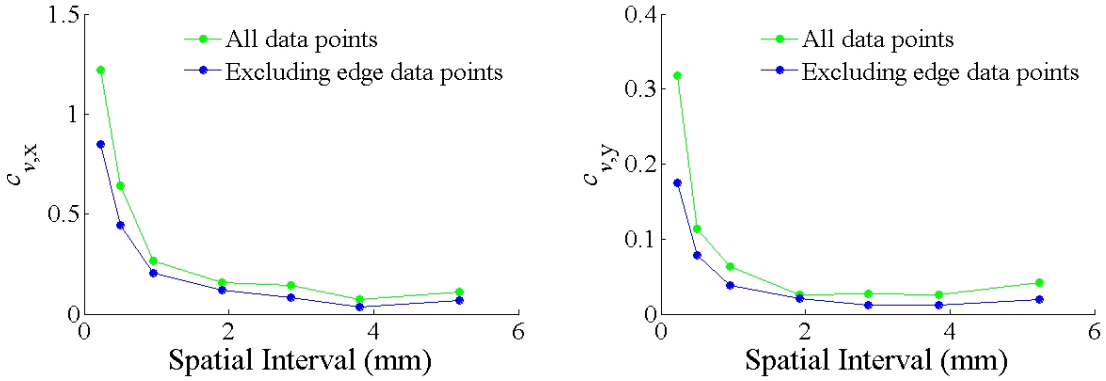

Figure 4.12. Variation coefficient ($c_{v,i}$) of the surface strain (ε_{xx} and ε_{yy}) versus the mesh spatial interval (Δx and Δy) of a scan grid (N_x x N_y) consisted of 19x19 data points. A third-order ($n = 3$). Savitzky-Golay differentiating filter was used with a filter size of 9x9 data point ($m = 4$). The plate specimens were subjected to approximately a 1.03MPa load.

4.2.6 Loading

The evaluated strain fields, and thus measured displacement, are proportional to the uniaxial applied load. With decreasing load, the amplitude of the displacement fields will also decrease and at some stage reach the noise floor for the specific data acquisition parameters utilised by the 3D SLDV system. At these small stress amplitudes, the evaluated strain fields will be significantly affected. Therefore, the relationship between the applied stress amplitude and the variation coefficient of the measured strain was investigated.

For the results presented Figure 4.13, the spatial interval between the 19x19 measurement points (N_x and N_y) was set to approximately 2mm and the velocity decoder used within the vibrometer was kept constant. The velocity decoder was setup such that when the acrylic plate was subjected to the maximum cyclic load of 1.05 MPa, the velocity decoder was on

the verge of signal saturation at the measurement point with maximum displacement. The variation coefficient ($c_{v,i}$) of evaluated surface strains (ε_{xx} and ε_{yy}) using a Savitzky-Golay filter was then investigated for varying in-plane stress amplitudes applied to the specimen and can be seen in Figure 4.13. The effect of stress amplitude above 400kPa has little effect on the accuracy of measured surface strains (for this testing arrangement and data acquisition parameters). This means that error in measured surface strains is not affected by the load amplitude, until the cyclic load amplitude is too small and some of the measured displacements of the plate begin to fall within the noise floor of the velocity decoder. Therefore, to ensure accurate strain measurements for the current experimental setup, the applied cyclic load amplitude must be greater than approximately 40% of the required load amplitude to saturate the velocity decoder.

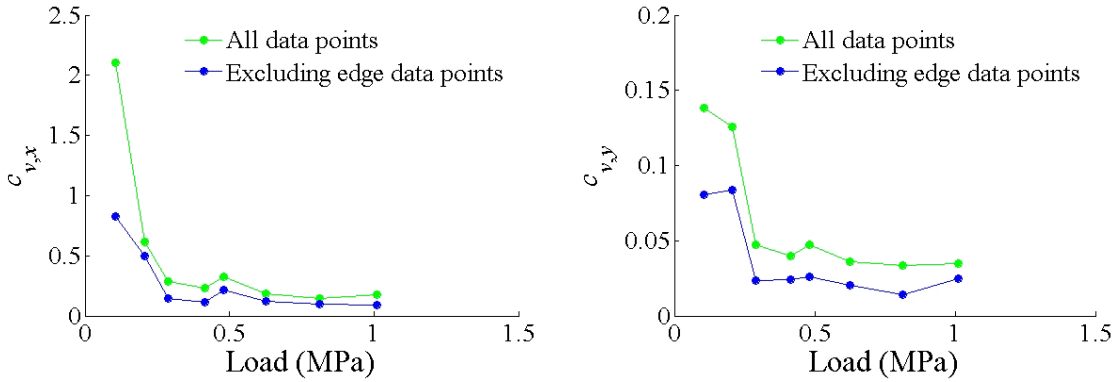

Figure 4.13. Variation coefficient ($c_{v,i}$) of the surface strain (ε_{xx} and ε_{yy}) versus the load applied to the plate specimen. A third-order ($n = 3$) Savitzky-Golay differentiating filter was used with a filter size of 9x9 data point ($m = 4$). The scan grid (N_x x N_y) consisted of 19x19 data points with a spatial interval (Δx and Δy) of 2mm.

4.2.7 Summary of In-Plane Measurement

An investigation into a new surface strain measurement technique was presented that utilises in-plane displacements measured from a 3D vibrometer and a 2D Savitzky-Golay differentiating filter. The accuracy of this technique is examined for varying experimental parameters, including distance between measurement points, amplitude of loading, and parameters within the 2D Savitzky-Golay differentiator. For this experimental investigation, these parameters were found to have a significant effect on the accuracy of evaluated surface strains. For the experimental test arrangement utilised in the current study, optimal accuracy and resolution was achieved when:

1. the mesh interval was 2mm or greater,
2. the 2D Savitzky-Golay differentiating filter utilised polynomial approximation of equal or less than a third-order polynomial ($n \leq 3$) and a filter size of equal or greater than 9x9 points ($m \geq 4$), and
3. the applied stress amplitude to the plate was above 400kPa, which avoided the noise floor for the specific data acquisition parameters and experimental setup.

As an example of the accuracy of the new surface strain measurement technique; a Savitzky-Golay filter with $n = 3$ and $m = 4$, mesh spatial interval of 2mm, with uni-axial loading and a stress amplitude of approximately 1.05MPa, produces a standard deviation in ε_{xx} and ε_{yy} of 15.9% (14.7 microstrain) and 2.6% (6.4 microstrain) from the mean values ($\bar{\varepsilon}_{xx} = -92.5$ microstrain and $\bar{\varepsilon}_{yy} = 247$ microstrain), respectively. When compared this result to the work presented by Cazzolato et al. (2008) on using 3- and 4-node finite elements to evaluate the strain field, there is a slight improvement in the evaluation of the strain. However, it is possible to vary the numerical method parameter used within the

Savitzky-Golay differentiator to increase the accuracy of the proposed technique.

Strain measurement techniques that utilise the 3D SLDV system demonstrate a marked improvement over other similar systems. For example, when comparing the 3D SLDV strain measurement techniques to the commonly used strain gauge method, 3D SLDV performed better in many aspects:

- Strain gauge techniques can measure within a ±2% accuracy (assuming accurately bonded and aligned) with a cross sensitivity as low as 0.2% (Parr 2000), whereas the 3D vibrometer can provide a wide range of accuracies, depending on the filter size used within the Savitzky-Golay differentiating filter ($2m + 1$), down to ±2% of the mean strain.
- Strain gauges can resolve strains as small as 3 microstrains, however, the 3D vibrometer can measure down to picometres of displacements, essentially allowing nanostrain level resolution at a 1mm mesh density.
- Strain gauges can only provide point strain measurements, whereas 3D vibrometer is able to provide full-field strain measurement.

3D SLDV provides a good alternative to commonly used strain gauges for quasi-static strain measurement. However, an investigation into the accuracy of the technique in measuring strains near a stress concentrator (i.e. crack, notch) is essential to determining the applicability of the proposed strain measurement technique.

4.3 Measurement of Strain at Stress Concentrations

In Section 4.2 the accuracy of the 3D SLDV strain measurement technique was evaluated for a uniform strain field. However, to be practically useful as an experimental technique, it is essential that the technique is able to accurately resolve strains in the vicinity of stress concentrators. To demonstrate the accuracy of the technique in evaluating strain fields near stress concentrators, two important cases, with practical application, are investigated:- a 90 degree notch length of 20mm and a 20mm long edge crack.

A square mesh of 39 x 39 points was placed 2mm ahead of the tip of the stress concentrator with a spatial mesh interval of 2mm, thus covering an area of 76mm x 76mm. The notched plate was subjected to nominal applied stress of 0.65 MPa, whereas the plate with an edge crack was subjected to a nominal applied stress of 0.78 MPa. A schematic of the two specimens and the mesh is given in Figure 4.14. For these tests the vibration signals were sampled at a frequency of 512Hz. A Fourier analysis was conducted at frequency resolution of 500mHz, utilising a rectangular window and employing 64 averages with 75% overlap.

To evaluate the accuracy of the measured strain fields in vicinity of a notch and edge crack, the results were compared against finite element simulations. The finite element analysis was conducted using the ANSYS 12 package. Full scale plane-stress models of the two specimens were constructed utilising a two-dimensional 8-node planar solid element (PLANE82). Initially the models were meshed with a 2mm interval. The model was refined twice in the vicinity of the notch and crack tip. The first refinement was

performed over the area of 6 elements out from the notch and crack tip, in order to reduce the mesh interval by half in that area. For the second refinement, the mesh interval was reduced by half over an area of 8 elements out from the crack and notch tip. The meshes of the two finite element models are shown in Figure 4.15. It should be noted that the crack was model exactly as it was created, which was a thin 0.3mm wide straight notch with a rounded crack tip.

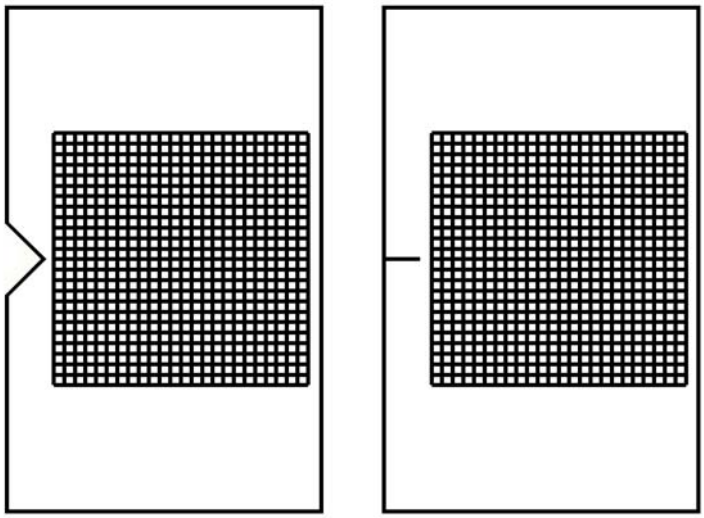

Figure 4.14. Illustration of the rectangular plate specimens and meshes used for strain measurement (a) with a notch and (b) with an edge crack.

From separate materials testing on the specimens, the Young's modulus was found to vary considerably between $E = 2900 \pm 400$ MPa. Therefore, to evaluate the accuracy of the measured strain fields, the material properties used within the finite element models were adjusted to minimise error between the strain produced by the models and that of the experiments. The material properties used, in the notch and edge crack finite element

models, were a modulus of elasticity of 2.7 GPa and 3.1GPa and a Poisson ratio of 0.35 and 0.35, respectively.

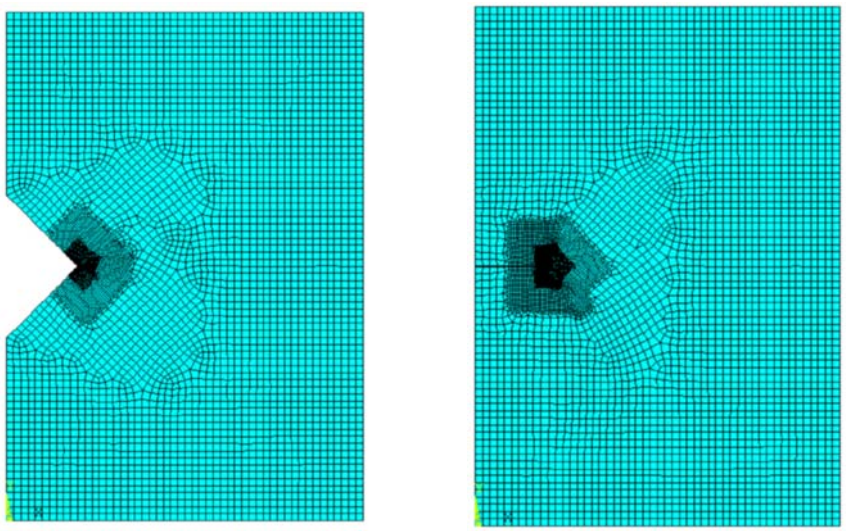

(a) (b)

Figure 4.15. The finite element meshes used to simulate the strain field of (a) notched and (b) edge crack specimens.

4.3.1 Results

The surface strain fields in the vicinity of the notch and edge crack were evaluated by applying the Savitzky-Golay differentiator to the measured displacement data (Figures 4.16 and 4.19, respectively) and are presented in Figures 4.17 and 4.20, respectively. For comparison, finite element results were compared with the experimentally obtained strain fields, which were in good agreement. Figures 4.18 and 4.21 plot the strain along a path ahead of the notch and crack, respectively, and compare the evaluated strain to the finite element results.

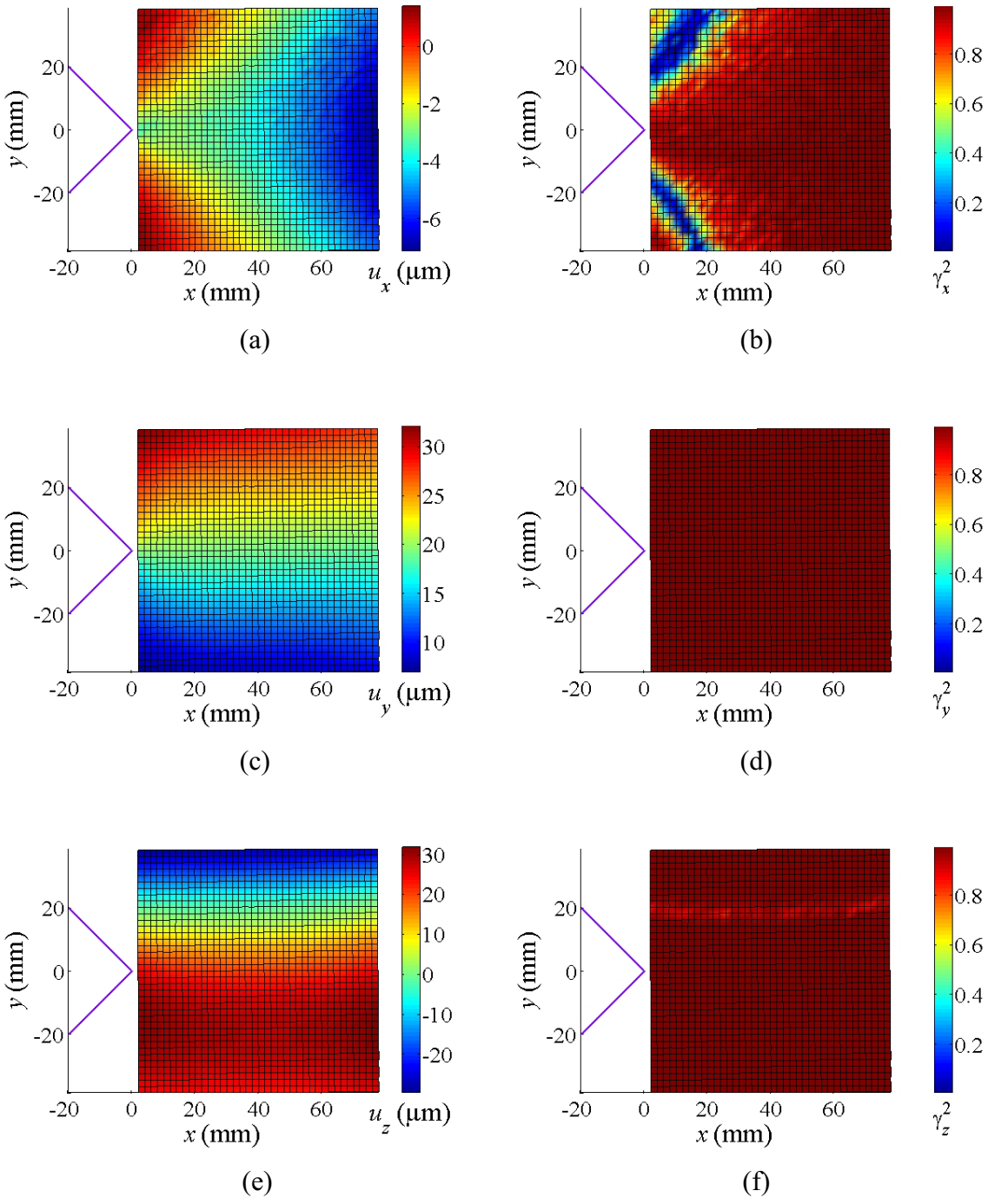

Figure 4.16. Displacements u_x, u_y and u_z and their coherence γ_x^2, γ_y^2 and γ_z^2 with the input voltage, for the rectangular plate with a notch. The plate specimen was subjected to approximately a 0.65 MPa load and the scan grid (N_x x N_y) consisted of 39x39 data points with a spatial interval (Δx and Δy) of 2mm.

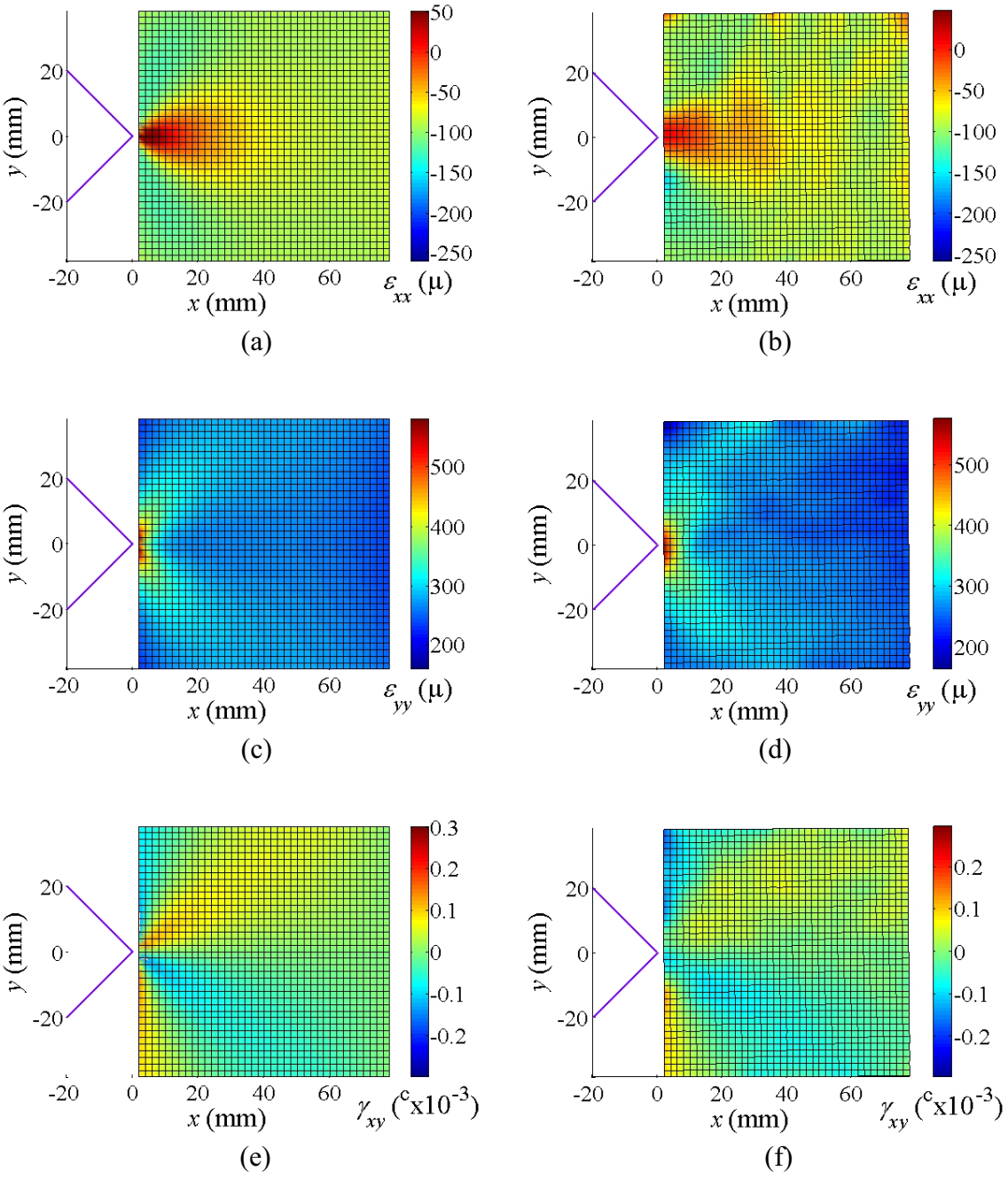

Figure 4.17. Surface strain (ε_{xx}, ε_{yy} and γ_{xy}) for the rectangular plate with a notch:- (left) FEA and (right) experimental results. A third-order ($n = 3$) Savitzky-Golay differentiating filter was used with a filter size of 13x13 data point ($m = 6$). The plate specimen was subjected to approximately a 0.65 MPa load and the scan grid (N_x x N_y) consisted of 39x39 data points with a spatial interval (Δx and Δy) of 2mm.

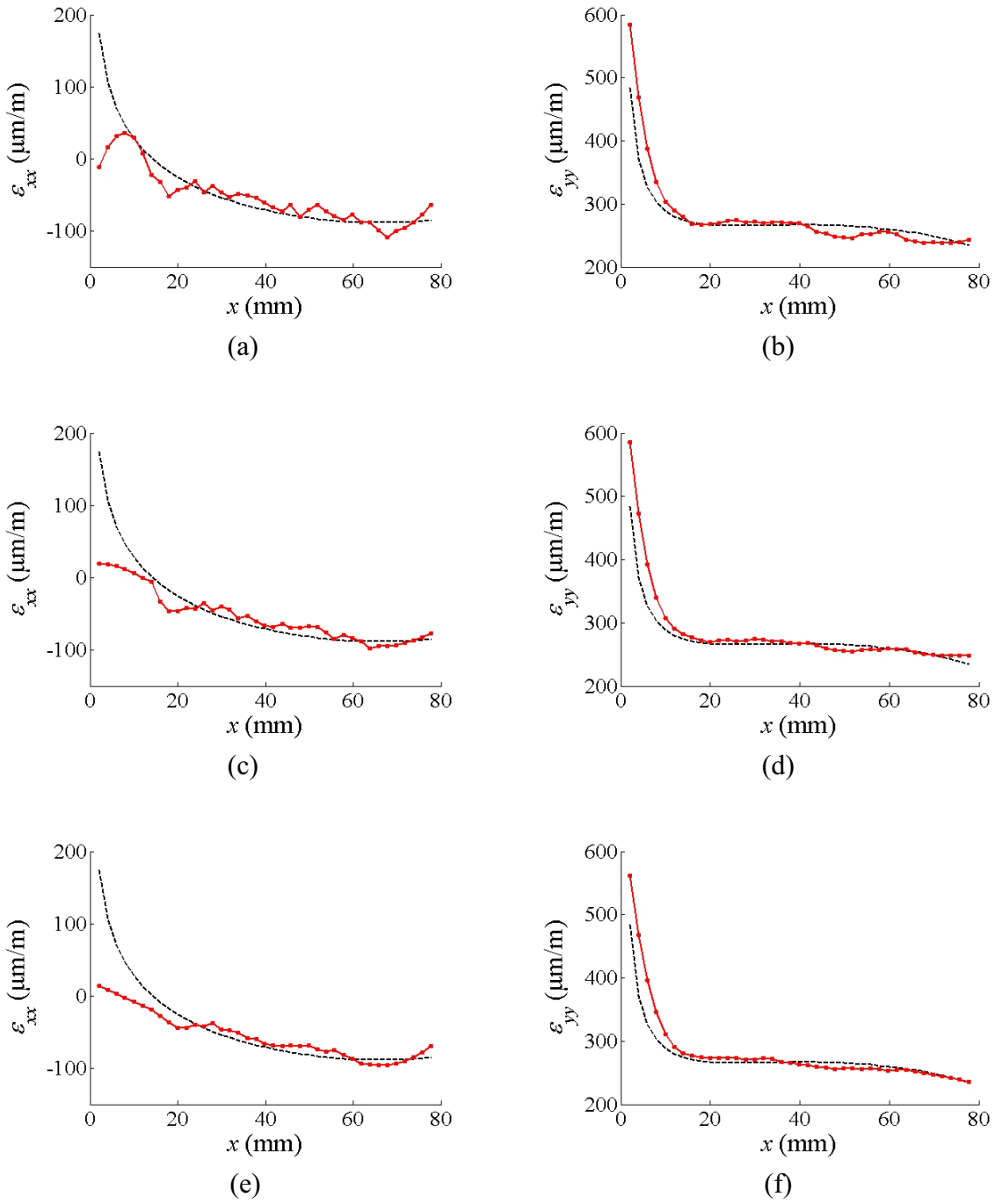

Figure 4.18. Strains extending out from the notch. Comparison of the experimental (red line) and numerical (black dashed line) solution of ε_{xx}, (left) and ε_{yy} (right) in-line with the notch, (a, b) $m = 4$, (c, d) $m = 5$, and (e, f) $m = 6$. The plate specimen was subjected to approximately a 0.65 MPa load and the scan grid (N_x x N_y) consisted of 39x39 data points with a spatial interval (Δx and Δy) of 2mm.

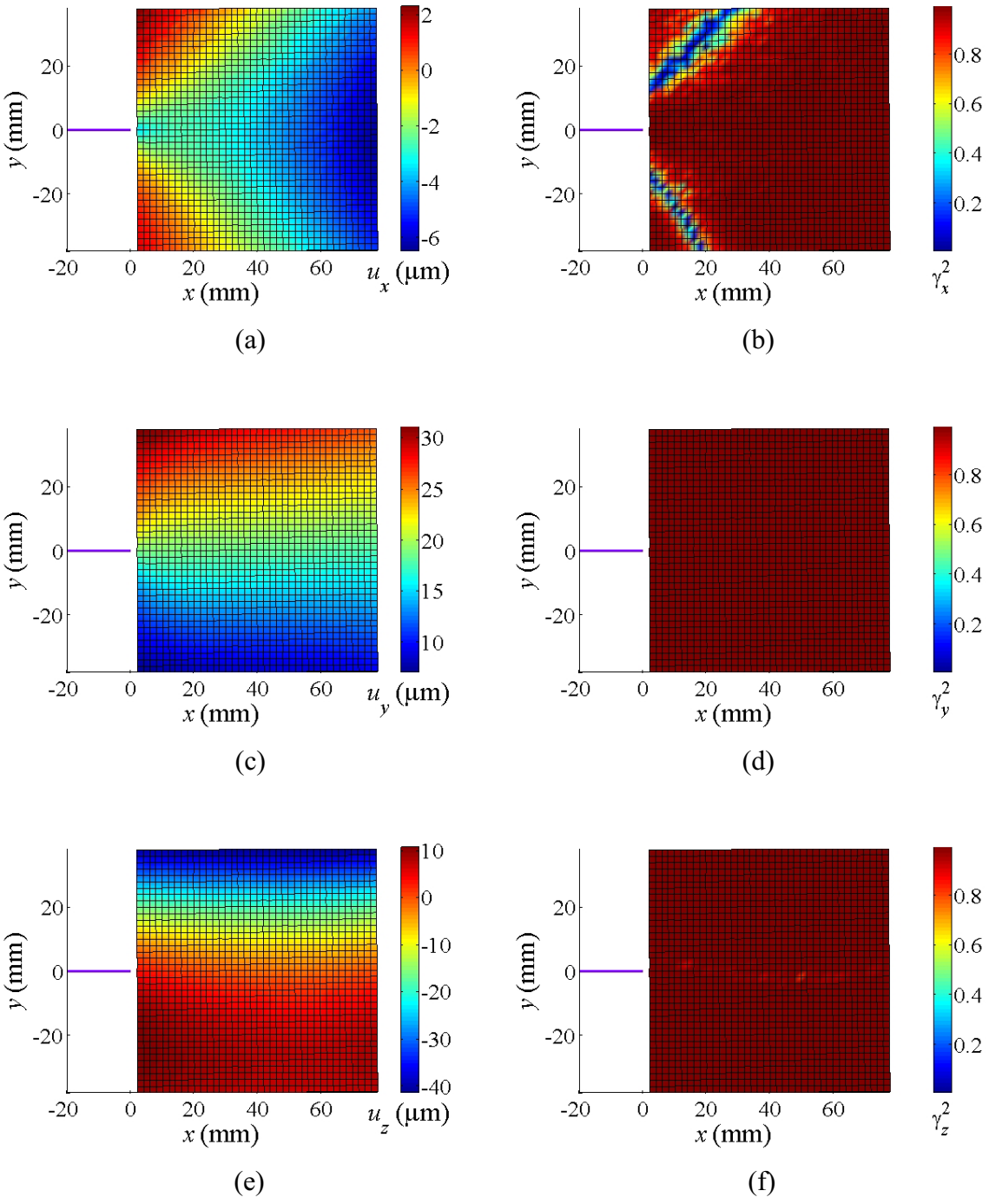

Figure 4.19. Displacements u_x, u_y and u_z and their coherence γ_x^2, γ_y^2 and γ_z^2 with the input voltage, for the rectangular plate with edge crack. The plate specimen was subjected to approximately a 0.78 MPa load and the scan grid (N_x x N_y) consisted of 39x39 data points with a spatial interval (Δx and Δy) of 2mm.

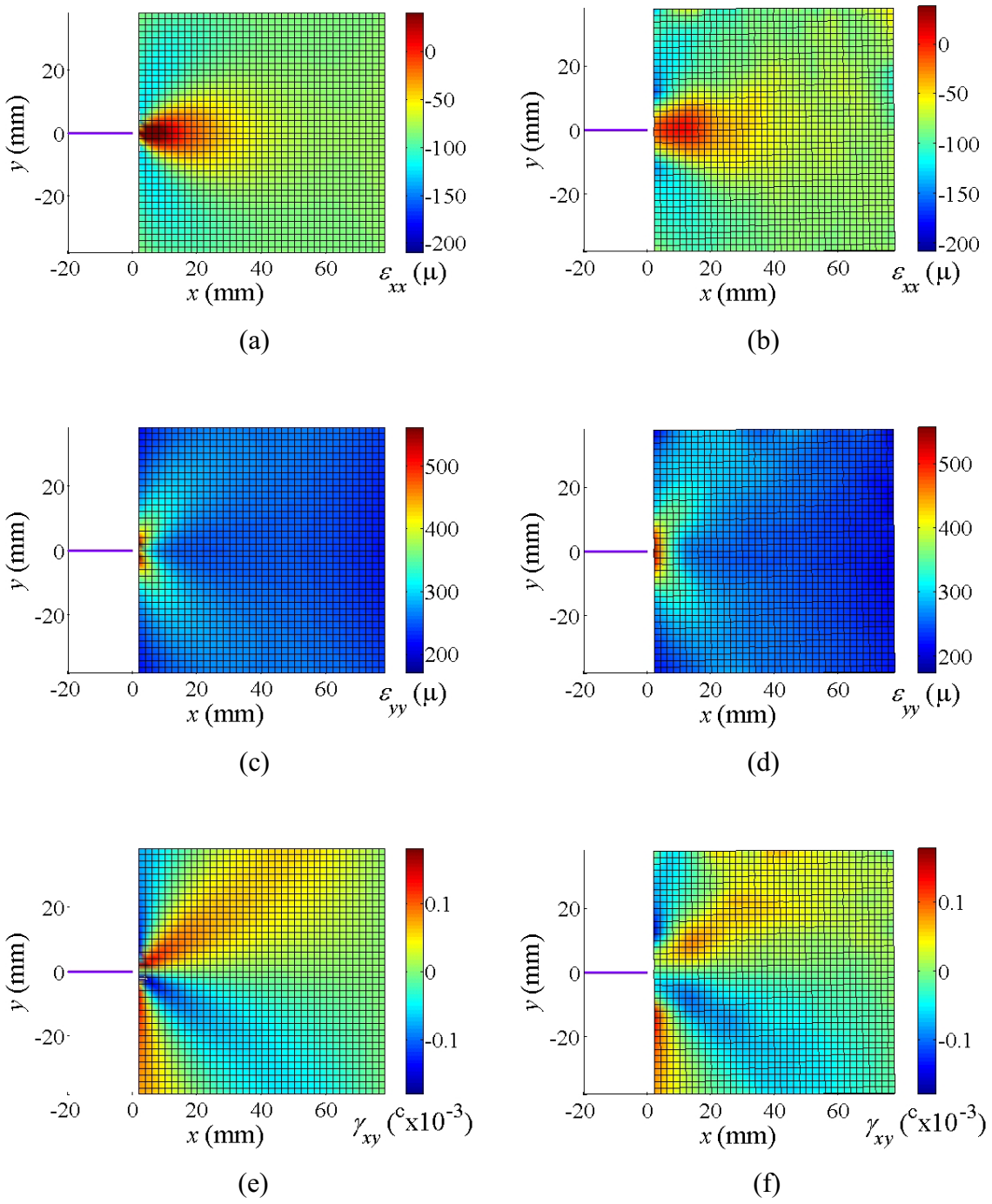

Figure 4.20. Surface strain (ε_{xx}, ε_{yy} and γ_{xy}) for the rectangular plate with edge crack:- (left) FEA and (right) experimental results. The plate specimen was subjected to approximately a 0.78 MPa load and the scan grid (N_x x N_y) consisted of 39x39 data points with a spatial interval (Δx and Δy) of 2mm.

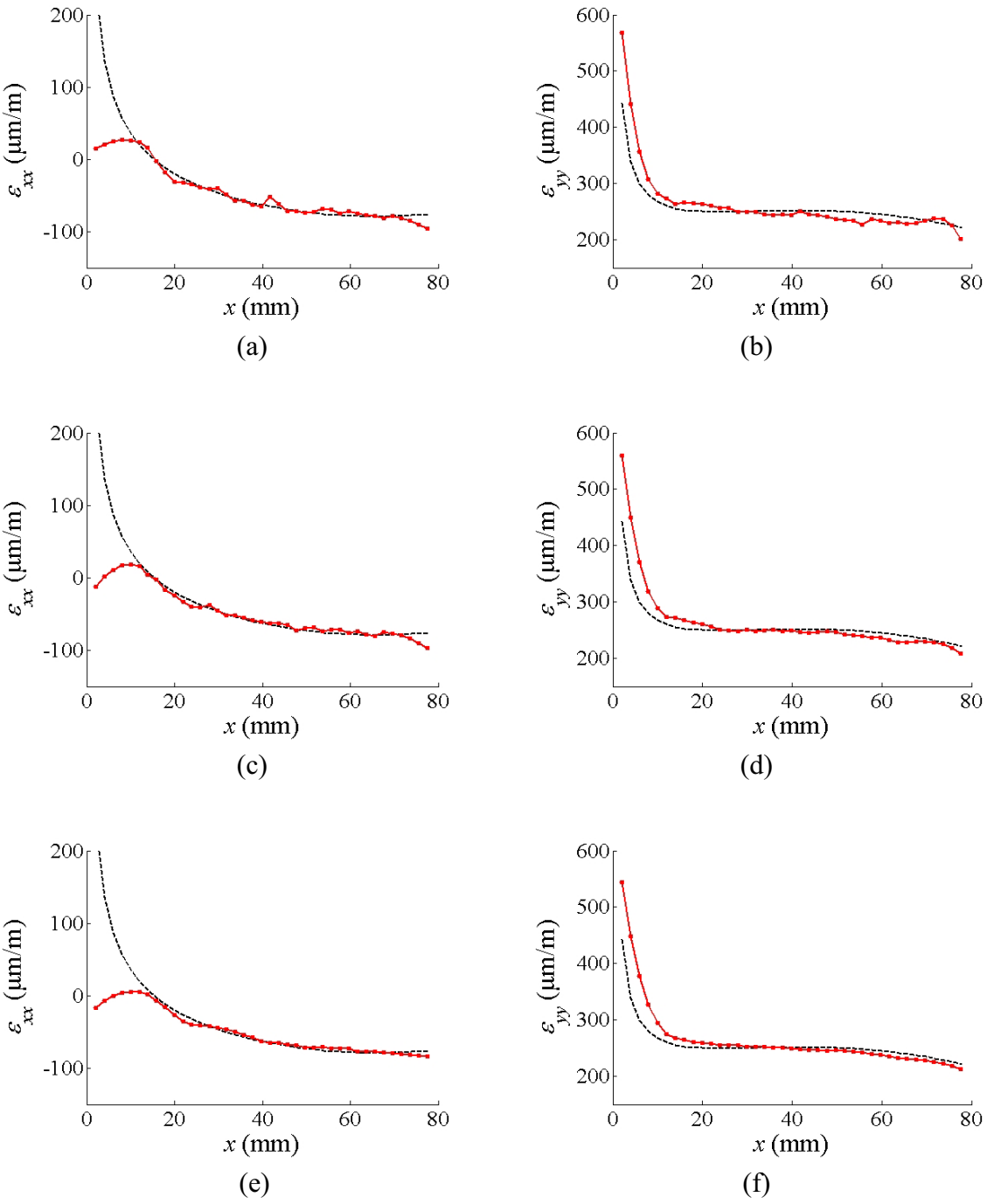

Figure 4.21. Strain extending out from crack tip. Comparison of the experimental (red line) and numerical (black dashed line) solution of ε_{xx}, (left) and ε_{yy} (right) in-line with the edge crack, (a, b) $m = 4$, (c, d) $m = 5$, and (e, f) $m = 6$. The plate specimen was subjected to approximately a 0.78 MPa load and the scan grid (N_x x N_y) consisted of 39x39 data points with a spatial interval (Δx and Δy) of 2mm.

4.3.1 Discussion

The measured displacements (u_x, u_y and u_z) in the vicinity of the notch and edge crack, as well as the corresponding coherence functions (γ_x^2, γ_y^2 and γ_z^2) between the input voltage and displacement signals, are depicted in Figures 4.16 and 4.19, respectively. As expected the displacement distorts significantly around the stress concentrators. Figures 4.16b and 4.19b show areas of low coherence of the displacement in the x-direction to the input voltage, corresponding to the areas of small displacements in the x-direction. In addition, Figures 4.16f and 4.19f show that there is also a slight decrease in coherence of the displacement in the z-direction (out-of-plane) where the amplitude of the displacement is close to zero.

The strain field in the vicinity of the notch and edge crack is evaluated from the measured in-plane displacement fields and is shown in the right columns of Figures 4.17 and 4.20, respectively. To validate the experimentally evaluated strain fields, a finite element model was developed for the notch and edge crack scenarios, which are depicted in the left column of Figures 4.17 and 4.20, respectively. When comparing the experimental strain fields to those produced by the finite element model, good agreement was observed. However, there are some slight distortions in the evaluated strain fields, which are due to the noise in the measured displacement field and the edge effect created by the filter.

Figures 4.18 and 4.21 illustrate the comparison between the experimentally measured, and finite element model evaluated strain distributions leading up to the tip of the notch and edge crack ($y = 0$), respectively, for three different filter sizes. An error in x- and y-strains (ε_{xx} and ε_{yy}) can be seen at both ends of the strain distributions of approximately m

measurement points in from the edge, due to the edge effect caused by the filter.

To quantitatively evaluate the deviation between the measured and finite element model evaluated surface strain, the coefficient of variation of the Root Mean Squared Deviation (RMSD) between the two was considered. The RMSD between measured ($\varepsilon_{ij,SG}$) and finite element model evaluated ($\varepsilon_{ij,FEA}$) surface strain can be expressed as

$$RMSD_i = \left[\frac{1}{N}\sum_{j=1}^{N}\left(\varepsilon_{ii,SG,j} - \varepsilon_{ii,FEA,j}\right)^2\right]^{1/2} \tag{4.22}$$

where N is the number of measurement points.

In order to compare the RMSD of the surface strain fields, the coefficient of variation of the RMSD is evaluated, which is defined as the ratio of the RMSD (Equation (4.21)) of the surface strains to the mean value of the measured surface strain ($\bar{\varepsilon}_{ii,SG}$) and is expressed as,

$$c_{RMSD,i} = \frac{RMSD_i}{\left|\bar{\varepsilon}_{ii,SG}\right|} \tag{4.23}$$

Tables 4.2 and 4.3 present the variation coefficient of the RMSD between the measured and finite element surface strains ($c_{RMSD,x}$ and $c_{RMSD,y}$) for various filter widths and leading up to the tip of the notch and edge crack ($y = 0$), shown in Figures 4.18 and 4.21, respectively. These tables separately consider the standard deviation for all the data points in the distribution, as well as the standard deviation that only considers the middle data points (i.e. excluding the data points m in from the edge). As previously seen in Section 4.2.4, the strain distribution is significantly affected by edge artefacts. In addition, the variation coefficient of the RMSD of the y-strain ($c_{RMSD,y}$) for both the notch and edge

crack give similar results, producing similar deviations to the uniform strain fields described in Section 4.2. However, the variation coefficient of the RMSD in the x-strain ($c_{RMSD,x}$) produced larger deviations, more notably in the notch than the edge crack. The reason the deviations in the x-strain were greater in the notch than the edge crack is most likely due to the decrease in coherence in the x-displacement in front of the notch, as seen in Figure 4.16b.

Table 4.2. Variation coefficient of the root squared mean deviation ($c_{RMSD,i}$) between the FE and measured x- and y-strain leading up to the tip of the notch specimen ($y = 0$) that are presented in Figure 4.18. The RMSD values are provided in brackets for each case.

Filter Size ($2m + 1$)	$c_{RMSD,x}$ ($RMSD_x$)		$c_{RMSD,y}$ ($RMSD_y$)	
	All data points	Excl. edge points	All data points	Excl. edge points
9	68.4% (35.9με)	22.7% (13.1με)	9.5% (26.5με)	3.7% (9.7με)
11	60.3% (32.2με)	19.8% (11.8με)	9.4% (26.8με)	2.2% (5.9με)
13	63.4% (34.9με)	17.4% (10.6με)	8.8% (24.8με)	2.4% (6.4με)

Table 4.3. Variation coefficient of the root squared mean deviation ($c_{RMSD,i}$) between the FE and measured x- and y-strain leading up to the tip of the edge crack specimen ($y = 0$) that are presented in Figure 4.21. The $RMSD$ values are provided in brackets for each case.

Filter Size ($2m + 1$)	$c_{RMSD,x}$ ($RMSD_x$)		$c_{RMSD,y}$ ($RMSD_y$)	
	All data points	Excl. edge points	All data points	Excl. edge points
9	93.3% (43.1με)	10.7% (5.3με)	11.3% (29.7με)	4.2% (10.3με)
11	101% (48.8με)	7.3% (3.8με)	11.4% (30.2με)	3.3% (8.2με)
13	102% (50.8με)	2.6% (4.0με)	11.0% (29.2με)	2.6% (6.5με)

This data shows that when evaluating the full-field strain with this method, there needs to be a compromise between accurate strain measurement in the middle of the strain distribution and the distortion of the strain at the edges of the measurement grid (m data points in from the edge).

4.3.2 Summary Strain Measurement at Stress Concentrators

This section has investigated an example application and shown the accuracy of the new experimental surface strain technique, which uses a 3D vibrometer. Utilising the displacement measurements from the laser vibrometer and a Savitzky-Golay differentiator, it is possible to experimentally evaluate surface strain fields arising from in-plane loading. Experimental surface strains were evaluated in the vicinity of a notch and edge crack using the new technique and compared with FE simulations, which showed good agreement.

4.4 Bending Strain

This section presents an investigation into the accuracy of 1D SLDV in measuring quasi-static surface strain, of an aluminium beam specimen, induced by bending. Previous studies conducted into the use of 1D SLDV in the measurement of bending strain are first examined. This is followed by the formulation and experimental setup of the strain measurement technique utilised in this study, as well as the approach used to evaluate the accuracy of the technique. Finally, the affect of various parameters have on the accuracy of the technique is then presented, including the parameters of the numerical method, spatial interval between measurement points and amplitude of loading.

4.4.1 Previous Studies

Ferguson and Carpentier (1989) were the first to conduct experiments into the use of a prototype 1D laser Doppler vibrometer for the measurement of dynamic bending strains on the surface of an aluminium beam, which were compared to strain gauge measurements. Five measurement points for the laser vibrometer were evenly spaced 10cm apart along the beam length, as seen in Figure 4.22. The bending strains were estimated at the three middle points and were evaluated by applying a second-order polynomial fit over three data points. The results obtained showed fair agreement between the strains measured by the strain gauges and those evaluated using the laser vibrometer, however no real attempt was made to evaluate the accuracy of the technique.

Another experimental study into quasi-static bending strain measurements using 1D vibrometer (an Ometron Vibration Pattern Imager) was conducted by Goetsch and Rowlands (1991). This experiment consisted of a clamped circular aluminium plate, excited at its centre by an electromagnetic shaker. The radial bending strains were evaluated from radial out-of-plane deflections, which were measured at a spatial interval of 2.5mm ($\Delta x = 2.5\text{mm}$). The quasi-static bending strains were determined by fitting a cubic spline to the measured plate deflections and then differentiating the function analytically. From their results they found that the strains closely correlated with the strain gauges in the vicinity of the edge of the plate, however, the strain deviated significantly when measured near the applied load, as seen in Figure 4.23

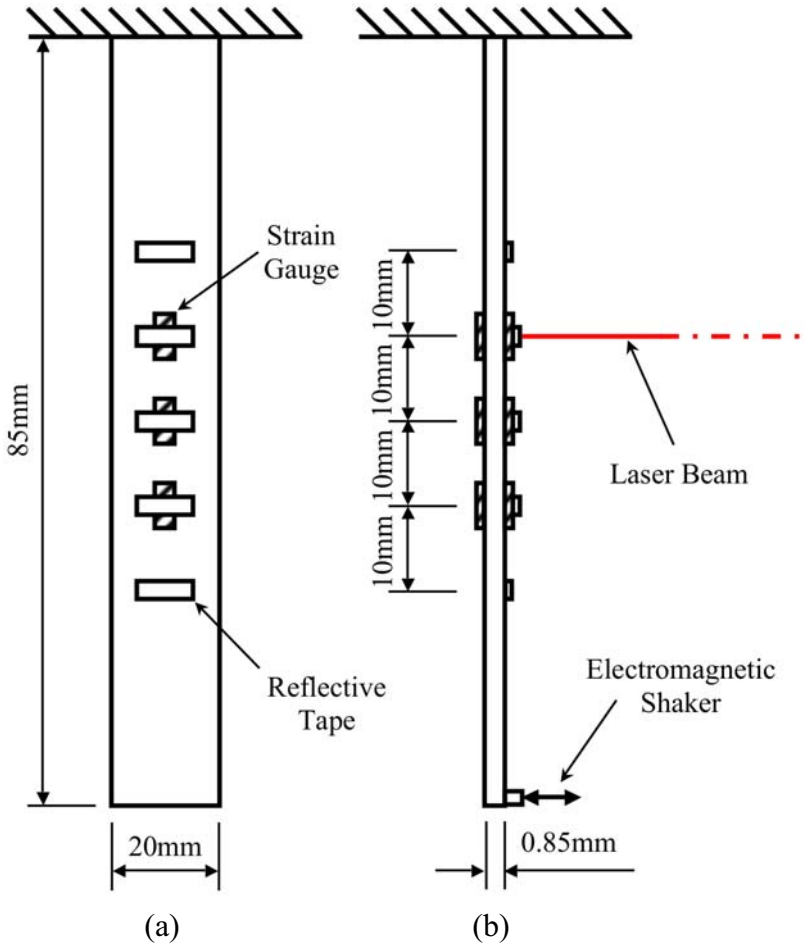

Figure 4.22. Experimental arrangement used by Ferguson and Carpentier (1989, p. 215) for the comparison between bending strains evaluated using prototype 1D laser Doppler vibrometry and strain gauges. (a) Front view and (b) side view.

These early investigations were devised to show the possibility of the use of laser Doppler vibrometry for the measurement of dynamic and quasi-static bending strain. As previously discussed in Section 2.4.1, significant research has been focused on determining the accuracy of the use of 1D SLDV for the measurement of broadband bending strain measurement (Miles, Bao & Xu 1994; Moccio & Miles 1996; Xu & Miles 1996a, 1996b), however, no recent investigations have been conducted to evaluate the accuracy of using a

1D vibrometer and more advanced differentiation techniques for the measurement of quasi-static bending strain.

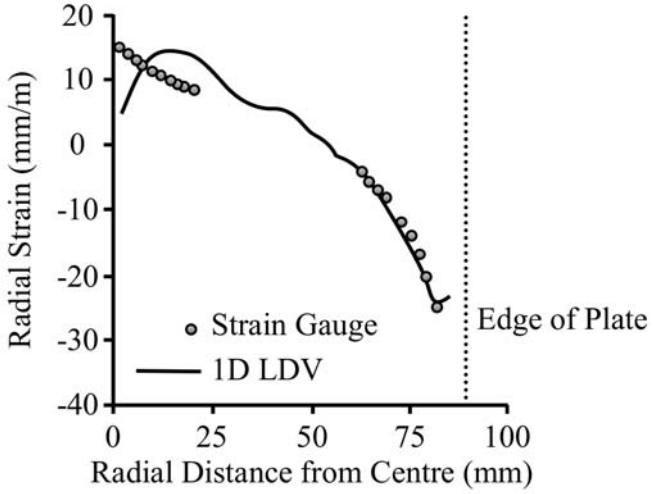

Figure 4.23. Previous results obtained by Goetsch and Rowlands (1991, p. 431) for the comparison between radial bending strains evaluated using 1D SLDV and strain gauges for a circular aluminium plate. The plate was vibrated at 20Hz at its centre with an unspecified load.

4.4.2 Surface Strains for a Plate Loaded in Bending

To measure surface strain induced in a plate loaded in bending using 1D SLDV, the kinematics of plate deflection first need to be established. Consider a flat, unloaded plate, with the mid-plane coinciding with the x-y plane, as seen in Figure 4.24a. At a point on the plate, the components of displacement occurring in the x-, y-, and z-directions are expressed by u_x, u_y, and u_z, respectively. When the plate is loaded, six strain components (normal and shear) can be considered at any point, which are linearly dependent on the three displacement components. Small-deflection theory, known as Kirchhoff's hypotheses

(Kirchhoff 1850), can be utilised to reduce the strain components. To apply this hypotheses the plate specimen must (Szilard 2004),

- be homogeneous, isotropic and linear elastic,
- be initially flat,
- have a constant thickness and the smallest lateral dimension must be 10 times larger than its thickness, and
- must not deflect more than one-tenth of the plate thickness.

The use of Kirchhoff's hypotheses is valid in the study presented in this section as the beam specimen used is a flat aluminium specimen with a width 17 times larger than its thickness and the deflections investigated are less than one-tenth the thickness of beam. From Kirchhoff's hypotheses, the normals (section m-n shown in Figure 4.24b) before and after bending remain straight, unstretched and normal to the mid-surface (Kirchhoff 1850). This implies that the transverse shear strains (γ_{xz} and γ_{yz}) and transverse normal strain (ε_{zz}) are negligible. Therefore, the strain-displacement relationship can be expressed as,

$$\varepsilon_{xx} = \frac{\partial u_x}{\partial x} \tag{4.24}$$

$$\varepsilon_{yy} = \frac{\partial u_y}{\partial y} \tag{4.25}$$

$$\gamma_{xy} = \frac{\partial u_x}{\partial y} + \frac{\partial u_y}{\partial x} \tag{4.26}$$

$$\varepsilon_{zz} = \frac{\partial u_z}{\partial z} \approx 0 \tag{4.27}$$

$$\gamma_{xz} = \frac{\partial u_z}{\partial x} + \frac{\partial u_x}{\partial z} \approx 0 \tag{4.28}$$

$$\gamma_{yz} = \frac{\partial u_z}{\partial y} + \frac{\partial u_y}{\partial z} \approx 0 \tag{4.29}$$

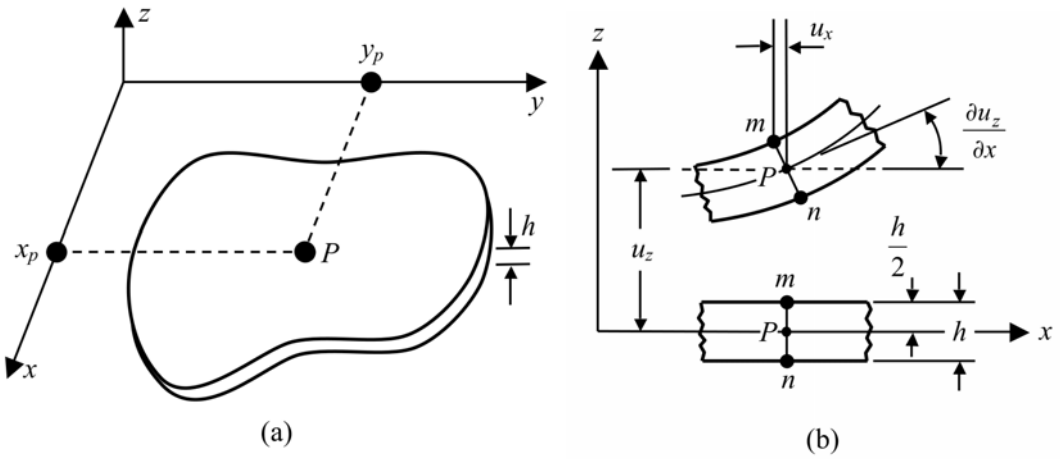

Figure 4.24. (a) A plate of constant thickness, (b) a cross-section of the plate before (lower) and after (upper) deflection.

The integration of Equations (4.27), (4.28) and (4.29) with respect to the z-direction (lateral direction), from the mid-plane ($z = 0$) to the plate surface ($z = h/2$), gives,

$$u_z = u_z(x, y) \tag{4.30}$$

$$u_x = \frac{h}{2}\frac{\partial u_z(x, y)}{\partial x} \tag{4.31}$$

$$u_y = \frac{h}{2}\frac{\partial u_z(x,y)}{\partial y} \tag{4.32}$$

Equation (4.30) shows that, by using small-deflection theory, the lateral deflection (u_z) does not vary across the plate thickness. Therefore, plate surface strains (ε_{xx}, ε_{yy} and γ_{xy}) can be evaluated purely from the measured surface out-of-plane displacement (u_z) and expressed as:-

$$\varepsilon_{xx} = \frac{h}{2}\frac{\partial^2 u_z}{\partial x^2} \tag{4.33}$$

$$\varepsilon_{yy} = \frac{h}{2}\frac{\partial^2 u_z}{\partial y^2} \tag{4.34}$$

$$\gamma_{xy} = h\frac{\partial^2 u_z}{\partial x \partial y} \tag{4.35}$$

In this section, the bending strain of a cantilever beam specimen is considered where there is no curvature in the y-direction, thus equation (4.33) will only be utilised. As this equation is based on small deflection theory, bending strains are evaluated using out-of-plane deflections, measured from a 1D vibrometer, that are much smaller than the thickness of the beam. This theory provides a basis of the bending strain measurement technique utilising the 1D vibrometer.

4.4.3 Investigation of Bending Strain

An experimental procedure was developed in order to evaluate how various parameters affect the accuracy of the 1D SLDV quasi-static bending strain measurement technique. As mentioned in Section 3.2.1, these experiments were conducted on an aluminium cantilever beam (with in-plane dimensions of 500mm x 51mm and thickness of 2.95mm), which was subjected to a 1Hz sinusoidal out-of-plane displacement at the free end. Deflection of the beam was measured at a number of points along the centre-line of the beam length.

This section investigates the affect of the mesh size, numerical method parameters and loading amplitude has on the effectiveness of using 1D SLDV in measuring bending strain on a beam. The vibrometer measured the vibration signals at a sample frequency of 512Hz. To obtain the displacement data at the 1Hz loading frequency, Fourier analysis was conducted with a frequency resolution of 500mHz, while utilising a rectangular window and 64 averages with 75% overlap.

An example of the measured displacement (u_z) along the aluminium beam and its coherence (γ_z^2) to the input vibration is shown in Figure 4.25. The coherence function (Bendat & Piersol 2010) provides a measure of the data quality (signal-to-noise ratio). From Figure 4.25, the coherence was found to be less than unity for the measurements points 53mm in from the clamped end, which correspond with deflection amplitude of 1.5μm, 1% of full scale. This reduction in coherence occurs because the measured deflection amplitudes decrease below the noise floor of the 1D vibrometer for current arrangement.

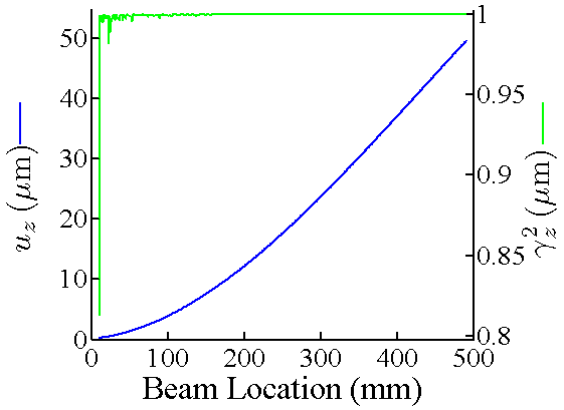

Figure 4.25. Experimentally measured deflection (u_z) measured on an aluminium beam (blue line) and its coherence (γ_z^2) to the input voltage (green line). The aluminium beam specimen was subjected to a maximum free-end deflection of 50μm and the scan line consisted of 499 points (N) with a spatial interval ($Delta_x$) of 0.97mm.

For a cantilever beam subjected to out-of-plane loading at the free end, the bending strain distribution along the beam length is linear. Furthermore, the bending strain is related to the out-of-plane displacement through Equation (4.33). This equation can be evaluated by numerical differentiation methods such as a Savitzky-Golay differentiating filter to obtain the bending strain ($\varepsilon_{xx,SG}$). To evaluate the deviation in the measured bending strain the Root Mean Square Deviation (RMSD) was determine between the measured bending strain ($\varepsilon_{xx,SG}$) and the expected bending strain, evaluated from a least-squares-fit of the displacement data ($\varepsilon_{xx,LS}$). The RMSD in the bending strain was expressed as

$$RMSD = \left[\frac{1}{N}\sum_{i=1}^{N}\left(\varepsilon_{xx,SG,i} - \varepsilon_{xx,LS,i}\right)^2\right]^{1/2} \tag{4.36}$$

where N is the number of measurement points.

The least-squares-fit is found by fitting a third-order polynomial to all measured deflection points. For each experiment, the coefficient of determination of the least-squares-fit was then determined and was found to almost unity ($R^2 \approx 1$), thus showing the third-order polynomial least-squares-fit to be a good approximation.

In order to compare results between the measured ($\varepsilon_{xx,SG}$) and expected ($\varepsilon_{xx,LS}$) bending strain, a variation coefficient of the RMSD in the bending strain (c_{RMSD}) was evaluated by normalising the RMSD in the bending strain by the mean of the measured bending strain ($\bar{\varepsilon}_{xx,SG}$). The variation coefficient of RMSD in the bending strain can be expressed as,

$$c_{RMSD} = \frac{RMSD}{\bar{\varepsilon}_{xx,SG}} \tag{4.37}$$

4.4.4 Savitzky-Golay Differentiation Parameters

When differentiating the measured displacements of a beam to evaluate the bending strain, measurement noise has an adverse affect on the estimate. In order to differentiate, but also filter the measured displacements and accurately estimate the bending strain, a 1D Savitzky-Golay differentiating filter is utilised. The 1D Savitzky-Golay differentiating filter is a convolution filter that needs very little computation time and is well suited to the current application. The main advantage of this differentiating filter is that it generally preserves features of the distribution such as relative maxima, minima and width (Savitzky & Golay 1964; Gorry 1990; Kuo, Wang, H & Pickup 1991). The application of the 1D Savitzky-Golay differentiating filter here essentially performs a local polynomial regression (of degree n) on a distribution of $2m + 1$ points to determine the smoothed value of the r derivative of the beam deflection ($u_{z,i}$) with respect to the length of the

beam (x-direction) for each point. The one-dimensional Savitzky-Golay differentiator has the form (Gorry 1990),

$$f_n^r(t) = \frac{1}{\Delta x^r} \sum_{i=-m}^{m} h_{t,i}^{n,r} \; u_{z,i} \tag{4.38}$$

where Δx is the distance between each data point and $h_{t,i}^{n,r}$ is the convolution weight for data point i, with polynomial order n, and r derivative, evaluated at point t. A detailed explanation of the 1D Savitzky-Golay differentiating filter can be found in Appendix B.1. To evaluate strain using the Savitzky-Golay differentiator is thus,

$$\varepsilon_{xx}(t) = \frac{h}{2} f_n^2(t) \tag{4.39}$$

When deriving bending strain from the measured beam deflection, using a 1D Savitzky-Golay differentiating filter, the accuracy of the derived strain field depends strongly on the number of data points used $(2m + 1)$ and the polynomial order approximation (n). An investigation was conducted into the accuracy of the derived bending strain $(\varepsilon_{xx,SG})$ for varying filter widths $(2m + 1)$ and polynomial orders (n) utilised within the Savitzky-Golay differentiating filter. During this experiment, the aluminium beam specimen was subjected to a 1Hz sinusoidal free end deflection of 50μm via an electromagnetic shaker. In addition, the scan grid consisted of 499 measurement points (N) with a spatial interval (Δx) of 0.97mm was used. Figure 4.26a shows the variation coefficient (c_{RMSD}) of RMSD in the bending strain for a varying number of data points used $(2m + 1)$ in the differentiator with a polynomial approximation of third-order $(n = 3)$. While, Figure 4.26b shows the effect of varying size of the polynomial approximation (n) of the differentiator

while using 151 data points ($m = 75$).

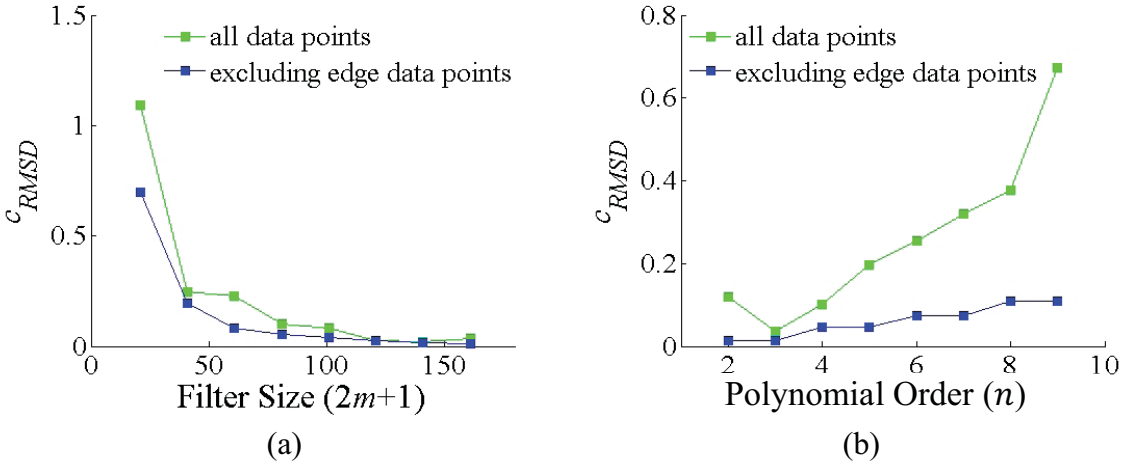

Figure 4.26. Variation coefficient (c_{RMSD}) of RMSD in the bending strain of the aluminium beam specimen versus (a) the number of data points used ($2m + 1$) in the Savitzky-Golay differentiator ($n = 3$) and (b) the polynomial order (n) used in the Savitzky-Golay differentiator ($m = 75$). The aluminium beam specimen was subjected to a maximum free-end deflection of 50μm and the scan grid consisted of 499 points (N) with a spatial interval (Δx) of 0.97mm.

It is seen from Figure 4.26a that the variation coefficient (c_{RMSD}) of the RMSD in the bending strain decreases with an increase of the number of data points used ($2m + 1$) in the Savitzky-Golay differentiator. In addition, Figure 4.26b shows that the strain caused by the deflection of the cantilever beam is best approximated using a third-order polynomial ($n = 3$) Savitzky-Golay differentiator, which was expected as this satisfies the governing differential equation of beam deflection. In other words, a C^3 differentiable function.

The Savitzky-Golay filter introduces artefacts at the edge points of the filter (up to m points in from the boundary nodes). These artefacts are characterised by a deviation from the linear trend of the evaluated strain field at these m points in from the boundary nodes,

the shaded areas seen in Figure 4.27. This is due to the fact that when the bending strain is evaluated at the edge points, the filter becomes asymmetrical. By introducing this asymmetry, the strain approximations are therefore degraded at the edges of the interval compared to the central points. In both Figures 4.26a and 4.26b, the variation coefficient (c_{RMSD}) the RMSD in of the bending strain is larger when the edge points are included. In addition, when the polynomial order (n) within the Savitzky-Golay filter deviates from a third-order polynomial, the edge artefacts become more pronounced.

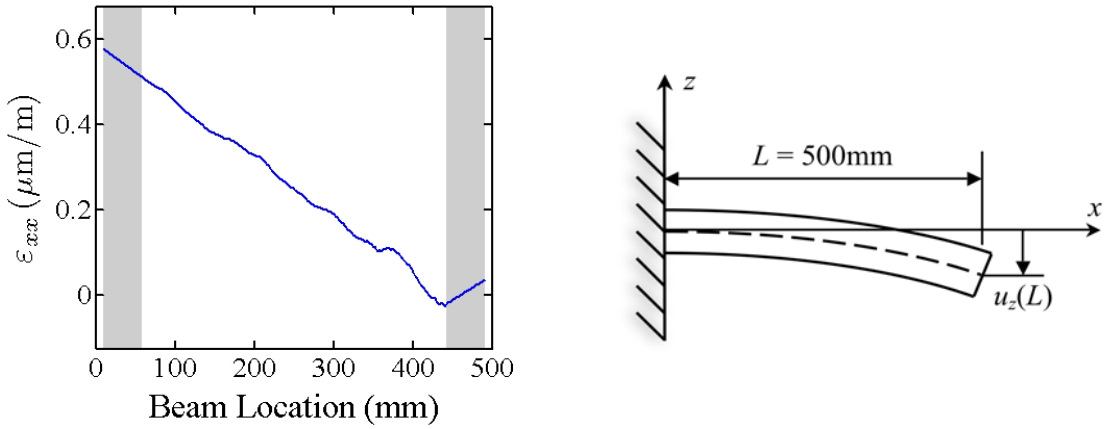

(a) (b)

Figure 4.27. (a) Estimated bending strain ($\varepsilon_{xx,SG}$) on the top of an aluminium cantilever beam using a third-order polynomial ($n = 3$) Savitzky-Golay differentiating filter, utilising 101 data points ($m = 50$). The aluminium beam specimen was subjected to a maximum free-end deflection of 50μm and the scan grid consisted of 499 points (N) with a spatial interval (Δx) of 0.97mm. The shaded area indicates m data points in from the boundary in which edge artefacts occur. (b) Schematic illustration of the deformed cantilever.

The graph in Figure 4.28 shows a close up of variation coefficient evaluated for various number of data points used in the Savitzky-Golay differentiator, which is seen in

Figure 4.26a. When excluding the edge data points, a variation coefficient less than 5.3% was produced when the Savitzky-Golay differentiating filter was of third polynomial order ($n = 3$) and had a filter width greater than 81 data points ($m = 40$), in addition to a maximum free end deflection of 50μm and a scan grid consisted of 499 points with a spatial interval of 0.97mm. This variation coefficient is equivalent to a 13.4 microstrain standard deviation.

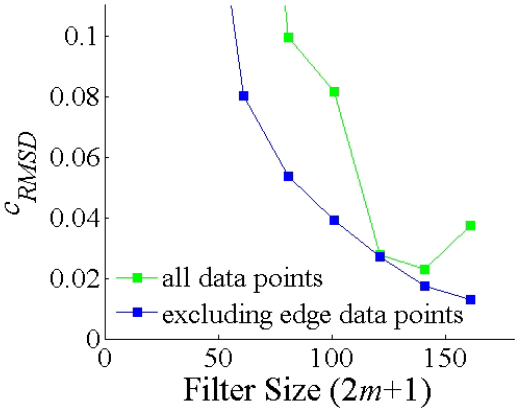

Figure 4.28. Close up of Figure 4.26a to clearly show the variation coefficient (c_{RMSD}) of the RMSD in the bending strain of the aluminium beam specimen versus the number of data points ($2m + 1$) used in the Savitzky-Golay differentiator ($n = 3$) graph for $2m + 1$ greater than 81 data points. The aluminium beam specimen was subjected to a maximum free-end deflection of 50μm and the scan grid consisted of 499 points (N) with a spatial interval (Δx) of 0.97mm.

4.4.5 Mesh Size

The SLDV system allows a maximum limit of 512 measurement points to be used to span the length of the beam specimen. Therefore, a compromise needs to be made between the

spatial interval connecting the measurement points and the number of measurement points that can be used to span the length of the entire beam specimen. In this subsection, the accuracy of the derived bending strain ($\varepsilon_{xx,SG}$) for varying spatial intervals between the measurement points (Δx) is investigated. The aluminium beam specimen was subjected to a 1Hz sinusoidal input with a deflection of approximately 100μm at the end of the beam via an electromagnetic shaker. For each spatial interval (Δx) used, the maximum number of points (N) that could span the length of the specimen was utilised.

Figure 4.29 shows the variation coefficient (c_{RMSD}) of the RMSD in the bending strain evaluated by the Savitzky-Golay differentiation for varying mesh spatial intervals (Δx). For these tests, two cases were considered, to investigate the accuracy of the strain measurement approach. In the first case, a fixed number of data points ($2m + 1$) was used in the Savitzky-Golay differentiator for each spatial interval (Δx), as shown in Figure 4.29a. In the second case, the number of data points ($2m + 1$) used within the Savitzky-Golay differentiator encompassed a fixed distance of approximately 143mm (approximately 30% of the total number of nodes (N) for each spatial interval (Δx)), as shown in Figure 4.29b. For the second case, the number of data points ($2m + 1$) used within the Savitzky-Golay differentiating filter encompassed is tabulated in Table 4.4. A schematic illustrating the scan grid is show in Figure 4.30.

Figure 4.29a (the first case) shows that with a fixed number of data points ($m = 20$) used within the Savitzky-Golay differentiator, the variation coefficient of the RMSD in the bending strain estimate significantly increases as the spatial interval (Δx) decreases. In contrast, in Figure 4.29b (the second case), the variation coefficient is not significantly affected for different spatial intervals (Δx) when the number of data points ($2m + 1$) used

within the Savitzky-Golay differentiator encompasses a fixed distance of approximately 143mm. The tests completed in the second case reveal that the variation coefficient of the bending strain does not vary with size of the spatial interval (Δx) between measurement points, but depends on the distance that spans the number of measurement points ($2m + 1$) used within the Savitzky-Golay filter. Essentially, in the second case, regardless of the size of the spatial interval (Δx) between the measurement points, a specific variation coefficient in the bending strain (c_{RMSD}) can be achieved that is dependent on the distance that encompasses the number of measurement point ($2m + 1$) used in the Savitzky-Golay filter. Therefore, small spatial intervals (Δx) will require a larger number of measurement points ($2m + 1$) to be utilised in the Savitzky-Golay filter to achieve adequate accuracy, which may potentially spatially filter any strain concentrators. However, larger spatial intervals (Δx) may miss strain concentrators completely.

Using Figure 4.29a, the relationship between the variation coefficient of the RMSD in the bending strain (c_{RMSD}) and the ratio of the number of measurement points used within the Savitzky-Golay differentiator to the total number of measurement points available ($\{2m + 1\}/N$) can be determined and is presented in

Table 4.5. This table shows that when the ratio of the number of measurement points used within the Savitzky-Golay differentiator ($2m + 1$) to total number of measurement points (N) is less than 25%, the noise within the strain estimate increases significantly. To achieve a strain estimate with a variation coefficient (c_{RMSD}) of approximately 2.2%, the number of measurement points needed within the Savitzky-Golay differentiator ($2m + 1$) needs to be 25% of the total available number of measurement points (N). This variation coefficient is equivalent to a 12.3 microstrain standard deviation.

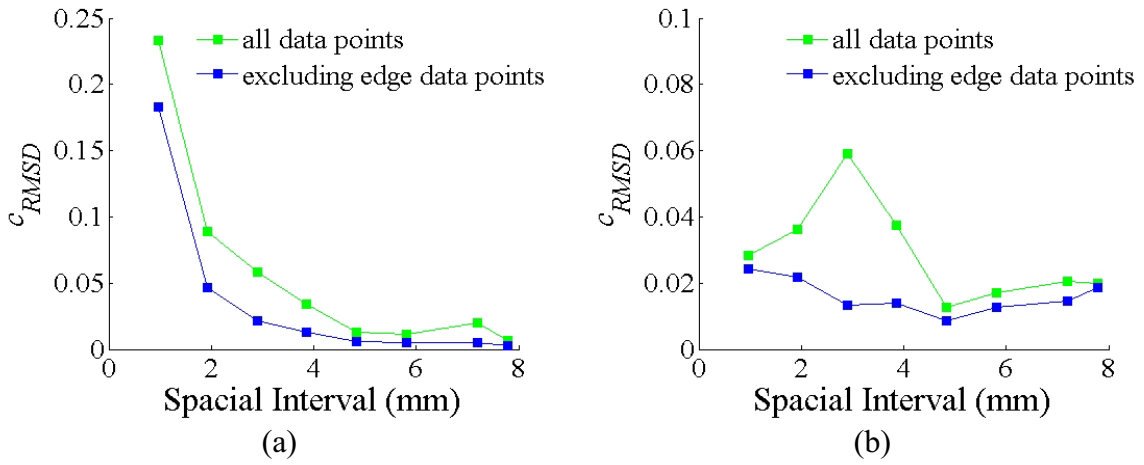

Figure 4.29. Variation coefficient (c_{RMSD}) of the RMSD in the bending strain evaluated using a Savitzky-Golay differentiator versus the spatial interval between measurement points (Δx). The Savitzky-Golay differentiator utilised a third-order polynomial approximation ($n = 3$) with (a) $m = 20$ and (b) $2m + 1$ spanning a fixed distance of approximately 143mm, which equal to approximately 30% of the available nodes for each spatial interval. The aluminium beam specimen was subjected to a maximum free-end deflection of 100μm.

Table 4.4. Illustration of the number of data points ($2m + 1$) required within the Savitzky-Golay differentiating filter to encompass a nominal fixed distance of approximately 143mm for each spatial interval (Δx) investigated.

Spatial Interval, Δx (mm)	Number of Measurement Points, N	$2m + 1$	Encompassed Distance (mm)
0.97	499	151	145.5
1.93	249	75	142.83
2.89	167	51	144.50
3.86	125	37	140.04
4.83	99	31	144.90
5.82	83	25	139.68
7.21	67	21	144.20
7.79	61	19	140.22

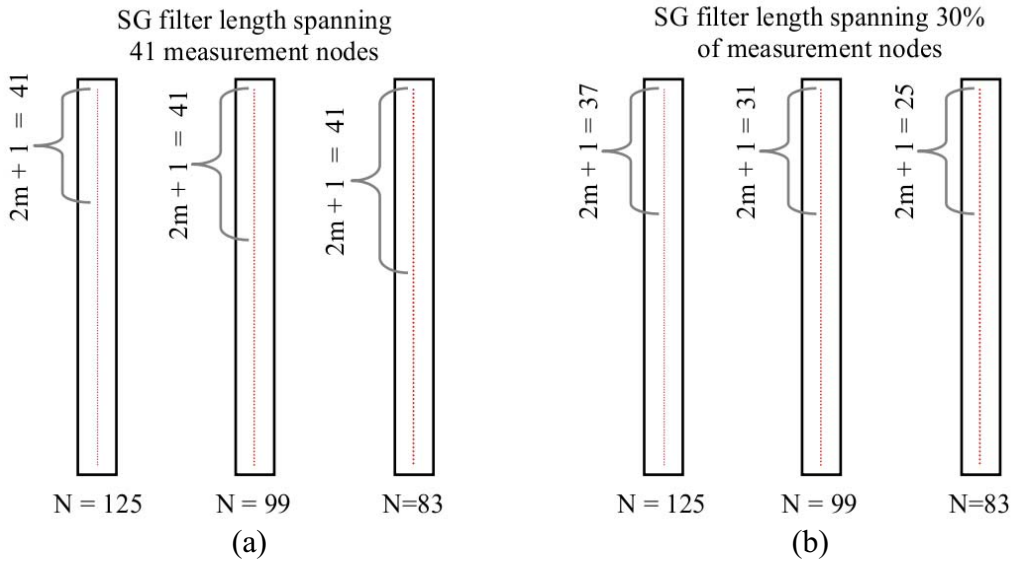

Figure 4.30. Schematic illustration of three scan grids used to evaluate bending strain, with the relative size of the filter length used to evaluate the bending strain. (a) shows the filter length of the Savitzky-Golay filter with a fixed 41 measurement nodes ($m = 20$) for each scan grid density, whereas (b) shows the filter length spanning approximately 30% of the scan grid length ($2m + 1 = 0.3N$) for each scan grid density.

Table 4.5. Relationship between the variation coefficient of RMSD in the bending strain (c_{RMSD}) in Figure 4.29a to the ratio of the number of measurement points used ($2m + 1 = 41$) within the Savitzky-Golay filter and total number of measurement points (N).

Spatial Interval, Δx (mm)	Number of Measurement Points, N	$\frac{2m+1}{N}100\%$	c_{RMSD} (all data points)		c_{RMSD} (excluding edge data points)	
			%	με	%	με
0.97	499	8.4%	22.3	129	18.3	106
1.93	249	16.9%	7.9	44.7	4.5	25.6
2.89	167	25.1%	5.1	28.6	2.2	12.3
3.86	125	33.6%	3.4	18.6	1.3	6.9
4.83	99	42.4%	1.3	7.2	0.6	3.5
5.82	83	50.6%	1.1	6	0.5	2.9
7.21	67	62.7%	1.5	8.6	0.4	2.4
7.79	61	68.9%	0.6	3.4	0.3	1.4

4.4.6 Out-of-plane Loading Amplitude

The accuracy of the derived bending strain using a Savitzky-Golay differentiator was investigated for varying amplitude deflections applied to the end of the aluminium cantilever beam. The spatial interval (Δx) between the measurement points was set to approximately 1mm, spanning a total distance of 500mm, which produced 499 nodal points. Figure 4.31 shows the variation coefficient (c_{RMSD}) of the RMSD in the bending strain evaluated at different amplitudes of deflection applied to the end of the cantilever beam. This figure shows that the amplitude of the deflection of the cantilever beam between 5μm to 160μm has no effect on the accuracy of the derived bending strain using the Savitzky-Golay differentiating filter. There is one outlying point in this figure that occured when the variation coefficient of the RMSD in the bending strain measurement was evaluated using all the data points specifically for the 75 mm maximum deflection of the cantilever beam. This outlier is most likely due to noise in the measured data in the vicinity of either end of the beam, as the variation coefficient evaluated excluding the edge data points does not show the same trend.

4.4.7 Summary of Bending Strain Measurement

This section has presented investigations into the accuracy of measuring quasi-static bending strain using a 1D scanning laser Doppler vibrometer and a 1D Savitzky-Golay differentiating filter. The accuracy of the estimated bending strain can be significantly affected by the parameters of the strain calculation technique, which include the Savitzky-Golay differentiation parameters and spatial interval between measurement points, as well as the stress amplitude.

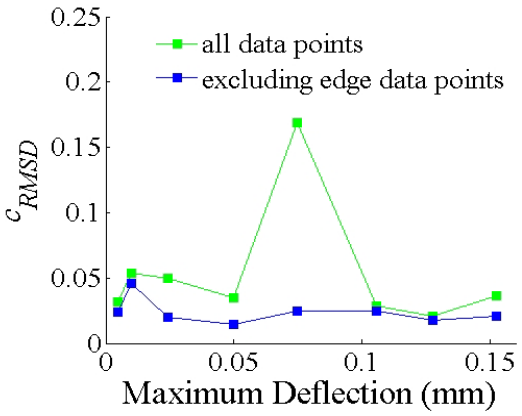

Figure 4.31. Variation coefficient (c_{RMSD}) of the RMSD in the bending strain versus maximum deflection experienced by the beam where $n = 3$ and $m = 75$. The scan grid consisted of 499 points (N) with a spatial interval (Δx) of 0.97mm.

From the investigations into the affect of these parameters on the accuracy of estimated bending strains, it was found that:

1. when the polynomial order utilised within the Savitzky-Golay filter deviated from third-order (the theoretical polynomial order required to define the deflection of a cantilever beam with a point load), there is a significant increase in the variation coefficient and edge artefacts.

2. the variation coefficient of the RMSD in the estimated bending strain does not depend on the number of measurement points used within the Savitzky-Golay filter, but on the distance which they span along the beam.

3. the amplitude of the applied load and size of the spatial interval were found to have little affect on the variation coefficient of the RMSD in the bending strain estimate.

To accurately detect variations in bending strain along a beam for the test arrangement that was utilised, the optimal parameters include:-

- a Savitzky-Golay differentiating filter with a third-order polynomial fit ($n = 3$), to;

- a filter width ($2m + 1$) of approximately 20% of the available measurement points and;
- a spatial interval (Δx) between the measurement points that is sufficient to resolve variations in the strain field.

For instance, with $n = 3$, $2m + 1$ approximately 20% of the available measurement points, and $\Delta x = 1$mm; the standard deviation of the evaluated bending strain was 2% of the fitted bending strain at the middle measurement point ($\varepsilon_{xx,LS,(N+1)/2}$).

4.5 Summary

In this chapter the accurate evaluation of bending and extensional strains were demonstrated using a 1D and 3D scanning Doppler laser vibrometer, respectively. The contributing factors to errors in measured displacement when using 1D and 3D SLDV systems were discussed, including perturbations in the movement of the object from external sources and the finite accuracy of the laser beam position to a point on the measurement object.

Two scenarios were considered for the measurement of strain:- the evaluation of bending strains from measured out-of-plane displacements and extensional strain from measured in-plane-displacements. Bending strain was evaluated from out-of-plane displacements along the mid-line of an aluminium cantilever beam, which were measured using a 1D vibrometer, while extensional strains were evaluated from a grid of measured in-plane displacements on a uniaxial loaded acrylic plate using the 3D SLDV system. For both scenarios the effect that mesh size, the parameters of the numerical method and loading amplitude have on the accuracy measured strains was investigated.

The numerical parameters of the Savitzky-Golay filter largely affected the accuracy of the measured strain. For both, the evaluated bending and extensional strains, a third-order polynomial ($n = 3$) approximation was found to give the best fit. To provide accurate extensional strain results, a filter width of 13 data points ($m = 6$) was required. However, for bending strains, accurate results could be produced for any spatial interval, as long the filter width spanned a fixed distance.

When investigating the effect of the spatial interval between scan points, on the accuracy of measured strain, the variation coefficient of the in-plane surface strain measurements was observed to sharply increase for mesh intervals less than 1.5mm. However, for the bending strain measurements, the variation coefficient was found to be independent of the spatial interval between the measurement points and primarily dependent on distance spanning the number of points used within the Savitzky-Golay filter.

As expected, from these experiments the applied stress amplitude was also found to have little effect on the accuracy of the evaluated bending and extensional strain. In addition, the spatial interval did not limit the accuracy for measurement of bending strain, however, when measuring extensional surface strains, the spatial interval was limited to a minimum value. This is due the finite accuracy of the three-dimensional alignment of the 3D vibrometer, which defines the position of the three laser beams at a point in space.

Finally, an investigation was conducted to validate that extensional strains can be successfully evaluated in the vicinity of stress concentrators. Two scenarios were considered, an edge crack and a 90° notch. The evaluated surface strains were compared with FE simulations and were shown to be in good agreement, however the edges of the strain filed distribution, m data points in from the edge were significantly affected by

artefacts created by the Savitzky-Golay differentiating filter. These SLDV strain measurement techniques have many advantages over other strain measurement techniques, such as strain gauges, and can be utilised in applications where high resolution and accurate strain measurements are required. Table 4.6 presents a comparison between a number of common techniques used to evaluate strain fields.

Table 4.6. Comparison of common strain measurement techniques.

Technique	Point / Full Field	Band Width (kHz)	Spatial Resolution	Accuracy	Strain Resolution	Source
Strain Gauge	P	>100	N/A	>2%	με	(Dally & Riley 2005)
Moiré	FF	<100	>40μm	>4%	mε	(Sciammarella 1982)
Holography	FF	<100	>40μm	>9%	με	(Ennos 1968)
Speckle	FF	<100	>40μm	> 6με	με	(Moore & Tyrer 1996)
Digital Image Correlation	FF	<100	1 pixel	5με to 100με	με	(Siebert et al. 2007)
3D SLDV	FF	>100	1mm	> 2%	nε	

The following points relating to 3D SLDV strain measurement techniques when compared to the other techniques, can be noted from Table 4.6:

- All of the strain measurement techniques can provide a full-field strain measurement, with the exception of the strain gauge;
- The 3D SLDV strain measurement technique can provide dynamic strain measurements up to a bandwidth of 350kHz, where as the majority of other full-

field strain measurement techniques utilise a camera that limits the bandwidth to less than half the frame rate of the camera;

- The spatial resolution of the 3D SLDV strain measurement technique for this study was found to be limited to a 1mm, whereas the other full-field strain measurement techniques could provide much greater spatial resolution;
- The accuracy of the 3D SLDV strain measurement technique was comparable to that of a strain gauge;
- Potentially the 3D SLDV strain measurement techniques presented in the chapter can measure down to nano-strain, whereas the other techniques can only measure down to microstrain.

Chapter 5. Detection of Crack Damage

This chapter presents an investigation into a newly proposed algorithm for the detection of crack damage in a plate experiencing in-plane loading. This algorithm is based on the governing differential equation (GDE) of in-plane deformations (*GDEP* algorithm) and is evaluated by differentiating the in-plane displacements measured using a 3D scanning laser Doppler vibrometer with a 2D Savitzky-Golay differentiating filter (Appendix B.2). The potential of this algorithm for detecting damage was compared against another two algorithms. The first is an algorithm based on the error in smoothed to measured displacements (*displacement error* algorithm) and the other uses surface strains normalised by their mean (*surface strain* algorithm).

To investigate the efficiency of the algorithms in detecting crack damage, a number of acrylic plate specimens were fabricated with three crack damage scenarios; an edge crack, centre crack and crack propagating from a V-notch (as seen in Figure 5.1 and discussed in Section 3.2.2). A range of crack lengths were tested to determine the effectiveness of the algorithms, which are tabulated in Table 3.2 in Section 3.2.2. The plate specimens were sinusoidally loaded in tension with a 1Hz signal, to ensure that the displacements were quasi-static, with an approximate peak to peak load of 200N. The resulting three-dimensional displacement fields were measured using a 3D vibrometer (PSV-400-3D). For each test, the surface displacements were measured on a square mesh of 39 x 39 points with a spatial mesh interval of approximately 2mm (seen in Figure 5.1), thus covering an

area of approximately 76mm x 76mm.

Within this study, similar results were observed for each damage scenario and, therefore, the investigation of the three algorithms presented in this chapter will only focus on one of the three damage scenarios, namely a crack propagating from a notch. Results obtained for the edge crack and centre crack studies are discussed briefly in Appendix D.

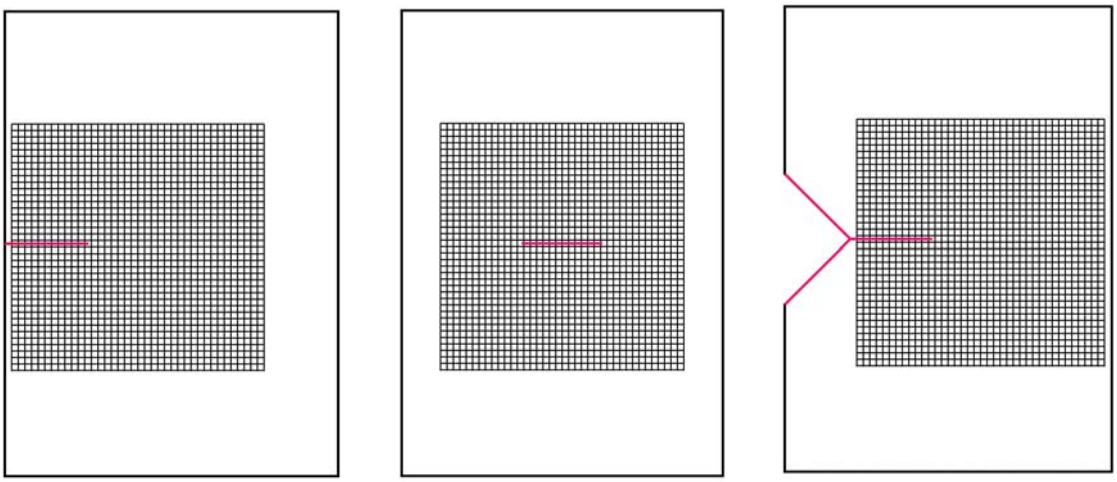

Figure 5.1. Measurement grids used for (a) edge crack, (b) centre crack and (c) crack with a notch.

This Chapter is intended as a preliminary study into the development of damage detection algorithms based on fundamental principles of kinematics of deformation. Only a pilot investigation into the potential of these algorithms in detecting moderately sized cracks (i.e. 5 mm, 10 mm, 15 mm, 20 mm and 25 mm) with the aid of 3D scanning laser Doppler vibrometry (SLDV) technology has been conducted. It is not intended to be an all inclusive study and further research will be required to identify the sensitivity of the algorithms to the cracks length, as well as the direction of the applied load.

5.1 Previous Studies

While there are a multitude of different techniques that are used to detect crack damage (for example ultrasonic, radiographic and eddy-current testing), this study focuses on the use of SLDV for the detection of crack damage. Therefore, this section will discuss alternate SLDV techniques specifically focusing on the detection of crack damage in plates.

Staszewski et al. (2007) investigated the use of 3D SLDV for sensing lamb waves propagating in a thin aluminium plate, in order to detect a 41.05 mm fatigue crack within the plate. Using a 3D vibrometer, a scan area of 60 × 110 mm2 (420 scan points) was utilised to measure the three-dimensional transient velocity response of the plate, at each scan point, from Lamb waves induced by a piezoceramic actuator, as seen in Figure 5.2. In their study, they looked at the transient velocity response of Lamb waves created by a piezoceramic actuator excited at 75 kHz, 325 kHz and 190 kHz. The 75 kHz excitation produced an A_0 out-of-plane Lamb wave mode, the 325 kHz excitation produce an S_0 in-plane Lamb wave mode, while the 190 kHz excitation frequency produced both A_0 and S_0 Lamb wave modes with the same velocity amplitude.

They first investigated the peak-to-peak amplitude of the three-dimensional transient Lamb wave response at all scanned grid points for different instances in time, after the plate had been excited. Figure 5.3 presents the three-dimensional transient response of the plate, for selected instances in time, from the piezoceramic actuator exciting the plate with a 75 kHz frequency. As expected, they observed that the strongest pattern created by the damage was in the out-of-plane direction, Figure 5.3(c), as the 75 kHz frequency primarily excites

the A_0 out-of-plane Lamb wave mode. For all excitation frequency ranges (including 190 kHz and 325 kHz), they found that once the wave hits the crack, areas of locally increased wave amplitude were observed in front of the crack, while there was an attenuation of the wave behind the crack.

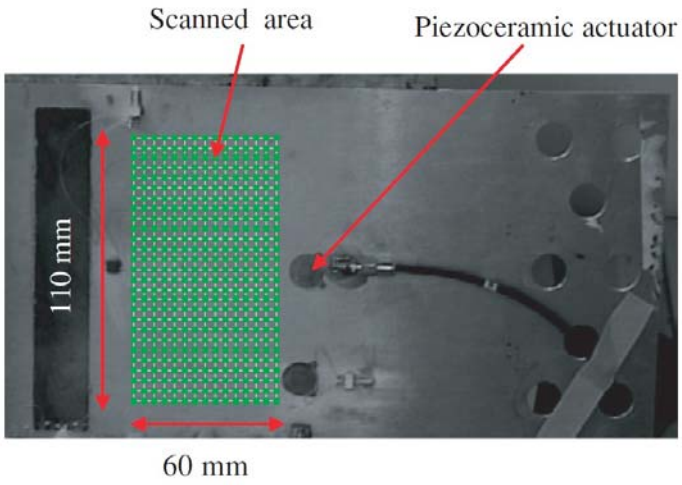

Figure 5.2. Laser scanned area with indicated data grid points used for Lamb wave sensing (Staszewski, Lee, B & Traynor 2007).

Further, they looked at the Root-Mean-Square (RMS) amplitude of in-plane and out-of-plane Lamb wave components for all scanned grid points for the excitation frequencies of 75 kHz, 325 kHz and 190 kHz. Figure 5.4 presents an example of the RMS velocity amplitude contour plot for the in-plane and out-of-plane directions when the plate was excited with a 75 kHz frequency excitation. They found that the contour plots for the in-plane components exhibit a locally increased amplitude in front of the centre of the crack, which can be seen in Figure 5.4(a and b). For the out-of-plane *z*-direction component

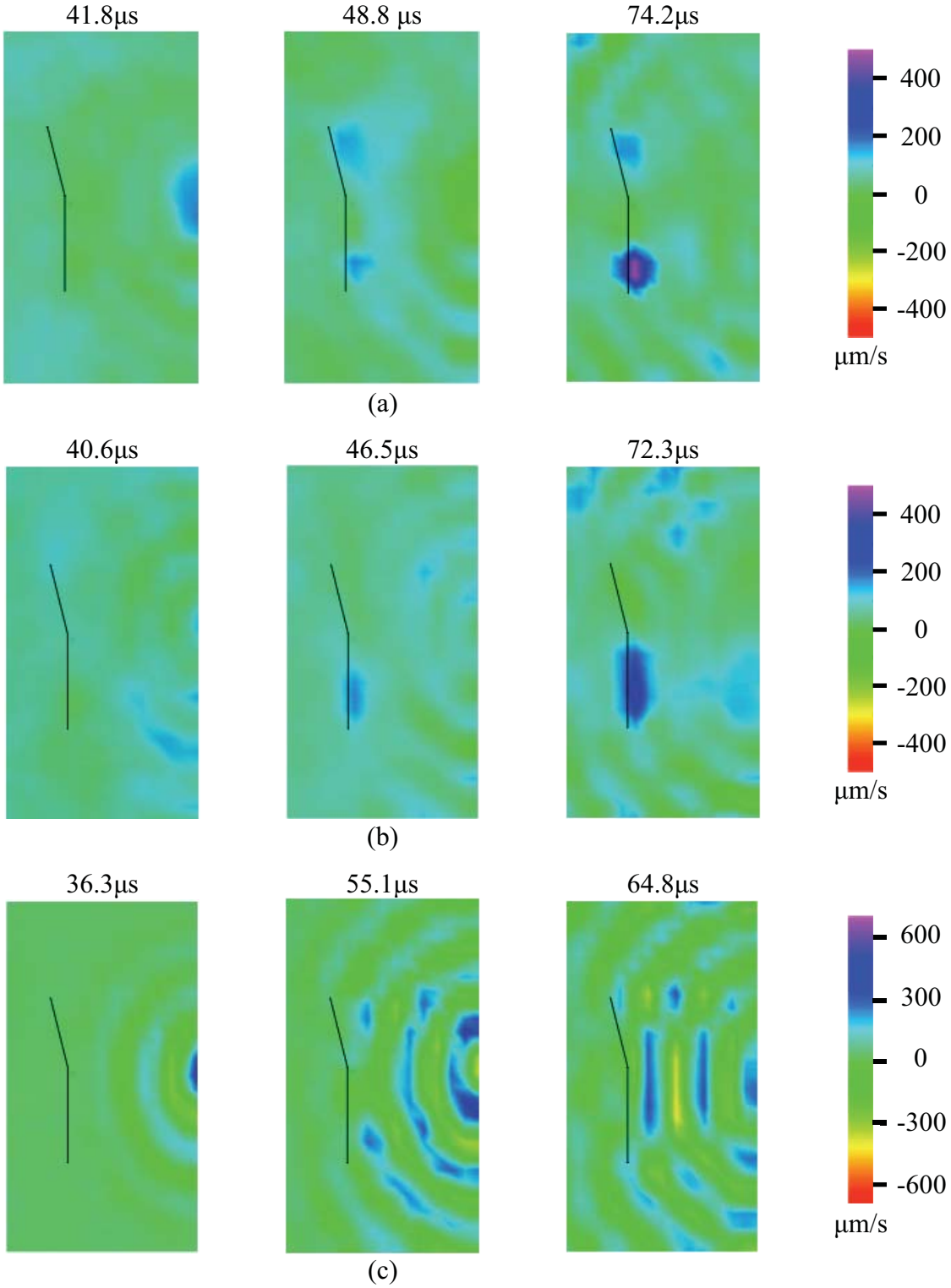

Figure 5.3. Lamb wave propagation contour plots in the time domain for 75 kHz excitation:- (a) in-plane x-direction, (b) in-plane y-direction and (c) out-of-plane z-direction (Staszewski, Lee, B & Traynor 2007).

(Figure 5.4(c)), the RMS velocity amplitude contour plot was observed to increase near the centre of the crack and attenuated in the area to the left of the crack (i.e. area behind the crack with respect to the actuator).

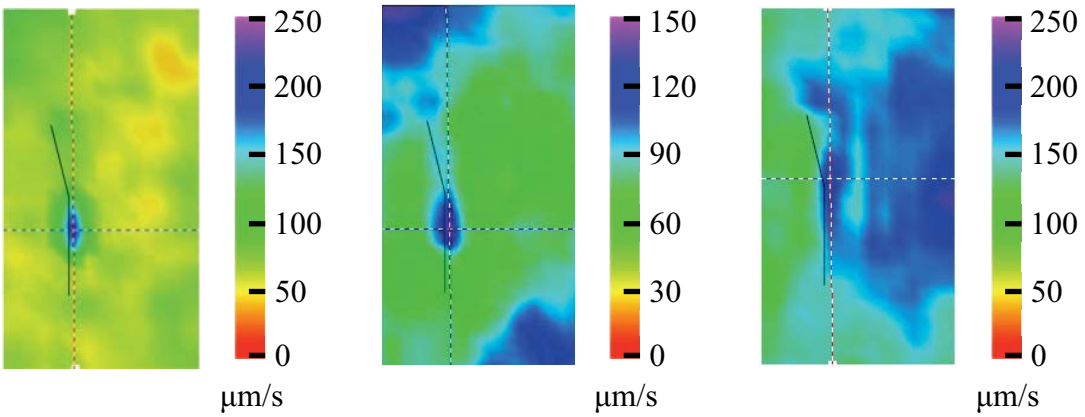

Figure 5.4. RMS amplitude contour plots for 75 kHz Lamb wave propagation (a) in-plane x-direction, (b) in-plane y-direction and (c) out-of-plane z-direction (Staszewski, Lee, B & Traynor 2007).

Staszewski et al. (2007) found that using 3D SLDV for the measurement of Lamb waves induced in a plate, and investigating the peak-to-peak and RMS velocity amplitude of the waves, was effective in the identification of the location of a fatigue crack. They stated that undamaged baseline measurements can be avoided, as the locally increased velocity amplitude of Lamb wave responses in the proximity of the crack, measured by the 3D SLDV, clearly identifies the crack damage with minimal signal processing. In addition, they also mentioned that the method also has the potential to estimate the severity of the crack.

5.2 Principles of Deformation in Thin Plates

This section will discuss the fundamental principles of Solid Mechanics, which can be utilised as a basis for Non-Destructive Evaluation (NDE) techniques to inspect flat plates subjected to in-plane deformations. Firstly, a description of the equations of equilibrium, strain compatibility and general governing equation of displacement for thin plates subjected to extensional deformations is provided. Finally, the application of these principles and equations for detecting mechanical damage will be discussed. This background theory is necessary for setting the foundations of this chapter.

5.2.1 Equations of Equilibrium

The conditions of equilibrium govern how stress varies from point to point within a stressed body (Chou & Pagano 1992). Mathematically, the conditions of equilibrium require that the summations of the forces and the moments at an arbitrary point are both equal to zero.

To illustrate the principle of equilibrium of a plate with in-plane loading, consider a small element $[dx, dy]$ of a plate, subject to body forces (F_x and F_y), normal stresses (σ_x and σ_y) and shear stress (τ_{xy}), as seen in Figure 3.2. As the element is considered to be small, the stress components can be assumed to be distributed uniformly over each face.

The equations of equilibrium of forces in the x- and y-direction are

$$\frac{\partial \sigma_{xx}}{\partial x} + \frac{\partial \tau_{xy}}{\partial y} + F_x = 0 \tag{5.1}$$

$$\frac{\partial \sigma_{yy}}{\partial y} + \frac{\partial \tau_{xy}}{\partial x} + F_y = 0 \tag{5.2}$$

The two equations of equilibrium can be rewritten in a combined form, by differentiating Equation (5.1) by x and Equation (5.2) by y and summing them together (Timoshenko & Goodier 1970, p. 24). Assuming that the body forces (F_x and F_y) are negligible, the combined form of the equations of equilibrium is given by,

$$2\frac{\partial^2 \tau_{xy}}{\partial x \partial y} = -\frac{\partial^2 \sigma_{xx}}{\partial x^2} - \frac{\partial^2 \sigma_{yy}}{\partial y^2} \tag{5.3}$$

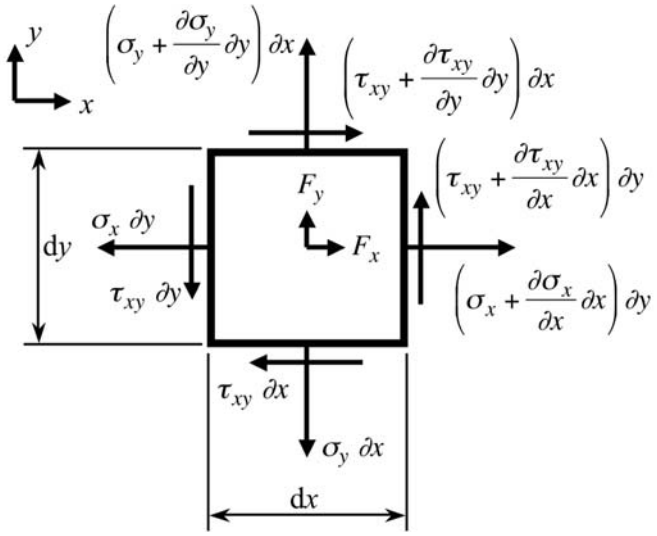

Figure 5.5. Forces acting on a small element $[dx, dy]$ of a plate in which stresses vary from point to point.

Introducing plane stress Hooke's law gives the combined equilibrium conditions in terms of strains, and can be expressed as,

$$\frac{\partial^2}{\partial x^2}\left(\varepsilon_{xx} + \nu\varepsilon_{yy}\right) + (1-\nu)\frac{\partial^2 \gamma_{xy}}{\partial x \partial y} + \frac{\partial^2}{\partial y^2}\left(\varepsilon_{yy} + \nu\varepsilon_{xx}\right) = 0 \tag{5.4}$$

where ν is Poisson's ratio.

5.2.2 Strain Compatibility

The relationship between strain and displacement is represented by six equations of compatibility, which are presented in Appendix A. These equations establish the geometrically possible form of strains varying from point to point within a continuous body. Physically, the principle of strain compatibility implies how a deformed body must be pieced together with no gaps, overlaps or other discontinuities, as shown in Figure 5.6. These equations were first derived by Saint-Venant (1870) and are widely used in the theory of continuum mechanics, in particular in the theory of elasticity.

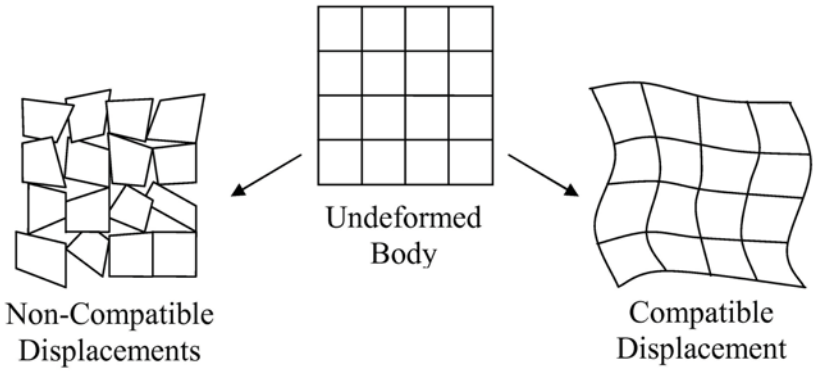

Figure 5.6. Illustration of strain compatibility principle.

For plates subjected to in-plane loading, the out-of-plane strain is a function of the in-plane strain components (i.e. $\varepsilon_{zz} = -\nu\left(\varepsilon_{xx} + \varepsilon_{yy}\right)$) and the out-of-plane shear strain component

are close to zero (i.e. $\gamma_{xz} = 0$ and $\gamma_{yz} = 0$). Thus, the six compatibility equations are reduced to

$$\frac{\partial^2 \varepsilon_{yy}}{\partial x^2} + \frac{\partial^2 \varepsilon_{xx}}{\partial y^2} = \frac{\partial^2 \gamma_{xy}}{\partial x \partial y} \tag{5.5}$$

which describes the continuous deformation in a plate.

This equation holds for isotropic and anisotropic materials, and plates experiencing elastic and non-elastic deformation.

5.2.3 Governing Differential Equation

A general GDE of surface strains can be evaluated for a thin plate with extensional deformation by equating the shear strain components of the equilibrium equation (5.4) and strain compatibility equation (5.5). The result is found to be,

$$\nabla(\varepsilon_{xx} + \varepsilon_{yy}) = 0 \tag{5.6}$$

and for a 1D plate this equation reduces to,

$$\frac{\partial^2 \varepsilon_{xx}}{\partial x^2} = 0 \tag{5.7}$$

By incorporating Equations (4.11) and (4.12) into the Equation (5.6), the GDE can be rearranged in terms of in-plane displacement components (u_x and u_y) and expressed as,

$$\frac{\partial^3 u_x}{\partial x^3} + \frac{\partial^3 u_x}{\partial x \partial y^2} + \frac{\partial^3 u_y}{\partial y^3} + \frac{\partial^3 u_y}{\partial x^2 \partial y} = 0 \tag{5.8}$$

An important feature to highlight regarding the GDE of in-plane displacement is that it is

independent of applied forces. This allows the GDE of in-plane displacement to be evaluated purely from measured plate displacements, without having to know the forces applied to the plate.

5.2.4 Application of GDE to Damage Detection

All damage detection techniques are based on a physical phenomena or principle that accompanies the damage evolution. Discussed in this section are the principles of extensional deformation in an undamaged, uniform, thin plate. At every discrete point on a plate structure (damaged or undamaged), the GDE of displacement is satisfied. However, to evaluate the GDE from measured displacements, a numerical differentiation process is required and is usually achieved by fitting a selection of data points to a specific degree of polynomial. Therefore, through the numerical process it must then be assumed that the GDE of displacement is satisfied over the entire area of the fitted data points. If damage occurs between any of the fitted points, this would produce a violation in the GDE of displacement over the area of the fitted points, which would enable the detection of the crack damage.

In this chapter, a new damage detection algorithm is proposed based on the GDE of displacement for the detection of crack damage within a plate structure. In addition, to evaluate the effectiveness of the GDE algorithms in detecting damage, commonly used damage detection algorithms are evaluated. These include the error in estimated-to-expected strain and the use of the error in the filtered-to-measured displacements.

As stated previously, to evaluate the GDE for in-plane displacements at a point on a plate structure from measurements of in-plane displacements, a number of neighbouring points

utilised in a numerical differentiation technique is required. Therefore, a discontinuity (i.e. due to a crack) in the measured displacements from point-to-point will produce a residual term for the GDEs. The residual term for the GDE of in-plane displacements on a plate (R_I) is expressed as,

$$R_I = \frac{\partial^3 u_x}{\partial x^3} + \frac{\partial^3 u_x}{\partial x \partial y^2} + \frac{\partial^3 u_y}{\partial y^3} + \frac{\partial^3 u_y}{\partial x^2 \partial y} \tag{5.9}$$

By using a number of neighbouring measurement points to evaluate the GDE, it is assumed that there are no cracks, voids or other discontinuities in between these measurement points. When crack damage occurs between the measurement points, the damage is then detectable if the evaluated residual term of the GDE for in-plane displacements is non-zero.

In order to evaluate the effectiveness of the proposed algorithm based on the GDE of in-plane displacement, two basic algorithms based on the evaluated strain and measured displacement fields were utilised. These are discussed in the following paragraphs.

A crack within a structure will generate large displacements between the faces of the crack relative to the plate displacement. If the crack lies within the measurement grid, a large discontinuous change in measured displacement will be observed on either side of the crack. Therefore, by applying a smoothing filter, which fits a specific polynomial order to a number of measured displacement points, a localised divergence from the measured displacements will be observed at the location of the discontinuous change in measured displacement (crack location). If a crack is present within the measurement grid, the difference in fitted ($u_{i,SG}$) to measured ($u_{i,m}$) displacements should indicate the presence of

the discontinuity and thus detect the crack damage. The displacement error ($\hat{u}_i$) can be expressed as,

$$\hat{u}_i = u_{i,SG} - u_{i,m} \tag{5.10}$$

where i is either x or y, m refers to the measured displacements and SG refers to the Savitzky-Golay smoothing filter used in this study to smooth the measured displacements.

The second comparative algorithm is based on the in-plane surface strain field. Utilising the numerical differentiation process that fits a specific polynomial order to a number of measurement points, it is assumed that there is no discontinuities within the plate surface strain field. Therefore, if a crack lies within the measurement grid, the surface strain estimated from this grid will show a large discontinuous change in strain across the crack faces, which will identify the location of the crack. To evaluate the in-plane surface strains of a vibrating plate with uniform loading, the first derivative of the measured points of in-plane displacement need to be calculated. A numerical differentiation processes can be utilised to estimate the in-plane surface strain ($\varepsilon_{ij,SG}$) at a point on a plate. To be able to remove load scaling effects, this estimated surface strain ($\varepsilon_{ij,SG}$) of the plate can then be mean centred, by subtracting the mean of the estimated in-plane strain ($\bar{\varepsilon}_{ij,SG}$). The centred surface strain ($\hat{\varepsilon}_{ij}$) can be expressed as,

$$\hat{\varepsilon}_{ij} = \varepsilon_{ij,SG} - \bar{\varepsilon}_{ij,SG} \tag{5.11}$$

where i and j are either x or y, $\gamma_{xy} = 2\varepsilon_{xy}$.

5.3 GDE of Plate Displacement Algorithm

For a plate oscillating at frequency within its stiffness controlled region, the GDE of in-plane plate displacement is given by Equation (5.8) and is satisfied at every point on the plate. To evaluate the GDE at a point on a structure using measurements of displacement, a number of neighbouring measurement points are required within the Savitzky-Golay differentiating filter. The filter is constructed under the assumption that there are no cracks, voids or other discontinuities in the vicinity or between these measurement points. Therefore, if a crack intersects any two neighbouring points used within filter, the large displacements that occur between the faces of the crack will violate the GDE and produce a non-zero residual term (R_I). This will be known as the *GDEP* algorithm and is expressed by Equation (5.9). A threshold value, Φ_I, that is greater than the noise floor of the evaluated GDE of plate displacement may then be used to identify the location and path of the crack damage,

$$|R_I| < \Phi_I \tag{5.12}$$

In the following experimental results a Savitzky-Golay differentiating filter utilising a 3rd order polynomial ($n = 3$) over a distribution of 5x5 points ($m = 2$) was employed to differentiate the measured in-plane displacements ($u_{x,m}$ and $u_{y,m}$) to determine the residual term (R_I) (Equation(5.9)). Again, the smallest possible filter and polynomial order was utilised to prevent the damage location being spatially smoothed over a large area. Figure 5.7 presents a flow diagram showing the filter process involved in evaluating the residual term of the GDE of displacement.

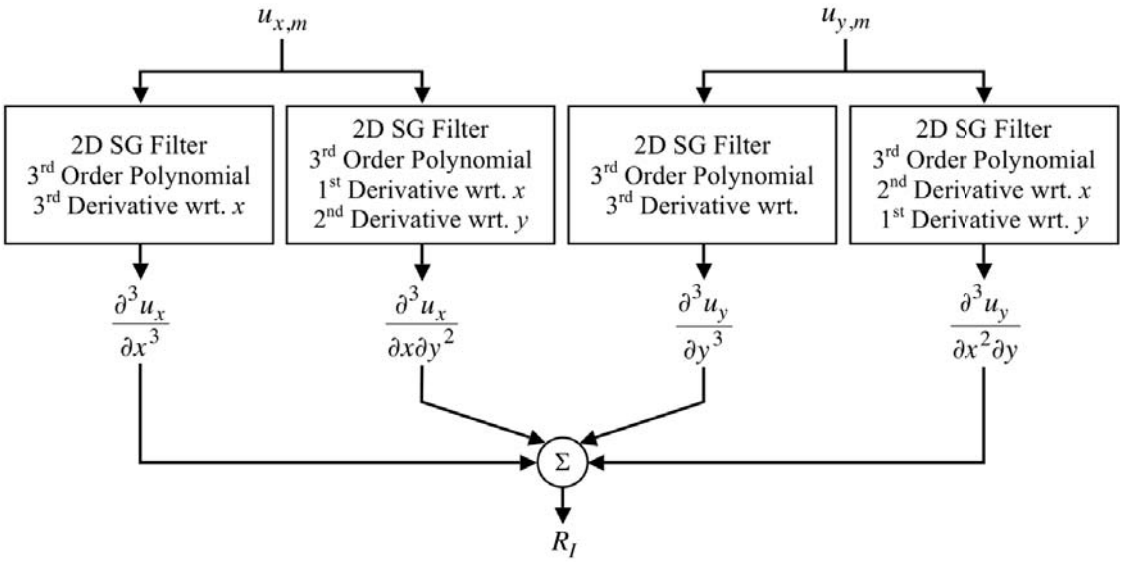

Figure 5.7. Flow diagram of the *GDEP* algorithm R_I.

The *GDEP* algorithm was then applied to the test specimens with a crack propagating from a notch, in order to identify the location and path of the crack. A threshold value was selected that was approximately equal to the noise level in the residual term. The threshold value was set as 200m^{-3}. Figure 5.8 shows the residual term of the governing equation for a plate specimen with a crack of various lengths propagating from a V-notch. The dark blue and dark red areas in the figure represent the locations where the residual term has exceeded the threshold. At $x = 0$ and $x = 100$ are the edges of the plate and the pink line defines the location of the notch and crack. A 3rd order polynomial ($n = 3$) 2D Savitzky-Golay differentiating filter was used with a filter size of 5x5 point ($m = 2$). The notch without a crack (Figure 5.8a) has no effect on the residual of the governing equation. However, the 5mm crack propagating from the notch causes the governing equation to exceed the threshold value along the crack length, thus allowing the location and length of the crack to be detected.

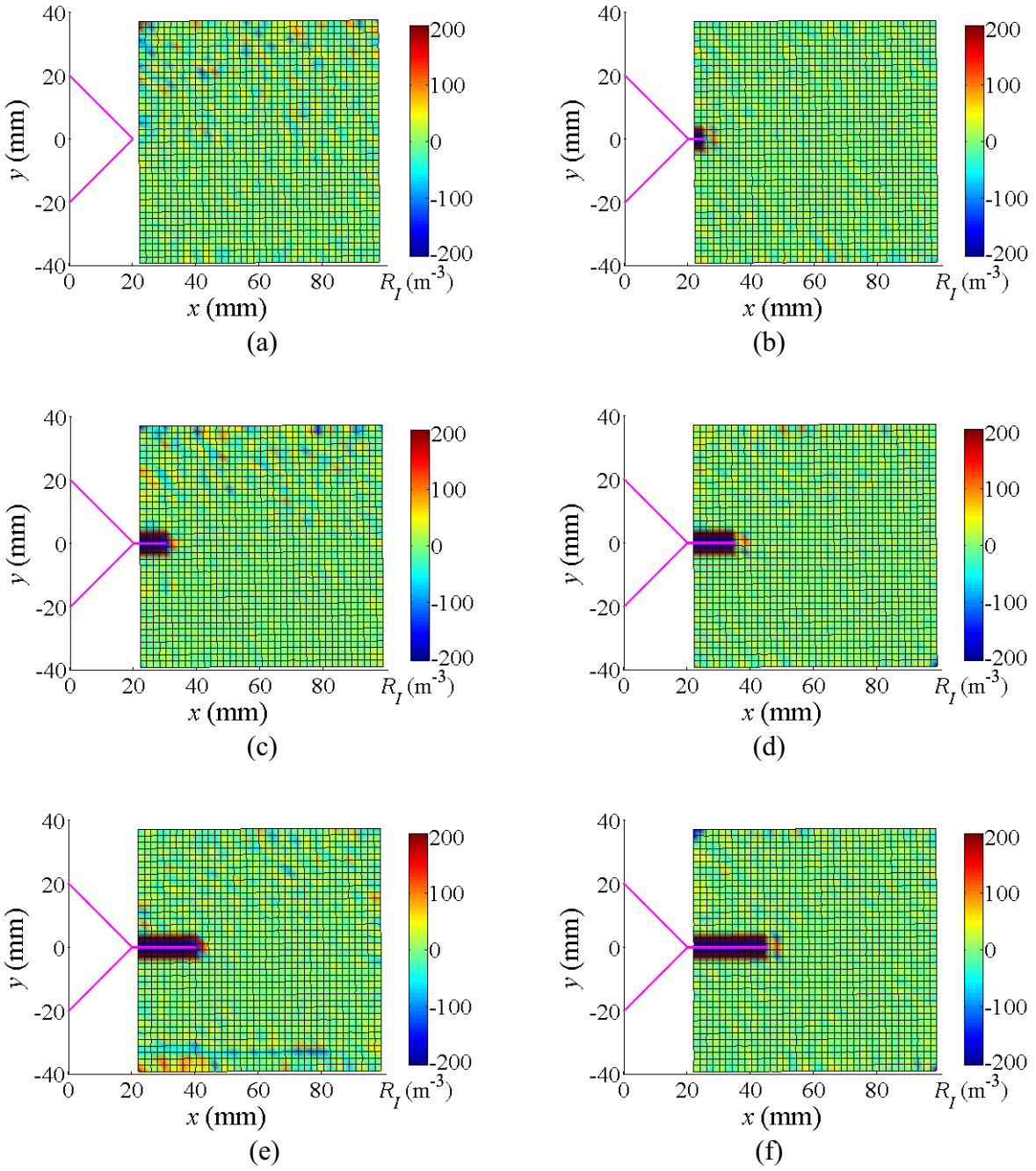

Figure 5.8. Acquired residual term of the GDE (R_I) for a notch with various crack lengths:- (a) 0 mm, (b) 5 mm, (c) 10 mm, (d) 15 mm, (e) 20 mm and (f) 25 mm. The dark blue and dark red areas on the graph represent the location where R_I has exceeded the threshold $\Phi_i = 200\text{m}^{-3}$. At $x = 0$ and $x = 100$ represents the edges of the plate and the pink line defines the location of the notch and crack. A 1st order polynomial ($n = 1$) 2D Savitzky-Golay smoothing filter was used with a filter size of 5x5 point ($m = 2$).

5.4 Displacement Error Algorithm

When a crack is loaded in mode I, a large displacement will occur between the crack faces. If the crack is located within the scan grid, the 2D Savitzky-Golay smoothing filter will spatially smooth the large displacement created by the crack opening. When comparing the raw measured displacement against the smoothed displacement, there will be a difference between the two along the large displacement created by the cracking opening, thus identifying the crack. A *displacement error* algorithm ($\hat{u}_x$ and $\hat{u}_y$) was developed that compares the raw measured displacement ($u_{x,m}$ and $u_{y,m}$) against the measured displacement smoothed ($u_{x,SG}$ and $u_{y,SG}$) using a 2D Savitzky-Golay smoothing filter ($r = 0$) and is expressed by Equation (5.10). Therefore, a threshold value (Θ_i) of the displacement error that is larger than the noise floor can then be used to detect the location and path of the crack within the measurement grid. The threshold of the displacement error is expressed as,

$$|\hat{u}_i| > \Theta_i \tag{5.13}$$

The smoothed in-plane displacements ($u_{x,SG}$ and $u_{y,SG}$) were obtained using a moving 1st order polynomial ($n = 1$) Savitzky-Golay smoothing filter ($r_x = 0$ and $r_y = 0$), with a size of 3x3 points ($m = 1$). The polynomial order and filter size were selected such that the filter can smooth over the smallest possible filter area, thus allowing the damage to be more accurately located. Utilising a larger filter size could obscure the location of the damage, as the filter would spatially smooth the large discontinuous displacement over the area of the filter. A flow diagram of how the *displacement error* algorithm is implemented is illustrated in Figure 5.9.

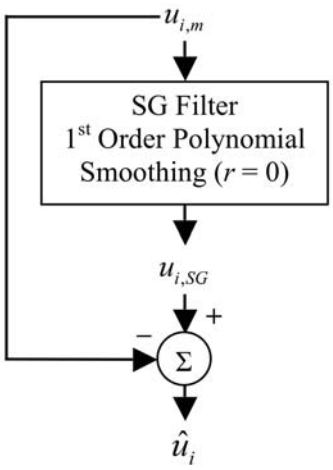

Figure 5.9. Flow diagram of the *displacement error* algorithm $\hat{u}_i$.

The *displacement error* algorithm was then applied to the test specimens with a crack propagating from a notch, for various crack lengths. A threshold value (Θ_i) of 0.7μm was selected, which was above the ambient noise in the displacement error. Figures 5.10 and 5.11 present the results for the displacement error in the x-direction ($\hat{u}_x$) and y-direction ($\hat{u}_y$), respectively. The dark blue and dark red areas on the graph represent the locations where the displacement error has exceeded the threshold. The results for the plate specimen without a crack are given in Figures 5.10a and 5.11a. The displacement error fields were observed not to be affected by the notch. For a 5mm crack propagating from the notch (Figures 5.10a and 5.11a), the crack will lie 3 mm inside the measurement grid. The x- and y-displacement errors both were able to identify the damage and the approximate the length of the crack. However, the x-displacement error does not produce a large enough error to reach the specified threshold, whereas the y-displacement error exceeds the threshold along the entire length of the crack. A higher performance of the y-displacement error is to be expected, as the specimen is loaded in the y-axis and majority

of the displacement associated with the crack will be in this direction. For longer cracks, the *displacement error* algorithm is able to successfully identify the damage and approximate the length of the crack. However, in Figure 5.11e there is a localised increase in y-displacement error below the crack, which does not show up in the x-displacement error (Figure 5.10e). This localised irregularity was presumably due to a localised measurement noise that occurred during the scan.

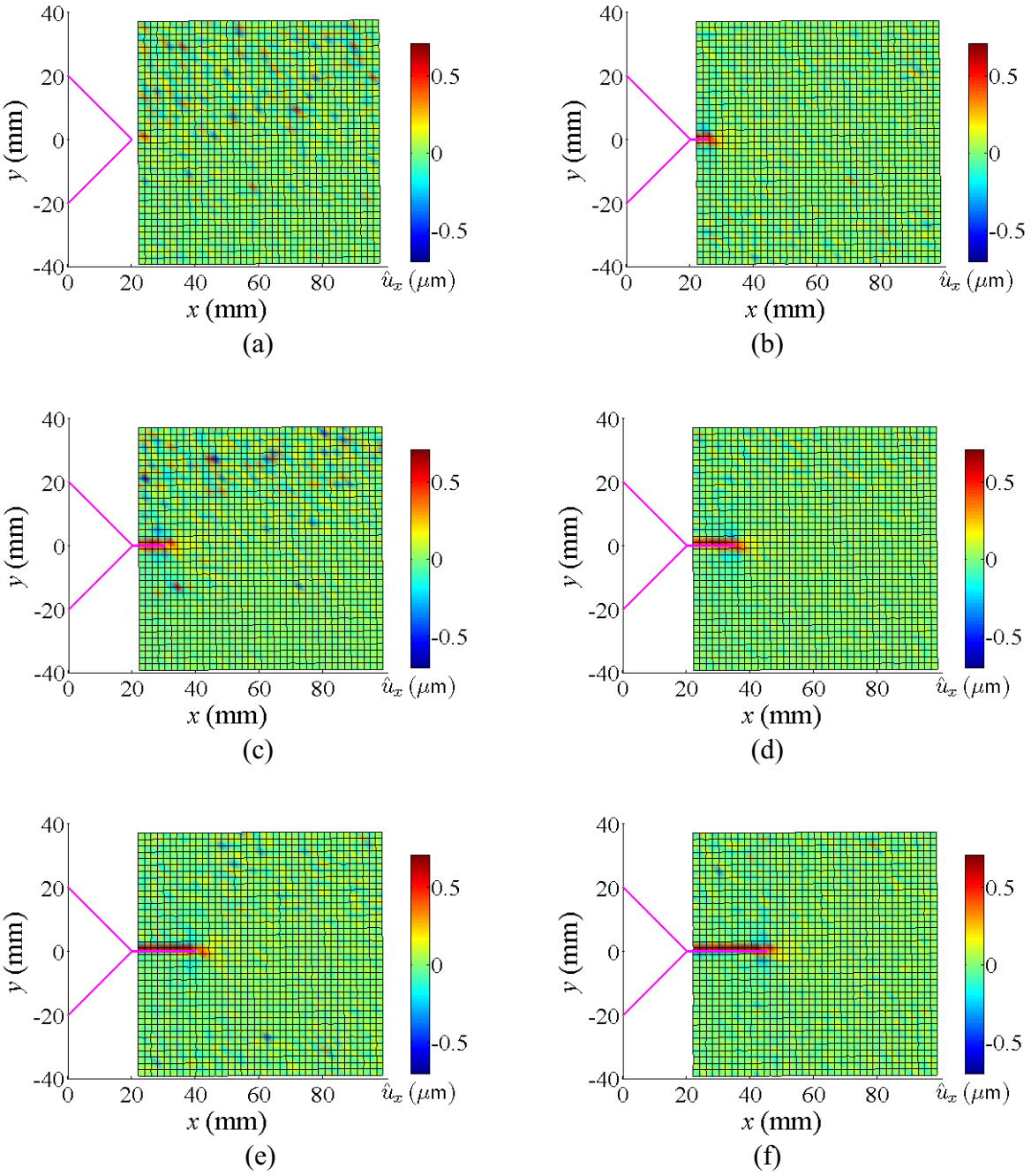

Figure 5.10. Acquired displacement error in the x-axis ($\hat{u}_x$) for a notch with various crack lengths:- (a) 0mm, (b) 5mm, (c) 10mm, (d) 15mm, (e) 20mm and (f) 25mm. The dark blue and dark red areas on the graph represent the location where $\hat{u}_x$ has exceeded the threshold $\Theta_x = 0.7\mu m$. At $x = 0$ and $x = 100$ represents the edges of the plate and the pink line defines the location of the notch and crack. A 1st order polynomial ($n = 1$) 2D Savitzky-Golay smoothing ($r_x = r_y = 0$) filter was used with a filter size of 3x3 point ($m = 1$).

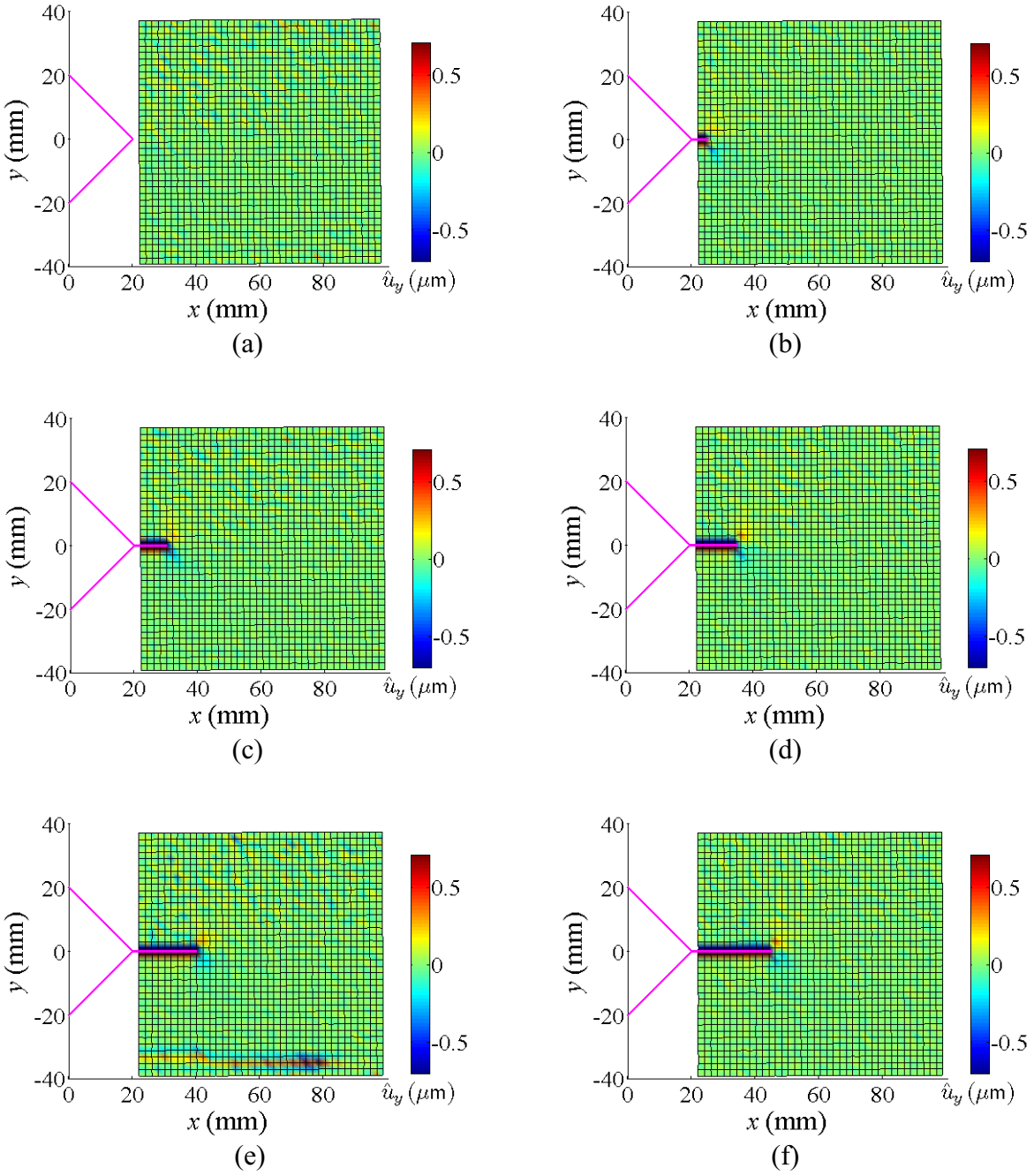

Figure 5.11. Acquired displacement error in the y-axis ($\hat{u}_y$) for a notch with various crack lengths:- (a) 0mm, (b) 5mm, (c) 10mm, (d) 15mm, (e) 20mm and (f) 25mm. The dark blue and dark red areas on the graph represent the location where $\hat{u}_y$ has exceeded the threshold $\Theta_y = 0.7$μm. At $x = 0$ and $x = 100$ represents the edges of the plate and the pink line defines the location of the notch and crack. A 1st order polynomial ($n = 1$) 2D Savitzky-Golay smoothing ($r_x = r_y = 0$) filter was used with a filter size of 3x3 point ($m = 1$).

5.5 Surface Strain Algorithm

As discussed previously, a crack loaded in mode I will produce a large displacements across the crack faces. When evaluating the surface strain with a Savitzky-Golay differentiating filter, it is assumed that surface under investigation is free of discontinuities, such as cracks. Therefore, when a crack is situated within the measurement grid, the large discontinuous displacements created between the crack faces will cause the Savitzky-Golay differentiating filter to evaluate large strains between the crack faces. A *surface strain* algorithm ($\hat{\varepsilon}_{ij}$) was developed that mean centres the surface strain evaluated using a 2D Savitzky-Golay differentiating filter ($\varepsilon_{ij,SG} - \bar{\varepsilon}_{ij,SG}$) and is expressed as Equation (5.11). Using a threshold value (Ψ_{ij}) of the mean centred surface strain, the location and path of the crack within the measurement grid can be observed. The threshold of the surface strain is expressed as:

$$\left|\hat{\varepsilon}_{ij}\right| > \Psi_{ij} \tag{5.14}$$

The surface strains (ε_{xx}, ε_{yy} and γ_{xy}) were evaluated using a moving 2nd order polynomial ($n = 2$) 2D Savitzky-Golay differentiating filter with a size of 3x3 points ($m = 1$). Similar to the *displacement error* algorithm, the polynomial order and filter size were selected such that the filter could differentiate the displacement measurements to evaluate the surface strains, while keeping the filter size as small as possible. Figure 5.12 shows a flow diagram of the how the *surface strain* algorithm is evaluated.

When applying the *surface strain* algorithms ($\hat{\varepsilon}_{xx}$, $\hat{\varepsilon}_{yy}$ and $\hat{\gamma}_{xy}$) to the test specimens with a crack extending from a notch, an appropriate threshold value (Ψ_{ij}) was selected in order

to identify the large discontinuous strain caused by the crack. The threshold value selected for the mean centred surface strain was 400nm/m. Figures 5.13, 5.14 and 5.15 present the results of the *surface strain* algorithm for the x-strain ($\hat{\varepsilon}_{xx}$), y-strain ($\hat{\varepsilon}_{yy}$), and shear strain ($\hat{\gamma}_{xy}$), respectively. The dark blue and dark red areas in the figures represent the location where the mean centred surface strains have exceeded the threshold.

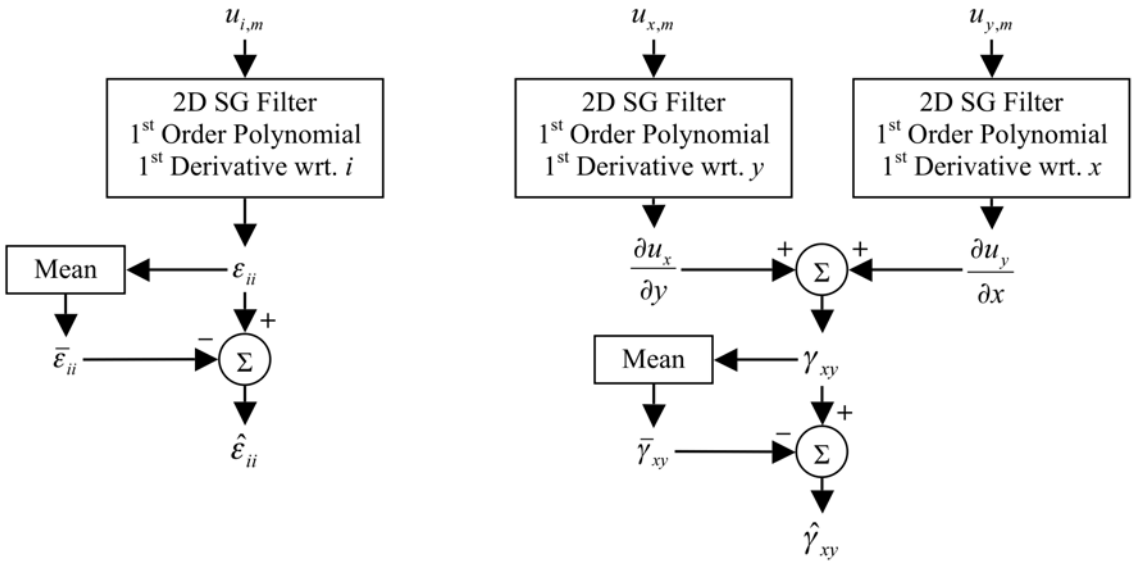

Figure 5.12. Flow diagram of the *surface strain* algorithm for (a) normal strains $\hat{\varepsilon}_{ii}$ and (b) shear strain $\hat{\gamma}_{xy}$.

Figure 5.13 shows that the mean centred x-strain faintly identifies the crack tip, however the mean centred x-strain does not exceed the threshold value. The crack tip location can be identified by the positive strain to the left and right of the crack tip and negative strain above and below. The mean centred y-strain distribution in front of the notch without a crack is presented in Figure 5.14a, which shows a positive increase in mean centred strain

in front of the notch tip, however the threshold was not exceeded. For the 5mm crack (Figure 5.14b), which intersects the measurement grid, the mean centred surface strain threshold was exceeded and matched closely to the location and size of the crack damage. For all of the crack lengths, the mean centred mean strain threshold was exceeded over the whole length of the crack. Characteristically, the mean centred y-strain distribution has a positive normalised strain in front of the crack tip, negative mean centred strain behind the crack tip and the threshold is exceeded across the crack with a positive mean centred y-strain.

Figure 5.15 shows the shear strain distribution in the vicinity of the notch without a crack. The shear strain does not exceed the threshold, however, the shear strain exceeds threshold with a crack length of 5mm. For the rest of the crack lengths it is possible to detect the location of the crack tip via the shear strain and the crack location is characterised by a small localised positive strain above and localised negative strain below the crack tip that both exceed the threshold value.

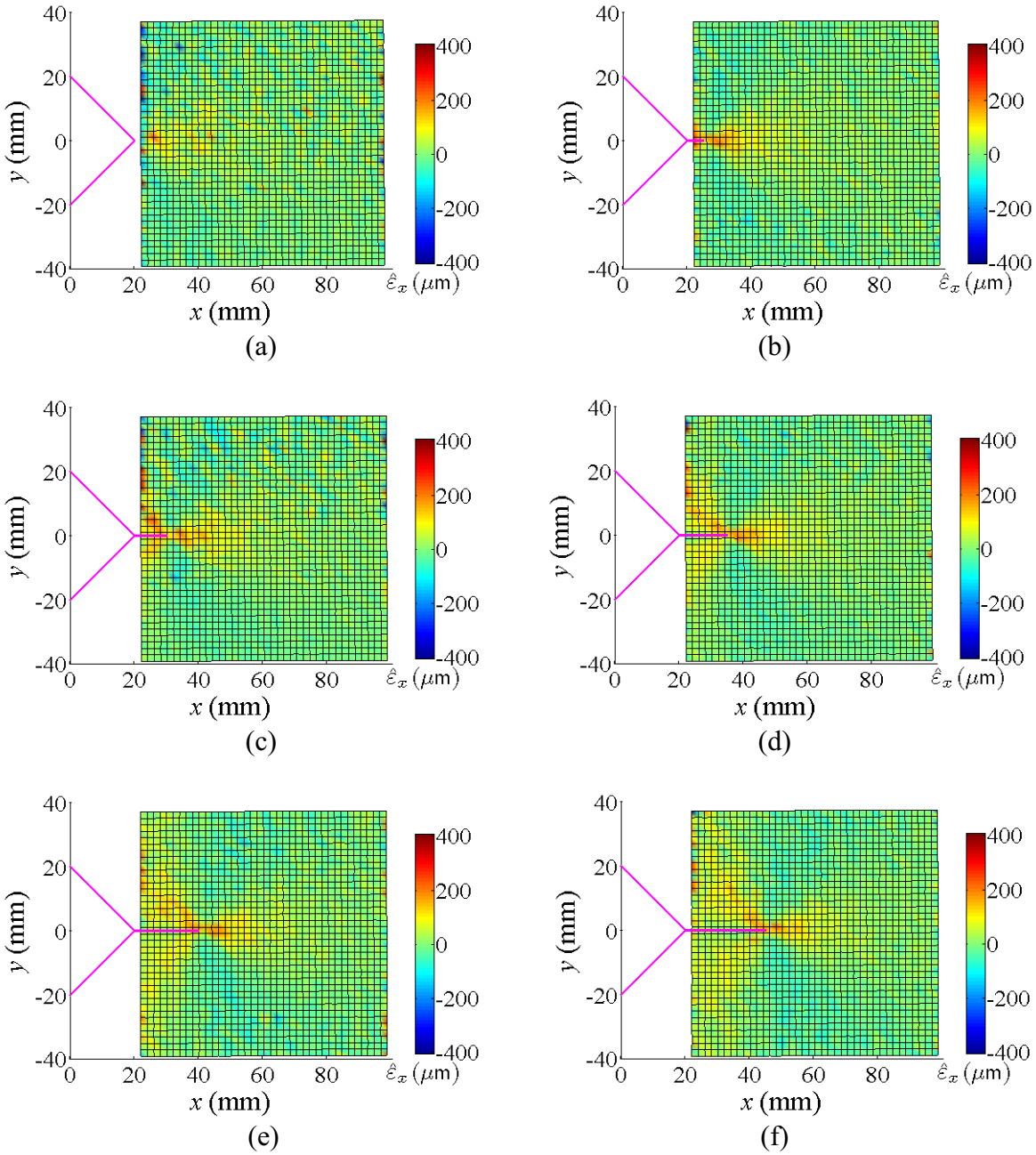

Figure 5.13. Acquired mean centred surface strain in the x-axis ($\hat{\varepsilon}_{xx}$) for a notch with various crack lengths:- (a) 0mm, (b) 5mm, (c) 10mm, (d) 15mm, (e) 20mm and (f) 25mm. The dark blue and dark red areas on the graph represent the location where $\hat{\varepsilon}_{xx}$ has exceeded the threshold $\Psi_{xx} = 400$μm/m. At $x = 0$ and $x = 100$ represents the edges of the plate and the pink line defines the location of the notch and crack. A 2nd order polynomial ($n = 2$) 2D Savitzky-Golay differentiating filter was used with a filter size of 3x3 point ($m = 1$).

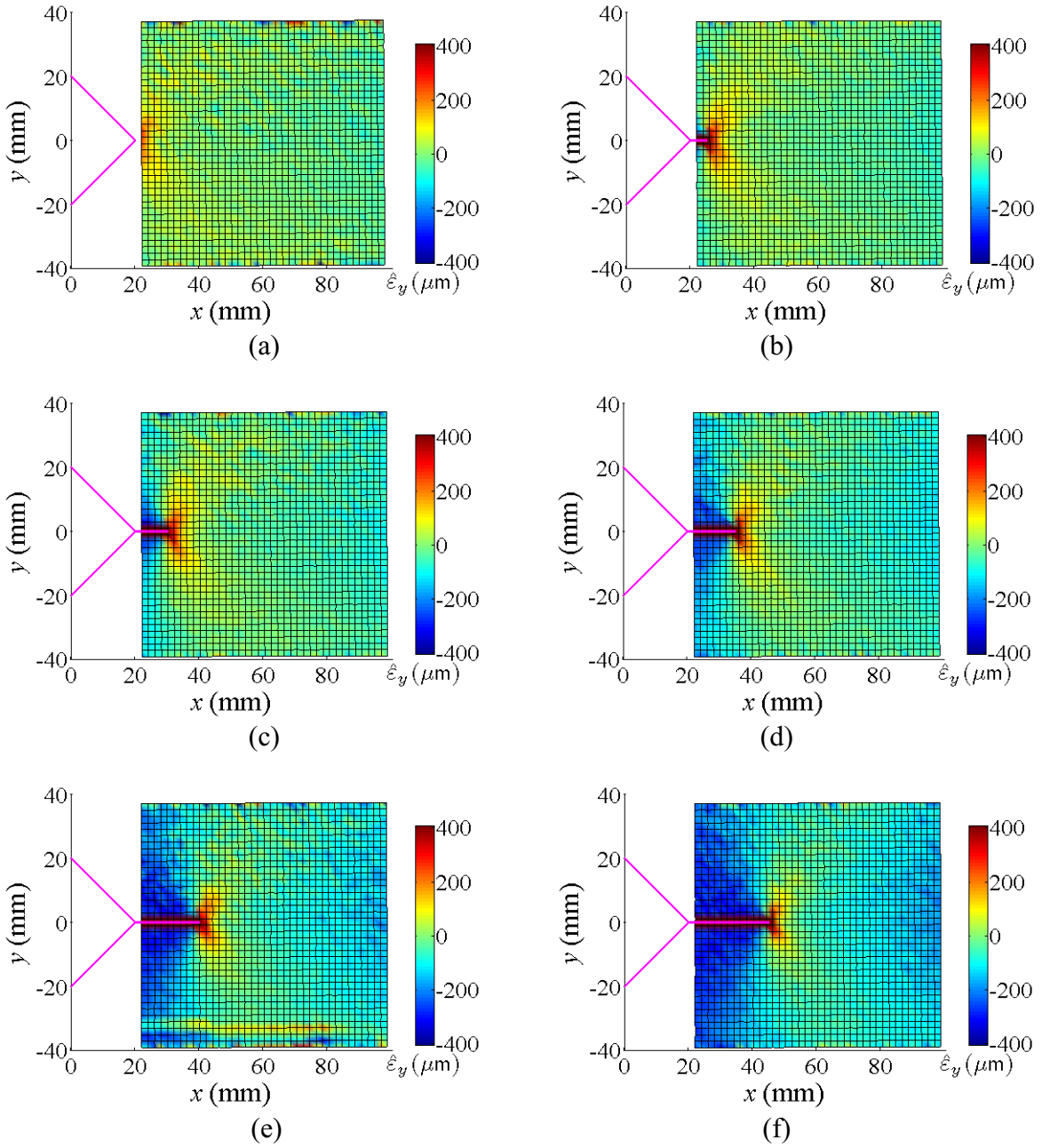

Figure 5.14. Acquired mean centred surface strain in the y-axis ($\hat{\varepsilon}_{yy}$) for a notch with various crack lengths:- (a) 0mm, (b) 5mm, (c) 10mm, (d) 15mm, (e) 20mm and (f) 25mm. The dark blue and dark red areas on the graph represent the location where $\hat{\varepsilon}_{yy}$ has exceeded the threshold $\Psi_{yy} = 400$μm/m. At $x = 0$ and $x = 100$ represents the edges of the plate and the pink line defines the location of the notch and crack. A 2nd order polynomial ($n = 2$) 2D Savitzky-Golay differentiating filter was used with a filter size of 3x3 point ($m = 1$).

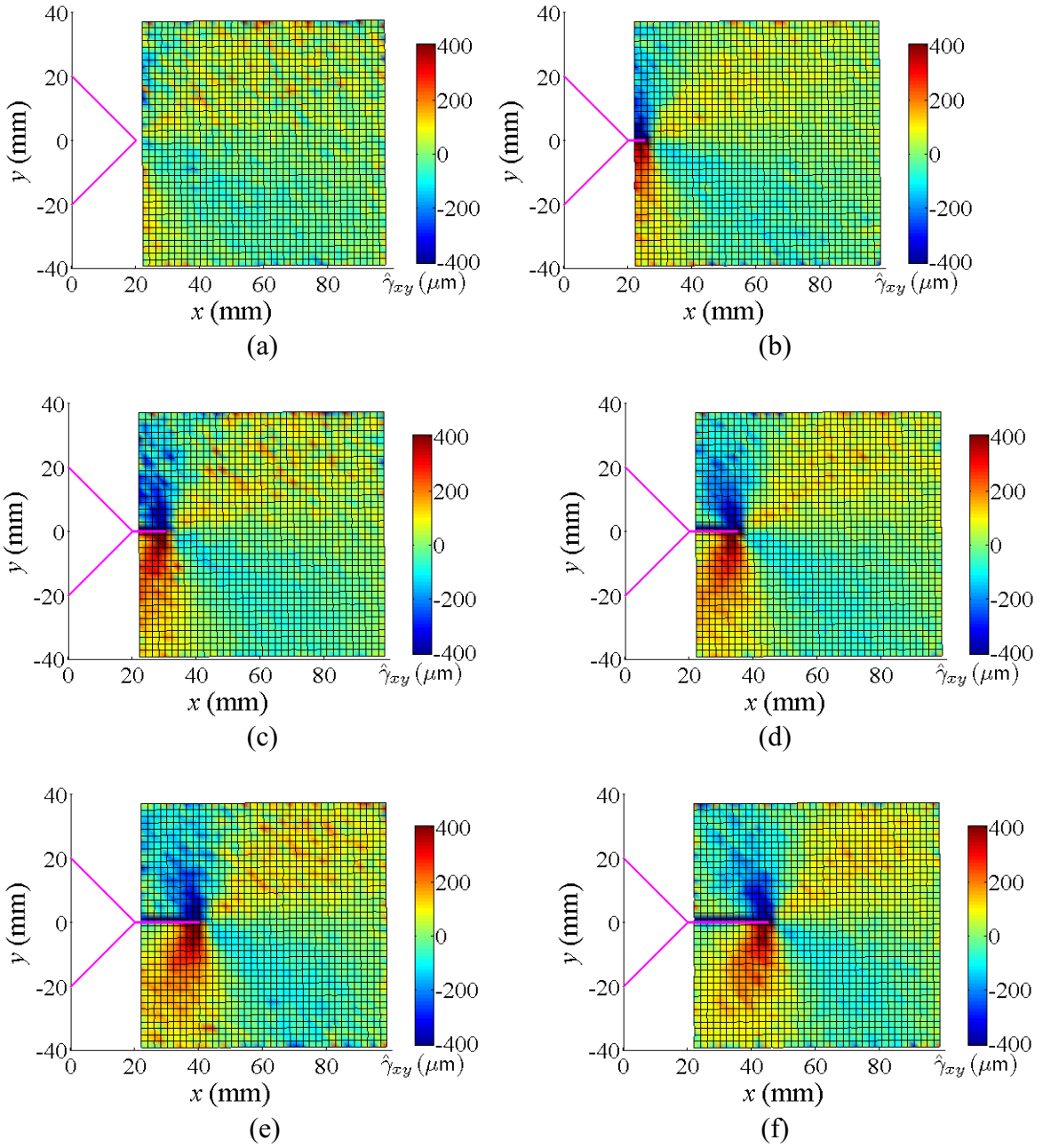

Figure 5.15. Acquired mean centred surface shear strain ($\hat{\gamma}_{xy}$) for a notch with various crack lengths:- (a) 0mm, (b) 5mm, (c) 10mm, (d) 15mm, (e) 20mm and (f) 25mm. The dark blue and dark red areas on the graph represent the location where $\hat{\gamma}_{xy}$ has exceeded the threshold $\Psi_{xy} = 400$μm/m. At $x = 0$ and $x = 100$ represents the edges of the plate and the pink line defines the location of the notch and crack. A 2nd order polynomial ($n = 2$) 2D Savitzky-Golay differentiating filter was used with a filter size of 3x3 point ($m = 1$).

5.6 Summary

A new algorithm was developed for the detection of crack damage in plate structures based on the GDE for in-plane deformation of a Plate (*GDEP* algorithm). The potential and effectiveness of the algorithm for the identification of crack damage was investigated using a 3D vibrometer and was evaluated through the use of a 2D Savitzky-Golay differentiating filter. In order to evaluate the effectiveness of the *GDEP* algorithm, two additional algorithms were developed for comparative purposes that utilise 3D SLDV displacement measurements and are able to be computed using a 2D Svaitzky-Golay differentiating filter. These algorithms were based on basic kinematics principles of deformation, including displacements (*displacement error* algorithm) and surface strain (*surface strain* algorithm).

An experimental investigation was conducted to evaluate the implementation of these algorithms for the detection of crack damage in plate structures. Using a 3D vibrometer, the in-plane displacement fields in vicinity of notched acrylic plate specimens were measured. A crack was extended from the tip of the notch, such that the crack would lie with in the measurement grid of the scanning laser. To determine whether the crack was detected, a threshold level was selected for each algorithm, which was chosen just above the noise level.

The aim of the first experiment was to see whether the notch without a crack (which is positioned out side of the measurement grid) would significantly affect the detection fields of each algorithm and produce a false-positive identification of the crack damage. For the *displacement error* and *GDEP* algorithms the notch tip did not produce any distortion in

damage detection field, whereas the *surface strain* algorithms showed distortions in its damage detection field in front of the notch tip. However, for all three algorithms, the notch without a crack did not produce any false-positive identification of the crack damage.

With an increase in crack length from the tip of the notch, the *GDEP* algorithm was able to reliably identify the crack. In contrast, the *displacement error* and *surface strain* algorithms were able to reliably identify the crack only when considering the *displacement error* and *surface strain* algorithms in the y-direction. The poor performance of the *displacement error* and *surface strain* algorithms in x-axis is attributed to the relatively small measured x-displacement when compared to the y-displacements.

From this study, the *displacement error* and *surface strain* algorithms were observed to be highly dependent on the direction of the applied load, whereas the *GDEP* algorithm should work regardless of the direction of the applied load. The positive identification of the crack damage, verifies the validity of these algorithms, which needs no a-priori information about the specimen geometry or construction.

Further investigations can be conducted to evaluate the sensitivity of the algorithms to indentify small crack damage, as well as the sensitivity of the algorithms to the direction of applied loads. However, the scope of this chapter is only intended to include the developing damage detection algorithms based on kinematic principles of in-plane deformation and an initial investigation into potential of these algorithms in detecting crack damage with the aid of 3D SLDV technology.

–

Chapter 6. Detection of Delamination in Composite Beams

Fibre-reinforced composite laminates are ideal for applications that require a lightweight, yet strong material. However, these composites are prone to delamination between the laminate layers. Delamination can cause a significant decrease in strength and can lead to premature structural failure of the materials. Thus, the detection of delamination damage in laminated composites is important in preventing structural failures.

A newly proposed algorithm for the detection of through-the-width delamination within a composite laminate beam is presented in this Chapter. This algorithm is based on the Governing Differential Equation (GDE) of beam deflection for quasi-static deflections (*GDEB* algorithm). Utilising deflection data measured by a 1D scanning laser Doppler vibrometer, the algorithm is determined using a Savitzky-Golay differentiating filter. An investigation was conducted to identify damage features of the algorithm and to evaluate its potential in detecting and locating delamination damage of various lengths and depths. As a comparison, the effectiveness of this algorithm in detecting delamination damage is compared to two commonly used algorithms:- the error in beam deflection (deflection error algorithm) and error in beam curvature (*curvature error* algorithm).

To evaluate the potential of the algorithms for detecting damage in a beam structure, a number of delaminated composite beams were analysed. As discussed in Section 3.2.1,

these composite beams were created with an artificial through-the-width delamination zone of various depths and lengths, tabulated in Table 3.1. This range of specimens was selected in order to evaluate the effectiveness of each damage detection algorithm for various delamination lengths and depths. As seen in Figure 6.1, the beams were clamped at one and were oscillated at the free end (i.e. cantilevered) with a 1Hz sinusoid frequency, to ensure that the beam deflections were quasi-static. Using a 1D vibrometer, the vibratory deflections of a delaminated composite beam specimen were measured at 501 points along the centreline of the beam length over a span of 250mm. The surface on which the laser measures the deflections will be referred to as the first layer of delaminated composite beam, and subsequent layers will be known as the second layer, third layer etc.

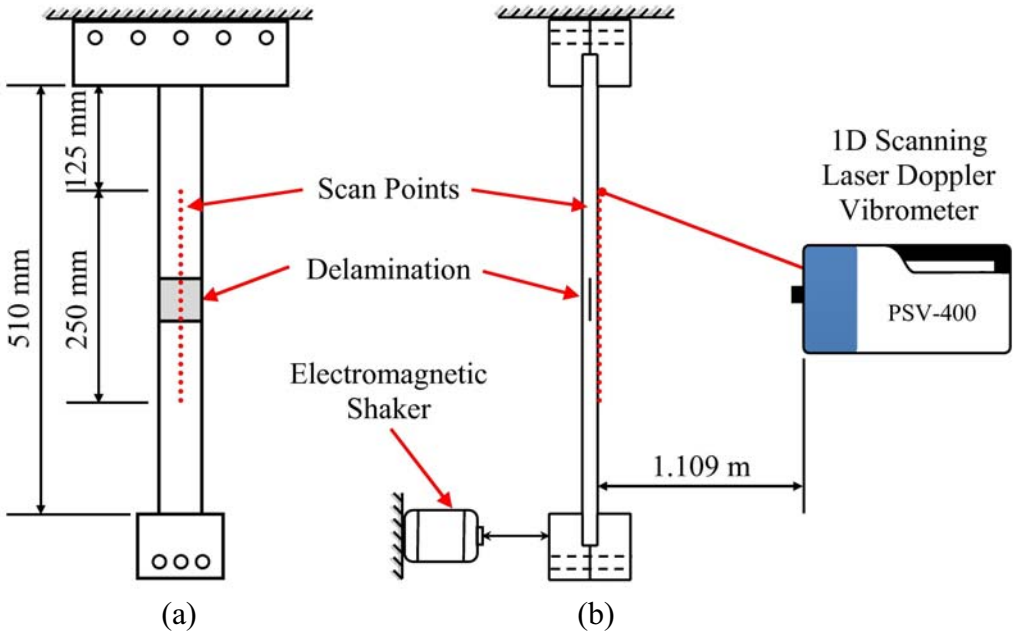

Figure 6.1. Experimental setup of the cantilever beam, (a) front view of the composite beam shows the scan points (red dots) used by the 1D vibrometer and (b) side view of the composite beam showing the position of the electromagnetic shaker and 1D vibrometer.

In these experiments, a 1D Savitzky-Golay differentiating filter (Appendix B.1) was utilised to determine each damage detection algorithm. To keep consistency throughout the results, one parameter was investigated at a time for each test set (i.e. filter width, delamination length and delamination depth), while keeping other parameters constant. The baseline values were a filter width of 151 points ($m = 75$), delamination length of 50mm ($L_d = 50\text{mm}$) and delamination depth between the fourth and fifth layer ($h_2/h = 0.5$) of the 8 layer layup. To assess the effectiveness of each algorithm, an analytical model of the delaminated beam was developed (presented in Section 6.1) and the experimental results were then compared to results obtained from the model.

The experiments examined in this chapter will include the use of three algorithms for the detection of delamination:

- *GDEB* algorithm – based on the GDE of beam deflection
- *Deflection error* algorithm – based on the error between measured and smoothed displacement, and
- *Curvature error* algorithm – based on the error in ideal and estimated beam curvature.

For each of these algorithms, the affect of different parameters on the detection of delamination will be investigated. Specifically,

- the size of the filter utilised within the Savitzky-Golay differentiating filter,
- the delamination length, and
- the delamination depth.

6.1 Principles of Bending in Thin Plates

This section discusses the principles related to thin composite plates subjected to bending, which can be utilised as a basis for a NDE technique to detect delamination damage within a composite thin plate. A description of the conditions of equilibrium and general governing equation of displacements for thin composite plates subjected to bending are initially discussed. Followed by a description of how these principles and equations may be used for detecting delamination damage. This background theory is necessary for setting the foundations for later chapters.

6.1.1 Equations of Equilibrium

For the conditions of equilibrium to be satisfied for a composite plate subjected to out-of-plane loading, the sum of all forces, as well as, moments at any point in a structure must equal zero.

Considering a small element $[dx, dy]$ of a plate, which is subject to a uniformly distributed load per unit area (p), shear forces (Q_x and Q_y) and bending moments (M_x, M_y and M_{xy}), as seen in Figure 6.2. If the element is considered to be small, the shear force and bending moment components can be assumed to be distributed uniformly over each face (Ugural 1999).

The equilibrium of forces in the x-, y-, z-directions leads to, respectively

$$\frac{\partial Q_x}{\partial x} + \frac{\partial Q_y}{\partial y} + p = 0 \tag{6.1}$$

$$\frac{\partial M_{xy}}{\partial x} + \frac{\partial M_y}{\partial y} - Q_y = 0 \tag{6.2}$$

$$\frac{\partial M_x}{\partial x} + \frac{\partial M_{xy}}{\partial y} - Q_x = 0 \tag{6.3}$$

Introducing the expressions for Q_y and Q_x from Equations (6.2) and (6.3) into Equation (6.1) yields,

$$\frac{\partial^2 M_x}{\partial x^2} + 2\frac{\partial^2 M_{xy}}{\partial x \partial y} + \frac{\partial^2 M_y}{\partial y^2} = -p \tag{6.4}$$

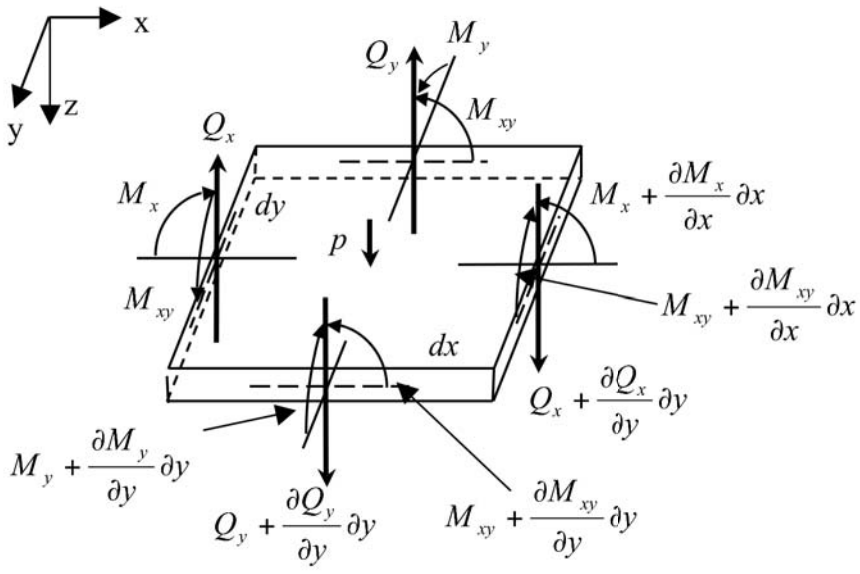

Figure 6.2. Shear forces and moments acting on a small element *dxdy* of a plate.

Equation (6.4) represents the differential equation of equilibrium for bending of thin plates. However, as this study will only consider structures with a remotely applied load, with no

lateral loading, $p = 0$. An alternative form of Equation (6.4) is determined by inserting the definitions of bending and twist moments in terms of the stress components (σ_{xx}, σ_{xx} and τ_{xy}),

$$\frac{\partial^2 \sigma_{xx}}{\partial x^2} + 2\frac{\partial^2 \tau_{xy}}{\partial x \partial y} + \frac{\partial^2 \sigma_{yy}}{\partial y^2} = -p \tag{6.5}$$

where

$$\sigma_{xx} = \frac{12 M_x z}{h^3} \tag{6.6}$$

$$\sigma_{yy} = \frac{12 M_y z}{h^3} \tag{6.7}$$

$$\tau_{xy} = \frac{12 M_{xy} z}{h^3} \tag{6.8}$$

The differential equation of equilibrium in terms of stress components, Equation (6.5), can then be represented via strain components by introducing plane strain Hooke's law. However, as these equations are being derived for a composite plate, orthotropic plane strain Hooke's law need to be introduced, which is expressed as (Ugural 1999),

$$\sigma_{xx} = E'_x \varepsilon_{xx} + E'_{xy} \varepsilon_{yy} \tag{6.9}$$

$$\sigma_{yy} = E'_y \varepsilon_{yy} + E'_{xy} \varepsilon_{xx} \tag{6.10}$$

$$\tau_{xy} = G\frac{\partial^2 \gamma_{xy}}{\partial x \partial y} \tag{6.11}$$

where *G* is the shear modulus and

$$E_x' = \frac{E_x}{1 - \nu_x \nu_y}$$

$$E_y' = \frac{E_y}{1 - \nu_x \nu_y} \tag{6.12}$$

$$E_x' = \frac{\nu_y E_x}{1 - \nu_x \nu_y} = \frac{\nu_x E_y}{1 - \nu_x \nu_y}$$

in which E_x, E_y and ν_x, ν_y are the moduli of elasticity and Poisson' ratio in the x- and y-directions, respectively.

Introducing orthotropic plane stress Hooke's law gives the combined equilibrium conditions in terms of strains, and can be expressed as,

$$\frac{\partial}{\partial x^2}\left(E_x' \varepsilon_{xx} + E_{xy}' \varepsilon_{yy}\right) + 2G \frac{\partial^2 \gamma_{xy}}{\partial x \partial y} + \frac{\partial}{\partial y^2}\left(E_y' \varepsilon_{yy} + E_{xy}' \varepsilon_{xx}\right) \tag{6.13}$$

6.1.2 Governing Differential Equations

For a plate subjected to small out-of-plane deflections, small deflection theory (Kirchhoff 1850) can be applied and the three z-components of the strain can be assumed to be negligible ($\varepsilon_z \approx 0$, $\gamma_{xz} \approx 0$ and $\gamma_{yz} \approx 0$), which reduces the six compatibility equations to Equation (5.5). By equating the shear strain components of the strain compatibility equation (5.5) and equilibrium equation (6.13), a general GDE of normal strains can be determined for an orthotropic thin plate, subjected to small deflection from out-of-plane loading. The result is found to be,

$$E_x \frac{\partial \varepsilon_{xx}}{\partial x^2} + (E_{xy} + 2G)\left(\frac{\partial \varepsilon_{xx}}{\partial y^2} + \frac{\partial \varepsilon_{yy}}{\partial x^2}\right) + E_y \frac{\partial \varepsilon_{yy}}{\partial y^2} = 0 \tag{6.14}$$

This equation can be rearranged purely in terms of the out-of-plane displacements and expressed as,

$$E_x \frac{\partial^4 u_z}{\partial x^4} + 2(E_{xy} + 2G)\left(\frac{\partial^4 u_z}{\partial x^2 \partial y^2}\right) + E_y \frac{\partial^4 u_z}{\partial y^4} = 0 \tag{6.15}$$

For an isotropic material ($E = E_x = E_y$, $\nu = \nu_x = \nu_y$ and $G = \frac{E}{2(1-\nu)}$) this equation reduces to

$$\frac{\partial^4 u_z}{\partial x^4} + 2\frac{\partial^4 u_z}{\partial x^2 \partial y^2} + \frac{\partial^4 u_z}{\partial y^4} = 0 \tag{6.16}$$

which represents the GDE of deflection for an isotropic thin plate with a remotely applied load. For a slender beam, this equation reduces again, to

$$\frac{\partial^4 u_z}{\partial x^4} = 0 \tag{6.17}$$

which represents the GDE of beam deflection.

6.1.3 Application of Principles for Damage Detection

The strategy for detecting through-the-width delamination within a composite beam is based on assessing the validity of the GDE of beam deflection for the measured deflections (u_z). By utilising the discretely measured deflections (u_z) to calculate the GDE of beam deflection, Equation (6.17), a residual term (R_z) can be determined. A non-zero residual term will signify a violation of this equation, thus indicating the presence of delamination.

The residual term of the GDE of beam deflection (R_z) is,

$$R_z = \frac{\partial^4 u_z}{\partial x^4} \tag{6.18}$$

To evaluate the effectiveness of the proposed algorithm, based on the GDE of beam deflection, two commonly used damage detection algorithms can also be used as a comparison:- curvature and operation deflection shape. The comparison algorithms are based on the most basic curvature and operation deflection shape damage detection algorithms, which are the error in filtered-to-measured beam deflection and the error in estimate-to-expected undamaged beam curvature.

When delamination forms within a composite beam, the deflection shape of the beam will deviate from the expected shape represented by a third-order polynomial, at the location of the delamination damage. Therefore, using a numerical smoothing filter, a discontinuity (a deviation) of the deflection, caused by delamination damage, would show a difference in smoothed ($u_{z,s}$) to measured ($u_{z,m}$) displacements. The displacement error ($\hat{u}_z$) can be expressed by Equation (5.10), where i is the z direction, as seen in Section 5.2.4.

The second comparison algorithm is based on beam curvature. Through-the-width delamination within a composite the beam structure causes a sharp change in the curvature over the delaminated section when the beam is loaded. A number of methods have been produced to determine the location of damage within beam based on changes in curvature (Fan & Qiao 2010). In this thesis, this algorithm was based on the most simple method:- the error in estimated-to-expected undamaged beam curvature of a beam structure. To estimate the curvature (κ) of a beam, a second-order numerical differentiation of the measured beam deflections with respect to the length of the beam needs to be performed.

This estimated curvature (κ) can then be compared against the expected undamaged curvature (κ_{LS}) of the beam, which in this study will be determined using a least-squares-fit of all the data points. By comparing the estimated (κ_{SG}) and expect undamaged (κ_{LS}) curvature, a curvature error term ($\hat{\kappa}$) is left and is expressed as,

$$\hat{\kappa} = \kappa_{SG} - \kappa_{LS} \tag{6.19}$$

6.2 Analytical Delaminated Beam Model

An analytical model of the delaminated cantilever beam (Figure 6.3) was developed based on Euler-Bernoulli beam theory to compare the theoretical and experimental performance of the damage detection algorithms (Valoor & Chandrashekhara 2000; Herath, Bandyopadhyay & Logan 2010). The model assumes a constant cross-section and modulus of elasticity across each section and is limited to long slender beams where shear deformation is negligible. The deflection of a beam is controlled by the GDE for beam deflection; Equation (6.17). Therefore, the deflection of each segment of the beam can be represented by a third-order polynomial and are expressed as,

$$u_{z,i}(x) = C_{i1}\frac{x^3}{6} + C_{i2}\frac{x^2}{2} + C_{i3} + C_{i4} \tag{6.1}$$

where C_{ij} are constants, i represents the beam segment and j is a value between 1 and 4. Full details of this analytical model are discussed in Appendix C.

To understand the characteristics of the damage detection algorithms, the experiments were simulated using the analytical model. These simulated results were then used to produce the beam deflection in the absence of measurement noise, thus providing a means

of understanding the characteristics of the damage detection algorithms. These simulated results were compared to the experimentally evaluated results by introducing noise to the simulated deflections, which was equivalent to that observed in the experimental results (SNR of 64dB).

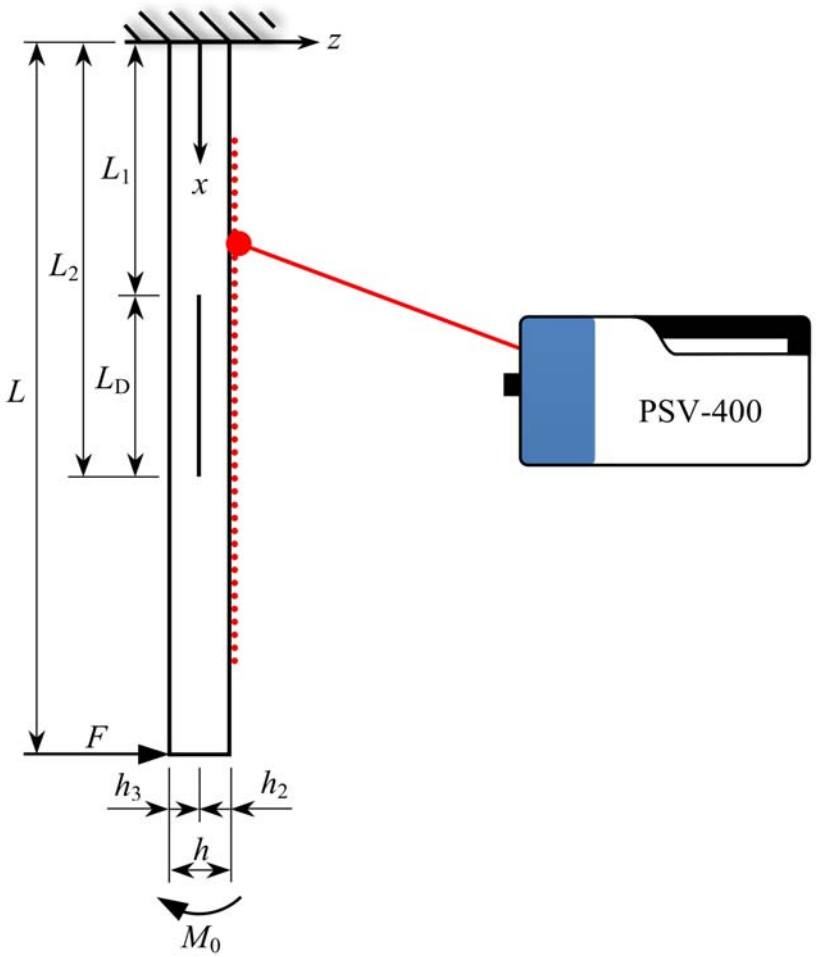

Figure 6.3. Dimensioned illustration of the delaminated cantilever beam.

6.3 Governing Equation of Beam Deflection

The GDE of beam deflection defines how a beam deflects at each point on the surface of the beam, regardless of whether it is damaged or undamaged. However, when determining the GDE of beam deflection, using a numerical differentiation process, a number of data points need to be fitted to a specific degree of polynomial. By utilising a numerical differentiation process, the GDE of beam deflection will only be satisfied if there are no discontinuities between the data points used within the numerical differentiation process. Therefore, if the boundaries of the delamination damage lie within these data points, the GDE of beam deflection will be violated.

The GDE of beam deflection is a combination of strain compatibility and the equations of equilibrium. With the increasing interest in developing better damage detection techniques for detecting structural damage, an algorithm based on the GDE of beam deflection has not be yet been developed or investigated. Section 6.3 present an investigation that indentifies the damage features of the newly proposed algorithm, as well as the effectiveness of the algorithm in detecting delamination damage. The formulation of the algorithm is first discussed, detailing the Savitzky-Golay differential filter parameters and the filtering procedure utilised. This is followed by an investigation into the effectiveness of the algorithm in detecting through-the-thickness delamination within a composite beam for various delamination depths and delamination lengths, as well as various filter sizes used within the Savitzky-Golay filter.

6.3.1 Algorithm

An algorithm was developed (*GDEB* algorithm) to specifically determine this residual term (R_O), by calculating the fourth derivative ($r = 4$) of the measured beam deflection using a fourth-order polynomial ($n = 4$) Savitzky-Golay differentiating filter. A flow diagram of the filtering process is illustrated in Figure 6.4.

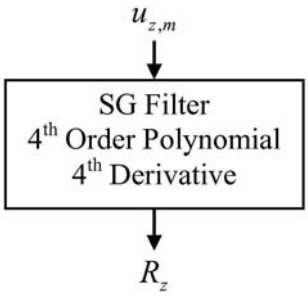

Figure 6.4. Flow diagram of the *GDEB* algorithm R_z.

The discrete nature of the numerical approach, as well as noise within the displacement measurements, will also cause a non-zero residual term, which could lead to damage being obscured or the creation of a false-positive identification Therefore, the effectiveness of the *GDEB* algorithm in detecting the delamination was investigated for varying filter widths used within the Savitzky-Golay filter, delamination lengths and delamination depths, and is presented in the following subsections. In order to assess the effectiveness of the *GDEB* algorithm, results obtain from the experiments were compared to that of the analytical model. In addition, the residual term was compared with the beam curvature.

6.3.2 Filter size

Figure 6.5 shows the residual term of the GDE (R_z) for a range of filter points ($2m + 1$) utilised within the Savitzky-Golay filter.

For the simulated results in the absence of noise, seen in Figure 6.5c, the delamination boundaries are observed to create two doublet-like curves that are each centred over one of the delamination boundaries. That is, the delamination boundaries are positioned at the points where the doublet curves cross over zero between their minima and maxima. When comparing the position of the doublet curve to the beam curvature (grey lines in Figure 6.5), the doublet curves are observed to correspond exactly to the sharp changes in curvature of the beam, caused by the boundaries of the delamination.

The lengths of the doublet curves are approximately equal to the length of the filter. As the filter length increases, the doublet curves are observed to proportionally increase in length. At the point where the length of the filter is greater than the length of the delamination, the two doublet curves created by each boundary of the delaminated zone begin to coincide and shift the centres of the doublet curves outward from the boundary location of the delamination. In addition, the amplitude of the doublet curves increases as the filter length decreases. However, with decreasing filter width, the filter is less effective in removing the noise from the measured deflection data, thus increasing the noise in the experimentally obtained results.

When using 51 or 101 filter points ($2m + 1$) to determine the residual term of GDE of deflection, the experimental data is significantly affected by noise (Figures 6.5(i)(a) and 6.5(ii)(a) respectively), making it incapable of localising the delaminated section. The use

of 151 or 201 filter points (Figures 6.5(i)(c) and 6.5(i)(d) respectively) effectively filters out this noise to reveal the peaks, which identifies the delaminated section. When comparing the experimental results (column a) to the simulated results with equivalent added measurement noise (column b), there is good is agreement between the two.

From these experimental results (column a), a 50mm delaminated zone between the mid-layers ($h_2/h = 0.5$) was able to be qualitatively identified using a 1D Savitzky-Golay differentiating filter ($r = 4$) of fourth-order polynomial ($n = 4$) with filter widths of 151 ($m = 75$) and 201 data points ($m = 100$).

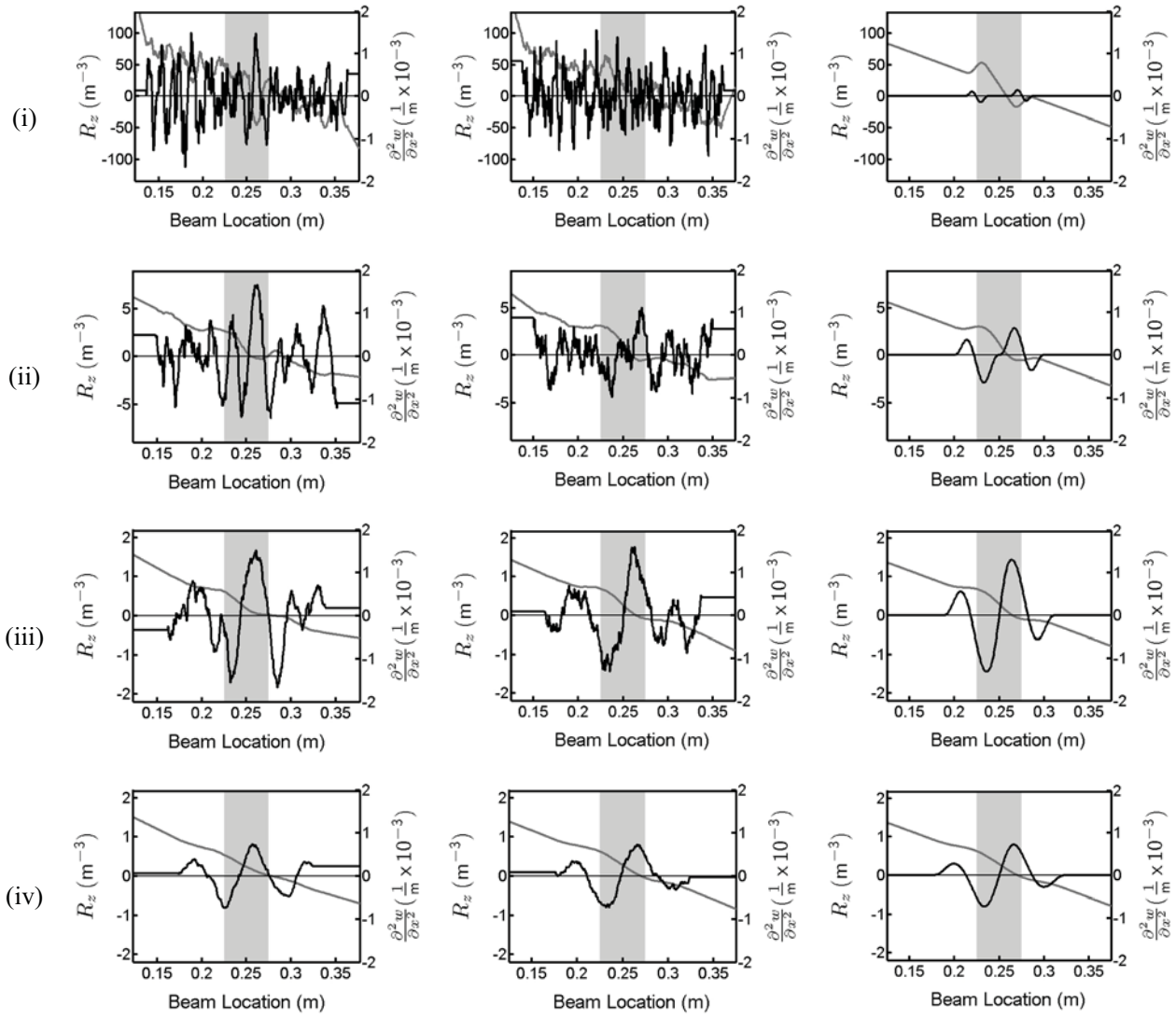

Figure 6.5. Acquired residual term of the GDE (R_z) for a delaminated cantilever beam for four different quantities of filter points ($2m+1$) utilised within the fourth-order polynomial ($n=4$) Savitzky-Golay smoothing ($r=0$) filter. The rows denote the filter widths of (i) $m=25$, (ii) $m=50$, (iii) $m=75$ and (iv) $m=100$. The columns show the (a) experimental results, (b) simulated results with equivalent noise and (c) simulated results in the absence of noise. The delamination is located between fourth and fifth layer and 50mm in length. The black line represents R_z, the grey line shows the beam curvature and the shaded section illustrates the location of the delaminated section.

6.3.3 Delamination Length

In Figure 6.6, the evaluated residual term of the GDE (R_z) is presented for four composite laminate cantilever beams, each with a different length of delamination (L_d) between the mid-layers ($h_2/h = 0.5$). The size of the Savitzky-Golay differentiating filter used to determine these results was 151 points, that were approximately 75mm in length.

By keeping the filter width constant, the experimental results (column a) contain a consistent level of signal to noise. This consistent level of signal to noise becomes a problem as the delamination length decreases. For instance, the characteristic doublet curves are completely obscured for a delamination length of 20mm. As the delamination length increases to 50mm, 75mm and 100mm the delamination can be qualitatively identified. When comparing the experimental results to the simulated results with equivalent added measurement noise, there is good agreement between the two.

From these observations, a delamination greater than 50mm in length can be qualitatively identified using a 1D Savitzky-Golay differentiating filter ($r = 4$) of fourth-order polynomial ($n = 4$) with a filter width of 151 point ($m = 75$), which is approximately 75mm in length.

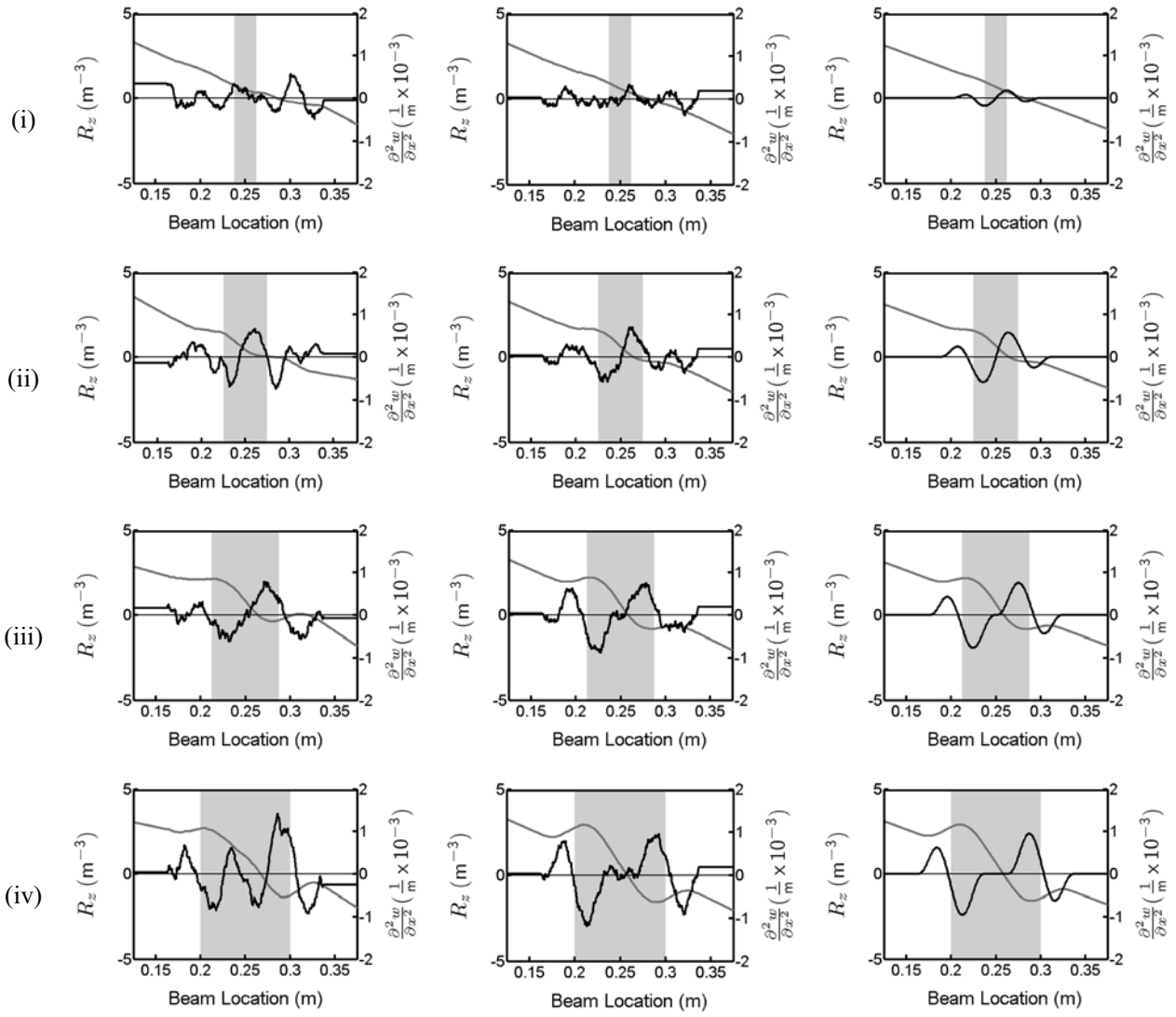

Figure 6.6. Acquired residual term of the GDE (R_z) for a delaminated cantilever beam for four different lengths of delamination between the mid-layers ($h_2/h = 0.5$). The rows denote the lengths of the delamination and are (i) $L_d = 25$mm, (ii) $L_d = 50$mm, (iii) $L_d = 75$mm and (iv) $L_d = 100$mm. The columns show the (a) experimental results, (b) simulated results with equivalent noise and (c) simulated results in the absence of noise. A fourth-order polynomial ($n = 4$) Savitzky-Golay smoothing ($r = 0$) filter was used with a filter width of 151 points ($m = 75$). The black line represents R_z, the grey line shows the beam curvature and the shaded section illustrates the location of the delaminated section.

6.3.4 Delamination Depth

Figure 6.7 shows the evaluated residual term of the GDE (R_O) for seven laminate cantilever beams, each having a delamination of 50mm in length between different layers.

The simulated results (column c) show that the maximum amplitude of the doublet curves occur when the delamination is in the middle of the beam ($h_2/h = 0.5$), and the amplitude of the doublet curves decreases the closer the delamination is to the surface. This amplitude change is dependent on the change in stiffness within the beam due to the delaminated zone.

In the experimental results (column a), a large spike is observed in the residual term over the area of the delaminated zone when the delamination is located between the first and second layer ($h_2/h = 0.125$), which is most likely due to the buckling of the first layer. The vibrometer measured the deflections of the beam along the outer surface of the first layer. The analytical model does not account for buckling of the delaminated layer and, thus, the simulated results will not match the experimental results for this buckling case.

The experimental results and the simulated results with added equivalent noise are in good agreement. However, the characteristic features of the doublet curves become increasingly obscured by noise when the delamination is located between layers closer to the surface, with the exception of when buckling occurs on the surface where the vibrometer is measuring the beam deflection.

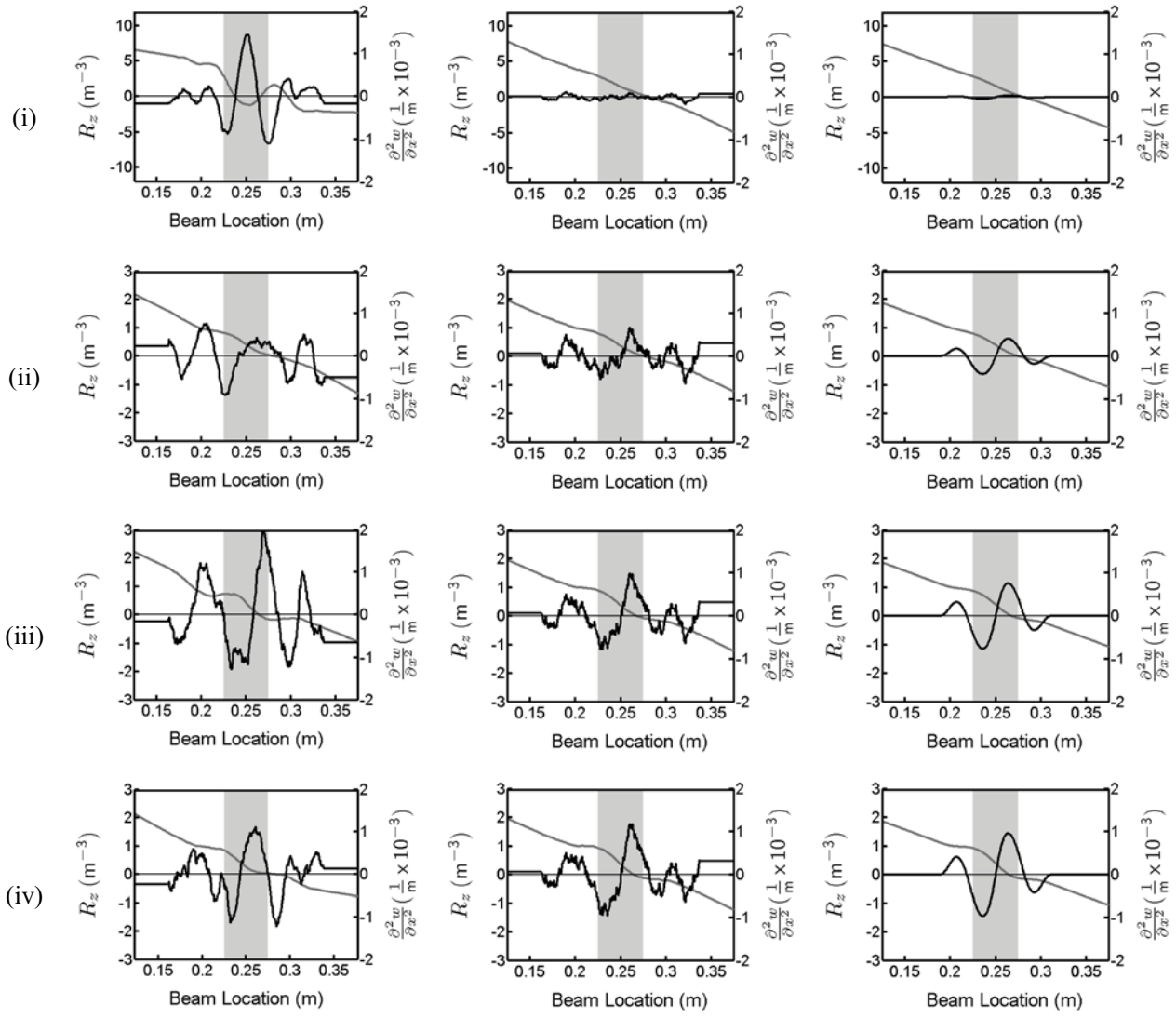

Figure 6.7. Continued on page 191

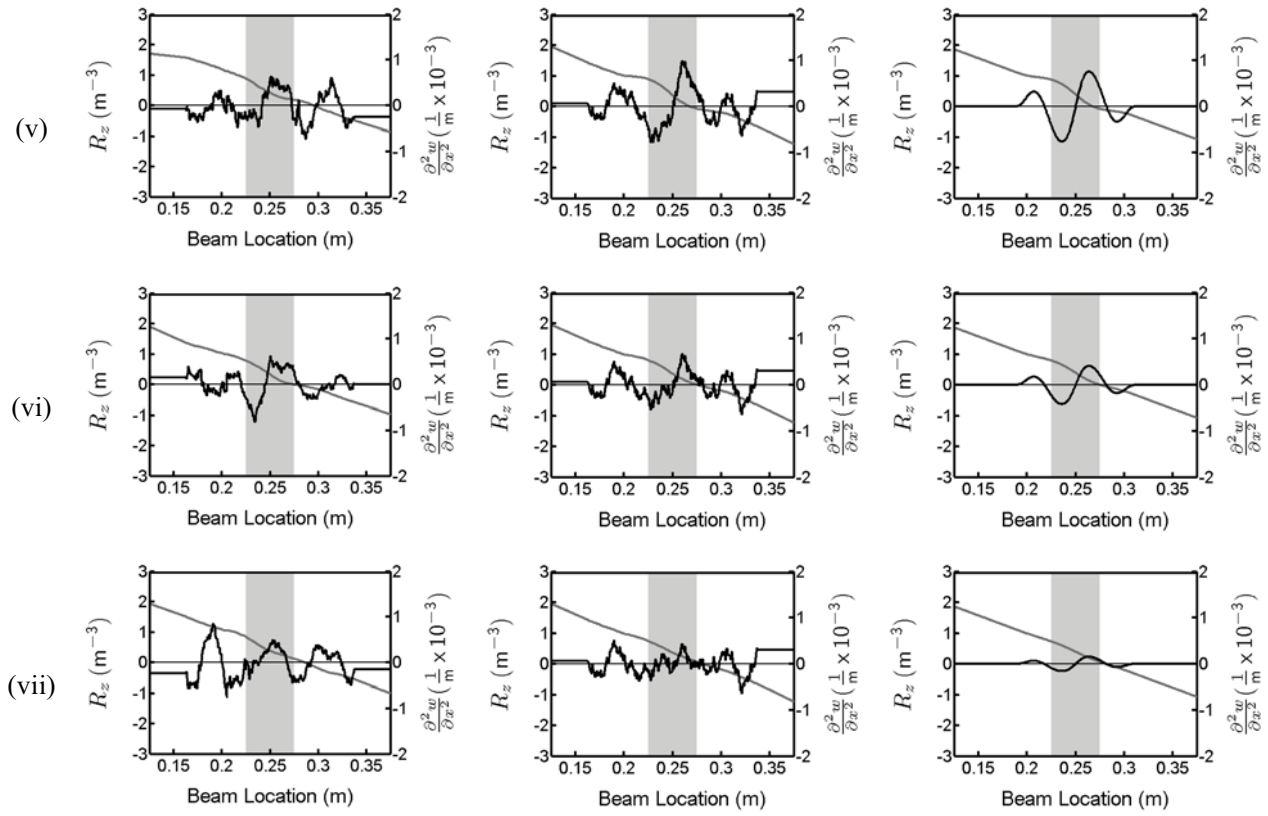

Figure 6.7. Acquired residual term of the GDE (R_z) for various laminate cantilever beams with a 50mm delamination at different depths. The rows denote the depths of the delamination and are (i) $h_2/h = 0.125$, (ii) $h_2/h = 0.25$, (iii) $h_2/h = 0.375$, (iv) $h_2/h = 0.5$, (v) $h_2/h = 0.625$, (vi) $h_2/h = 0.75$ and (vii) $h_2/h = 0.875$. The columns show the (a) experimental results, (b) simulated results with equivalent noise and (c) simulated results in the absence of noise. A fourth-order polynomial ($n = 4$) Savitzky-Golay smoothing ($r = 0$) filter was used with a filter width of 151 points ($m = 75$). The shaded section illustrates the location of the delaminated section.

6.4 Beam Deflection Error

This section presents an investigation into the use of an algorithm based on the beam deflection error to detect through-the-width delamination within a composite laminate beam. The damage features of the algorithm are investigated and the effectiveness of the algorithm in detecting delamination is evaluated for various delamination length and depth, as well as filters parameters. Previous studies that have looked into the use of beam deflection error for the detection of delamination damage are first discussed. This is followed by the formulation of the algorithm used in this section and a discussion of the experimental results.

6.4.1 Previous Studies

Ghoshal et al. (2003) conducted an investigation into the use of deflection as an indicator of delamination damage in composite laminate beams. Ghoshal et al. undertook various experiments using a 1D vibrometer to determine the effect of delamination depth and length on the vibratory deflection shapes. These experiments first involved the modal analysis of the composite beam to determine its natural frequencies. The beam was then vibrated at the natural frequencies using a piezoelectric patch and the vibrational deflection shapes of the beam were measured using a 1D vibrometer. From these experiments, Ghoshal et al. (2003) observed that

1. low natural frequencies were not useful in determining the location and extent of the delamination,
2. the vibration deflection shape of the beam significantly distorts when the delamination is closer to the mid-plane of the composite beam,

3. larger sized delamination is easier to detect as smaller delaminations require a higher natural frequency to localise the delamination.

Ghoshal et al. (2003) developed a technique that is able to detect the presence and location of delamination damage, however, the technique does not provide an exact ply level location within the delamination. The need to use higher frequency modes to detect small changes is not surprising, as modes with wavelengths of similar size to the damage will be more susceptible to changes than modes with big wavelengths.

An algorithm investigated by Pai et al. (2004) performed a sliding-window, least-squares curve-fitting of a free-undamped deflection shape of a beam, harmonically vibrating at its seventh mode. This study looked at how crack damage affected the constant terms evaluated in the fitting process, as well as the sectional standard deviation between measured and fitted beam deflection data. Pai et al. (2004) explain that crack damage within the beam structure will create an intermediate boundary zone within the beam at the location of the damage. This will then cause a sharp change in the constant terms of the curve fitting process, thus allowing the damage to be identified. From the experimental investigation, the technique was found to be able to successfully detect the crack damage, however, Pai el al. (2004) realised that:-

1. damage is difficult to detect if located at a vibration node;
2. high frequency operation deflection shapes are more sensitive to damage;
3. the specimens must have a uniform thickness, as uniformity introduces boundary effects into the operational deflection shapes.

6.4.2 Algorithm

In the research presented in this section; an investigation into a damage detection technique, is conducted, which compares the smoothed to measured quasi-static beam deflections, similar to the sectional standard deviation algorithm used by Pai et al. (2004). The beam deflections were measured using a 1D vibrometer and the technique was utilised for the detection of through-the-width delamination in a cantilever, composite beam. Through-the-width delamination, within a beam, will create a localised stiffness change over the delaminated area, causing a slight discontinuous deviation in the beam deflection at the boundaries of the delaminated zone. Assuming the beam is undamaged and oscillating at a frequency within the stiffness controlled region with no lateral applied distributed loads, the deflection of the beam needs to satisfy the GDE of beam deflection (Equation (6.17)) and, can be represented by a third-order polynomial.

Using a 1D Savitzky-Golay smoothing filter, a third-order polynomial could be fitted to the beam deflection measurements. However, the filter provides a continuous polynomial fit over a number of measurement points and, thus, the discontinuous deviation in beam deflection at the boundaries of a delaminated zone would not be able to be fitted properly by the filter. This would then create a divergence of the smoothed beam deflections from the measured beam deflections. Using this phenomenon, a damage detection algorithm was developed based on the error in beam deflection between the smoothed and measured deflections.

The *deflection error* algorithm compares the raw measured beam deflections $u_{z,m}$ against the smoothed deflections $u_{z,SG}$ and can be expressed as,

$$\hat{u}_z = u_{z,SG} - u_{z,m} \qquad 6.2$$

After the beam deflections were measured using the 3D vibrometer, they were passed through a 1D smoothing ($r = 0$) Savitzky-Golay filter of third polynomial order ($n = 3$). The *deflection error* algorithm was then determined by comparing the smoothed and measured deflections, however, significant noise was present. To alleviate this noise, the result was passed through another 1D smoothing ($r = 0$) Savitzky-Golay filter of third polynomial order ($n = 3$) with a filter width of 101 points ($m = 50$). A flow diagram of the filtering process is illustrated in Figure 6.8.

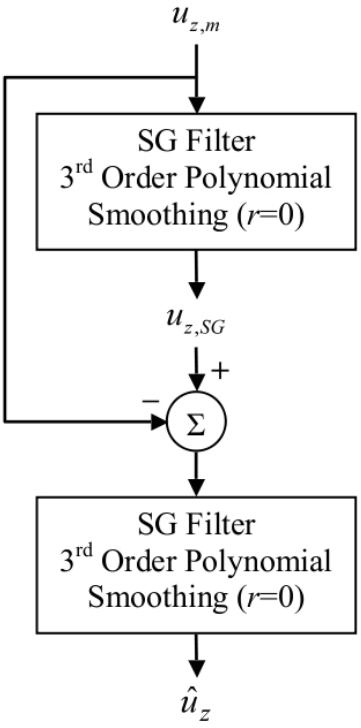

Figure 6.8. Flow diagram of the *deflection error* algorithm $\hat{u}_z$.

An investigation of the *deflection error* algorithm was conducted in order to detect

through-the-width delamination within a composite laminate beam for varying lengths and depths. The following subsections present investigations into the effectiveness of the *deflection error* algorithm in detecting the delamination for varying filter widths used within the Savitzky-Golay filter, delamination lengths and delamination depths. In order to assess the effectiveness of the *deflection error* algorithm, results obtained from experiments were compared to that of the analytical model developed previously in Section 6.1.

6.4.3 Filter Size

Figure 6.9 shows the evaluated beam deflection error ($\hat{u}_z$) for a range of filter points ($2m + 1$) utilised within the Savitzky-Golay filter, which has been determined experimentally (column a), analytically (column c) and analytically with added equivalent experimental noise (column b).

The simulated results (column c) show a localised distortion in the displacement field at the boundaries of the delaminated zone. This violation is represented by a doublet curve and the boundaries of the delaminated zone occur approximately where the signal crosses over zero between the minimum and maximum of the doublet curve.

As the filter width increases, the doublet curve also increases spatially. When the filter width spans the width of the delaminated zone, the two doublet curves start to coincide and the centres of the doublet curves start to move outward from the location of the boundaries of the delamination. In addition, with an increase in filter width, there is also an increase in the amplitude of deflection error. This increase in deflection error amplitude is due to the fact that, as the filter width becomes larger, more data points are utilised to compare the

smoothed and measured deflections. This causes the difference between the smoothed and measured deflections to increase at the boundaries of the delaminated zone. Consequently, a small filter width (as seen in Figure 6.9(c)(i)) will not span enough points to show a noticeable difference between the smoothed and measured deflections at the boundaries of the delaminated zone.

The experimental results (column a) show that filter widths of 51 ($m = 25$) and 101 points ($m = 50$) do not alleviate enough of the measurement noise to be able to distinguish the distortion created by the boundaries of the delaminated zone, as seen in the simulated results (column c). At filter widths of 151 ($m = 75$) and 201 points ($m = 100$) the characteristic doublet curves appear. When comparing the experimental results to the simulated results with equivalent added measurement noise, there is good is agreement between the two.

From these experimental results it is possible to qualitatively identify the 50mm delaminated zone between the mid-layers ($h_2/h = 0.5$) of a composite laminated beam using 1D Savitzky-Golay smoothing ($r = 0$) filter of third-order polynomial ($n = 3$) with a filter widths of 151 ($m = 75$) and 201 points ($m = 100$).

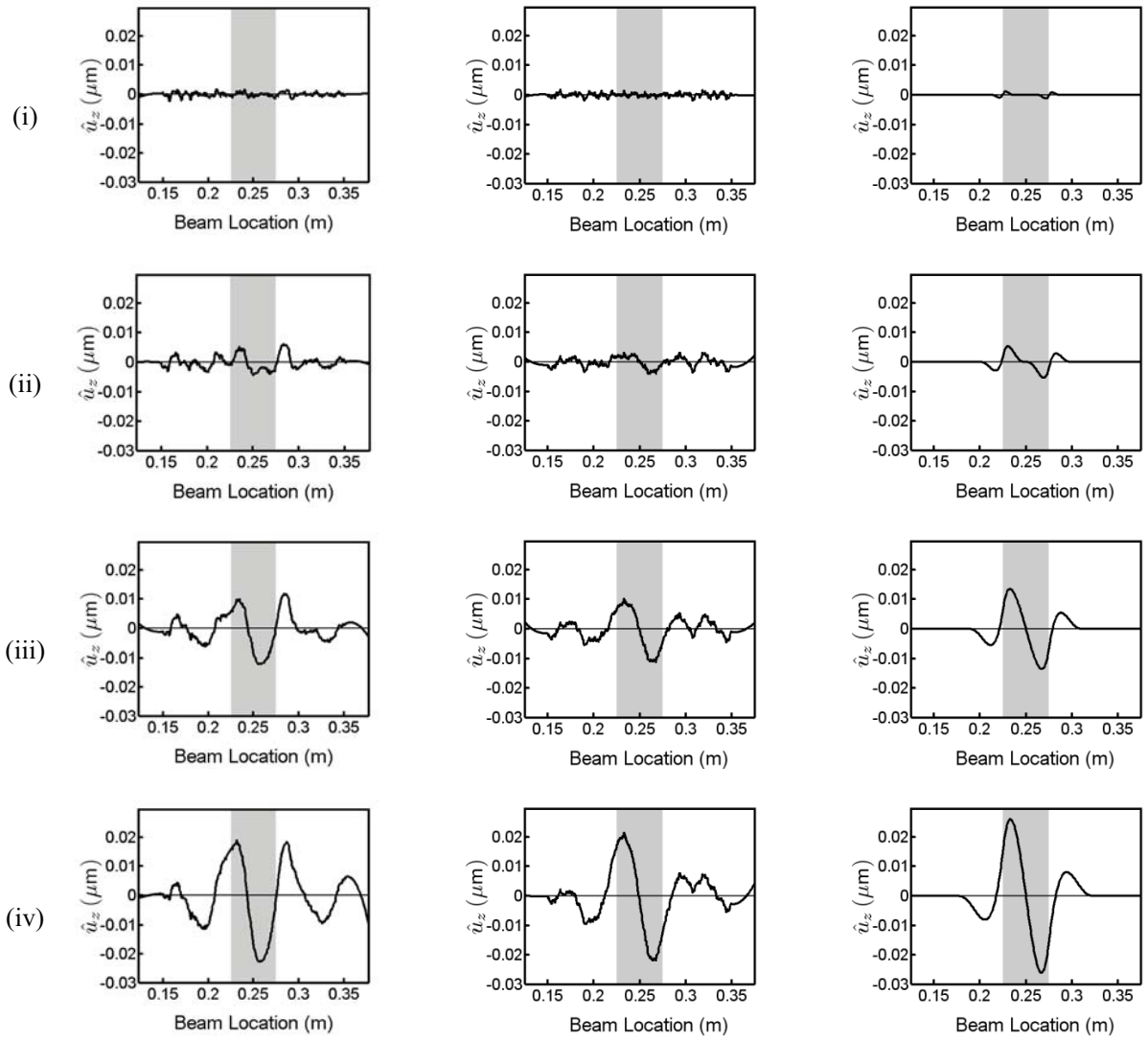

Figure 6.9. Acquired error in deflection ($\hat{u}_z$) for a delaminated cantilever beam for four different quantities of filter points ($2m + 1$) utilised within the third-order polynomial ($n = 3$) Savitzky-Golay smoothing ($r = 0$) filter. The rows denote the filter widths of (i) $m = 25$, (ii) $m = 50$, (iii) $m = 75$ and (iv) $m = 100$. The columns show the (a) experimental results, (b) simulated results with equivalent noise and (c) simulated results in the absence of noise. The delamination is located between fourth and fifth layer and 50mm in length. The shaded section illustrates the location of the delaminated section.

6.4.4 Delamination Length

In Figure 6.10, the evaluated deflection error ($\hat{u}_z$) is presented for four composite laminate cantilever beams, each with a different length of delamination between the mid-layers ($h_2/h = 0.5$). For these results, a filter width of 151 ($m = 75$) points (which approximately spans a length of 75mm) was used for the Savitzky-Golay filter.

From the simulated results, the doublet curves are again identified and are approximately centred at the boundaries of the delaminated zone. For delamination lengths greater than the filter length, two distinct doublet curves can be identified and are centred at the boundary of the delaminated zone. However, at delamination lengths less than the filter length, the two doublet curves coincide and the centres of the two doublet curves shift outward from the location of the delamination boundaries. In addition, the amplitude of the two doublet curves is observed to decrease with a decrease in length of the delamination.

The experimental results (column a) show that the measurement noise conceals the distortion created by the boundaries of the 25mm length delamination. At delamination lengths of 50mm and 75mm the characteristic doublet curves appear and the location of the delamination zone can be identified. However, for the delamination length of 100mm (row vi), an uncharacteristic spike occurs in the experimentally measured deflection error in the middle of the delaminated zone, which prevents the delamination from being positively identified. This uncharacteristic spike is most likely due to the large length of the delaminated zone, as the length of the zone might be causing new contact and boundary conditions within the zone. This would then cause the deflection shape across the delaminated zone to not match the analytical model. There is good agreement between the experimental results (column a) with the simulated results with added equivalent

measurement noise (column b), except for the delamination length of 100mm (row iv).

To conclude, utilising 1D Savitzky-Golay smoothing ($r = 0$) filter of third-order polynomial ($n = 3$) with a filter width of 151 ($m = 75$), the *deflection error* algorithm was able to qualitatively identify a delaminated zone between the mid-layers ($h_2/h = 0.5$) within a composite laminate beam that was 50mm and 75mm in length.

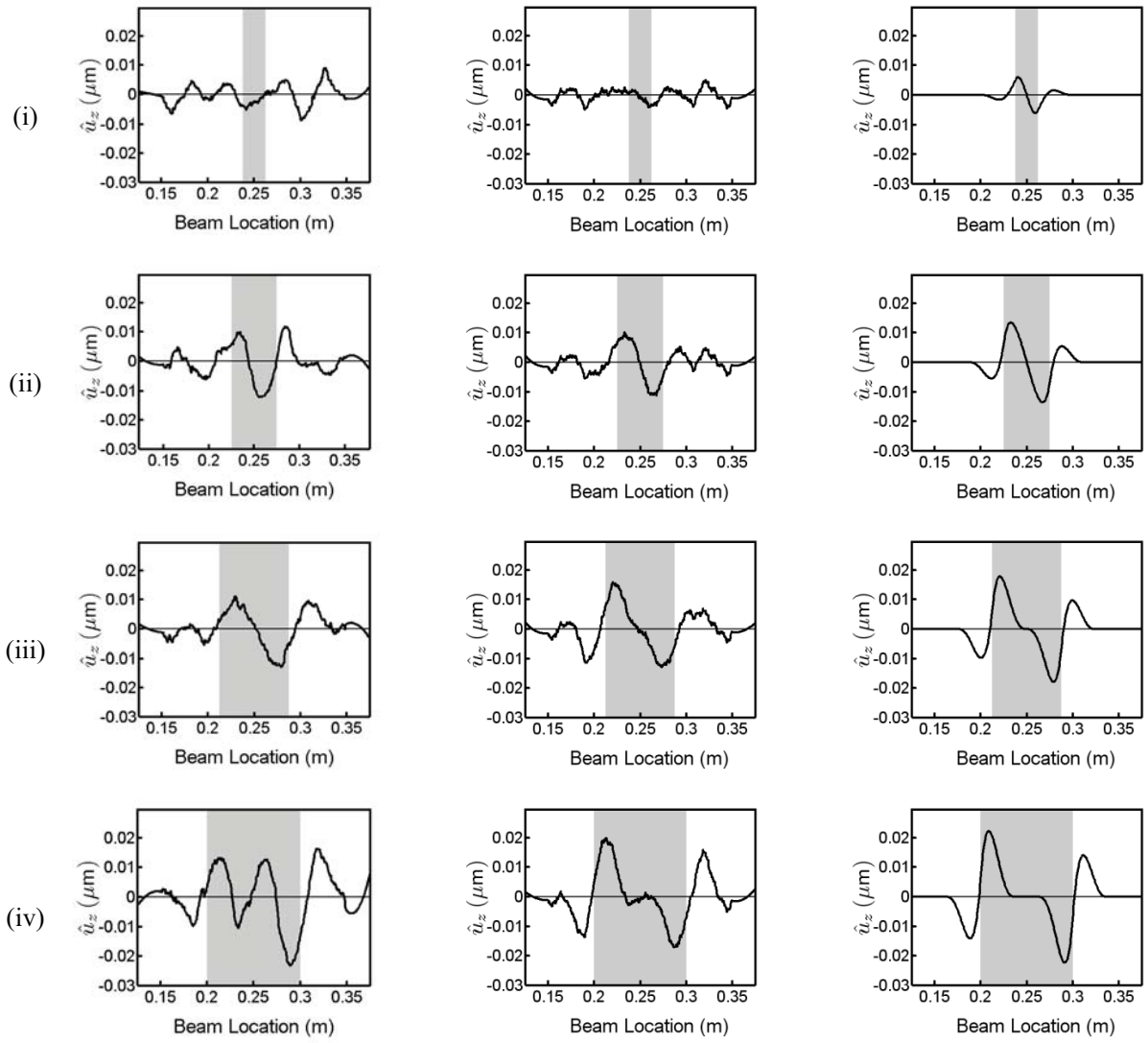

Figure 6.10. Acquired error in deflection ($\hat{u}_z$) for a delaminated cantilever beam for four different lengths of delamination between the mid-layers ($h_2/h = 0.5$). The rows denote the lengths of the delamination and are (i) $L_d = 25$mm, (ii) $L_d = 50$mm, (iii) $L_d = 75$mm and (iv) $L_d = 100$mm. The columns show the (a) experimental results, (b) simulated results with equivalent noise and (c) simulated results in the absence of noise. A third-order polynomial ($n = 3$) Savitzky-Golay smoothing ($r = 0$) filter was used with a filter width of 151 points ($m = 75$). The shaded section illustrates the location of the delaminated section.

6.4.5 Delamination Depth

Figure 6.11 shows the evaluated deflection error ($\hat{u}_z$) for seven laminate cantilever beams, each having a delamination of 50mm in length between different layers.

Similar to the *GDEB* algorithm (Section 6.3.4), the simulated results show that the amplitude of the doublet curves are at a maximum when the delamination is situated between the middle layers of the composite laminated beam (fourth and fifth layer) and amplitude of the doublet curves decreases as the delamination is located closer to the surface. As mentioned previously, the amplitude change is related to the change in stiffness due to the depth of the delaminated zone.

In the experimental results, a large spike is observed at the delaminated zone for the delamination position between the first and second layer ($h_2/h = 0.125$) which is not predicted in the simulated results. This large spike occurs as the first layer is the one from which the vibrometer measures the beam deflections. When this beam is oscillated, localised buckling in the first layer of the composite beam would account for the significant increase in the deflection error at the delaminated zone.

Experimental and simulated results closely match. However, delamination can only be identified when the delamination is positioned between the middle layers ($h_2/h = 0.5$) of the laminate beam, as the measurement noise begins to obscure the results if the damage is situated in layers closer to the surface from either side of the beam.

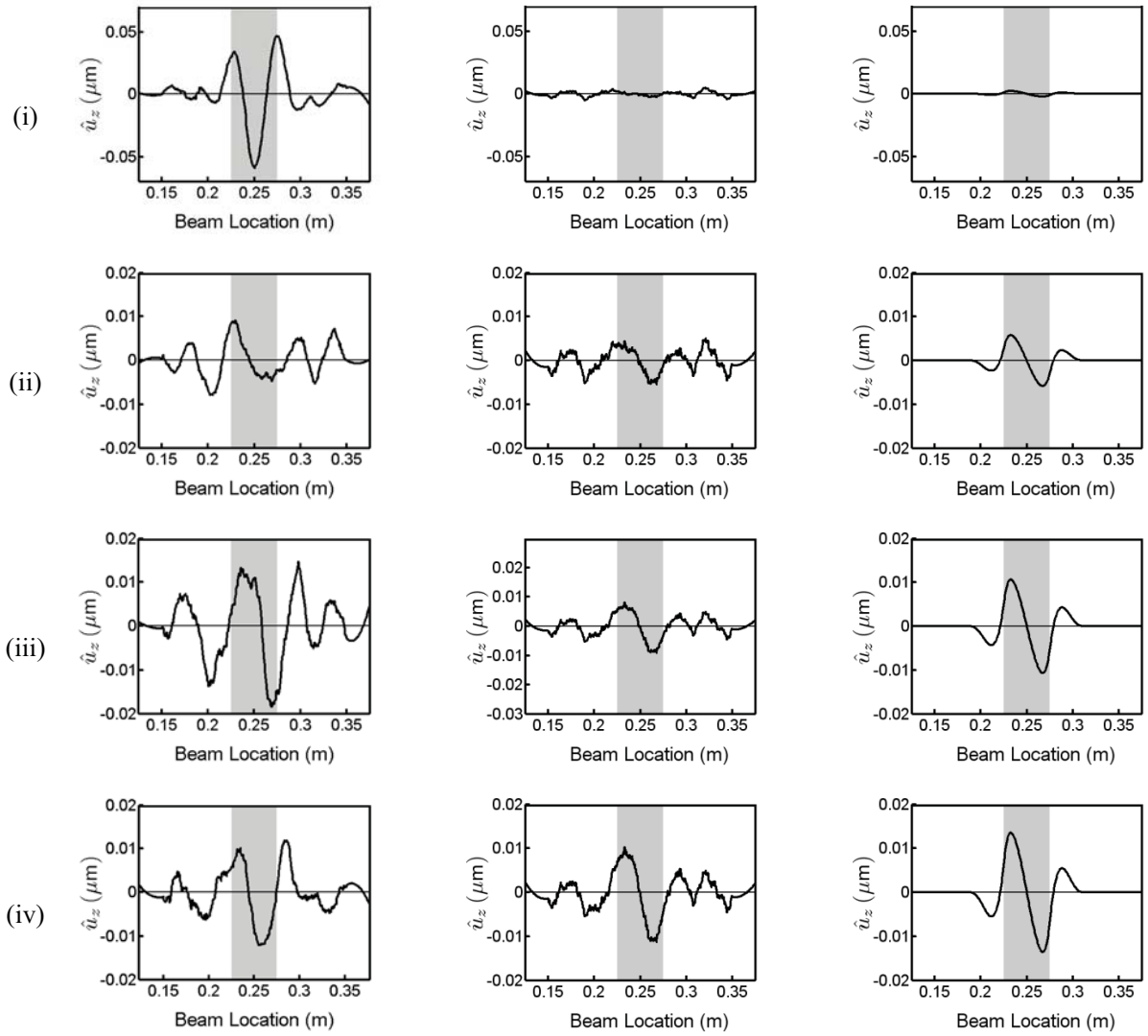

Figure 6.11. Continued on page 204

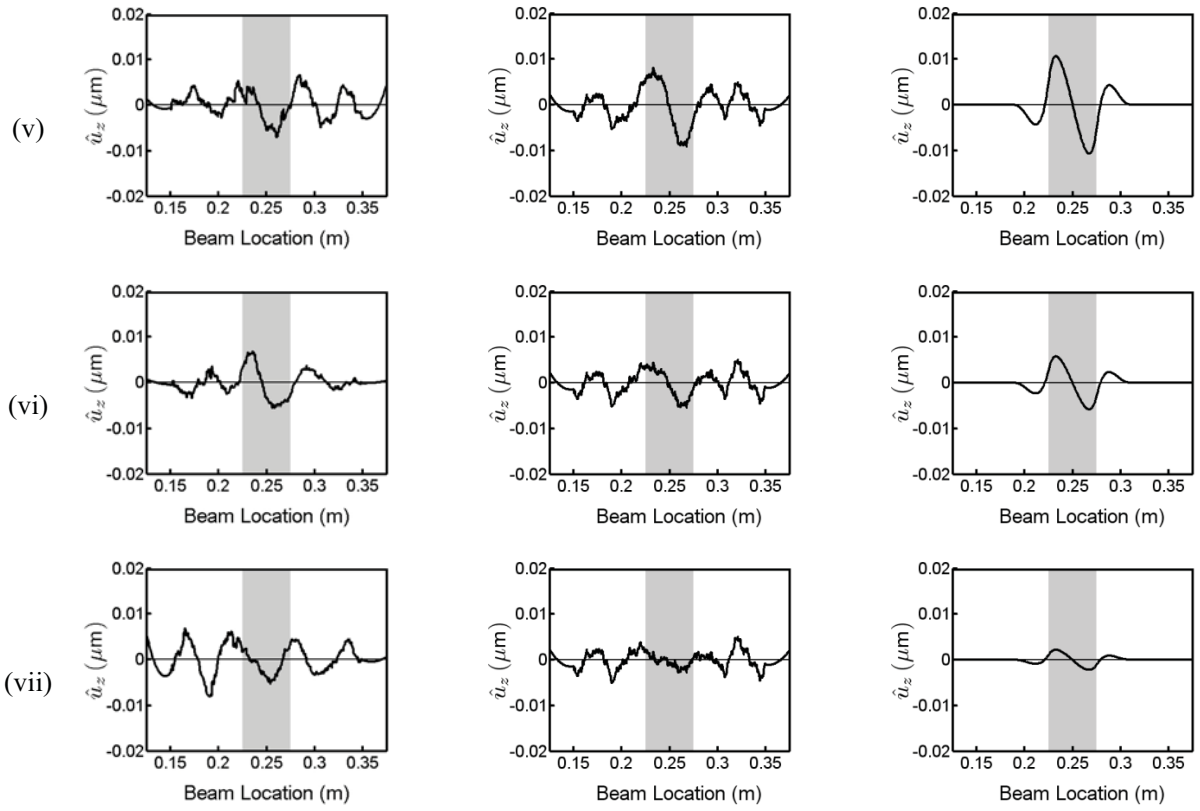

(a) (b) (c)

Figure 6.11. Acquired error in deflection ($\hat{u}_z$) for various laminate cantilever beams with a 50mm delamination at different depths. The rows denote the depths of the delamination and are (i) $h_2/h = 0.125$, (ii) $h_2/h = 0.25$, (iii) $h_2/h = 0.375$, (iv) $h_2/h = 0.5$, (v) $h_2/h = 0.625$, (vi) $h_2/h = 0.75$ and (vii) $h_2/h = 0.875$. The columns show the (a) experimental results, (b) simulated results with equivalent noise and (c) simulated results in the absence of noise. A third-order polynomial ($n = 3$) Savitzky-Golay smoothing ($r = 0$) filter was used with a filter width of 151 points ($m = 75$). The shaded section illustrates the location of the delaminated section.

6.5 Beam Curvature Error

An algorithm based on beam curvature error for the detection of through-the-width delamination within a composite laminate beam is presented in this section. For various delamination lengths and depths, as well as filters parameters; damage features of the algorithm are investigated and the effectiveness of the algorithm in detecting delamination is evaluated. Initially, an examination of previous research into the use of beam curvature error for the detection of delamination is presented. This is followed by the formulation of the algorithm and discussion of the experimental results.

6.5.1 Previous Studies

A previous investigation conducted by Qiao et al. (2007a) assessed the use of 1D SLDV for the evaluation of various curvature based damage detection methods. In order to obtain the curvature of a beam from deflections measured using a 1D vibrometer, the second-order derivate of the measured deflections were calculated using the fourth-order central difference approximation. Using the evaluated curvature, a number of damage detection algorithms were investigated, including uniform load surface (Farrar, CR & Jauregui 1998), gapped-smoothed (Ratcliffe & Bagaria 1998), generalised fractal dimension (Hadjileontiadis, Douka & Trochidis 2005), and strain energy method (Cornwell, Doebling & Farrar, C 1999). From their investigation, Qiao et al. (2007a) found that gap-smoothed and strain energy methods provided the best damage detection and identification using 1D scanning laser Doppler vibrometry (SLDV).

More recently, Cao and Qiao (2009) developed an algorithm, which determines the curvature from measured beam deflection using an *à trous* Laplace operator that has been

smoothed using a Gaussian filter. The damage features are then intensified using a smoothing Teager energy operator (Kaiser 1993). Cao and Qiao (2009) conducted an experimental investigation to detect and locate a large delaminated zone, artificially produced within a composite E-glass fibre laminate cantilever beam. The beam was vibrated with a continuous sweep sine excitation via a piezoelectric patch attached at the clamped end. Using a 1D vibrometer the beam deflections of the second mode was utilised to determine the developed algorithm. The curvature based algorithm was highly successful in locating the damage, which was identified by large peaks at the boundaries of the delaminated zone.

6.5.2 Algorithm

This section presents a curvature based algorithm for detecting delamination, which can be compared to the *GDEB* algorithm. However, it is not intended as a full investigation of the use of curvature based methods, as this has already been established previously (Qiao et al. 2007a; Cao & Qiao 2009). For this reason the most simple curvature based algorithm was utilised that required the least amount of signal processing and did not require previous measurements of the undamaged structure to be taken. Through-the-width delamination within a composite beam creates a local change in stiffness over the length of the delaminated zone and, thus, generates a discontinuous change in beam curvature over the delamination length. An algorithm to detect this change in curvature can be produced by comparing the curvature of the delaminated beam to the curvature of an equivalent undamaged beam.

The *curvature error* algorithm ($\hat{\kappa}$) compares the curvature of an equivalent undamaged

beam, determined by a least-squares-fit of all the measured beam deflections (κ_{LS}), against the curvature evaluated by a 1D Savitzky-Golay differentiating filter (κ_{SG}) and can be expressed by Equation (6.19). For an undamaged beam oscillating at a frequency within its stiffness controlled region, the beam deflection can be represented by a third-order polynomial, as discussed in Section 6.3.1. A least-squares-fit of all the measured beam deflection provides a baseline estimation of the undamaged curvature of the beam. The actual curvature of the beam is then determined by evaluating the second derivative ($r = 2$) of deflection with respect to the length of the beam using a 1D Savitzky-Golay differentiating filter of third-order polynomial ($n = 3$). A flow diagram of the filtering process is illustrated in Figure 6.12.

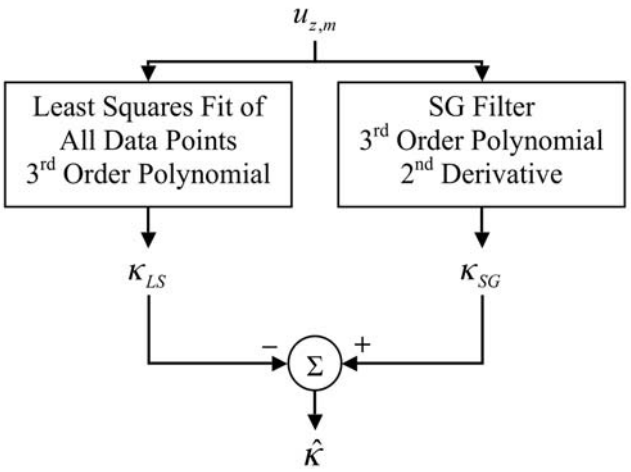

Figure 6.12. Flow diagram of the *curvature error* algorithm $\hat{\kappa}$.

The *curvature error* algorithm was investigated for use in detecting through-the-width delamination of various lengths and depths within a composite laminate beam. The

effectiveness of the *curvature error* algorithm in detecting the delamination for varying filter widths used within the Savitzky-Golay filter, delamination lengths and delamination depths is presented in the following subsections. In order to assess the effectiveness of the *curvature error* algorithm, results obtained from experiments were compared to that of the analytical model.

6.5.3 Filter Size

Figure 6.13 shows the evaluated beam curvature error ($\hat{\kappa}$) for a range of filter points ($2m + 1$) utilised within the Savitzky-Golay filter. The simulated results (column c) show that there is a change in curvature over the area of the delaminated section. Leading up to the delamination, the curvature error is approximately zero. At the left boundary of the delamination there is an increase in curvature error from zero to a maximum peak value. This curvature error then decreases linearly, passing through zero in the middle of the delaminated zone and continues until the curvature error reaches its minimum peak value at the right boundary of the delamination. At this right boundary, the curvature error has an increase back to zero. Within this distribution the delamination boundaries are located at the mid-point of the increase in curvature.

There is a slight error in beam curvature that occurs in the non-delaminated regions of the beam. This non-zero region is due to the fact that the undamaged baseline curvature of the beam is estimated using a least-squares-fit of the measured deflection from the damaged beam. This process causes the estimated undamaged baseline curvature to diverge from the actual undamaged curvature of the beam, which skews and distorts the *curvature error* algorithm making it harder to positively identify the delamination damage with certainty.

The amplitude of the curvature distortion was shown to increase with a decrease in filter length. Essentially, as the filter length increases, the curvature distortion becomes spatially smoothed. This effect significantly influences the ability of this algorithm to detect the delamination. As the filter length is decreased, the amplitude of the distortion increases, with an additional increase in the noise within the distribution, which would obscure the distortion. Whereas, when the filter length is increased, the distortion becomes spatially smoothed, thus decreasing its amplitude. This makes identification of the delamination difficult.

From the experimental results, it was observed that for a filter width of 51 points ($m = 25$) the error in beam deflection is severely affected by noise. As the filter width increases to 101 points, the measurement noise is alleviated and the delamination can be qualitatively identified. However, as the filter is increased to 151 and 201 data points, the error in beam curvature becomes spatially smoothed, preventing the delaminated zone being positively identified with certainty.

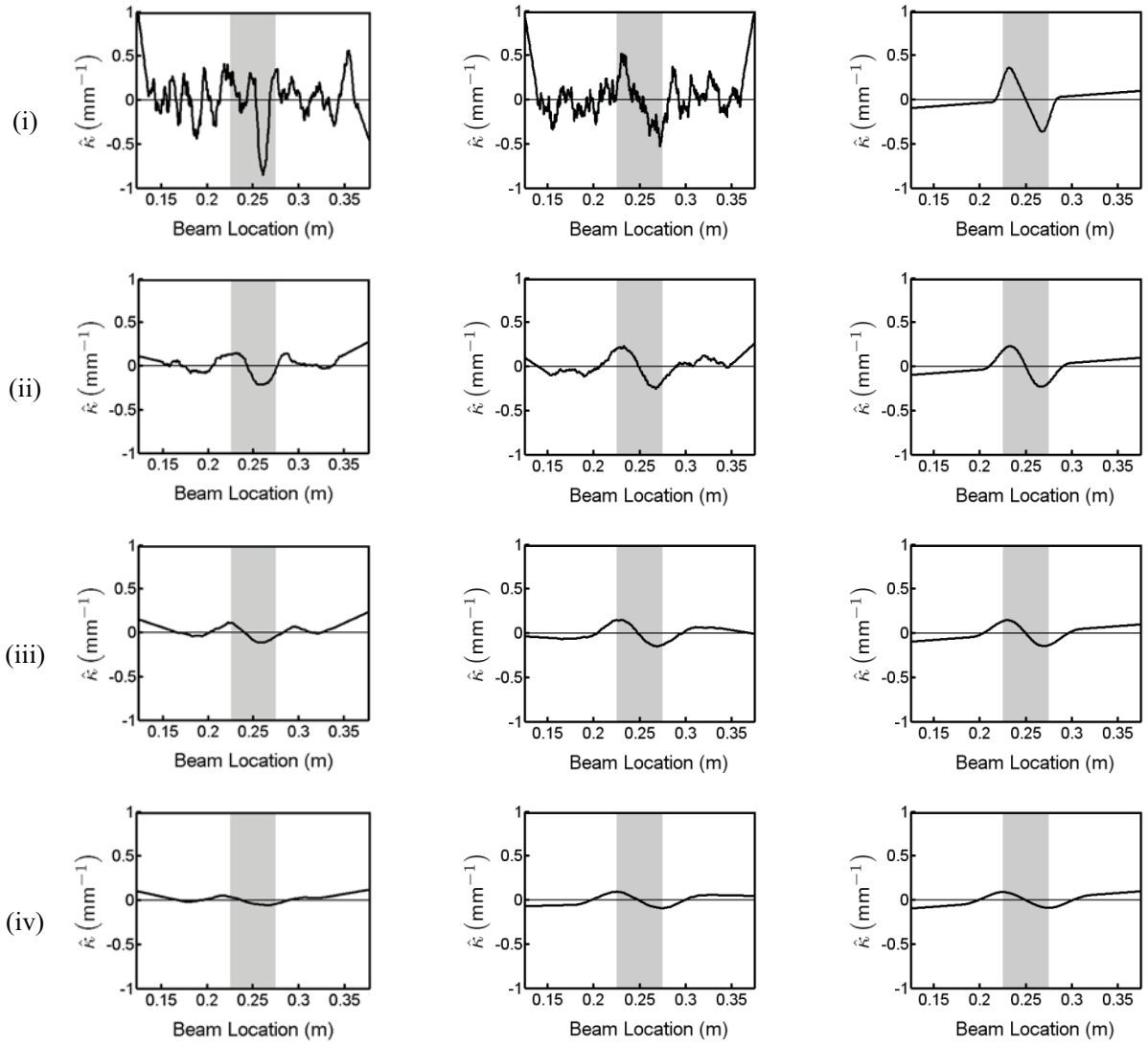

Figure 6.13. Acquired error in curvature ($\hat{\kappa}$) for a delaminated cantilever beam for four different quantities of filter points ($2m + 1$) utilised within the third-order polynomial ($n = 3$) Savitzky-Golay smoothing ($r = 0$) filter. The rows denote the filter widths of (i) $m = 25$, (ii) $m = 50$, (iii) $m = 75$ and (iv) $m = 100$. The columns show the (a) experimental results, (b) simulated results with equivalent noise and (c) simulated results in the absence of noise. The delamination is located between fourth and fifth layer and 50mm in length. The shaded section illustrates the location of the delaminated section.

6.5.4 Delamination Length

In Figure 6.14, the evaluated beam curvature error ($\hat{\kappa}$) is presented for four composite laminate cantilever beams, each with a different length of delamination between the mid-layers ($h_2/h = 0.5$). The simulated results (column c) show that a decrease in the length of the delamination results in a decrease in the amplitude of the distortion. However, this increase in delamination length also exacerbates the divergence in the undamaged baseline curvature estimate, and causes large non-zero curvature errors at the non-delaminated regions. The main reason for this divergence is because of the relatively large length of the delamination with respect the length of the measured data points. If this is taken to the extreme and the delamination zone spans the entire beam, then the least-squares-polynomial-fit will match the delaminated beam perfectly, and theoretically no curvature error would be observed.

From the experimental results, a delamination length of 25mm cannot be detected. The measurement noise affects the results significantly and the change in curvature at the delaminated zone is not clearly distinguishable. For a delamination length of 50mm the change in curvature at the delaminated zone can begin to be observed, which matches the simulated results with added measurement noise. At large delamination lengths the change in curvature is easily detectable.

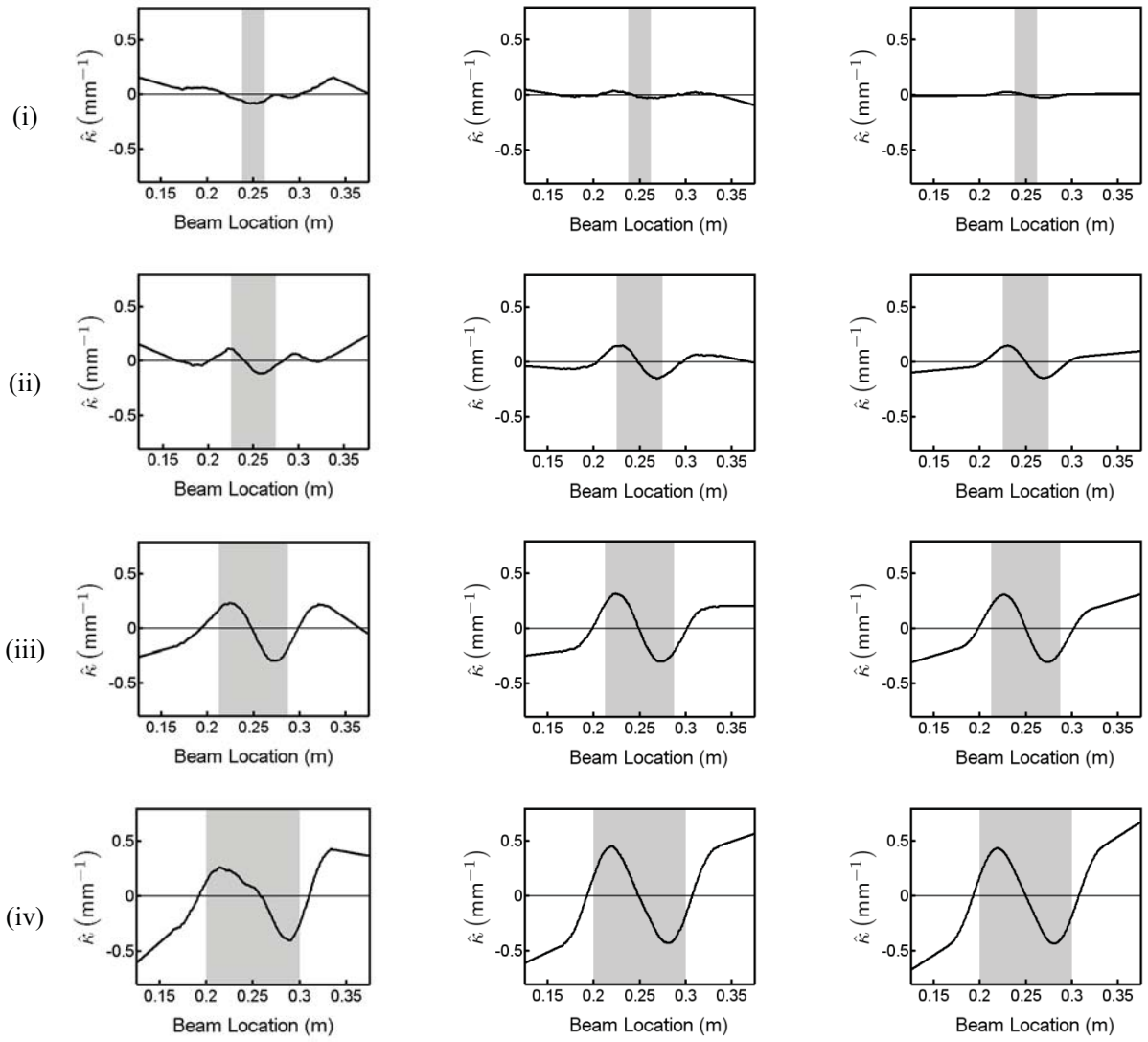

Figure 6.14. Acquired error in deflection ($\hat{\kappa}$) for a delaminated cantilever beam for four different lengths of delamination between the mid-layers ($h_2/h = 0.5$). The rows denote the lengths of the delamination and are (i) $L_d = 25$mm, (ii) $L_d = 50$mm, (iii) $L_d = 75$mm and (iv) $L_d = 100$mm. The columns show the (a) experimental results, (b) simulated results with equivalent noise and (c) simulated results in the absence of noise. A third-order polynomial ($n = 3$) Savitzky-Golay smoothing ($r = 0$) filter was used with a filter width of 151 points ($m = 75$). The shaded section illustrates the location of the delaminated section.

6.5.5 Delamination Depth

Figure 6.15 shows the evaluated curvature error ($\hat{\kappa}$) for seven laminate cantilever beams, each having a delamination of 50mm in length between different layers.

The simulated results (column c) reveals that the maximum amplitude change in curvature error occurs when the delamination is between the middle layers (i.e. between the fourth and fifth layer, $h_2/h = 0.5$). As the delamination gets closer to the surface there is a decrease in the amplitude of the distortion.

From the experimental results (column a), a large spike in the curvature error at the delaminated zone was observed for the beam with delamination between the first and second layer ($h_2/h = 0.125$), as seen in Figure 6.15(a)(i). This spike did not match the simulated results (Figure 6.15(c)(i)). As discussed in the previous Section 3.2.1, the first layer is the layer which is being measured by the 1D vibrometer. In this case the first layer buckles, creating a large deflection and, thus, a large curvature change.

All delaminated depths examined agree with the simulated results, but large edge effects cause difficulty in qualitatively identifying the delaminated zone.

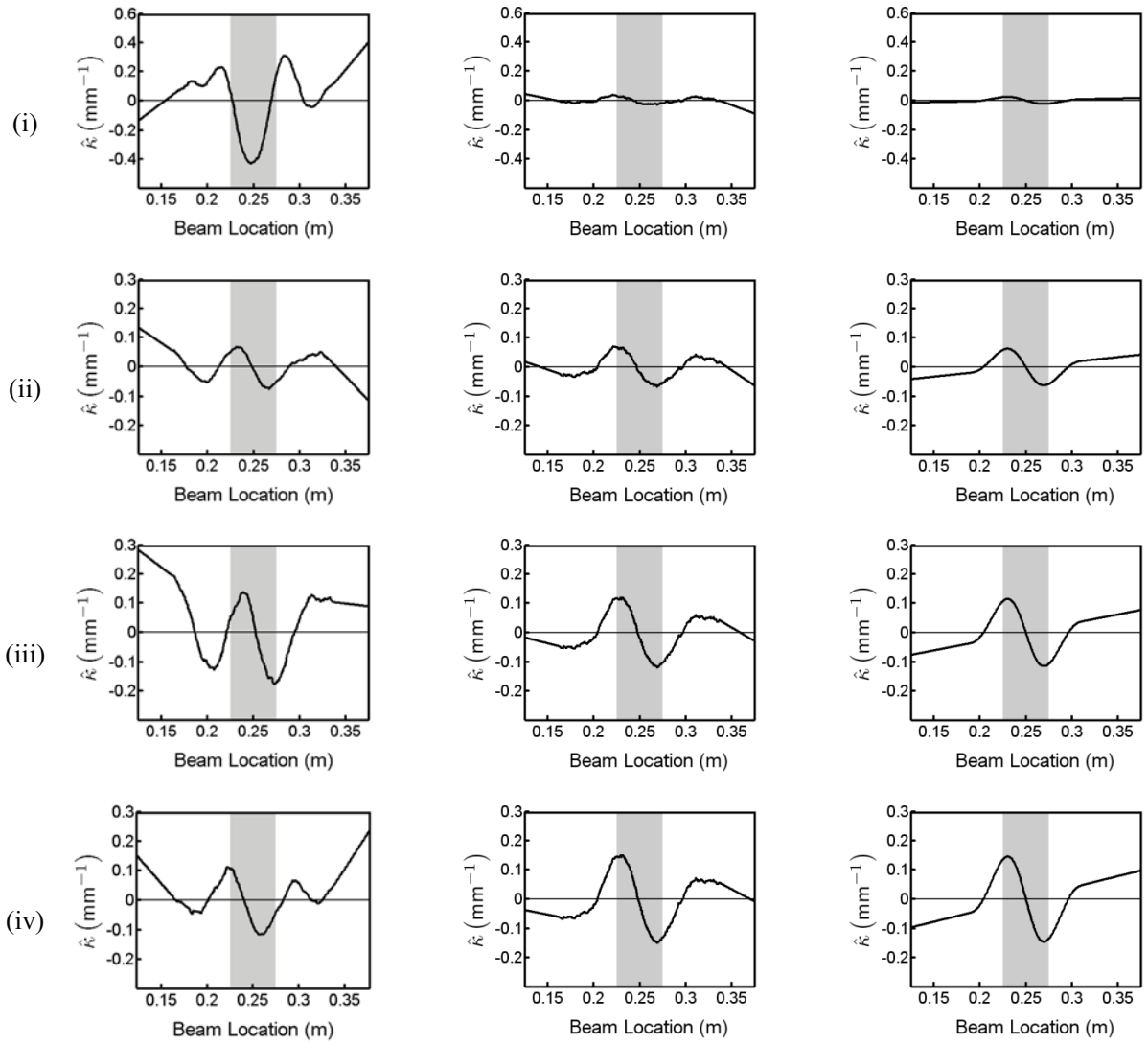

Figure 6.15. Continued on page 215

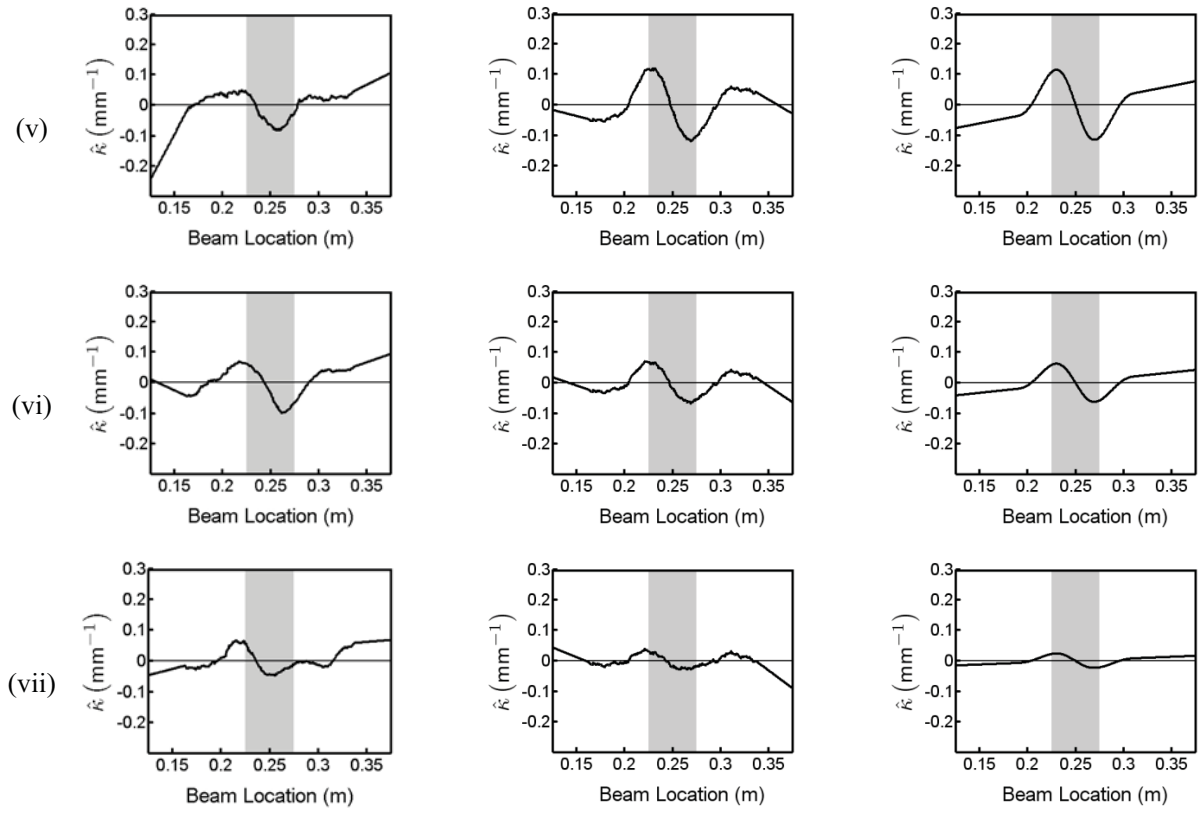

(a) (b) (c)

Figure 6.15. Acquired error in curvature ($\hat{\kappa}$) for various laminate cantilever beams with a 50mm delamination at different depths. The rows denote the depths of the delamination and are (i) $h_2/h = 0.125$, (ii) $h_2/h = 0.25$, (iii) $h_2/h = 0.375$, (iv) $h_2/h = 0.5$, (v) $h_2/h = 0.625$, (vi) $h_2/h = 0.75$ and (vii) $h_2/h = 0.875$. The columns show the (a) experimental results, (b) simulated results with equivalent noise and (c) simulated results in the absence of noise. A third-order polynomial ($n = 3$) Savitzky-Golay smoothing ($r = 0$) filter was used with a filter width of 151 points ($m = 75$). The shaded section illustrates the location of the delaminated section.

6.6 Summary

A number of researchers have investigated the use of beam deflections measured using 1D scanning laser Doppler vibrometry for the detection of damage. Two different types of algorithms based on the kinematics of beam deformation, specifically deflection and curvature, have been investigated by these researchers (Pai et al. 2004; Cao & Qiao 2009). Interestingly, the use of the GDE of beam deflection has not been investigated as a basis for a damage detection algorithm, even though both beam deflection and curvature are governed by this equation.

In this chapter, three algorithms for the detection of through-the-width delamination in a composite beam were presented. These algorithms were all developed to utilise quasi-static measurements of displacement, taken using a 1D vibrometer and included deflection, curvature and the GDE for beam deflection. These algorithms were based on:-

- the evaluation of the residual term of the GDE of beam deflection using a 1D Savitzky-Golay differentiating filter (*GDEB* algorithm);
- the error between the deflection measured by the 1D vibrometer and same deflection smoothed by 1D Savitzky-Golay smoothing filter (*deflection error* algorithm), and;
- the error in curvature determined using a 1D Savitzky-Golay differentiating filter and an estimate of the undamaged curvature using a least-squares-fit of all the deflection (*curvature error* algorithm).

Each of the above algorithms assumes that the beam is undamaged and will produce zero deflection error, zero curvature error or a zero residual term in the GDE of beam deflection. However, if through-the-width delamination is introduced into the beam,

discontinuities are observed in the *GDEB* and *deflection error* algorithms at the boundary locations of the delamination. For the *curvature error* algorithm, the curvature error was observed to change over the entire area of the delaminated zone.

To evaluate the effectiveness of the algorithms for the detection of through-the-width delamination in composite laminate beams, a number of experiments were conducted. These experiments were aimed at investigating the effect of the length and depth of the delamination, as well as the filter length used within the Savitzky-Golay differentiator, on identifiable damage features of each algorithm. An analytical model was also developed, based on Euler-Bernoulli beam theory, which provided a means of understanding the characteristics of the damage detection algorithms. The simulations were conducted with and without added noise, and were compared to the trends observed in the experimental results.

The simulated results showed that the *deflection error* and *GDEB* algorithms both experience local distortions centred at the two boundaries of the delaminated zone, which were characterised by doublet-like curves. For the *deflection error* algorithm, the minima and maxima of the doublet-like curves were on the left and right, respectively, whereas the *GDEB* algorithm was opposite. In addition, the delamination was observed to be located at the point where the doublet curve crossed over the zero point between the minima and maxima. This mid-point of the doublet curves can therefore be used to identify the boundaries of a delamination zone. For the *curvature error* algorithm, the delamination was observed to produce a distortion over the entire length of the delamination zone. This distortion was characterised by an increase in the curvature error from zero at the left boundary, then a linear decrease in curvature error which passes through zero in the middle

of the delamination zone and then an increase back to zero at the right boundary. The position of the delamination boundaries was observed to be located in the middle of the increases in curvature error.

A number of tests were conducted to evaluate the effectiveness of each algorithm in detecting delamination for various lengths and depths, as well as for different filter lengths used within the Savitzky-Golay filter. From this study, three significant observations were made, relating to:-

1. the effect the filter width has on noise reduction and the damage features of each algorithm;
2. the shape of the damage features created by a delamination, and;
3. the amplitude of the damage features created by a delamination.

For the *deflection error* and *GDEB* algorithms, the length of the doublet curve distribution is approximately equal to the filter length. When the filter length is greater than the delamination length, the two doublet curves will coincide and the centres of the doublet curves will shift outward from the location of the delamination boundaries. This shifting of the mid-points of the doublet curves produces an over estimate of the delamination length, however, a correction factor could be applied that is based on the length of the filter. In addition, the distortion, due to the delamination experienced by the *curvature error* algorithm, also becomes spatially smoothed with an increase in filter length. However, excessive spatial smoothing of the distortion makes the evaluation of the location of the delamination boundaries difficult to determine.

By increasing the filter length there is a decrease in noise in the evaluated distribution.

However, by changing the filter length, the distortion created by the delamination in each algorithm also changes in amplitude. For the *deflection error* algorithm, an increase in filter length caused an increase in the amplitude of the distortion. This effect significantly aids the detection of delamination, however, it is also limited by experimental constraints. The vibrometer system can only measure a line of 501 points, therefore, the filter sizes required to alleviate noise and increase the amplitude of the doublet curves is currently constrained. Conversely, for the *curvature error* and *GDEB* algorithms, an increase in filter length causes a decrease in amplitude of the distortion created by the delamination. This effect significantly influences the length of delamination detectable by these algorithms. With a decrease in filter length the amplitude of the distortion would increase. However, the noise in the distribution would also increase and, therefore, obscure the distortion created by the delamination. With an increase in filter size the amplitude of the distribution would be spatially smoothed and decreased in amplitude, making the features of the distortion harder to distinguish.

The amplitude of the distortion created by the delamination in each algorithm will decrease with a decrease in length of the delamination and also with a delamination depth that is positioned further from the mid-layer of the beam. These two observations have significant implications for the detection of delamination. Damage that is small in length, and/or positioned closer to the surface, will produce a distortion for each algorithm that is of small amplitude. For the *deflection error* algorithm, this type of delamination would require a large filter length to resolve the distortions, however, due to the current constraints with the vibrometer, these types of delamination cannot be detected. Conversely, for the *curvature error* and *GDEB* algorithms, the filter length that can be used to resolve the

distortion created by delamination is limited to a specific range. The lower limit of this range is bound by the point at which the filter length is too small and noise obscures the distortion. The upper limit is bound by the point at which the filter is too large and the distortion is too spatially smoothed to distinguish any features. Therefore, as the delamination length decreases and/or the delamination depth is located nearer to the surface, the upper filter length limit will move closer to the lower filter length limit, restricting the size of the delamination that is detectable.

The experimental results obtained in this study were in good agreement with the simulated results. Though, due to the levels of noise experienced in the measurements of deflection, only qualitative detection of the delamination can be performed. A recommendation from the research in this study (which agrees with the findings with previous studies (Ghoshal et al. 2003; Pai et al. 2004)) is to increase the oscillatory frequency of the beam into the dynamic region. This is instead of using quasi-static measurements of deflection and would remove noise created by low frequency ground-borne vibrations. However, by utilising the dynamic region of the beam, the *governing equation* algorithm will need to take into account inertial and damping effects.

In conclusion, the *deflection error* algorithm has significant advantages. The main being that the amplitude of the doublet curves created at the boundaries of the delamination zone increases with an increase of the filter length used within the Savitzky-Golay filter. Although, the noise in the deflection measurements means that significant filtering is required. The *curvature error* algorithm has a significant disadvantage, as an undamaged or estimated baseline measurement of curvature is required to evaluate the damage. The damage feature created by the delamination produces a non-zero curvature error

distribution over the entire length of the delaminated zone, which peak near the boundaries of the zone. Lastly, the *GDEB* algorithm has the most promise, as (unlike the *curvature error* algorithm) this algorithm does not require an undamaged baseline measurement to evaluate the damage, and (unlike the *deflection error* algorithm) it utilises a simple filtering process with the location of the delamination boundaries being related to features of the distribution.

Chapter 7. Conclusion

The aim of this thesis is to investigate and develop new non-destructive evaluation techniques for strain measurement and damage detection utilising 1D and 3D scanning laser Doppler Vibrometry (SLDV). To achieve this aim, specific chapters focus on aspects of strain measurement and damage detection, presenting newly developed techniques and detailing the experimental setup utilised. These chapters contribute to the field of knowledge within non-destructive testing through the use of state-of-the-art 1D and 3D SLDV technology and the Governing Differential Equation (GDE) of displacement.

The review of the literature related to this study (Chapter 2) broadly discusses existing strain measurement and damage detection techniques and then current techniques that utilise SLDV technology. The literature review establishes gaps in the field of research, which are:

- a thorough investigation of accuracy of quasi-static bending strain measurements using current 1D SLDV technology is required;
- an examination of the accuracy of a newly developed full-field surface strain measurement technique utilising 3D SLDV is required and;
- there is potential for a damage detection algorithm technique based on the violation of the GDEs of displacement.

Therefore the specific aims of this thesis are to:

- determine the accuracy of a bending strain measurement technique;

- determine the accuracy of in-plane surface strain measurement technique, and;
- develop and investigate the effectiveness of the proposed damage detection techniques in common damage scenarios.

Chapter 3 describes the two experimental rigs, which were developed to evaluate the strain measurement techniques and damage detection algorithms based on either out-of-plane or in-plane displacement. The first experimental rig provides out-of-plane displacement to a cantilever beam structure using an electromagnetic shaker, to evaluate the accuracy of the bending strain measurement technique and the algorithms for the detection of through-the-width delamination in a composite structure. The second rig provides in-plane displacements to a plate structure using a piezo-stack actuator in order to evaluate accuracy of the newly developed surface strain measurement technique. This rig is also used to investigate the application of the damage detection algorithms for the detection of crack damage in plate structures.

7.1 Strain Measurement

The first part of this thesis presents investigations into two experimental strain measurement techniques. The first is a newly developed, full-field surface strain measurement technique that utilises 3D SLDV technology. This full-field surface strain technique is entirely new and has only been possible in the last few years with the development of 3D SLDV. The second technique employs the use of 1D SLDV for the measurement of bending strain, in a beam, from measured out-of-plane deflections.

To determine strain from measured displacement, a Savitzky-Golay differentiation filter is used. This filter essentially performs a local polynomial regression on a number of points

to determine the smoothed spatial derivative of the displacement. The filter smooths and differentiates the displacement to determine strain, but is able to preserve the relative maxima, minima and width of the strain distribution. For both the extensional and bending strain measurement techniques, the Savitzky-Golay filter is found to introduce artefacts (distortions in the determined strain) at the edge points of the measurement grids, up to half the length of the filter width in from the edge. These edge artefacts contribute significant errors to the evaluation of strain, and the accuracy of strain measurement was evaluated both excluding and including these edge points.

For the in-plane and bending strain measurement techniques, the effect of the distance between the measurement points, applied load and the numerical differentiation parameters on the accuracy of strain estimation is investigated. In addition, a series of experiments are conducted to validate the newly developed in-plane strain measurement technique, by measuring the strain field in the vicinity of two simple stress concentration cases:- an edge crack and a notch.

7.1.1 In-Plane Strain

To investigate the newly developed 3D SLDV surface strain measurement technique, an acrylic plate is excited at 1Hz with uniaxial quasi-static loading. Displacement measurements of the plate, taken from a mesh 19 x 19 points and a 2D Savitzky-Golay differentiating filter are utilised to determine the surface strain from the measured displacements.

For the surface strain measurement technique, optimal accuracy and resolution is achieved when the polynomial approximation of the strain field used within the Savitzky-Golay

differentiating filter is equal or less than a third-order polynomial. In addition, for the specific data acquisition parameters and experimental setup used in this study, the accuracy of the surface strain measurement technique significantly decreases when the measurement grid interval is less than 2mm and the applied stress amplitude to the plate is less than 400kPa.

When using a third-order polynomial ($n = 3$) Savitzky-Golay differentiating filter over a filter distribution of 9x9 measurement points ($m = 4$), a mesh spatial interval of 2mm and a stress amplitude of approximately 1.05MPa, a standard deviation of in ε_x and ε_y of 15.9% (14.7 microstrain) and 2.6% (6.4 microstrain) from the mean values ($\bar{\varepsilon}_x$=-92.5 microstrain and $\bar{\varepsilon}_y$=247 microstrain) is produced, respectively.

Finally, an investigation of the in-plane surface strain measurement technique is presented, which evaluates the effectiveness and accuracy of the technique in measuring the surface strain field in the vicinity of stress concentrator compared to a numerically determined strain field. Two stress concentrators are considered:- a crack and a notch in a plate. Both surface strain fields are found to produce similar root mean standard deviations to those observed for the uniform strain fields. In addition, the distortions at the edge points of the strain field, which are due to the edge artefacts created by the Savitzky-Golay differentiating filter, significantly increase the error in measured strains and need to be excluded.

7.1.2 Bending Strain

For the bending strain measurement technique, experimental results are presented for an aluminium cantilever beam, which is subjected to a 1Hz sinusoidal out-of-plane

displacement at the free end. The deflection of the beam is measured using a 1D vibrometer at a number of points along the centre-line of the beam length, and bending strain is determined by a 1D Savitzky-Golay differentiating filter.

A number of findings, from the investigations undertaken to evaluate the accuracy of the bending strain measurement technique, are presented. The bending strain measurement technique is best approximated by using a third-order polynomial in the Savitzky-Golay differentiator. An accurate bending strain measurement can be produced at any spatial interval, as long as the filter width spans a fixed distance. In addition, changes in applied load have no effect on the accuracy of the technique. When using a third-order polynomial Savitzky-Golay differentiating filter with a filter width of approximately 20% of the available measurement points and a spatial interval of 1mm, the standard deviation of the determined bending strain is 2% of the fitted bending strain at the middle measurement point.

7.2 Damage Detection

Chapters 5 and 6 comprise the second part of this thesis, focusing on damage detection. They introduce new damage detection algorithms based on the GDE of in-plane and out-of-plane displacement, respectively.

Each of these chapters discusses the theory surrounding the new damage detection algorithms, based on derivations of the GDE of displacement, which are a combination of the conditions of equilibrium and strain compatibility. Two algorithms are proposed for the detection of damage, by evaluating the residual term of the governing differentiation equation of displacement. The first algorithm utilises the GDE of in-plane plate

displacement to detect crack damage within a plate (*GDEP* algorithm). The second algorithm utilises the GDE of beam deflection to detect through-the-width delamination in a composite laminate beam (*GDEB* algorithm).

The proposed algorithms numerically differentiate measured quasi-static displacement in order to determine the residual term of the GDEs of displacement. Ideally, a non-zero residual term would indicate a violation of the GDE and the presence of damage. In this study a Savitzky-Golay differentiating filter is utilised to differentiate the displacement measurements.

7.2.1 Detection of Crack Damage

In Chapter 5 the effectiveness of the *GDEP* algorithm is compared with two additional damage detection algorithms:- error in measured and smoothed displacement (*displacement error* algorithm) and surface strain normalised by its mean (*surface strain* algorithm). Each algorithm utilises in-planes displacements measured using a 3D vibrometer and is determined by a smoothing and/or differentiating the measured displacements using a 2D Savitzky-Golay filter.

When crack damage propagates into the measurement area, the discontinuity in the displacement field created by the crack will create a large non-zero term in each algorithm. To evaluate the location of the crack damage, a threshold value is utilised for each algorithm, which is greater than the noise level in the measurements.

The three algorithms are utilised for the detection of crack damage in a plate structure from measured in-plane displacements using a 3D vibrometer. Experimental investigation determined that the *GDEP* algorithm and *displacement error* algorithm are not affected by

structural geometries, such as a notch in the vicinity of the measurement grid, whereas the *surface strain* algorithm is affected. When a crack lies within the measurement grid, each technique is successful in detecting all the lengths tested. For the *displacement error* and *surface strain* algorithms, a crack could only be detected when considering the algorithm in the direction of the applied load. The GDEP algorithm however is independent of the applied load. The accurate detection and localisation of crack damage verifies the validity of these algorithms and they need no a-priori information about the specimen geometry or construction unlike other damage detection techniques.

7.2.2 Detection of Delamination in a Composite Beam

Chapter 6 introduces the algorithm based on the GDE of beam deflection (*GDEB* algorithm) for the detection of through-the-width delamination in a composite laminate beam. The investigation evaluates the effectiveness of the algorithm in detecting various delamination lengths and depths, as well as assessing the optimal filter width used within the Savitzky-Golay differentiating filter. The effectiveness of the algorithm is also compared with two commonly used damage detection algorithms:- error in measured and smoothed displacement (*deflection error* algorithm) and error in evaluated and expected undamaged curvature (*curvature error* algorithm). Each algorithm utilises beam deflections measured using a 1D vibrometer and is determined by smoothing and/or differentiating the measured deflections using a 1D Savitizky-Golay filter.

An analytical model of the delaminated beams is developed based on Euler-Bernoulli beam theory in order to provide an understanding of damage detection techniques in the absence of noise. In order to compare the experimental results with that of the analytical

results, noise was also added to the analytical displacement equivalent to that observed in the measured displacements.

A number of observations from the simulated results are presented in Chapter 6.

All of the damage detection techniques are found to be less sensitive to detecting delamination with decreasing length and proximity to the surface. The exception is where the delamination buckles when adjacent to the surface of the beam.

With increasing filter width, the *curvature error* algorithm and *GDEB* algorithm become less sensitive, whereas the *deflection error* algorithm becomes more sensitive to the damage. Even though the *deflection error* algorithm becomes more sensitive to the damage as the filter width is increased, the size of the filter width is limited to the number of measurement points that can be taken. In addition, with an increase in filter width, multiple delaminations will be spatially filtered to coincide and could therefore make detection difficult. This limitation makes the deflection error algorithm not very suitable for detecting delamination.

For the *curvature error* algorithm and *GDEB* algorithm, it is observed that there is a specific range of delamination lengths and depths that can be detected, dependent on the filter length. The lower limit of this range is the point at which the filter length is too small to remove noise from the signal. The upper limit of this range is at the point at which the filter is too large and the signal is spatially smoothed, such that the damage indicators are not discernable.

The main advantage of the *GDEB* algorithm over the *curvature error* algorithm is that the *GDEB* algorithm does not require an undamaged estimate of the damaged beam and the

location of the boundaries are related to features in the signal distribution. When comparing the simulated results with the experimental results there is good agreement. However, due to the high levels of noise experienced in the measured deflections, only qualitative detection of the delamination is possible.

7.3 Overview

The research presented in this thesis has contributed to the fields of strain measurement and damage detection by investigating and determining the accuracy of new strain measurement techniques for both in-plane and bending strain. This research has also developed, investigated and experimentally validated the sensitivity of the proposed damage detection techniques, in common damage scenarios.

Through Chapter 4, this thesis provides an in-depth investigation of the use of 1D SLDV for the measurement of bending strain in beam structures, as well as the use of 3D SLDV for the measurement of surface strain induced by in-plane loading. This work will allow researchers to understand the limitation of the Savitzky-Golay differential filter for use in evaluating strain, as well as give a point of reference for the type of accuracies that are achievable when using such systems to measure strain.

The developed damage detection algorithms based on the GDE of displacement presented in Chapters 5 and 6 show significant promise in detecting damage. They perform equally well, if not better than commonly used damage detection algorithms based on kinematic parameters such as displacement and curvature/strain.

7.4 Further Research Possibilities

There are several future research possibilities arising from this work. For the strain measurement and damage detection techniques, possibilities exist in the application of these techniques to curved or shell-like structures and different types of composite materials. In addition, the investigation of different differentiating and filtering techniques could be investigated.

For both the in-plane and bending strain measurement techniques, this research could also be extended by investigating the accuracy of the strain measurement techniques to measure broadband and dynamic strains. Investigations could be conducted into the measurement of bending strains measured on plates and shells.

When investigating the use of the GDE for beam deflection for the detection of through-the-width delamination, there was significant noise within the measured displacement, which caused a poor performance in the ability of the *GDEB* algorithm to detect delamination. This is an area that requires further development. Instead of using quasi-static measurement of deflection, the vibratory frequency of the beam could be increased into its dynamic region. This would remove noise created by low frequency, ground borne vibrations. By utilising the dynamic region of the beam, future research into the *GDEB* algorithm will need to consider the dynamic differential equations of beam deflection, which take into account inertial and damping effects.

With regards to the crack detection algorithm based on the GDE displacement, further investigations can be conducted to evaluate the sensitivity of the algorithm to identify small crack damage, as well as the sensitivity of the algorithm to the direction of applied

loads.

It is the author's intention to develop a system, using 3D SLDV, that is not only able to determine the surface strain on a vibrating plate- or shell-like structure, but also able to determine the presence of damage within the structure and, more importantly, able to evaluate the severity of the damage.

For the strain measurement and damage detection techniques researched in this thesis, there are many more future research opportunities than have been proposed, as these techniques are new to the important field of non-destructive testing.

Structural failures can be disruptive, cause economic loss or inflict severe injury. Being able to evaluate the strength and integrity of engineering structures in order to prevent catastrophic failure due to mechanical damage is of great importance. The techniques presented in this thesis go some way to providing a new means of detecting fatigue cracks or delamination for composite materials, through the use of new SLDV technologies.

References

Albrecht, H, Borys, M, Damaschke, N & Tropea, C 2003, *Laser doppler and phase doppler measurement techniques*, Berlin, Germany.

Annamdas, V & C. Soh 2010, 'Application of Electromechanical Impedance Technique for Engineering Structures: Review and Future Issues', *Journal of Intelligent Material Systems and Structures*, vol. 21, no. 1, pp. 41–59.

ASC 2005, *Aviation Occurrence Report Volume I, In-flight breakup over the Taiwan Strait, Northeast of Makung, Penghu Island, China Airlines Flight CI611, Boeing 747-200, B-18255, May 25, 2002*, no. ASC-AOR-05-02-001, Aviation Safety Council, Taipei, Taiwan.

ASM 1972, 'Eddy current inspection', in *Metals Handbook*, 8th ed., vol 9, American Society for Metals (ASM), Metals Park, Ohio.

ASTM, SE 2010, *Standard Terminology for Nondestructive Examinations*, ASTM International, West Conshohocken, PA.

Auld, B & Moulder, J 1999, 'Review of Advances in Quantitative Eddy Current Nondestructive Evaluation', *Journal of Nondestructive Evaluation*, vol. 18, no. 1, pp. 3–36.

Bendat, J & Piersol, A 2010, *Random Data: Analysis and Measurement Procedures*, 4th Ed., John Wiley and Sons, USA.

Black, J & Kohser, R 2008, *DeGarmo's Materials and Processes in Manufacturing*, 10th edn, John Wiley and Sons, USA.

Blitz, J & Simpson, G 1996, *Ultrasonic Methods of Non-Destructive Testing*, Springer, London, UK.

Bray, D & McBride, D 1992, *Nondestructive Testing Techniques*, John Wiley and Sons, New York, USA.

Cantwell, W & Morton, J 1992, 'The significance of damage and defects and their detection in composite materials: A review', *Journal of Strain Analysis for Engineering Design*, vol. 27, no. 1, pp. 29–42.

Cao, M & Qiao, P 2009, 'Novel Laplacian scheme and multiresolution modal curvatures for structural damage identification', *Mechanical Systems and Signal Processing*, vol. 23, no. 4, pp. 1223–1242.

Carden, E & Fanning, P 2004, 'Vibration Based Condition Monitoring: A Review', *Structural Health Monitoring*, vol. 3, no. 4, pp. 355 –377.

Cartz, L 1995, *Nondestructive Testing: Radiography, Ultrasonics, Liquid Penetrant, Magnetic Particle, Eddy Current*, ASM International.

Cazzolato, B, Wildy, S, Codrington, J, Kotousov, A & Schuessler, M 2008, 'Scanning laser vibrometer for non-contact three-dimensional displacement and strain measurements', in *Acoustics 2008: Acoustics and Sustainability*, Australian Acoustical Society, Geelong, Victoria, Australia.

Chang, P & Liu, S 2003, 'Recent Research in Nondestructive Evaluation of Civil Infrastructures', *Journal of Materials in Civil Engineering*, vol. 15, no. 3, pp. 298–304.

Chou, P & Pagano, N 1992, *Elasticity: Tensor, Dyadic, and Engineering Approaches*, Dover Publications, New York, USA.

Cornwell, P, Doebling, S & Farrar, C 1999, 'Application of the strain energy method to plate-like structures', *Journal of Sound and Vibration*, vol. 224, no. 2, pp. 359–374.

Dally, J & Riley, W 2005, *Experimental Stress Analysis*, Fourth, College House Enterprises, Tennesse, US.

Doebling, S, Farrar, C, Prime, M & Shevitz, D 1996, *Damage identification and health monitoring of structural and mechanical systems from changes in their vibration characteristics: A Literature Review*, no. LA-13070-MS, Los Alamos National Laboratory, Los Alamos, USA.

Dulieu-Barton, J & Stanley, P 1998, 'Development and applications of thermoelastic stress analysis', *The Journal of Strain Analysis for Engineering Design*, vol. 33, no. 2, pp. 93–104.

Durelli, A & Parks, V 1970, *Moiré analysis of strain*, Prentice Hall, New Jersey, US.

Ennos, A 1968, 'Measurement of in-plane surface strain by hologram interferometry', *Journal of Physics E: Scientific Instruments*, vol. 1, no. 7, pp. 731–734.

Fan, W & Qiao, P 2010, 'Vibration-based damage identification methods: a review and comparative study', *Structural Health Monitoring*, vol. 10, no. 1, pp. 83–111.

Farrar, CR & Jauregui, D 1998, 'Comparative study of damage identification algorithms applied to a bridge: I. experiment', *Smart Materials and Structures*, vol. 7, no. 5, pp. 704–719.

Ferguson, N & Carpentier, J 1989, 'Use of laser vibrometer as an alternative to strain gauges to measure bending strain', *Proceedings of SPIE*, vol. 1084, pp. 202–216.

Fernández, M, Calderón, J, Díez, P & Segura, I 2010, 'Stress-separation techniques in photoelasticity: a review', *The Journal of Strain Analysis for Engineering Design*, vol. 45, no. 1, p. 17pp.

Fiene, J 2010, *Photoelastic imaging of a polycarbonate plate with a uniform hole*, Photograph, University of Pennsylvania, viewed 5 February 2010, <http://alliance.seas.upenn.edu/~medesign/wiki/uploads/Main/photoelasticity2.jpg>.

Firestone, F 1946, 'The Supersonic Reflectoscope, an Instrument for Inspecting the Interior of Solid Parts by Means of Sound Waves', *The Journal of the Acoustical Society of America*, vol. 17, no. 3, pp. 287–299.

Gan, Y & Steinchen, W 2008, 'Speckle methods', in *Springer Handbook of Experimental Solid Mechanics*, ed W Sharp, Springer, New York, US, pp. 655–673.

Gehman, H 2003, *Columbia Accident Investigation Board Report*, vol 1, NASA, USA.

Ghoshal, A, Chattopadhyay, A, Schulz, M, Thornburgh, R & Waldron, K 2003, 'Experimental investigation of damage detection in composite material structures using a laser vibrometer and piezoelectric actuators', *Journal of Intelligent Material Systems and Structures*, vol. 14, no. 8, pp. 521–537.

Ghoshal, A, Sundaresan, M, Schulz, M & Pai, P 2000, 'Structural health monitoring techniques for wind turbine blades', *Journal of Wind Engineering and Industrial Aerodynamics*, vol. 85, no. 3, pp. 309–324.

Giurgiutiu, V & Cuc, A 2005, 'Embedded non-destructive evaluation for structural health monitoring, damage detection, and failure prevention', *Shock and Vibration Digest*, vol. 37, no. 2, pp. 83–105.

Goetsch, D & Rowlands, R 1991, 'Doppler interferometric stress analysis of statically and dynamically loaded isotropic and composite plates', in *Proceedings of SEM Spring Conference on Experimental Mechanics*, Milwaukee, pp. 427–431.

Gorry, P 1990, 'General least-squares smoothing and differentiation by the convolution (Savitzky-Golay) method', *Analytical Chemistry*, vol. 62, no. 6, pp. 570–573.

Grandt, A 2004, *Fundamentals of Structural Integrity: Damage Tolerant Design and Non-Destructive Evaluation*, John Wiley and Sons, New York, USA.

Greene, R, Patterson, E & Rowlands, R 2008, 'Thermoelastic stress analysis', in *Springer Handbook of Experimental Solid Mechanics*, ed W Sharp, Springer, pp. 743–768.

Hadjileontiadis, L, Douka, E & Trochidis, A 2005, 'Fractal dimension analysis for crack identification in beam structures', *Mechanical Systems and Signal Processing*, vol. 19, no. 3, pp. 659–674.

Han, B & Post, D 2008a, 'Geometric moiré', in *Springer Handbook of Experimental Solid Mechanics*, ed W Sharp, Springer, US, pp. 601–626.

Han, B & Post, D 2008b, 'Moiré interferometry', in *Springer Handbook of Experimental Solid Mechanics*, ed W Sharp, Springer, US, pp. 627–653.

Hannah, R & Reed, S 1992, *Strain gage users' handbook*, Springer, Cambridge, UK.

Hellier, C 2003, *Handbook of Nondestructive Evaluation*, McGraw-Hill, New York, USA.

Herath, M, Bandyopadhyay, K & Logan, J 2010, 'Modelling of delamination damage in composite beams', in *Proceedings of the Sixth Australasian Congress on Applied Mechanics*, 12-15 December, Perth, Australia.

Holister, G 1967, *Experimental Stress Analysis: Principles and Methods*, Cambridge University Press, Cambridge, UK.

Hopkins, A 2000, *Lessons From Longford: The Esso Gas Plant Explosion*, CCH Australia, North Ryde, N.S.W.

Inechen, B, Eglin, P & Dändliker, R 1980, 'Hybrid optical and electronic image processing for strain measurement by speckle photography', *Appllied Optics*, vol. 19, no. 13, pp. 2191–2195.

Jin, S & Pai, P 2000, 'Locating structural defects using operational deflection shapes', *Journal of Intelligent Material Systems and Structures*, vol. 11, no. 8, pp. 613–630.

Kaiser, J 1950, 'Untersuchen über das auftreten gerauschen beim zugversuch', Ph.D. thesis, Technische Hochscule, Munich, Germany.

Kaiser, J 1993, 'Some useful properties of Teager's energy operators', in *Proceedings of the IEEE International Conference on Acoustics, Speech, and Signal Processing*, vol 3, IEEE, Minneapolis, Minnesota, USA, pp. 149 –152.

Karasik, A, Rinkevichius, B & Zubov, V 1995, *Principles of Laser Interferometry*, 1st edn, CRC Press.

Khan, A & Wang, X 2001, *Strain Measurement and Stress Analysis*, Prentice Hall, New Jersey, US.

Kirchhoff, G 1850, 'Über das gleichgewicht und die bewegung einer elastischen scheibe', *Journal für die Reine und Angewandte Mathematik*, vol. 40, no. 1, pp. 51–58.

Kuo, J, Wang, H & Pickup, S 1991, 'Multidimensional least-squares smoothing using orthogonal polynomials', *Analytical Chemistry*, vol. 63, no. 6, pp. 630–635.

Lee, B & Staszewski, W 2007, 'Lamb wave propagation modelling for damage detection: II. Damage monitoring strategy', *Smart Materials and Structures*, vol. 16, no. 2, pp. 260–274.

Leong, W, Staszewski, W, Lee, B & Scarpa, F 2005, 'Structural health monitoring using scanning laser vibrometry: III. Lamb waves for fatigue crack detection', *Smart Materials and Structures*, vol. 14, no. 6, pp. 1387–1395.

Liang, C, Sun, F & Rogers, C 1994, 'Coupled Electro-Mechanical Analysis of Adaptive Material Systems – Determination of the Actuator Power Consumption and System Energy Transfer', *Journal of Intelligent Material Systems and Structures*, vol. 5, no. 1, pp. 12–20.

Maev, R 2009, 'New Generation of High Resolution Ultrasonic Imaging Technique for Advanced Material Characterization: Review', in *Acoustical Imaging*, ed I Akiyama, vol 29, Acoustical Imaging, Springer Netherlands, pp. 163–172.

Mallet, L, Lee, B, Staszewski, W & Scarpa, F 2004, 'Structural health monitoring using scanning laser vibrometry: II. Lamb waves for damage detection', *Smart Materials and Structures*, vol. 13, no. 2, pp. 261–269.

Mascarenas, D, Todd, M, Park, G & Farrar, C 2007, 'Development of an impedance-based wireless sensor node for structural health monitoring', *Smart Materials and Structures*, vol. 16, no. 6, pp. 2137–2145.

Mase, G 1969, *Schaum's outline of theory and problems of continuum mechanics*, Schaum's Outline Series.

Miles, R, Bao, W & Xu, Y 1994, 'Estimation of random bending strain in a beam from discrete vibration measurements', *Journal of Sound and Vibration*, vol. 174, no. 2, pp. 191–199.

Mitchell, L, West, R & Wicks, A 1998, 'An emerging trend in experimental dynamics: merging of laser-based three-dimensional structural imaging and modal analysis', *Journal of Sound and Vibration*, vol. 211, no. 3, pp. 323 – 333.

Moccio, C & Miles, R 1996, 'Measurement of the transfer function between bending strain and a transient load using a scanning laser vibrometer', *Journal of Sound and Vibration*, vol. 189, no. 5, pp. 661–668.

Moore, A & Tyrer, J 1996, 'Two-dimensional Strain Measurment with ESPI', *Optics and Lasers in Engineering*, vol. 24, no. 5-6, pp. 381–402.

Nair, A & Cai, C 2010, 'Acoustic emission monitoring of bridges: Review and case studies', *Engineering Structures*, vol. 32, no. 6, pp. 1704–1714.

Pai, P & Huang, L 2006, 'Dynamics- and laser-based boundary effect evaluation method for damage inspection of one- and two-dimensional structures', *Journal of Nondestructive Evaluation*, vol. 25, pp. 83–105.

Pai, P, Huang, L, Gopalakrishnamurthy, S & Chung, J 2004, 'Identification and applications of boundary effects in beams', *International Journal of Solids and Structures*, vol. 41, no. 11-12, pp. 3053–3080.

Pai, P & Jin, S 2000, 'Locating structural damage by detecting boundary effects', *Journal of Sound and Vibration*, vol. 231, no. 4, pp. 1079–1110.

Pai, P, Kim, B & Chung, J 2004, 'Dynamics-based damage inspection of an aircraft wing panel', *Journal of Intelligent Material Systems and Structures*, vol. 15, no. 11, pp. 803–821.

Pai, P, Oh, Y & Lee, S 2002, 'Detection of defects in circular plates using a scanning laser vibrometer', *Structural Health Monitoring*, vol. 1, no. 1, pp. 63 –88.

Pai, P & Young, L 2001, 'Damage detection of beams using operational deflection shapes', *International Journal of Solids and Structures*, vol. 38, no. 18, pp. 3161–3192.

Pai, P, Young, L & Lee, S 2003, 'A dynamics-based method for crack detection and estimation', *Structural Health Monitoring*, vol. 2, no. 1, pp. 5–25.

Palmer, C & Green, R 1977, 'Optical detection of acoustic emission waves', *Applied Optics*, vol. 16, no. 9, pp. 2333–2334.

Pan, B, Xie, H, Kishimoto, S & Xing, Y 2006, 'Experimental study of moiré method in laser scanning confocal microscopy', *Review of Scientific Instruments*, vol. 77, no. 4, p. 5.

Pandey, A, Biswas, M & Samman, M 1991, 'Damage detection from changes in curvature mode shapes', *Journal of Sound and Vibration*, vol. 145, no. 2, pp. 321–332.

Park, G & Inman, D 2005, 'Impedance-based structural health monitoring', in *Damage prognosis: for aerospace, civil and mechanical systems*, eds D Inman, C Farrar, V Lopes & V Steffen, John Wiley and Sons, USA, pp. 275–292.

Parr, E 2000, *Industrial control handbook*, 3rd Ed, Industrial Press Inc., New York, USA.

Polytec 2004, *Polytec Scanning Vibrometer PSV 400-3D Hardware Manual*, Polytec GmbH.

Polytec 2011, *PSV-400 Scanning Vibrometer*, Polytec GmbH.

Pryputniewicz, R 2008, 'Holography', in *Springer Handbook of Experimental Solid Mechanics*, ed W Sharp, Springer, US, pp. 675–700.

Qiao, P, Lestari, W, Shah, M & Wang, J 2007a, 'Dynamics-based damage detection of composite laminated beams using contact and noncontact measurement systems', *Journal of Composite Materials*, vol. 41, no. 10, pp. 1217–1252.

Qiao, P, Lu, K, Lestari, W & Wang, J 2007b, 'Curvature mode shape-based damage detection in composite laminated plates', *Composite Structures*, vol. 80, no. 3, pp. 409–428.

Raghavan, A & Cesnik, C 2007, 'Review of guided-wave structural health monitoring', *The Shock and Vibration Digest*, vol. 39, no. 2, pp. 91–114.

Raj, B, Jayakumar, T & Thavasimuthu, M 2002, *Practical Non-Destructive Testing*, Woodhead, Cambridge, UK.

Ratcliffe, C & Bagaria, W 1998, 'Vibration technique for locating delamination in a composite beam', *AIAA journal*, vol. 36, no. 6, pp. 1074–1077.

Roberts, R 1992, 'Visual Inspection', in *Non-Destructive Testing Handbook*, John Wiley and Son, New York, USA, pp. 27–53.

Robinson, A, Dulieu-Barton, J, Quinn, S & Burguete, R 2009, 'A review of residual stress analysis using thermoelastic techniques', *Journal of Physics: Conference Series*, vol. 181, no. 1.

Rontgen, W 1896, 'On A New Kind of Rays', *Nature*, vol. 53, pp. 274–276.

Rose, J 1999, *Ultrasonic Waves in Solid Media*, Cambridge University Press, Cambridge, UK.

Saint-Venant, A 1870, 'Mémoire sur l'établissement des équations différentielles des mouvements intérieurs opérés dans les corps solides ductiles au delà des limites où l'élasticité pourrait les ramener à leur premier état', *Comptes rendus hebdomadaires des séances de l'Académie des Sciences*, vol. 70, pp. 474–480.

Sanford, R 2005, *Principles of Fracture Mechanics*, Pearson Education, New York, USA.

Savitzky, A & Golay, M 1964, 'Smoothing and differentiation of data by simplified least squares procedures', *Analytical Chemistry*, vol. 36, no. 8, pp. 1627–1639.

Schüssler, M 2007, *PSV-3D for strain measurements*, Vibrometer Technology Workshop (Presentation), Loughborough University, UK.

Schüssler, M, Mitrofanova, M & Retze, U 2011, 'Measurement of 2D dynamic stress distributions with a 3D-scanning laser doppler vibrometer', in *Modal Analysis Topics, Volume 3*, ed T Proulx, Springer, New York, NY, pp. 141–151.

Sciammarella, C 1982, 'The moiré method - a review', *Experimental Mechanics*, vol. 22, no. 11, pp. 418–433.

Sharpe, W 2008, *Springer Handbook of Experimental Solid Mechanics*, Springer, US.

Siebert, T, Becker, T, Spiltthof, K & Krupka, R 2007, 'High-speed digital image correlation: error estimations and applications', *Optical Engineering*, vol. 46, no. 5, p. 7pp.

Sjödahl, M 1995, 'Electronic speckle photography: measurement of in-plane strain fields through the use of defocused laser speckle', *Applied Optics*, vol. 34, no. 25, pp. 5799–5808.

Sjödahl, M 1997, 'Accuracy in electronic speckle photography', *Applied Optics*, vol. 36, no. 13, pp. 2875–2885.

Spencer, F 1996, *Visual Inspection Research Project Report on Benchmark Inspections*, Technical Report, no. DOT/FAA/AR-96/65, Department of Transportation, Federal Aviation Administration, Washington, DC.

Staszewski, W, Lee, B, Mallet, L & Scarpa, F 2004, 'Structural health monitoring using scanning laser vibrometry: I. Lamb wave sensing', *Smart Materials and Structures*, vol. 13, no. 2, pp. 251–260.

Staszewski, W, Lee, B & Traynor, R 2007, 'Fatigue crack detection in metallic structures with Lamb waves and 3D laser vibrometry', *Measurement Science and Technology*, vol. 18, no. 3, pp. 727–739.

Staszewski, W, Mahzan, S & Traynor, R 2009, 'Health monitoring of aerospace composite structures - active and passive approach', *Composites Science and Technology*, vol. 69, no. 11-12, pp. 1678–1685.

Stress Photonics, Inc. 2007, *Thermoelastic stress measurement: automobile connecting rod*, Infrared Image, viewed 5 February 2010, <http://www.stressphotonics.com/PageMill_Gifs/TSA/Stress_Images/CONROD.JPG>.

Su, Z, Ye, L & Lu, Y 2006, 'Guided Lamb waves for identification of damage in composite structures: A review', *Journal of Sound and Vibration*, vol. 295, no. 3-5, pp. 753–780.

Sundaresan, M, Ghoshal, A, Li, J, Schulz, M, Pai, P & Chung, J 2003, 'Experimental Damage Detection on a Wing Panel Using Vibration Deflection Shapes', *Structural Health Monitoring*, vol. 2, no. 3, pp. 243–256.

Sutton, M 2008, 'Digital image correlation for shape and deformation measurements', in *Springer Handbook of Experimental Solid Mechanics*, ed W Sharp, Springer, US, pp. 565–600.

Szilard, R 2004, *Theories and applications of plate analysis: classical, numerical, and engineering methods*, Wiley, Hoboken, New Jersey.

Thomson, J 1994, 'The role of strain measurement technology in structural evaluation', *Strain*, vol. 30, pp. 119–130.

Timoshenko, S & Goodier, J 1970, *Theory of Elasticity*, ed 3, McGraw-Hill, Tokyo, Japan.

Ugural, A 1999, *Stresses in Plates and Shells*, McGraw-Hill, Singapore.

Unknown 2008, *Photograph of ESPI fringe*, Photograph, Wikimedia Commons, viewed 5 February 2010, <http://upload.wikimedia.org/wikipedia/commons/0/0e/ESPI.jpg>.

Valoor, M & Chandrashekhara, K 2000, 'A thick composite-beam model for delamination prediction by the use of neural networks', *Composites Science and Technology*, vol. 60, no. 9, pp. 1773–1779.

Vuye, C, Vanlanduit, S, Presezniak, F, Steenackers, G & Guillaume, P 2011, 'Optical measurement of the dynamic strain field of a fan blade using a 3D scanning vibrometer', *Optics and Lasers in Engineering*, vol. 49, no. 7, pp. 988–997.

Waldron, K, Ghoshal, A, Schulz, M, Sundaresan, M, Ferguson, F, Pai, P & Chung, J 2002, 'Damage detection using finite element and laser operational deflection shapes', *Finite Elements in Analysis and Design*, vol. 38, no. 3, pp. 193–226.

Watson, R 2008, 'Bonded electrical resistance strain gages', in *Springer Handbook of Experimental Solid Mechanics*, ed W Sharp, Springer, US, pp. 283–334.

Window, A 1992, *Strain Gauge Technology*, 2nd Ed, Springer.

Xu, Y & Miles, R 1996a, 'Experimental determination of bending strain power spectra from vibration measurements', *Experimental Mechanics*, vol. 36, pp. 166–172.

Xu, Y & Miles, R 1996b, 'Full-field random bending strain measurement of a plate from vibration measurement', *Journal of Sound and Vibration*, vol. 191, no. 5, pp. 847–858.

Zagrai, A & Giurgiutiu, V 2001, 'Electro-Mechanical Impedance Method for Crack Detection in Thin Plates', *Journal of Intelligent Material Systems and Structures*, vol. 12, no. 10, pp. 709–718.

Zhilkin, V & Popov, A 1976, 'Sensitivity and accuracy of moiré methods in strain measurement', *Strength of Materials*, vol. 8, no. 1, pp. 83–87.

Appendix A. Strain Compatibility Equations

The three-dimensional equations of compatibility for small strains, experienced by a solid body, can be written as (Timoshenko & Goodier 1970, p. 237; Sanford 2005),

$$\frac{\partial^2 \varepsilon_{yy}}{\partial x^2} + \frac{\partial^2 \varepsilon_{xx}}{\partial y^2} = \frac{\partial^2 \gamma_{xy}}{\partial x \partial y} \tag{A.1}$$

$$\frac{\partial^2 \varepsilon_{yy}}{\partial z^2} + \frac{\partial^2 \varepsilon_{zz}}{\partial y^2} = \frac{\partial^2 \gamma_{yz}}{\partial y \partial z} \tag{A.2}$$

$$\frac{\partial^2 \varepsilon_{zz}}{\partial x^2} + \frac{\partial^2 \varepsilon_{xx}}{\partial z^2} = \frac{\partial^2 \gamma_{xz}}{\partial x \partial z} \tag{A.3}$$

$$2\frac{\partial^2 \varepsilon_{xx}}{\partial y \partial z} = \frac{\partial^2 \gamma_{yz}}{\partial x^2} + \frac{\partial^2 \gamma_{xz}}{\partial x \partial y} + \frac{\partial^2 \gamma_{xy}}{\partial x \partial z} \tag{A.4}$$

$$2\frac{\partial^2 \varepsilon_{yy}}{\partial x \partial z} = \frac{\partial^2 \gamma_{yz}}{\partial x \partial y} + \frac{\partial^2 \gamma_{xz}}{\partial y^2} + \frac{\partial^2 \gamma_{xy}}{\partial y \partial z} \tag{A.5}$$

$$2\frac{\partial^2 \varepsilon_{zz}}{\partial x \partial y} = \frac{\partial^2 \gamma_{yz}}{\partial x \partial z} + \frac{\partial^2 \gamma_{xz}}{\partial y \partial z} + \frac{\partial^2 \gamma_{xy}}{\partial z^2} \tag{A.6}$$

where ε is the normal strain, γ is the engineering shear strain and x, y and z are the Cartesian coordinates.

Appendix B. Savitzky-Golay Differentiating Filter

The Savitzky-Golay differentiating filter is able differentiate measured displacement field, as well as alleviate the adverse effect of noise. The main advantage of this filter is that it generally preserves features of the distribution such as relative maxima, minima and width (Savitzky & Golay 1964; Gorry 1990; Kuo, Wang, H & Pickup 1991). This section briefly introduces the main concepts behind the Savitzky-Golay filter.

B.1 1D Filter Structure

Consider a sample containing q evenly spaced data points (y_i), which is required to be smoothed or differentiated (to order r), with a $2m+1$ point filter and polynomial order n. Since this requires repeatedly fitting a polynomial of order n to $2m+1$ consecutive points, we convert each group of points to a temporary coordinate system in which the ordinate values range from $i=-m$ to $i=m$, i.e. the midpoint is $i=0$. The one-dimensional Savitzky-Golay differentiator has the form (Gorry 1990),

$$f_n^r(t) = \frac{1}{\Delta x^r} \sum_{i=-m}^{m} h_{t,i}^{n,r} y_i \tag{B.1}$$

where Δx is the distance between each data point and $h_{t,i}^{n,r}$ is the convolution weight for data point i, with polynomial order n, and r derivative, evaluated at point t, and is given

by

$$h_{t,i}^{n,r} = \sum_{k=0}^{n} \frac{(2k+1)(2m)^k}{(2m+k+1)^{k+1}} P_k^{m,0}(i) P_k^{m,r}(t) \quad \text{(B.2)}$$

$P_k^{m,r}(s)$ is the Gram polynomial of order n, derivative r, over a $2m+1$ points and evaluated at point s, and is given by

$$P_k^{m,r}(s) = \frac{2(2k-1)}{k(2m-k+1)}\left[sP_{k-1}^{m,0}(s) + rP_{k-1}^{m,r-1}(s)\right] - \frac{(k-1)(2m+k)}{k(2m-k+1)} P_{k-2}^{m,r}(s) \quad \text{(B.3)}$$

with $P_0^{m,r}(s) = 0$ and $P_{-1}^{m,r}(s) = 0$.

B.2 2D Filter Structure

Consider a rectangular sample grid containing q evenly spaced data points (g_{i_x,i_y}), which is required to be smoothed or differentiated to order r_x and r_y, with a $2m+1$ by $2m+1$ point filter and polynomial order n_x and n_y, with respect to the x- and y-direction. Since this requires repeatedly fitting a polynomial of order n_x and n_y to $2m+1$ by $2m+1$ consecutive points in the x- and y-direction respectively, each group of points is converted to a temporary coordinate system in which the ordinate values range from $(i_x, i_y) = (-m_x, -m_y)$ to $(i_x, i_y) = (m_x, m_y)$, i.e. the midpoint is $(i_x, i_y) = (0,0)$. The two-dimensional Savitzky-Golay differentiator has the form (Gorry 1990; Kuo, Wang, H & Pickup 1991),

$$f_{n_x,n_y}^{r_x,r_y}(t_x, t_y) = \frac{1}{\Delta x^{r_x} \Delta y^{r_y}} \sum_{i_x=-m_x}^{m_x} \sum_{i_y=-m_y}^{m_y} h_{t_x,i_x}^{n_x,r_x} h_{t_y,i_y}^{n_y,r_y} g_{i_x,i_y} \quad \text{(B.4)}$$

where Δx and Δy is the distance between each data point in the x- and y-direction respectively, and $h_{t_x,i_x}^{n_x,r_x}$ and $h_{t_y,i_y}^{n_y,r_y}$ is the convolution weights for data points (i_x, i_y), with polynomial order n_x and n_y, and derivative order r_x and r_y with respect to the x- and y-direction, evaluated at the data point (t_x, t_y).

Appendix C. Delaminated Beam Model

An analytical model of a delaminated cantilever beam was developed based on Euler-Bernoulli beam theory, with applied boundary and continuity conditions (Valoor & Chandrashekhara 2000). As seen in Figure C.1a, the model of the beam is of thickness h, width b and length L. A delaminated section occurs L_1 in from the clamped end of the beam, with a length of L_D and depth from the upper surface of h_2. Shown in Figure C.1b,

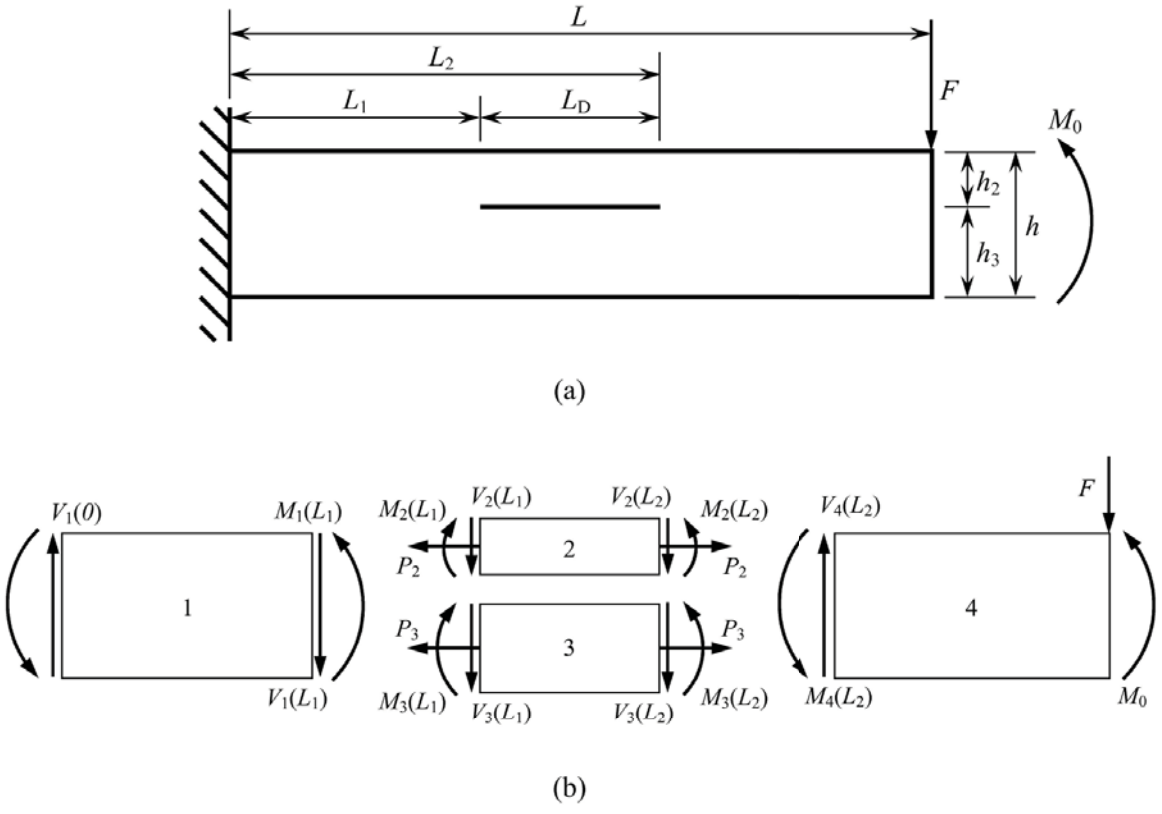

Figure C.1. Delaminated beam model.

the model is partitioned into four segments and each segment is modelled as an individual beam.

The deflection of a beam is governed by the governing differential equation for beam deflection; Equation (6.17) in Section 6.1.2. Therefore, the deflection of each segment of the beam can be represented by a third-order polynomial and are expressed as,

$$w_i(x) = C_{i1}\frac{x^3}{6} + C_{i1}\frac{x^2}{2} + C_{i3} + C_{i4} \tag{C.1}$$

where C_{ij} are constants, i represents the beam segment and j is a value between 1 and 4. The boundary condition of the first segment of the beam are expressed as,

$$w_1(0) = 0 \tag{C.2}$$

$$\frac{\partial}{\partial x}w_1(0) = 0 \tag{C.3}$$

$$\frac{\partial^2}{\partial x^2}w_1(L_1) = \frac{M_1(L_1)}{EI_1} \tag{C.4}$$

$$\frac{\partial^3}{\partial x^3}w_1(L_1) = \frac{V_1(L_1)}{EI_1} \tag{C.5}$$

and the fourth segment of the beam are expressed as,

$$\frac{\partial^2}{\partial x^2}w_4(L_2) = \frac{M_4(L_2)}{EI_4} \tag{C.6}$$

$$\frac{\partial^3}{\partial x^3}w_4(L_2) = \frac{V_4(L_2)}{EI_4} \tag{C.7}$$

$$\frac{\partial^2}{\partial x^2}w_4(L) = \frac{M_4(L)}{EI_4} \tag{C.8}$$

$$\frac{\partial^3}{\partial x^3} w_4(L) = \frac{V_4(L)}{EI_4} \tag{C.9}$$

where I is the moment of inertia of the undelaminated beam segments.

The bending moment and shear force loading conditions across the undelaminated segments are, respectively,

$$M_1(x) = M_4(x) = F(L - x) - M_0 \tag{C.10}$$

$$V_1(x) = V_4(x) = -F \tag{C.11}$$

Therefore, by applying Equations (C.10) and (C.11) to the boundary conditions for the first and fourth segment (Equations (C.4) through (C.9)) and evaluating the constant terms, six constant terms were solved and were equal to,

$$C_{13} = C_{14} = 0 \tag{C.12}$$

$$EI_1 C_{11} = EI_4 C_{41} = -F \tag{C.13}$$

$$EI_1 C_{12} = EI_4 C_{42} = FL - M_0 \tag{C.14}$$

Applying these constant terms to the beam segment deflection gives,

$$w_1(x) = \frac{Fx^2[3L - x]}{6EI_1} - \frac{M_0}{2EI_1} x^2 \tag{C.15}$$

$$w_4(x) = \frac{Fx^2[3L - x]}{6EI_4} - \frac{M_0}{2EI_4} x^2 + C_{43}x + C_{44} \tag{C.16}$$

At the junctions of the delaminated and undelaminated segments, continuity conditions

need to be satisfied. This includes compatibility of displacements, equilibrium of forces and equilibrium of bending moments.

The equilibrium of shear forces dictates that the shear force on each side of a junction between the undelaminated and delaminated segments needs to be equal, and can be expressed as,

$$V_1(L_1) = V_2(L_1) + V_3(L_1) \tag{C.17}$$

and reduces to,

$$EI_2C_{21} + EI_3C_{31} = -F \tag{C.18}$$

The equilibrium of axial force within the delaminated segments requires,

$$P_2 = -P_3 \tag{C.19}$$

The equilibrium of bending moments ensures that the bending moment between the undelaminated and delaminated segments at a junction is equal, and is expressed,

$$M_1(L_1) = M_2(L_1) + M_3(L_1) + \frac{h}{2}P_2 \tag{C.20}$$

which equates to,

$$(C_{21}L_1 + C_{22})EI_2 + (C_{31}L_1 + C_{32})EI_3 + \left(\frac{h}{2}\right)P_2 = (L - L_1)F - M_0 \tag{C.21}$$

Continuity of beam deflection requires that the deflection and rotation at junction between two segments are equal, thus giving,

$$w_1(L_1) = w_2(L_1) = w_3(L_1) \tag{C.22}$$

$$\frac{\partial}{\partial x} w_1(L_1) = \frac{\partial}{\partial x} w_2(L_1) = \frac{\partial}{\partial x} w_3(L_1) \tag{C.23}$$

$$w_4(L_2) = w_2(L_2) = w_3(L_2) \tag{C.24}$$

$$\frac{\partial}{\partial x} w_4(L_2) = \frac{\partial}{\partial x} w_2(L_2) = \frac{\partial}{\partial x} w_3(L_2) \tag{C.25}$$

Substituting the definitions of beam deflection for each segment provides,

$$C_{i1}\frac{L_1^3}{6} + C_{i2}\frac{L_1^2}{2} + C_{i3}L_1 + C_{i4} = \frac{FL_1\left[3L - L_1\right]}{6EI_1} - \frac{M_0}{2EI_1}L_1^2 \tag{C.26}$$

$$C_{i1}\frac{{L_1}^2}{2} + C_{i2}L_1 + C_{i3} = \frac{FL_1\left[2L - L_1\right]}{2EI_1} - \frac{M_0}{EI_1}L_1 \tag{C.27}$$

$$C_{i1}\frac{{L_2}^3}{6} + C_{i2}\frac{{L_2}^2}{2} + C_{i3}L_2 + C_{i4} = \frac{F{L_2}^2\left[3L - L_2\right]}{6EI_4} - \frac{M_0}{2EI_4}{L_2}^2 + C_{43}L_2 + C_{44} \tag{C.28}$$

$$C_{i1}\frac{{L_2}^2}{2} + C_{i2}L_2 + C_{i3} = \frac{FL_1\left[2L - L_2\right]}{2EI_4} - \frac{M_0}{EI_4}L_2 + C_{43} \tag{C.29}$$

where i is equal to either 2 or 3. Lastly, the continuity of axial displacements at each junction gives,

$$\frac{h}{2}\frac{\partial}{\partial x} w_1(L_1) = u_2\left(L_1, \frac{h}{2}\right) - u_3\left(L_1, \frac{h}{2}\right) \tag{C.30}$$

$$\frac{h}{2}\frac{\partial}{\partial x} w_4(L_2) = u_2\left(L_2, \frac{h}{2}\right) - u_3\left(L_2, \frac{h}{2}\right) \tag{C.31}$$

By subtracting Equation (C.30) from (C.31) gives

$$\frac{h}{2}\left[\frac{\partial}{\partial x}w_4(L_2)-\frac{\partial}{\partial x}w_1(L_1)\right]=\left[u_2\left(L_2,\frac{h}{2}\right)-u_2\left(L_1,\frac{h}{2}\right)\right]-\left[u_3\left(L_2,-\frac{h}{2}\right)-u_3\left(L_1,-\frac{h}{2}\right)\right] \quad \text{(C.32)}$$

Substituting the definition for beam deflection of the first and fourth segments and the axial displacement within the delaminated segments (second and third segments) in terms of axial load, Equation (C.23) reduces to

$$P_2\frac{L_D}{Eb}\left(\frac{2}{h_2h_3}\right)-C_{43}=\frac{L_2}{EI_4}\left[\left(L-\frac{L_2}{2}\right)F-M_0\right]-\frac{L_1}{EI_1}\left[\left(L-\frac{L_1}{2}\right)F-M_0\right]- \quad \text{(C.33)}$$

After applying the boundary and continuity conditions, the analytical model has 11 unknown constants within a set of 11 simultaneous linear homogeneous algebraic equations (Equations (C.18), (C.21), (C.26), (C.27), (C.28), (C.29) and (C.33)). These 11 unknown terms can be evaluated by solving the system of equations and is expressed as,

$$C=M^{-1}R \quad \text{(C.34)}$$

where C is the constant term matrix,

$$C=\begin{bmatrix}C_{21} & C_{22} & C_{23} & C_{24} & C_{31} & C_{32} & C_{33} & C_{34} & C_{41} & C_{42} & P_2\end{bmatrix} \quad \text{(C.35)}$$

M is,

$$M = \begin{bmatrix} \frac{L_1^3}{6} & \frac{L_1^2}{2} & L_1 & 1 & 0 & 0 & 0 & 0 & 0 & 0 & 0 \\ \frac{L_1^2}{2} & L_1 & 1 & 0 & 0 & 0 & 0 & 0 & 0 & 0 & 0 \\ 0 & 0 & 0 & 0 & \frac{L_1^3}{6} & \frac{L_1^2}{2} & L_1 & 1 & 0 & 0 & 0 \\ 0 & 0 & 0 & 0 & \frac{L_1^2}{2} & L_1 & 1 & 0 & 0 & 0 & 0 \\ EI_2 & 0 & 0 & 0 & EI_3 & 0 & 0 & 0 & 0 & 0 & 0 \\ EI_2 L_1 & EI_2 & 0 & 0 & EI_3 L_1 & EI_2 & 0 & 0 & 0 & 0 & \frac{h}{2} \\ \frac{L_2^3}{6} & \frac{L_2^2}{2} & L_2 & 1 & 0 & 0 & 0 & 0 & L_2 & -1 & 0 \\ \frac{L_2^2}{2} & L_2 & 1 & 0 & 0 & 0 & 0 & 0 & -1 & 0 & 0 \\ 0 & 0 & 0 & 0 & \frac{L_2^3}{6} & \frac{L_2^2}{2} & L_2 & 1 & L_2 & -1 & 0 \\ 0 & 0 & 0 & 0 & \frac{L_2^2}{2} & L_2 & 1 & 0 & -1 & 0 & 0 \\ 0 & 0 & 0 & 0 & 0 & 0 & 0 & 0 & \frac{L_D}{Eb}\left(\frac{2}{h_2 h_3}\right) & 0 & -1 \end{bmatrix} \tag{C.36}$$

and, R is

$$R = \begin{bmatrix} \frac{FL_1^2[3L - L_1]}{6EI_1} - \frac{M_0}{2EI_1} L_1^2 \\ \frac{FL_1[2L - L_1]}{2EI_1} - \frac{M_0}{EI_1} L_1 \\ \frac{FL_1^2[3L - L_1]}{6EI_1} - \frac{M_0}{2EI_1} L_1^2 \\ \frac{FL_1[2L - L_1]}{2EI_1} - \frac{M_0}{EI_1} L_1 \\ -F \\ (L - L_1)F - M_0 \\ \frac{FL_2^2[3L - L_2]}{6EI_4} - \frac{M_0}{2EI_4} L_2^2 \\ \frac{FL_2[2L - L_2]}{2EI_4} - \frac{M_0}{EI_4} L_2 \\ \frac{FL_2^2[3L - L_2]}{6EI_4} - \frac{M_0}{2EI_4} L_2^2 \\ \frac{FL_2[2L - L_2]}{2EI_4} - \frac{M_0}{EI_4} L_2 \\ \frac{L_2}{EI_4}\left[\left(L - \frac{L_2}{2}\right)F - M_0\right] - \frac{L_1}{EI_1}\left[\left(L - \frac{L_1}{2}\right)F - M_0\right] \end{bmatrix} \tag{C.37}$$

Appendix D. Damage Detection Results

This appendix presents the evaluated damage detection results for a plate with an edge crack and a centre crack, which were omitted from Chapter 5. The result presented include the violation of the Governing Differential Equation (GDE) of plate displacement (Appendix D.1), displacement error in the in x- and y-direction (Appendix D.2), and normalised surface strain in x, y and shear directions (Appendix D.3). Only a single scenario, crack propagating from a notch, was presented in Chapter 5, and the two scenarios presented here were omitted from the chapter, due to the extensive similarity of the results across all of the experimental scenarios.

D.1 Governing Differential Equation of In-Plane Displacement

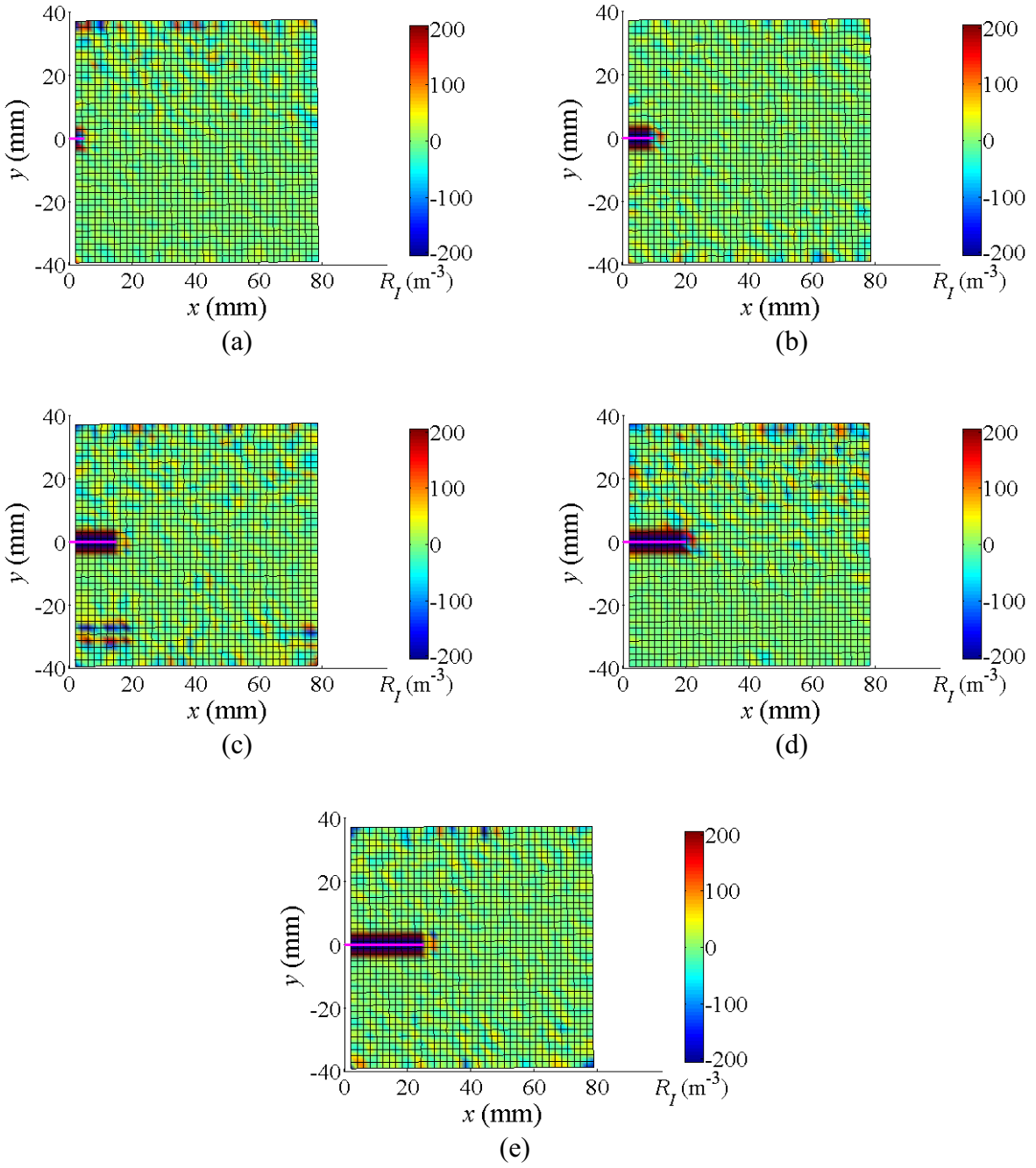

Figure D.2. Acquired residual term of GDE (R_I) for an edge crack with various crack lengths:- (a) 5mm, (b) 10mm, (c) 15mm, (d) 20mm and (e) 25mm. The dark blue and dark red areas on the graph represent the location where R_I has exceeded the threshold $\Phi_I = 200\text{m}^{-3}$. At $x = 0$ and $x = 100$ represents the edges of the plate and the pink line defines the location of the crack. A third-order polynomial ($n = 3$) 2D Savitzky-Golay differentiating filter was used with a filter size of 5x5 point ($m = 2$).

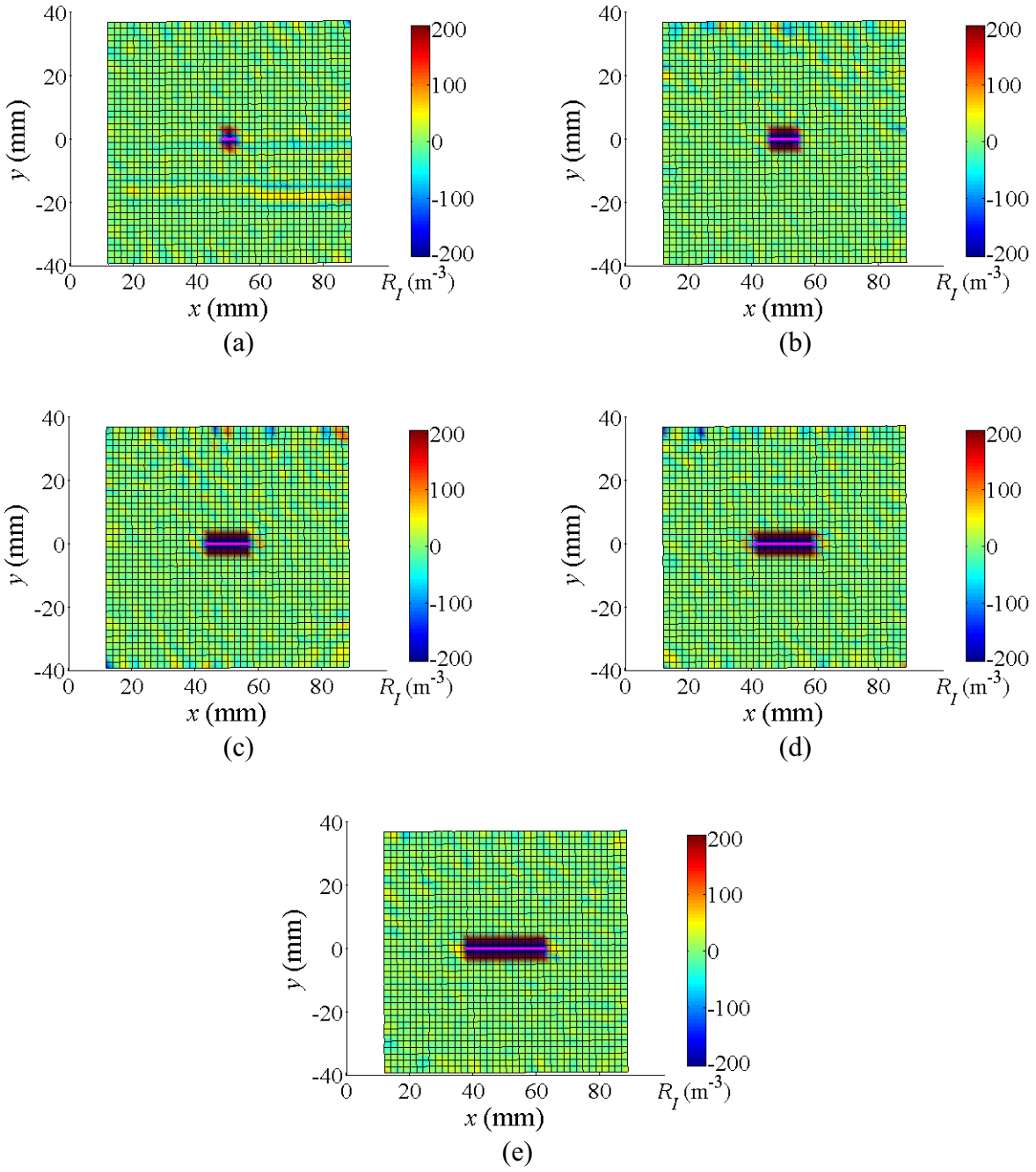

Figure D.3. Acquired residual term of GDE (R_I) for a centre crack with various crack lengths:- (a) 5mm, (b) 10mm, (c) 15mm, (d) 20mm and (e) 25mm. The dark blue and dark red areas on the graph represent the location where R_I has exceeded the threshold $\Phi_I = 200\text{m}^{-3}$. At $x = 0$ and $x = 100$ represents the edges of the plate and the pink line defines the location of the crack. A third-order polynomial ($n = 3$) 2D Savitzky-Golay differentiating filter was used with a filter size of 5x5 point ($m = 2$).

D.2 Displacement Error

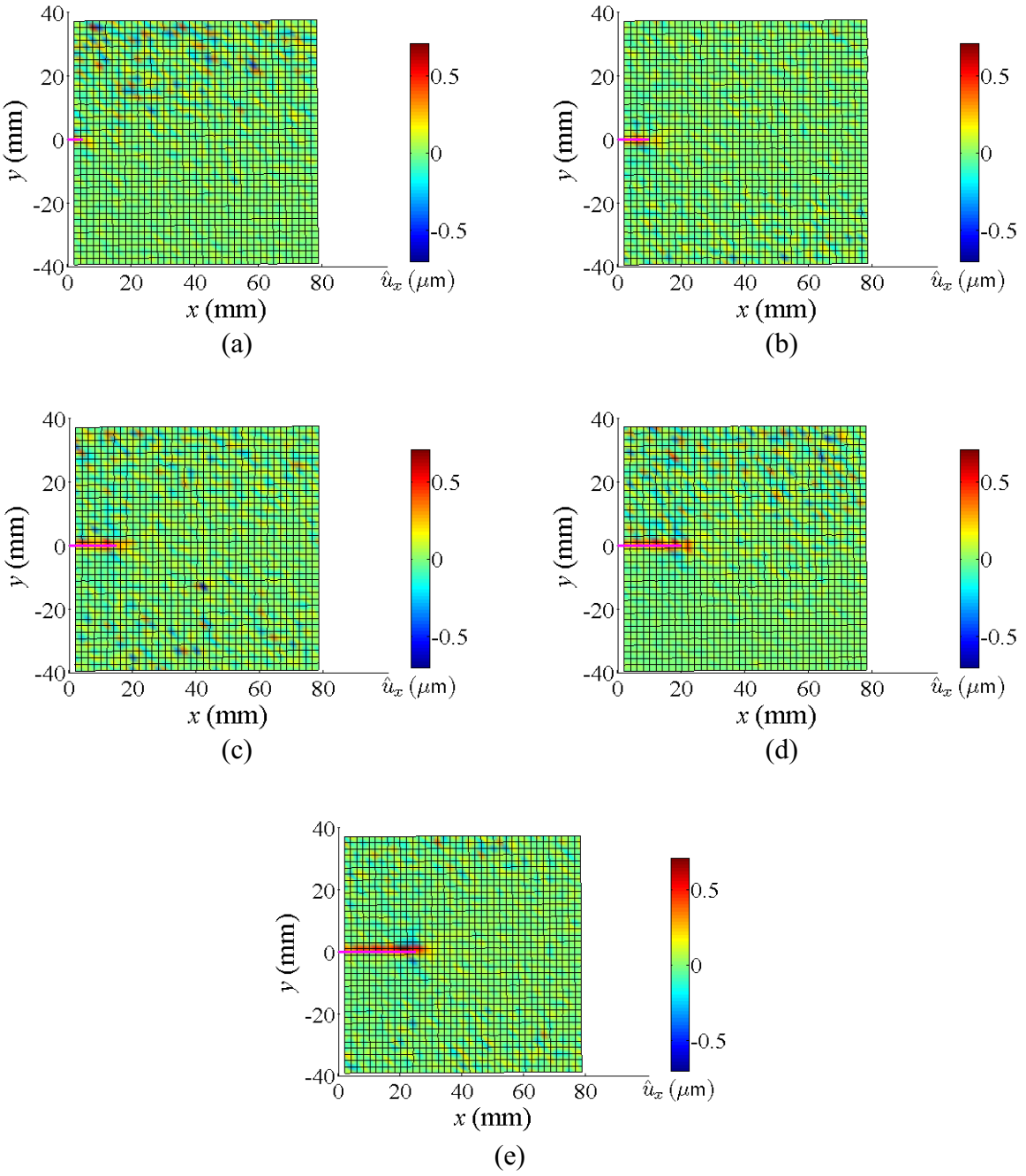

Figure D.4. Acquired displacement error in the x-direction ($\hat{u}_x$) for an edge crack with various crack lengths:- (a) 5mm, (b) 10mm, (c) 15mm, (d) 20mm and (e) 25mm. The dark blue and dark red areas on the graph represent the location where $\hat{u}_x$ has exceeded the threshold $\Theta_x = 0.7\mu$m. At $x = 0$ and $x = 100$ represents the edges of the plate and the pink line defines the location of the crack. A first-order polynomial ($n = 1$) 2D Savitzky-Golay smoothing ($r_x = r_y = 0$) filter was used with a filter size of 3x3 point ($m = 1$).

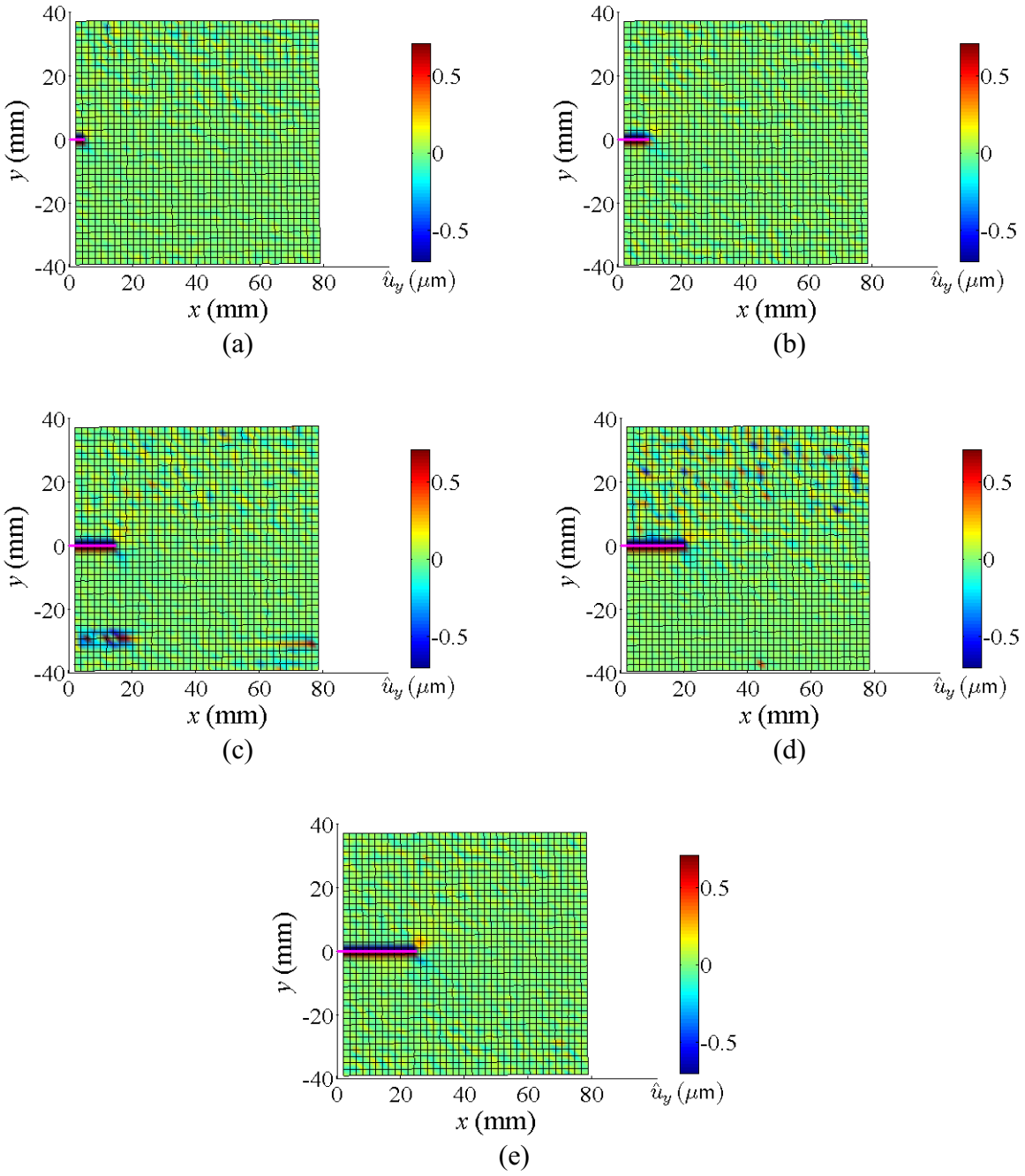

Figure D.5. Acquired displacement error in the y-direction ($\hat{u}_y$) for an edge crack with various crack lengths:- (a) 5mm, (b) 10mm, (c) 15mm, (d) 20mm and (e) 25mm. The dark blue and dark red areas on the graph represent the location where $\hat{u}_y$ has exceeded the threshold $\Theta_y = 0.7$μm. At $x = 0$ and $x = 100$ represents the edges of the plate and the pink line defines the location of the crack. A first-order polynomial ($n = 1$) 2D Savitzky-Golay smoothing ($r_x = r_y = 0$) filter was used with a filter size of 3x3 point ($m = 1$).

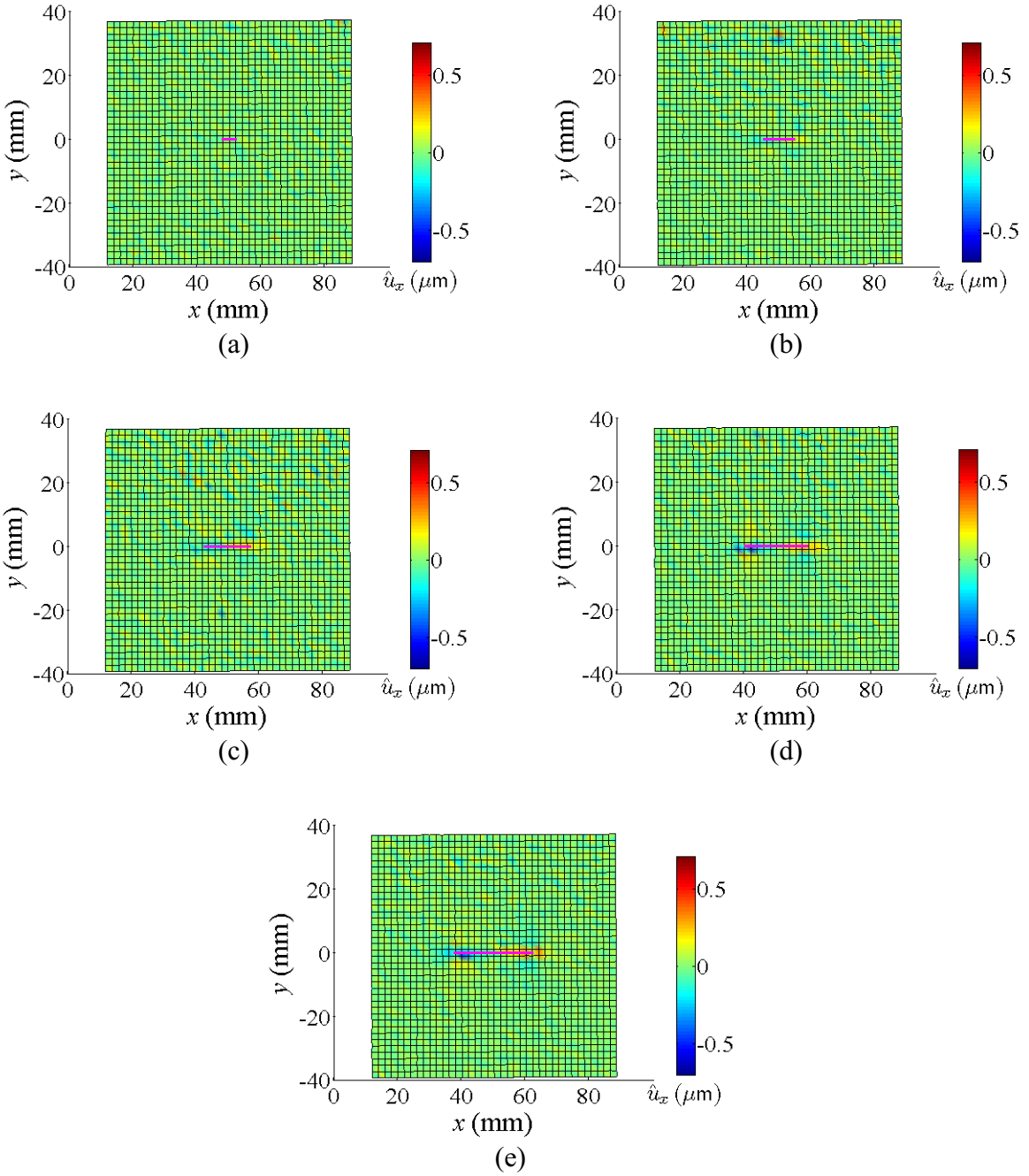

Figure D.6. Acquired displacement error in the x-direction ($\hat{u}_x$) for a centre crack with various crack lengths:- (a) 5mm, (b) 10mm, (c) 15mm, (d) 20mm and (e) 25mm. The dark blue and dark red areas on the graph represent the location where $\hat{u}_x$ has exceeded the threshold $\Theta_x = 0.7$μm. At $x = 0$ and $x = 100$ represents the edges of the plate and the pink line defines the location of the crack. A first-order polynomial ($n = 1$) 2D Savitzky-Golay smoothing ($r_x = r_y = 0$) filter was used with a filter size of 3x3 point ($m = 1$).

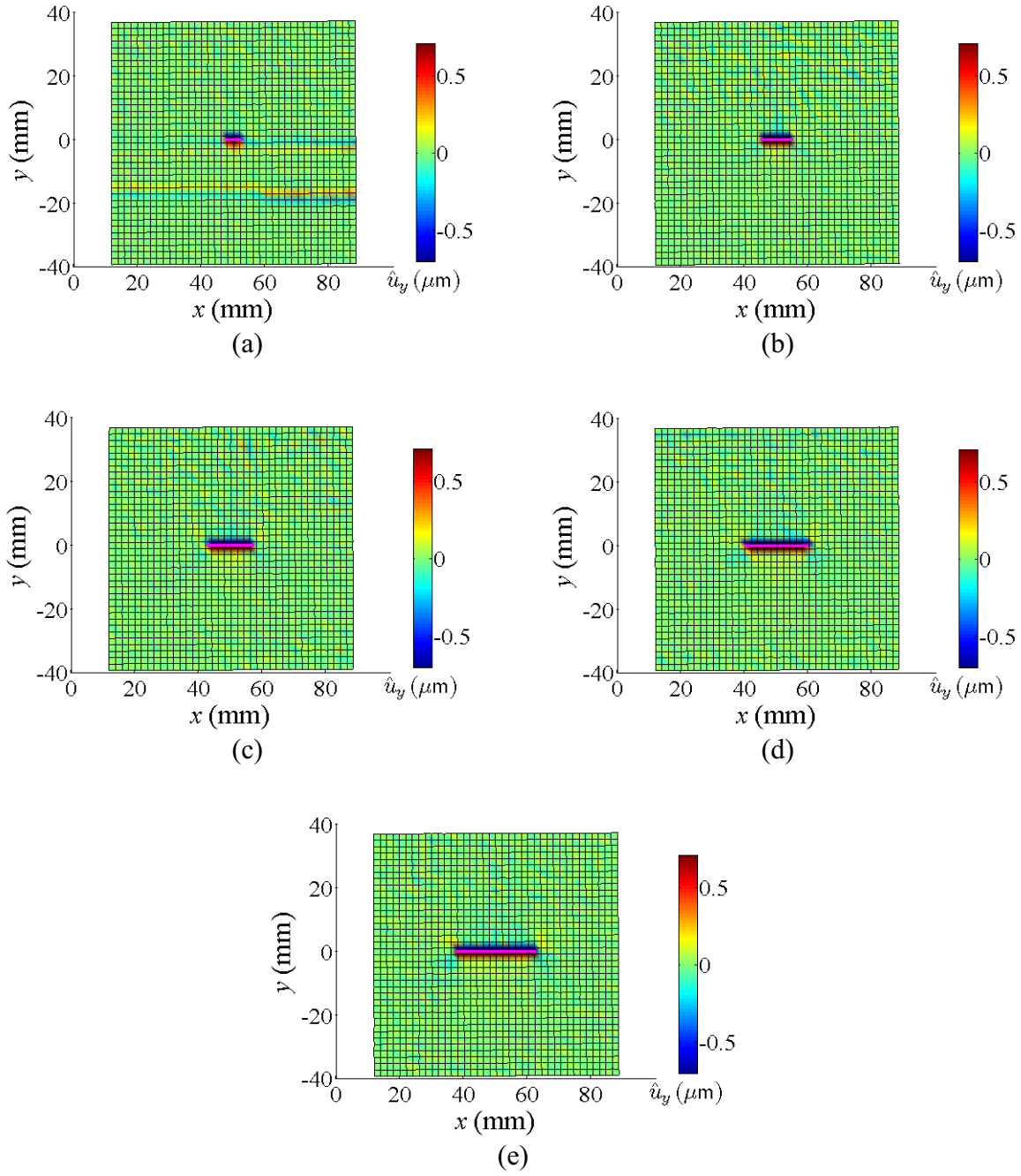

Figure D.7. Acquired displacement error in the y-direction ($\hat{u}_y$) for a centre crack with various crack lengths:- (a) 5mm, (b) 10mm, (c) 15mm, (d) 20mm and (e) 25mm. The dark blue and dark red areas on the graph represent the location where $\hat{u}_y$ has exceeded the threshold $\Theta_y = 0.7$µm. At $x = 0$ and $x = 100$ represents the edges of the plate and the pink line defines the location of the crack. A first-order polynomial ($n = 1$) 2D Savitzky-Golay smoothing ($r_x = r_y = 0$) filter was used with a filter size of 3x3 point ($m = 1$).

D.3 Surface Strain Algorithm

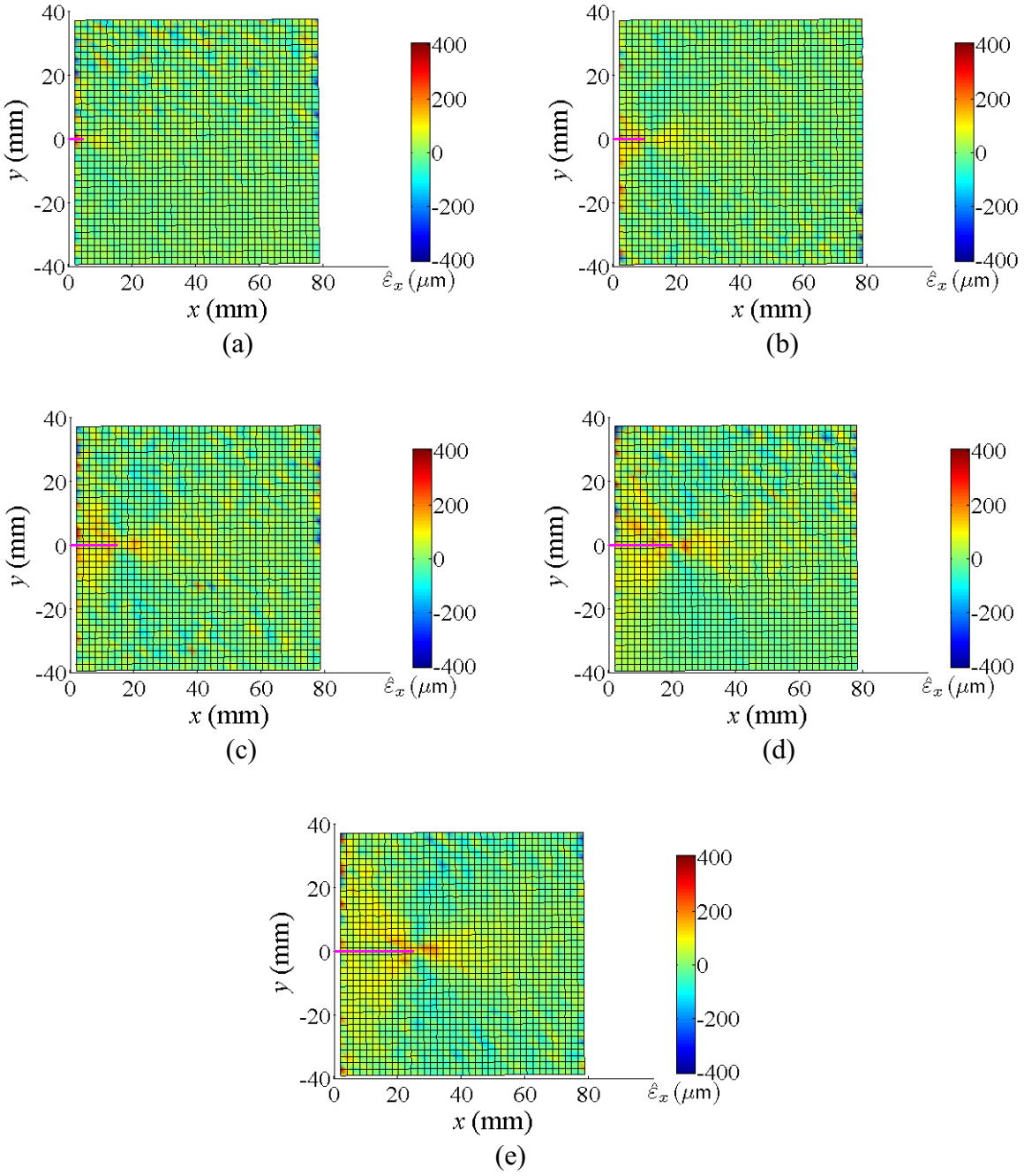

Figure D.8. Acquired normalised surface strain in the x-direction ($\hat{\varepsilon}_{xx}$) for an edge crack with various crack lengths:- (a) 5mm, (b) 10mm, (c) 15mm, (d) 20mm and (e) 25mm. The dark blue and dark red areas on the graph represent the location where $\hat{\varepsilon}_{xx}$ has exceeded the threshold $\Psi_{xx} = 400$mm/m. At $x = 0$ and $x = 100$ represents the edges of the plate and the pink line defines the location of the crack. A second-order polynomial ($n = 2$) 2D Savitzky-Golay differentiating filter was used with a filter size of 3x3 point ($m = 1$).

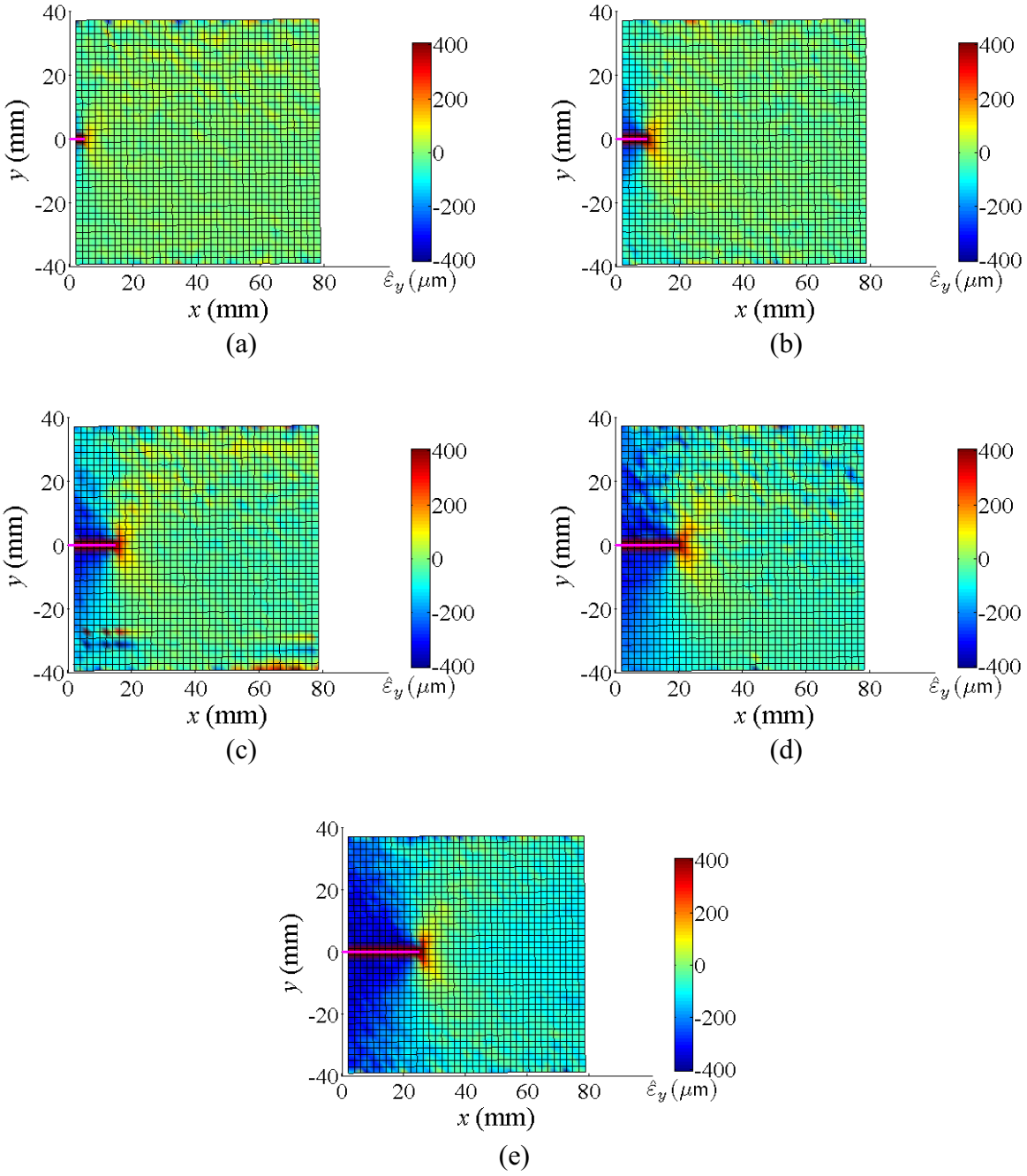

Figure D.9. Acquired normalised surface strain in the y-direction ($\hat{\varepsilon}_{yy}$) for an edge crack with various crack lengths:- (a) 5mm, (b) 10mm, (c) 15mm, (d) 20mm and (e) 25mm. The dark blue and dark red areas on the graph represent the location where $\hat{\varepsilon}_{yy}$ has exceeded the threshold $\Psi_{yy} = 400$mm/m. At $x = 0$ and $x = 100$ represents the edges of the plate and the pink line defines the location of the crack. A second-order polynomial ($n = 2$) 2D Savitzky-Golay differentiating filter was used with a filter size of 3x3 point ($m = 1$).

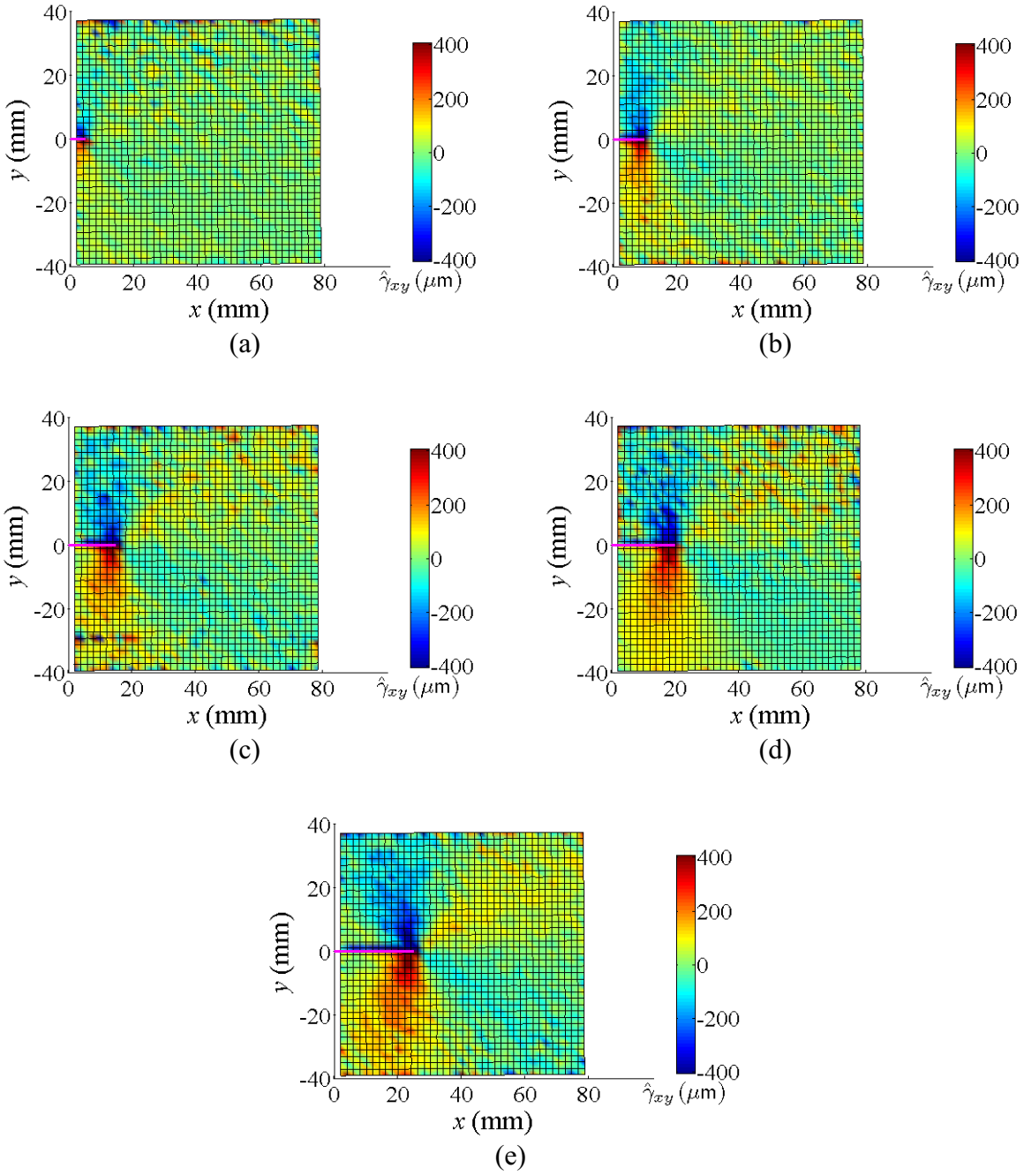

Figure D.10. Acquired normalised surface shear ($\hat{\gamma}_{xy}$) for an edge crack with various crack lengths:- (a) 5mm, (b) 10mm, (c) 15mm, (d) 20mm and (e) 25mm. The dark blue and dark red areas on the graph represent the location where $\hat{\gamma}_{xy}$ has exceeded the threshold $\Psi_{xy} = 400$mm/m. At $x = 0$ and $x = 100$ represents the edges of the plate and the pink line defines the location of the crack. A second-order polynomial ($n = 2$) 2D Savitzky-Golay differentiating filter was used with a filter size of 3x3 point ($m = 1$).

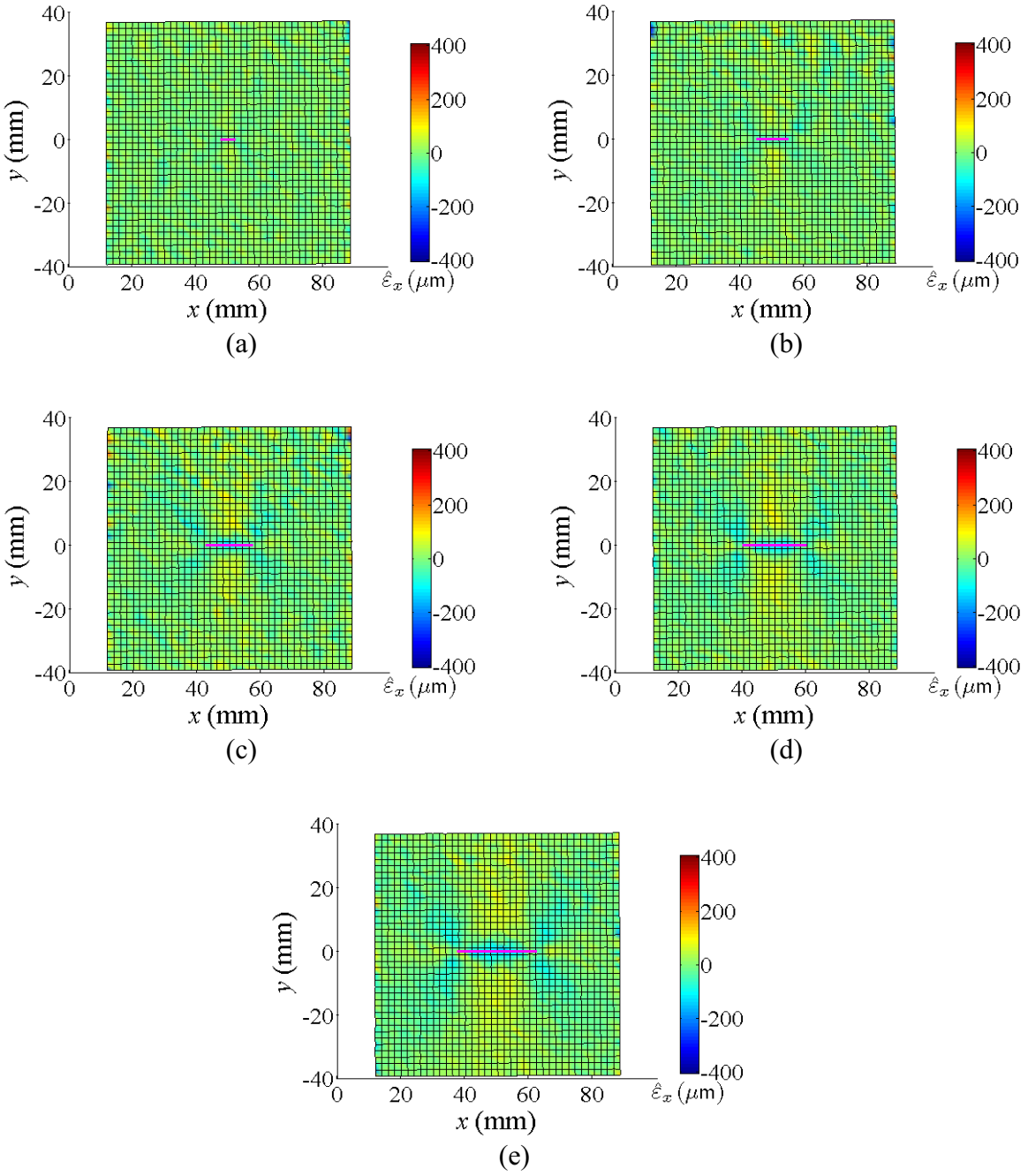

Figure D.11. Acquired normalised surface strain in the x-direction ($\hat{\varepsilon}_{xx}$) for a centre crack with various crack lengths:- (a) 5mm, (b) 10mm, (c) 15mm, (d) 20mm and (e) 25mm. The dark blue and dark red areas on the graph represent the location where $\hat{\varepsilon}_{xx}$ has exceeded the threshold $\Psi_{xx} = 400$mm/m. At $x = 0$ and $x = 100$ represents the edges of the plate and the pink line defines the location of the crack. A second-order polynomial ($n = 2$) 2D Savitzky-Golay differentiating filter was used with a filter size of 3x3 point ($m = 1$).

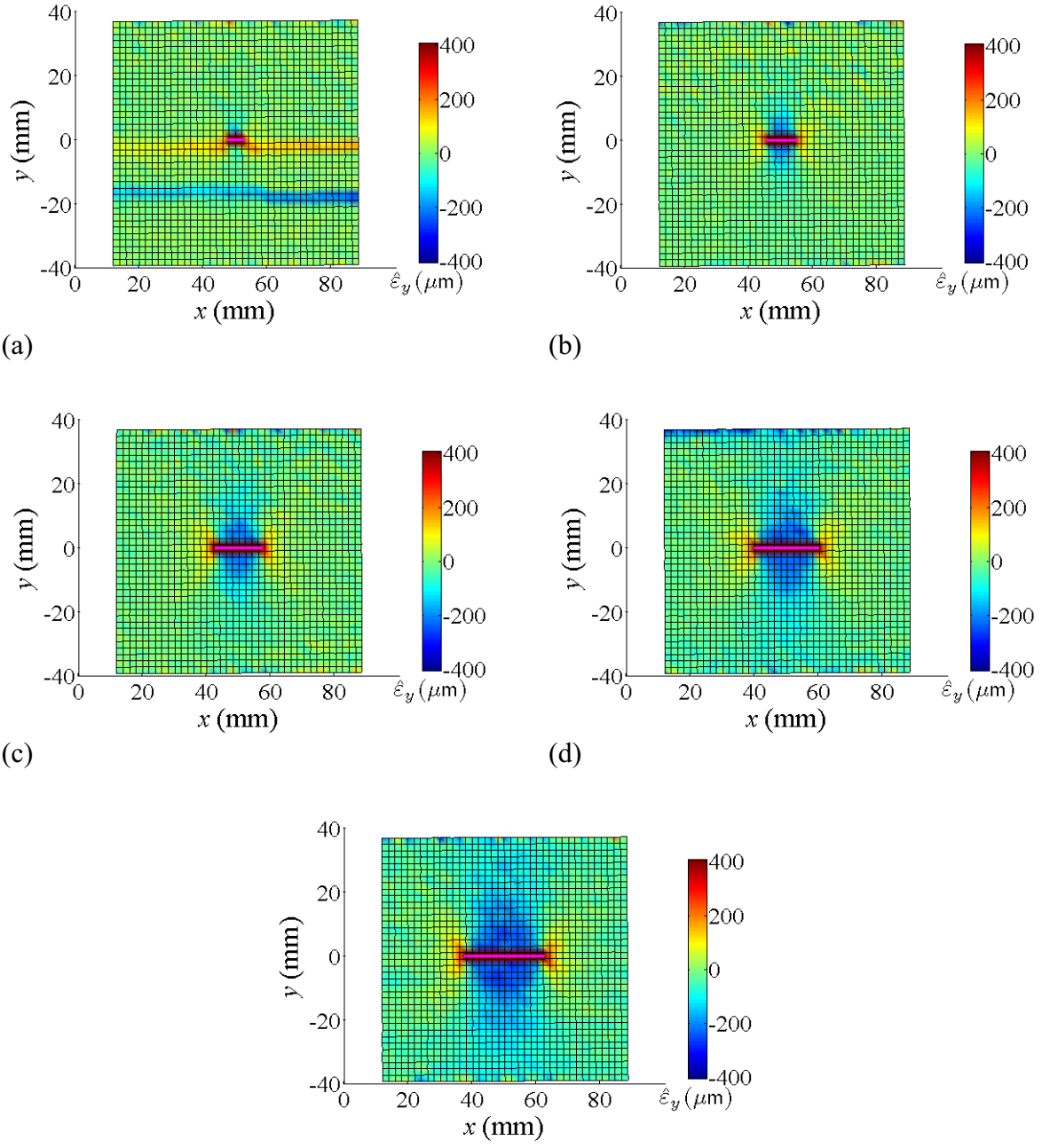

Figure D.12. Acquired normalised surface strain in the y-direction ($\hat{\varepsilon}_{yy}$) for a centre crack with various crack lengths:- (a) 5mm, (b) 10mm, (c) 15mm, (d) 20mm and (e) 25mm. The dark blue and dark red areas on the graph represent the location where $\hat{\varepsilon}_{yy}$ has exceeded the threshold $\Psi_{yy} = 400$mm/m. At $x = 0$ and $x = 100$ represents the edges of the plate and the pink line defines the location of the crack. A second-order polynomial ($n = 2$) 2D Savitzky-Golay differentiating filter was used with a filter size of 3x3 point ($m = 1$).

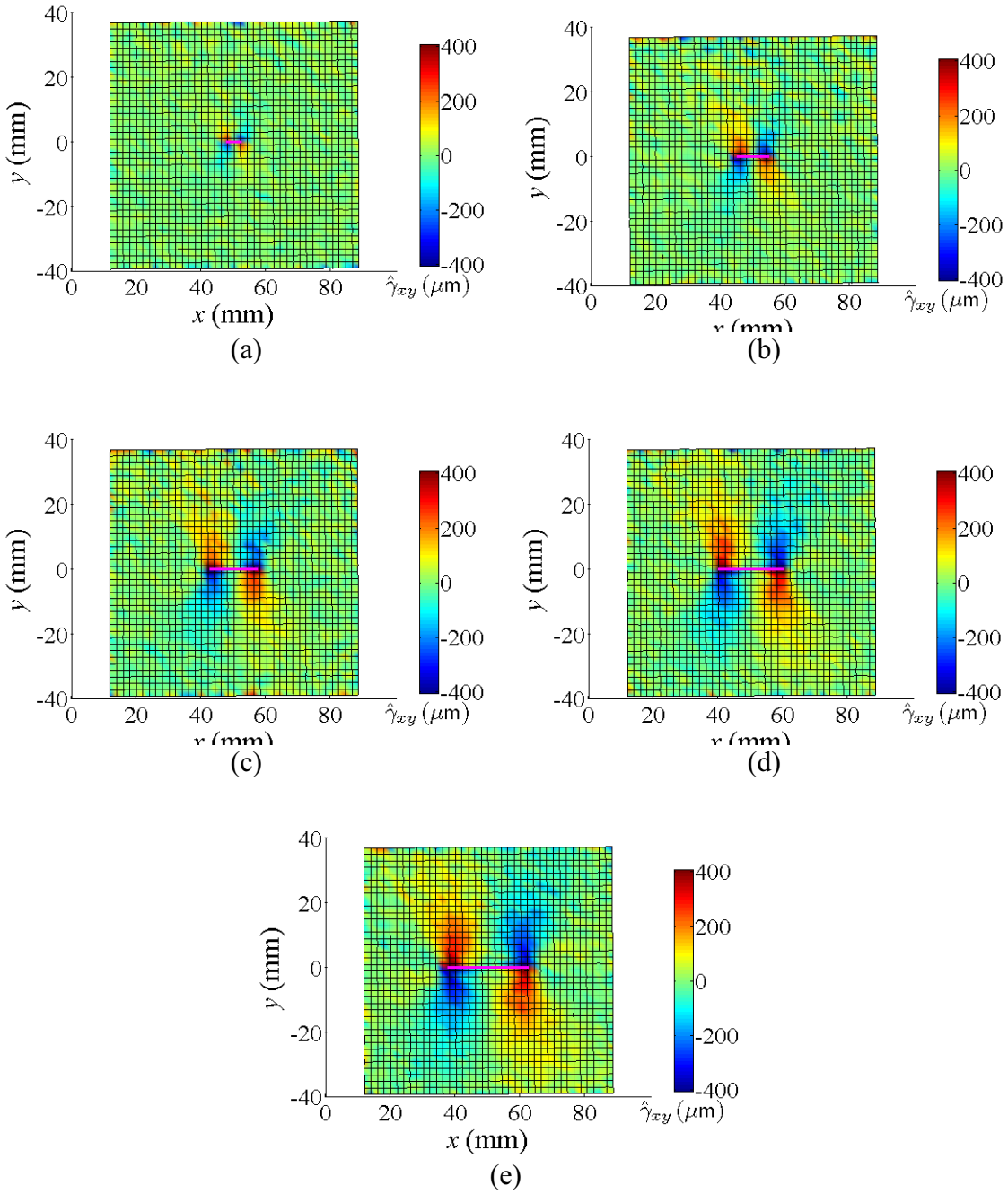

Figure D.13. Acquired normalised surface shear strains ($\hat{\gamma}_{xy}$) for a centre crack with various crack lengths:- (a) 5mm, (b) 10mm, (c) 15mm, (d) 20mm and (e) 25mm. The dark blue and dark red areas on the graph represent the location where $\hat{\gamma}_{xy}$ has exceeded the threshold $\Psi_{xy} = 400$mm/m. At $x = 0$ and $x = 100$ represents the edges of the plate and the pink line defines the location of the crack. A second-order polynomial ($n = 2$) 2D Savitzky-Golay differentiating filter was used with a filter size of 3x3 point ($m = 1$).

Appendix E. Related Publications

E.1 Referred Journal Publications

Wildy, S., Cazzolato, B. and Kotousov, A. 2010, 'Detection of delamination damage in a composite laminate beam utilising the principle of strain compatibility', *Key Engineering Materials*, vol. 417-418, pp. 269-272.

Codrington, J., Kotousov, A., Wildy, S. and Ho, S. 2010, 'Effect of plate thickness and load history on fatigue crack growth', *Key Engineering Materials*, vol. 417-418, pp. 201-204.

Nguyen, P., Kotousov, A., Ho, S. and Wildy, S. 2010, 'Investigation of thermo-mechanical properties of slurry based thermal barrier coatings under repeated thermal shock', *Key Engineering Materials*, vol. 417-418, pp. 197-200.

Wildy, S., Kotousov, A. and Codrington, J. 2008 'A new passive defect detection technique based on the principle of strain compatibility', *Smart Materials and Structures*, vol. 17, no. 4.

Wildy, S., Kotousov, A. and Codrington, J. 2008, 'New passive defect detection technique', *Australian Journal of Mechanical Engineering*, vol. 6, no. 2, pp. 101-106.

Weisbecker, H., Cazzolato, B., Wildy, S., Marburg, S., Codrington, J. and Kotousov A. 2010, 'Surface strain measurements using a 3D scanning laser vibrometer', *Experimental Mechanics*, Accepted.

E.2 Refereed Conference Publications

Wildy, S., Kotousov, A., Cazzolato, B. and Codrington, J. 2010, 'New damage detection technique based on governing differential equations of continuum mechanics. part I: out-of-plane loading', *in Proceedings of the Sixth Australasian Congress on Applied Mechanics*, Perth, Australia.

Wildy, S., Cazzolato, B., Kotousov, A. and Codrington, J. (2010) 'New damage detection technique based on governing differential equations of continuum mechanics. part II: in-plane loading', *in Proceedings of the Sixth Australasian Congress on Applied Mechanics*, Perth, Australia.

Wildy, S., Cazzolato, B., Weisbecker, H., Kotousov, A. and Codrington, J. (2010) 'New experimental strain measurement technique utilising a 3D scanning laser vibrometer', *in Proceedings of the Sixth Australasian Congress on Applied Mechanics*, Brisbane, Australia.

Wildy, S., Cazzolato, B. and Kotousov A. (2009) 'Detection of damage in beams utilising the principle of strain compatibility', *in Proceedings of the International Conference on CRACK PATHS*, Vecenza, Italy, pp. 671-678.

Cazzolato, B., Wildy, S., Codrington, J., Kotousov, A. and Schuessler, M. 2008, 'Scanning laser vibrometer for non-contact three-dimensional displacement and strain measurements', *in Proceedings of the Australian Acoustical Society National Conference*, Geelong, Australia.

Wildy, S., Kotousov, A. and Codrington, J. 2008, 'New passive defect detection technique', *in Proceedings of the Fifth Australasian Congress on Applied Mechanics*, Brisbane, Australia.

Wildy, S., Kotousov, A. and Codrington, J. 2008, 'Monitoring of crack propagation using a cluster of piezo-sensors', *in Proceedings of the Fifth Australasian Congress on Applied Mechanics*, Brisbane, Australia.

E.3 Abstract Reviewed Conference Publication

Wildy, S., Weisbecker, H., Cazzolato, B. and Kotousov, A. 2009, 'Integration of governing differential equations of continuum mechanics with scanning laser vibrometry technology for monitoring of structural damage', in Proceedings of the NDT in PROGRESS, Prague, Czech Republic.

Appendix F. Awards and Achievements

A list of conference publications that the author has been recognized for the quality of his written and oral presentation skills is presented. These publications are attached to this appendix.

Awarded fourth prize for the "Best Student Paper" at the 6th Australasian Congress on Applied Mechanics in 2010 for the paper:

> Wildy, S., Cazzolato, B., Kotousov, A. and Weisbecker, H. (2010) 'New method for accurate strain measurements utilising a 3D scanning laser Doppler vibrometer', *in Proceedings of the Sixth Australasian Congress on Applied Mechanics*, Perth, Australia, pp. 738-747.

Conference paper was chosen as one of only thirteen articles, selected from over 130 that were presented at the 5th Australasian Congress on Applied Mechanics in 2007, to be published in a special issue of the Australian Journal of Mechanical Engineering

> Wildy, S., Kotousov, A. and Codrington, J. 2008, 'New passive defect detection technique', Australian Journal of Mechanical Engineering, vol. 6, no. 2, pp. 101-105.

Awarded runners up for the “Best Student Poster Presentation” at the 5th Australasian Congress on Applied Mechanics in 2007 for the paper:

> Wildy, S., Lee, C. and Yong, S. 2008, ‘Monitoring of crack propagation using a cluster of piezo-sensors’, *in Proceedings of the Fifth Australasian Congress on Applied Mechanics*, Brisbane, Australia, pp. 366-371.